Development of a novel uncovered stent system for the management of complex aortic aneurysms

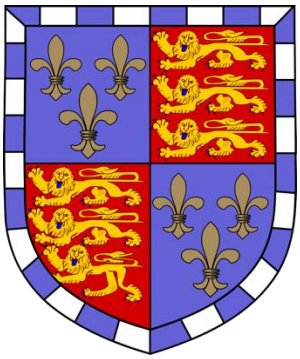

Shuo Wang

Department of Radiology

University of Cambridge

This dissertation is submitted for the degree of

Doctor of Philosophy

Christ's College

28/09/2018

Declaration

I hereby declare that except where specific reference is made to the work of others, the contents of this dissertation are original and have not been submitted in whole or in part for consideration for any other degree or qualification in this, or any other University.

The work was conducted in the Department of Radiology, University of Cambridge, under supervision of Dr Zhongzhao Teng and Professor Jonathan H Gillard.

This dissertation is the result of my own work and includes nothing which is the outcome of work done in collaboration, except where specifically indicated in the text. This dissertation contains less than 65,000 words including appendices, bibliography, footnotes, tables and equations and has less than 150 figures.

Shuo Wang

28/09/2018

Acknowledgements

Firstly, I would like to express my very great appreciation and deep gratitude to my supervisors, Dr Zhongzhao Teng and Professor Jonathan H Gillard. They offered me the opportunity to start the doctoral degree in Cambridge and have been supporting me from the very first day. Dr Teng inspired me to purse the research of clinical biomechanics and provided me continuous guidance with great knowledge and patience. Professor Gillard has created such an open environment in our group, where the collaborations between clinicians and engineers are extremely close. He gave me enormous freedom to explore my interests and kept my progress on schedule. I feel incredibly privileged to have them as my supervisors.

I wish to thank various people for their contribution to this project. I would like to thank Mr Aziz Tokgoz for the collaborations on material tests and enlightening discussions. I am very thankful to Dr Yuan Huang for his expertise on statistics and image processing. I would like to express my special thanks to Dr Yongxue Zhang, Dr Yanqing Chen, Dr Jiaxuan Feng, Professor Qingsheng Lu, Dr Adam Brown, Dr Umar Sadat, Dr Ammara Usman, Dr Priya Sastry for collecting the tissue samples and providing imaging data, as well as sharing their invaluable clinical insights. I am also thankful to Ms Nichola Figg and Professor Martin R Bennet for their guidance in histological analysis. I want to thank Mr Hao Li, Dr Jianmin Yuan, Mr Pascal Ruetten for their helpful suggestions in MRI. I am thankful to Mr Richard Black for the maintenance of computer clusters.

I would like to acknowledge the China Scholarship Council for funding my PhD. I am thankful to Christ's College and Cambridge Philosophical Society for travel grants.

I want to express my thanks to college tutors, Professor David Newman and Professor Gábor Betegh, for their encouragements and suggestions. I wish to thank Dr Chao Li, Mr Xiaojian She, Mr Ran Guan, Dr Jing He, Ms Elyn Shen and all my friends for their help in the life.

I would like to thank all my family for their love and support. I would like to give my deepest thanks to my wife Ms Xiaoyue Wang for her unconditional accompanying and support.

Abstract

Endovascular aortic repair (EVAR) is a minimally invasive alternative to open surgery for the treatment of aortic aneurysms (AA). However, standard EVAR is not applicable to complex AA with involvement of vital branches, which could be occluded by the endograft. As an emerging technique, the multiple overlapping uncovered stents (MOUS) have been proposed to manage complex lesions. MOUS was used to modulate the flow pattern inside the aneurysm sac, and promote the thrombus formation followed by the aneurysm shrinkage. In this dissertation, we sought to investigate the mechanism of MOUS-induced flow modulation and the key factors associated with the success of this novel technique:

- The mechanical behaviour of AA was characterised by uniaxial material tests (Chapter 4). A Bayesian framework was proposed for material constants identification. They were found correlated to the microstructure of tissue fibre network and were capable in differentiating tissue types.

- Solid-to-solid interaction and one-way fluid-solid interaction (FSI) analysis was performed based on patient-specific computer tomography angiography (Chapters 5&6). Structural stress concentrations were observed within the landing zones, which increased with the number of stents deployed. In the parameter studies (Chapter 6), the overall porosity was identified as the dominant factor of the flow-diverting outcome, while cross-stent structures of MOUS had limited influence.

- The pathological effect of structural stress concentration induced by an implanted device was further studied in rabbit models (Chapter 7). The wall structural stress and fluid shear stress were obtained from FSI analysis based on magnetic resonance imaging (MRI), and correlated to plaque characteristics. Both high structural stress and low fluid shear stress were found correlated to plaque initialisation and increased inflammation.

Overall, MOUS modulates the blood flow with robust performance under different overlapping patterns. Image-based biomechanical analysis can optimise MOUS design and can contribute to personalised pre-surgery planning.

Contents

List of Figures

List of Tables

List of Publications

Peer-reviewed journal publications directly relevant to this thesis (* equal authorship)**:**

1. **Shuo Wang***, Aziz Tokgoz*, Yuan Huang, Yongxue Zhang, Jiaxuan Feng, Priya Sastry, Chang Sun, Nichola Figg, Qingsheng Lu, Michael PF Sutcliffe, Zhongzhao Teng, Jonathan H Gillard. *IEEE Transactions on Biomedical Engineering*. 2018.
2. **Shuo Wang**, Yongxue Zhang, Jiaxuan Feng, Yuan Huang, Aziz Tokgoz, Umar Sadat, Jonathan H Gillard, Qingsheng Lu, and Zhongzhao Teng. Influence of overlapping pattern of multiple overlapping uncovered stents on the local mechanical environment: A patient-specific parameter study. *Journal of biomechanics*. 2017.
3. Zhongzhao Teng, Jianmin Yuan, Jiaxuan Feng, Yongxue Zhang, Adam J. Brown, **Shuo Wang**, Qingsheng Lu, and Jonathan H Gillard. The influence of constitutive law choice used to characterise atherosclerotic tissue material properties on computing stress values in human carotid plaques. *Journal of biomechanics*. 2015.

Manuscripts under review/revision/in preparation (* equal authorship)**:**

1. Aziz Tokgoz*, **Shuo Wang***, Priya Sastry, Chang Sun, Nichola Figg, Yuan Huang, Martin R. Bennett, Sanjay Sinha, Jonathan H Gillard, Michael PF Sutcliffe, Zhongzhao Teng. *Journal of Thoracic and Cardiovascular Surgery*. (*under review*).
2. **Shuo Wang**, Yongxue Zhang, Jiaxuan Feng, Yuan Huang, Aziz Tokgoz, Umar Sadat, Jonathan H Gillard, Qingsheng Lu, and Zhongzhao Teng. Influence of cross-stent structure and optimised design of multiple overlapping uncovered stents. (*in preparation*)

Conference presentation

1. **Shuo Wang**, Yongxue Zhang, Jiaxuan Feng, Yuan Huang, Aziz Tokgoz, Umar Sadat, Jonathan H Gillard, Qingsheng Lu, and Zhongzhao Teng. Influence of multiple overlapping uncovered stents on the local mechanical environment: porosity and cross-stent structure. *8th World Congress of Biomechanics*, Dublin, 2018 July.
2. Aziz Tokgoz*, **Shuo Wang***, Priya Sastry, Chang Sun, Nichola Figg, Yuan Huang, Martin R. Bennett, Sanjay Sinha, Jonathan H Gillard, Michael PF Sutcliffe, Zhongzhao Teng. Fracture behaviour and microstructure-mechanics relationship of human aortic aneurysms. *8th World Congress of Biomechanics*, Dublin, 2018 July.
3. **Shuo Wang**, Yongxue Zhang, Jiaxuan Feng, Yuan Huang, Umar Sadat, Jonathan H Gillard, Qingsheng Lu, and Zhongzhao Teng. MOUS: a novel management strategy for aortic aneurysms, *Endovascology*, Shanghai, 2016 October. (*best oral presentation award*)

Other publications produced during the period of this thesis

1. Chao Li, **Shuo Wang**, Jiun-Lin Yan, Rory J Piper, Hongxiang Liu, Turid Torheim, Hyunjin Kim et al. Intratumoral heterogeneity of tumor infiltration of glioblastoma revealed by joint histogram analysis of diffusion tensor imaging. *Neurosurgery*. 2018.
2. Chao Li, **Shuo Wang**, Angela Serra, Turid Torheim, Jiun-Lin Yan, Natalie R. Boonzaier, Tomasz Matys, Mary A. McLean, Florian Markowetz, Stephen J. Price. Multi-parametric and multi-regional histogram analysis of MRI: revealing imaging phenotypes of glioblastoma correlated with patient Survival. *European Radiology*. 2018.

Other conference presentations

1. Hao Li, **Shuo Wang**, Andrew Priest, Martin M Graves and David Lomas. An optimised subtraction approach for subtractive NCE-MRA techniques based on robust regression using the deviation angle. *30th annual SMRA conference*, Glasgow, 2018 August. (*best poster presentation*)
2. Chao Li, **Shuo Wang**, Angela Serra, Turid Torheim, Jiun-Lin Yan, Natalie R Boonzaier, Tomasz Matys, Mary A McLean, Florian Markowetz, Stephen J Price. Multi-parametric and multi-regional histogram analysis of MRI: revealing imaging phenotypes of glioblastoma correlated with patient survival. *ISMRM Annual Meeting*, Paris, 2018 June. (*Magna Cum Laude Merit*)
3. Chao Li, **Shuo Wang**, Turid Torheim, Florian Markowetz Stephen J Price, S. Mutual information: depicting the interdependence of perfusion and diffusion magnetic resonance imaging in glioblastoma patients. *ISMRM Annual Meeting*, Paris, 2018 June.
4. Hao Li, **Shuo Wang**, Andrew Priest, Martin M Graves and David Lomas. An optimised subtraction approach for subtractive NCE-MRA techniques based on principal component analysis. *ISMRM Annual Meeting*, Paris, 2018 June.

Glossary

2D	Two-dimensional
3D	Three-dimensional
AA	Aortic aneurysm
AAA	Abdominal aortic aneurysm
CCA	Common carotid artery
CD68	Cluster of differentiation 68
CE-MRA	Contrast-enhanced magnetic resonance angiography
CFD	Computational fluid dynamics
CT	Computerised tomography
CTA	Computerised tomographic angiography
CVD	Cardiovascular disease
ECG	Electrocardiographic
ECM	Extracellular matrix
EEL	External elastic lamina
EVAR	Endovascular aneurysm repair
EVG	Verhoeff–van Geisen
FC	Fibrous cap
^{18}FDG-PET	18-fluorodeoxyglucose positron emission tomography
FEM	Finite element method
FSE	Fast spin echo
FSI	Fluid-structure interaction
Gd	Gadolinium

HE	Haematoxylin and Eosin
HDL	Low density lipoprotein
HU	Hounsfield unit
IEL	Internal elastic lamina
ILT	Intraluminal thrombus
IPH/T	Intraplaque haemorrhage/thrombus
IVUS	Intravascular ultrasound
LDL	Low density lipoprotein
MCMC	Markov Chain Monte Carlo
MFM	Multilayer flow modulator
MMP	Matrix metalloproteinase
MOUS	Multiple overlapping uncovered stents
MRA	Magnetic resonance angiography
MRI	Magnetic resonance imaging
MTH	Mean thickness of healthy section
MWT	Maximum wall thickness
OLS	Ordinary least square
OSI	Oscillatory shear index
PAR	Plaque area ratio
PC	Phase-contrast
PDF	Probability density function
PET	Positron emission tomography
PSR	Picrosirius Red
RCT	Randomised clinical trial
RGD	Arg-Gly-Asp
ROI	Region of interest
ROS	Reactive oxygen species
RR	Relative risk
RRT	Relative residence time

$\overline{RRT}$	Normalised relative residence time
SEDF	Strain energy density function
SNR	Signal-to-noise ratio
SSFP	Steady-state free precession
TAA	Thoracic aortic aneurysm
TAAA	Thoracoabdominal aortic aneurysm
TAWSS	Time-averaged wall shear stress
T	Tesla
TIMP	Tissue inhibitor of metalloproteinase
TOF	Time-of-flight
US	Ultrasonography
VSMC	Vascular smooth muscle cells
VSS	Vascular structural stress
WSS	Wall shear stress

Chapter 1 Introduction

In this chapter, the pathophysiology of aortic aneurysms is summarised, including the biological and biomechanical factors that may contribute to the formation and development of aortic aneurysms. The current clinical management and challenges of complex aortic aneurysms are reviewed. Moreover, as an emerging technique, the rationale and features of multiple overlapping uncovered stents are discussed. The purpose of this chapter is to discuss the underlying processes during the structural degradation of aortic aneurysm, providing an overview of the disease and treatment.

1.1 Overview of aortic aneurysms

The term aneurysm originates from the ancient Greek word aneurusma, which means "a widening/an opening" [1]. Aortic aneurysm (AA) is defined as a permanent localised dilation of the aorta by more than 50% of its original diameter (Figure 1.1) [2]. Aneurysm is the second most frequent disease of the aorta following atherosclerosis. It is estimated that 1-2% of the population have AAs with an increased prevalence of up to 10% in older age groups (>65 years) [3]. Risk factors for AA formation include increasing age, male sex, high blood pressure, smoking and family history.

Most AAs are asymptomatic until catastrophic rupture, which causes life-threatening haemorrhage or sudden death without apparent prior warnings [4]. The mortality rate of ruptured AAs is up to 90%, which is ranked as the 13th most common cause of death [5]. According to the latest statistics from Global Burden of Disease Study, AAs are the primary cause of approximately 8,000 deaths per year in the United Kingdom [6,7]. A better understanding of the anatomy and structure of aorta, and the pathophysiology of AAs are crucial for their clinical management.

1.2 Normal aorta

The aorta is the largest artery of the human body (Figure 1.1A), which delivers about 200 million litres of oxygenated blood throughout the body, with more than 3.0 billion heartbeats in a lifetime [8]. The aorta expands and contracts repeatedly to help propel blood distally through the systemic circulation, while withstanding pulsatile loadings from the blood flow. Therefore, the structural integrity and durability are essential to maintain the normal pumping function.

1.2.1 Aortic anatomy

Anatomically, the aorta ascends from the left ventricle of the heart and extends inferiorly to the aortic bifurcation, where it diverges into the left and right common iliac arteries [4]. The aorta is classically divided into two sections, namely the thoracic and abdominal aorta, by their relative locations to the diaphragm (Figure 1.1A).

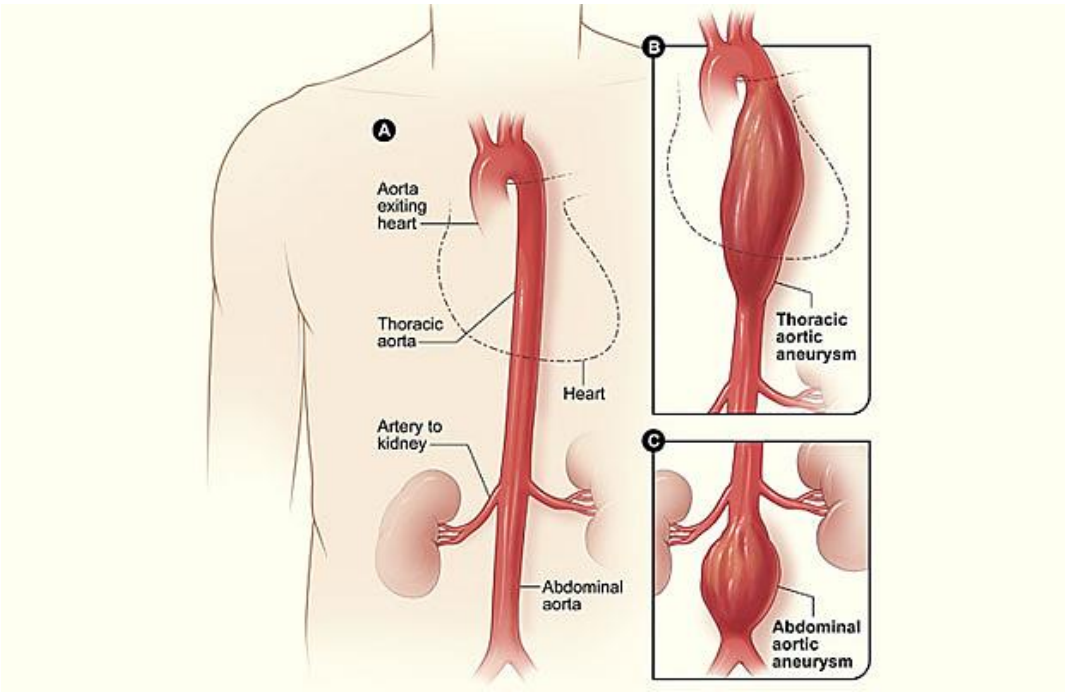

Figure 1.1 Types of aortic aneurysm: **(A)** A normal aorta. **(B)** A thoracic aortic aneurysm, which is located behind the heart. **(C)** An abdominal aortic aneurysm, which is located below the renal arteries. (Reproduced with permission from National Institutes of Health)

Accordingly, aortic aneurysms can be generally classified as a thoracic aortic aneurysm (TAA) (Figure 1.1B) or as abdominal aortic aneurysm (AAA) (Figure 1.1C), involving different aortic segments. AAs that co-exist in both segments of the descending aorta and abdominal aorta are termed as thoracoabdominal aortic aneurysm (TAAA). Although aneurysms may arise at any site along the course of aorta, they most frequently occur in the abdominal aorta or at the descending portion of thoracic aorta.

1.2.2 Structure of the aortic wall

The healthy aorta is composed of three distinct layers: the intima, media and adventitia (Figure 1.2). These three layers have different extracellular components and functions, separated by the internal elastic lamina (IEL) and the external elastic lamina (EEL) [9]:

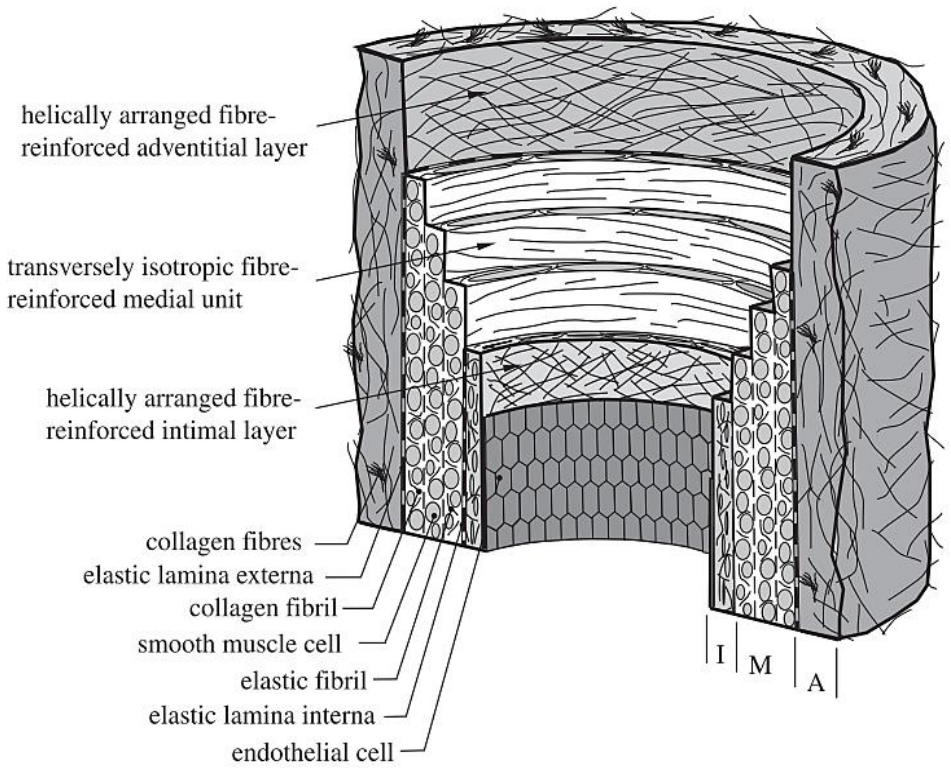

Figure 1.2 Idealised architecture of a healthy human aorta. The healthy aorta is composed of three distinct layers: the intima, media and adventitia. (Reproduced from Gasser *et. al* [9], with permission from Elsevier)

- **Intima (I)**: the innermost layer consists of a monolayer of endothelial cells overlying a thin basal membrane and a subendothelial layer of collagen fibres. The intima is in direct contact with the blood providing a smooth non-thrombogenic surface for the blood flow [10].
- **Media (M)**: the middle layer is composed of extracellular connective elements including a network of elastin, collagen, proteoglycans and vascular smooth muscle cells (VSMCs). Multiple layers of elastic lamellae separate the media into several transversely isotropic medial units. The media is the main load-bearing layer which provides elasticity of the normal aorta under physiological conditions.
- **Adventitia (A)**: the outermost layer is primarily composed of thick collagen fibres which are arranged in helical structures. This outer layer is surrounded by loose connective tissue. The adventitia provides additional structure and support to the aorta.

The three-layer composite structure provides the overall elasticity of the aorta. Elastin (elastic fibres) and collagen are two important structural components of the aortic wall, which however have different mechanical properties. Elastin is easily stretched (up to 70% of its original length), which helps the recoil process of the aorta by storing energy during cardiac contraction and releasing the energy during cardiac relaxation [11]. Compared to elastin, collagen fibres have much higher stiffness and tensile strength (about 20 times more than elastin), but lower distensibility. Specifically, the collagen fibres are coiled up under a stress-free state, and are only engaged to bearing loadings when the stretch exceeds a threshold. In contrast, the elastin is engaged from the initial stretch. As a result, the elasticity of aortic wall is non-linear in the inflation test, with the transition pressure from distensible to stiff behaviour near 80 mmHg [8]. A more distensible behaviour characterising elastin is observed at a lower blood pressure, whereas a stiffer behaviour characterising tensed collagen is observed at a higher pressure. In a normal aorta, only about 6-7% collagen fibres are engaged during physiological deformation [12,13]. Therefore, elastin is the principle load-bearing element for normal conditions, while the collagen acts as a stiff reinforcing ‘safety net’.

The aortic architecture is not uniform along the aorta. The abdominal aorta is thinner with only about 28 layers of elastic lamellae, compared to 35-56 layers in the thoracic aorta [14]. The greater concentration of elastin in the thoracic aorta leads to more compliance than the abdominal

aorta. These differences in wall structure may contribute to the susceptibility of aneurysm formation, which will be discussed in Section 1.4.

1.2.3 Aging of the aorta

Increasing age is a well-known risk factor for many aortic diseases including AAs [4]. Vascular aging starts from infancy being "identifiable" at around 40 years of age. The morphological changes include the enlargement of diameter and the elongation of total length [10]. Another significant change with increasing age is the stiffening of aorta, which is caused by microstructural changes within the aortic wall. A positive correlation between increasing age and arterial stiffness has been demonstrated in a series of studies by measuring pulse wave velocity [15–18].

As mentioned above, the aortic compliance is dependent on the relative composition ratio of elastin and collagen. The decreasing compliance is caused by the fragmentation of elastin and alteration of the collagen. A fracture of the elastic lamella is estimated to occur after around 1 billion cycles, equating to an age of approximately 40 years [10]. Meanwhile, the regenerative potential of elastin diminishes: the expression of tropoelastin (the precursor of elastin) decreases by 50% in each age decade [19]; the quantity of smooth muscle cells, where the elastin is synthesised, also decreases with increasing age [19]. Moreover, following the disorganisation and loss of interlaminar cross-links, the elastic lamellae are further apart and filled with altered collagen – which becomes thicker and more linear in arrangement with increasing age. As a result, the age-related remodelling of aorta alters the biomechanical properties of the aortic wall, which may cause pathological changes.

1.3 Pathophysiology

Similarly to the aging process, the formation and development of AAs are closely related with remodelling of the aortic wall. The pathophysiology of AA is characterised by the extensive structural degradation, which is frequently observed in histological examinations (Figure 1.3). In 1987, Campa *et al.* reported thinning of the media, disruption of the connective tissue structure, and loss of elastin within AAs [20]. Following studies reported that, collagen contents

are also decreased in aneurysmal walls, with increased ratio of collagen to elastin [21] and increased number of collagen cross-links [22]. Along with the structural changes in ECM, the cell density of VSMCs is also reported to decrease [23].

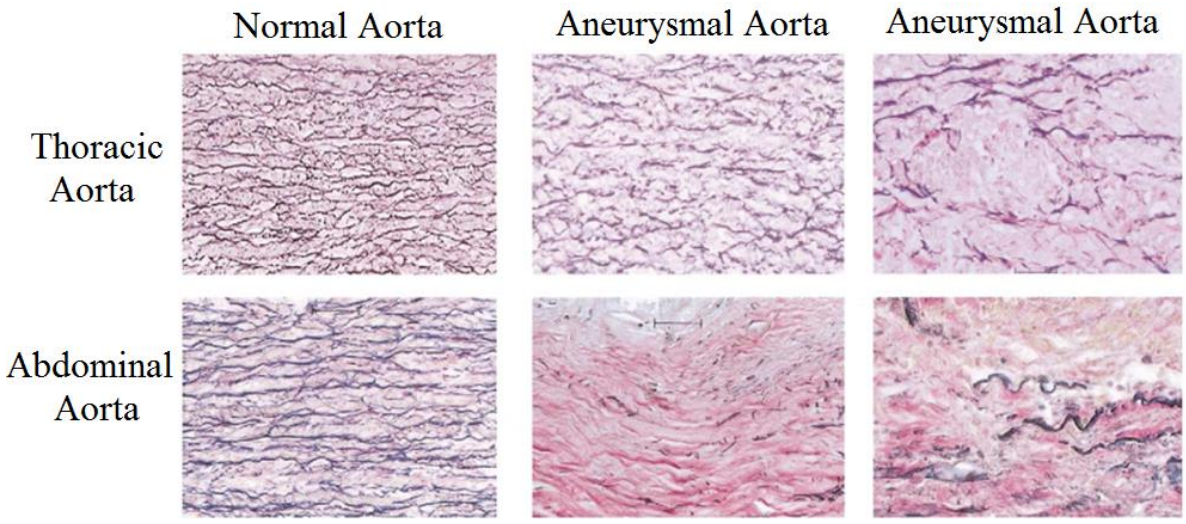

Figure 1.3 Histopathology of aortic aneurysms. Representative sections of aortic wall tissue stained with Verhoeff–van Geisen (EVG) for elastin (dark purple fibres). Extensive structural degradation is observed in both TAAs and AAAs. Compared with normal aorta, TAAs exhibited disruption, fragmentation and disorganisation of medial elastic fibres, and loss of nuclei (upper panels). AAAs exhibited more extreme destruction of medial elastin and replacement by fibrocollagenous extracellular matrix (pink), along with depletion of medial smooth muscle cells and mononuclear inflammatory cell infiltration in direct association with areas of elastic fibre degeneration (lower panels). (Reproduced from Absi *et al.* [24], with permission from Elsevier)

Although the pathophysiology of different aortic segments may differ, the formation of AAs is well recognised as the consequence of structural degradation within the aortic wall. Below is an introduction of several important factors resulting in the structural degradation, including proteolytic degradation and inflammation [3].

■ Proteolytic degradation

Proteolytic degeneration is a well-known factor associated with AA formation and progression (Figure 1.4, left). The underlying biochemical process is the degradation of extracellular matrix (ECM), which is primarily catalysed by matrix metalloproteinases (MMPs). So far, about 30 individual proteinases have been identified and classified into several categories of MMPs, including collagenases, gelatinases, stromelysins, matrilysins, membrane-type (MT)-MMPs [25]. The most frequently overexpressed proteinase in aortic aneurysms are MMP-1 (collagenase), MMP-2 (gelatinase A), MMP-3 (stromelysin) and MMP-9 (gelatinase B), which catalyse the degradation of elastin and collagen [26].

Since the first report of increased MMP production within aneurysms in 1991 [27,28], the roles of different MMPs in the development of AAs have been extensively investigated, in both human and animal subjects. Expression of MMP-2 and MMP-9 are higher in human aneurysmal tissues than normal arterial tissues [29,30]. Studies using animal aneurysm models also supported the role of MMP-2 and MMP-9 in aneurysm formation. In a previous study, MMP-2 and MMP-9 knock-out mice models did not form aneurysms after the abluminal application of calcium chloride ($CaCl_2$). By contrast, the increased level of MMP-2 and MMP-9 by reinfusing competent macrophages into above models enabled aneurysm formation [31]. In other studies, increased production of MMP-1, MMP-8 and MMP-9 was found to associate with AA rupture risk [32,33]. In addition to the increased expression of MMPs, the abnormal regulation of MMP levels has been found to be important for aneurysm formation. The activity of MMPs is primarily controlled by the tissue inhibitor of metalloproteinase (TIMP) at the molecular level. The imbalance between MMPs and TIMPs may contribute to AA formation, which is supported by the decreased concentrations of TIMPs in human aneurysm tissues [34]. Other pathways regulating MMPs include: augmented gene expression, post-translational activation by the cleavage of pro-MMP protein, by MMP-MMP interactions and by plasmin, thrombin and reactive oxygen species (ROS) [10,25,35,36].

The contribution of MMPs to AA pathophysiology has been validated by the beneficial effect of medications reducing MMPs levels. In several small randomised phase 2 trials, doxycycline, a recognised inhibitor of MMPs, was related to a reduced expansion rate of AA [37].

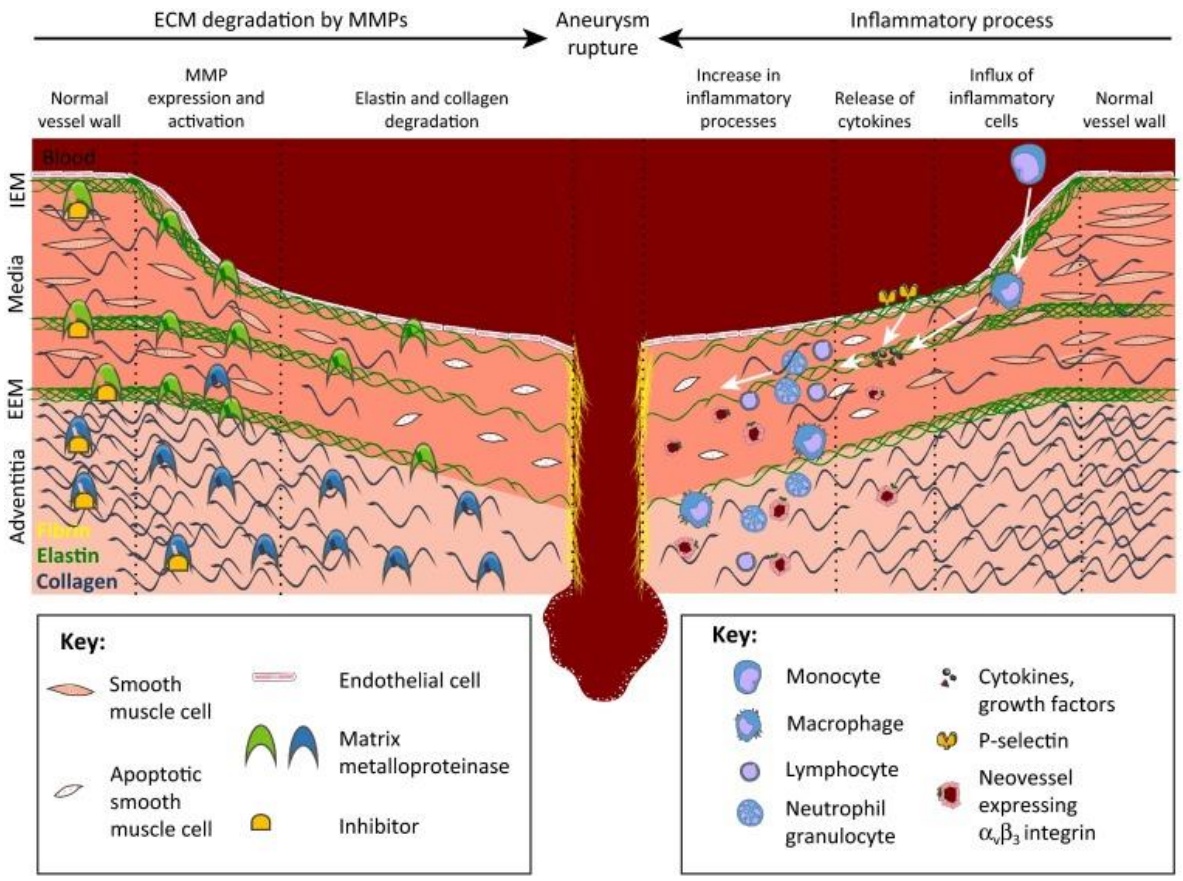

Figure 1.4 The schematic depicts the pathophysiological processes associated with the development of aneurysms, which involve two different but connected key processes: the degradation of extracellular matrix proteins and the occurrence of inflammatory processes. (From the left) Degradation of the ECM, including elastin and collagen, catalysed by matrix metalloproteinases (MMPs) is shown. The imbalance between MMPs and their inhibitors (including /2-macroglobulin) results in aneurysm initiation and progression. (From the right) Proinflammatory cells (macrophages, neutrophils, lymphocytes, etc.) migrate from the vascular lumen into the aortic wall via adhesion molecules (e.g., P-selectin), secreting various factors including cytokines and growth factors. This leads to further recruitment of proinflammatory cells. Angioneogenesis occurs simultaneously with inflammatory processes in the vascular media, providing an additional route of entry for proinflammatory cells. The production of cytotoxic mediators leads to a reduction of smooth muscle cells density (apoptotic smooth muscle cells) and a thinning of the tunica media. Owing to the combination of inflammation and ECM degradation, as well as the biomechanical factors, the aortic diameter increases, ultimately resulting in the rupture of the aortic vessel wall with potentially lethal consequences. Abbreviations: EEM, external elastic membrane; IEM, internal elastic membrane. (Reproduced from Brangsch *et al.* [38], with permission from Elsevier)

■ Inflammation

The role of inflammation in different arterial diseases is well established, which is closely related to the degradation of ECMs [39]. In 1981, Rose and Dent reported the inflammatory findings in AAAs, where they found mild inflammation in 73% and moderate inflammation in 16% of resected AAAs [40]. Subsequently, the quantities of lymphocytes and macrophages were found greater in AAAs than in normal aortas [41]. Similarly, increased levels of various pro-inflammatory cytokines were observed in aneurysms compared to normal control [42]. In addition, increased levels of other acute-phase proteins were reported in the plasma and the aortic wall [43]. The inflammatory response is also supported by the studies using 18-fluorodeoxyglucose positron emission tomography imaging (^{18}FDG-PET) with and advanced magnetic resonance imaging (MRI) with contrast media such as ultrasmall superparamagnetic iron oxide [25,44].

Most of the inflammatory mediators derive from infiltrating macrophages; Lymphocytes, aortic endothelium cells and smooth muscle cells also contribute to the inflammatory milieu [3]. These immune cells invade the aortic wall, become activated, and create an inflammatory environment through the release of a cascade of cytokines (Figure 1.4, right). This process results in the expression of cell adhesion molecules, increased protease expression, and the release of ROS causing degradation of the ECM through the activation of MMPs [34]. Higher cytokine levels in ruptured AAs than asymptomatic AAs were reported in some studies [45]. Several animal studies have also supported that increased inflammation promotes the development of AAs [34]. However, the mechanism of molecular signalling pathways that modulate inflammatory cell recruitment in AAs remain unclear.

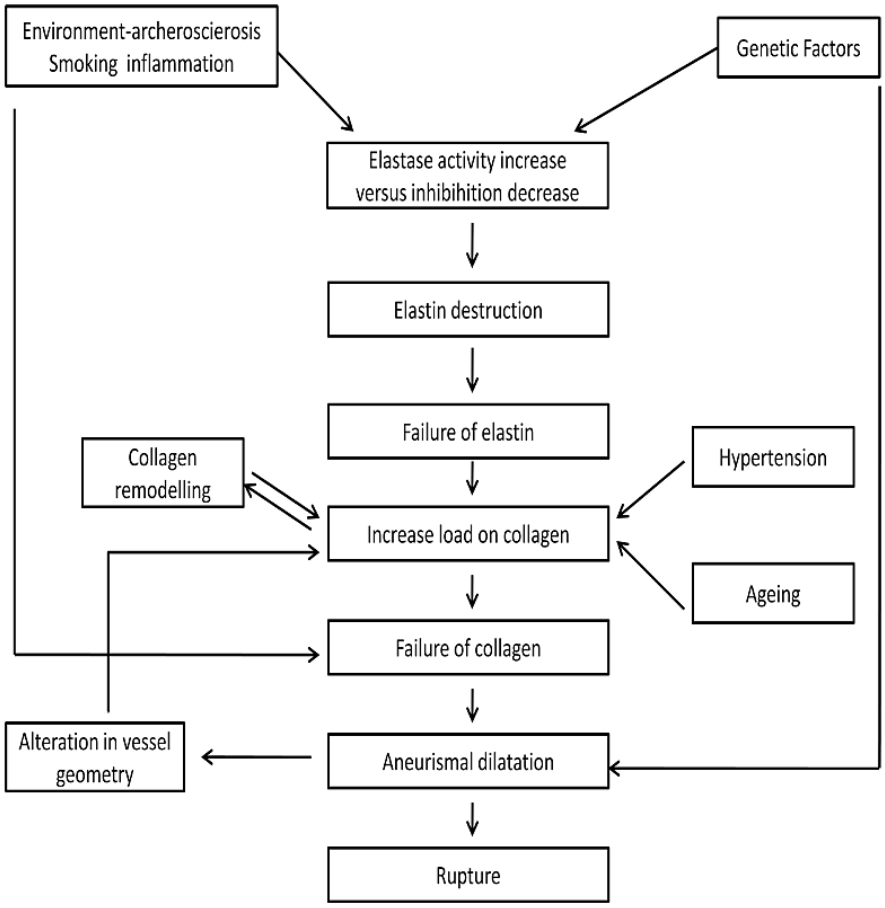

Figure 1.5 Chart showing the general pathogenesis of aortic aneurysm. (Reproduced from MacSweeney *et al.* [46], with permission from Elsevier John Wiley and Sons).

As discussed above, the pathophysiology of AA is a chronic and multifactorial process that involves biological and biochemical factors. The general pathogenesis of an AA is demonstrated in Figure 1.5. In most cases, the initial degeneration is a reduction of elastin content as a result of proteolytic processes [47], regulated by genetic and environmental factors. Along with the elastin destruction, the collagen remodelling and the relative balance between elastin and collagen are critical for the development of AA. In earlier stages of the disease progression, production of collagen is up-regulated to compensate the loss of elastin [48], which leads to the expansion of aorta. In later stages, the degradation of collagen results in progressive dilation. In an *in vitro* study, collagen degradation was found to be the ultimate cause of AA rupture [48].

1.4 Biomechanical factors

The higher incidence of AA formation in the abdominal aorta compared with other aortic segments suggests a predisposition in this area. Adverse blood flow patterns and relative structural deficiencies in the abdominal aorta are considered as important biomechanical factors associated with the development of AA.

■ Wall shear stress

The bifurcation of the aorta results in turbulence and areas of abnormal wall shear stress (WSS) [49]. In physiological conditions, optimal WSS is essential to maintain the survival, quiescence and alignment of endothelial cells in the direction of the blood flow. It is also central to the secretion of vasoactive substances that promote either vasodilatation or anticoagulation. In pathological conditions, however, both higher and lower WSSs than normal are reported to be associated with the development of AAs. In areas of high WSS, the production of endothelial nitric oxide, MMP-2 and MMP-9, and transforming growth factor-beta (TGF-β) are found to be up-regulated in endothelial cells [50]. On the other hand, in areas of low wall shear stress, nuclear factor-κB (NF-κB) and endothelin-1 were found overexpressed in endothelial cells [51]. The abnormal WSS can trigger the pathological remodelling of the aortic wall, leading to aneurysm formation. Vollmar *et al.* studied 329 subjects who lost a leg in World War II and 702 war veterans [52]. They observed AAAs in 6% of the amputees compared to 1% of the non-amputees, concluding that the abnormal flow pattern caused a late damage to the aorta. With the expansion of AAs, the turbulent flow inside the aneurysm sac would cause separated regions of rotational flow with vertical structures, which may result in further aortic remodelling and disease progression [53,54].

■ Structural loading

In addition to WSS, the structural loading within the aortic wall is also considered important to AA formation and development. As mentioned in Section 1.2.2, the physiological loading from blood pressure is mainly absorbed by the lamellar units within the aortic media. The abdominal aorta is more susceptible to the elastin breakdown, due to the higher structural loading withstood by each lamellar unit – there are more lamellar units in the abdominal aorta

compared with thoracic aorta [14], as well as the higher pulse pressure in the abdominal aorta. The structural loading also contributes to aneurysm progression. It can be approximately estimated by the Laplace's Law [55]:

$$\bar{\sigma} = \frac{pD}{2h} \tag{1.1}$$

where $\bar{\sigma}$ is the averaged circumferential stress or wall tension; p is the blood pressure; D and h denote the inner diameter and thickness of the vessel, respectively. The structural loading within the aortic wall was demonstrated to increase proportionally during the expansion of aorta, which accelerates the structural breakdown of elastin and collagen elements. Moreover, high wall tension was reported to up-regulate the MMP promoter activity, which could cause further degradation of the aortic wall [56,57]. On the other hand, to maintain the structural integrity, vascular cells within the aortic wall attempt to produce more elastin to repair the degrading ECM, which is evidenced by a four to six-fold increase in tropoelastin level in resected aneurysm samples [58]. However, the compensatory elastin deposition is not organised, as demonstrated by a nine-fold reduction of desmosine which is a marker for mature elastin cross-linking [58]. Therefore, the disordered elastin does not restore the aortic elasticity. As a result, the imbalance between increasing structural loading and degrading aortic wall results in the progressive expansion of AAs. The ultimate rupture occurs when the structural loading exceeds the local strength of the aortic wall [59].

1.5 Clinical management

AA is clinically stratified and managed based on the characteristics of this disease – a history of progressive expansion with an increasing rupture risk [60]. The expansion rate of AAs varies 1-6 mm/year, depending on aetiological types and locations of the AA [61,62]. Rupture risk increases rapidly when the aortic diameter exceeds a threshold (around 60 mm for the ascending aorta and 70 mm for the descending thoracic and abdominal aorta) [62]. Therefore, the primary goal is to slow the expansion rate and reduce the risk of rupture.

According to the guidelines of the European Society of Cardiology [62], emergent aneurysm repair should be undertaken for ruptured AAs to achieve the best chance for survival. An urgent AA repair is also suggested for patients with non-ruptured but symptomatic AAs, if the risk of aortic repair is not prohibitive. For asymptomatic AAs, however, the decision for elective repair relies on the assessment of the rupture risk, compared to the expected risk of perioperative morbidity and mortality associated with aneurysm repair [60]. Two randomised clinical trials (RCT), the Aneurysm Detection and Management (ADAM) and the UK Small Aneurysm Trial (UKSAT), have compared the benefits of early surgery for AAs against the surveillance strategy. Summarising the results, the annual risk of AA rupture was similar with, or lower than the repair risk for small- and medium-sized aneurysms (<55 mm in diameter) [63–67]. Therefore, for patients with small AAs, it is regarded as a safe strategy to take conservative management with periodic imaging surveillance of the asymptomatic aneurysm until it reaches 55 mm or becomes symptomatic or fast growing (> 10 mm/year). For good-risk surgical candidates with AA diameter >55 mm, elective repair (open or endovascular) is recommended. The threshold for AA repair is not absolute and depends on the patient's status and the aneurysm location. Patients with syndromic AAs such as Marfan syndrome, should generally undergo elective repair at a smaller aortic diameter (>45 mm). Other factors that need to be accounted for include the patient's age and gender, expansion rates, and the presence of other peripheral aneurysms.

The potential use of pharmacological therapies to suppress the growth rate of small AAs includes the use of beta-adrenergic receptor-blocking agents to diminish aortic stress, and the use of MMP inhibitors [68]. However, none of these approaches have been demonstrated to provide benefits in RCTs [69,70].

Currently, elective aneurysm repair remains the most effective management for preventing rupture. The purpose of aneurysm repair is to restore the biomechanical balance between the structural loading and the aortic wall structure. This can be accomplished by open surgery, which replaces the diseased segment with prosthetic graft, or by endovascular repair which occludes the diseased wall from the mechanical loading.

1.5.1 Open surgery

Since it was first introduced by Dubost *et al.* in the 1950s, open surgery has been regarded as the default surgical intervention of AA [71]. During the surgery, an open incision is made to enter the chest or abdomen. Then the surgeon incises the aorta and puts a synthetic graft connecting the two ends of healthy aorta by sutures, in order to bridge the affected segment of aorta, as shown in Figure 1.6. The diameter of the graft should match the diameter of the healthy aorta. To extent the patient life, the graft needs a good tensile strength and compliance to withstand mechanical loadings from blood pressure and flow. The common graft materials include polyethylene terephthalate (Dacron) and expanded polytetrafluoroethylene (ePTFE) [72,73]. It can be expected that a successful surgical repair will be durable and protective from AA rupture throughout the lifetime of the patient [4].

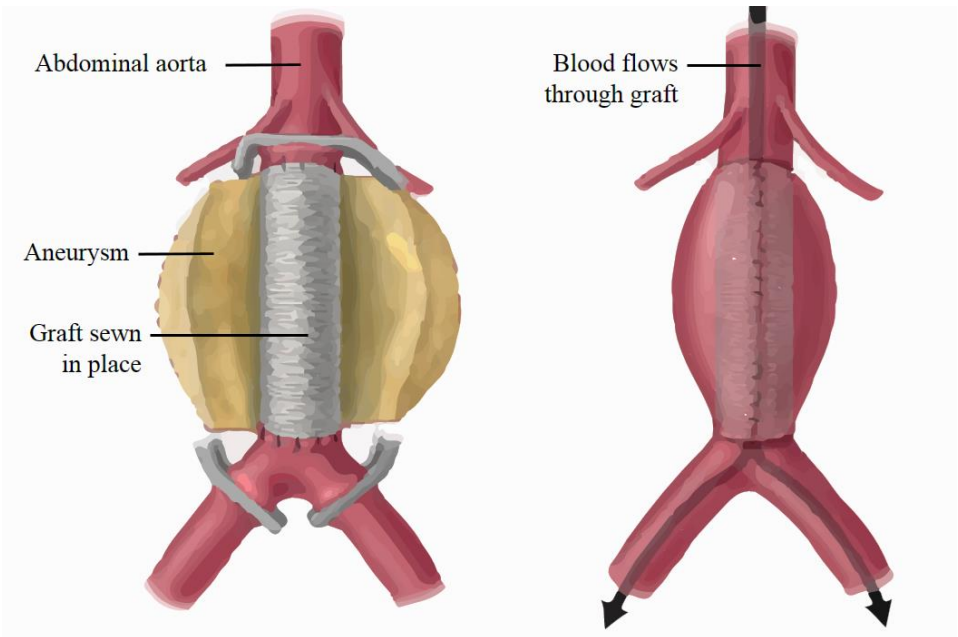

Figure 1.6 Open surgical repair showing the graft inside the aortic aneurysm. (Adapted from Eidt *et al.* [74] with permission from UpToDate)

However, open surgical repair is a highly invasive technique. An operative mortality rate of 2%-6% has been reported in elective repairs and over 15% in leaking or ruptured aneurysms [75,76]. The patients are required to be hospitalised typically for one week and to recuperate at home for several more weeks. Early complications include postoperative bleeding and ischaemic complications. Postoperative bleeding can lead to cardiac tamponade and

haemothorax, as well as shock, dilutional coagulopathy, and transfusion-related complications. Ischaemic complications are related with inadequate perfusion of the brain (stroke), spine (paraplegia, paraparesis), viscera (intestinal infarction, renal failure), and extremity (critical limb ischaemia). Life-threatening long-term complications include wound and graft material infections [77].

1.5.2 Endovascular aortic repair

To avoid invasive aortic surgery, the concept of endovascular aneurysm repair (EVAR) was first presented by Volodos in 1986 [78] and performed by Parodi in 1991 [79], where they used a Dacron graft sutured onto a balloon expandable Palmaz-Schatz stent. Since then, EVAR has become widely accepted as a safe alternative for AA treatment [75,80]. EVAR involves the placement of an endograft across the aneurysm and its fixation to the aortic wall at both ends, as shown in Figure 1.6. The endograft is composed of fabric and metal stents and is deployed in a catheter system. Under fluoroscopic guidance, the delivery system is fed through the iliac arteries until the endograft is positioned and deployed correctly. Successful deployment of the endograft can exclude blood flow mechanically from the aneurysm sac and reduce structural loadings within the wall [5].

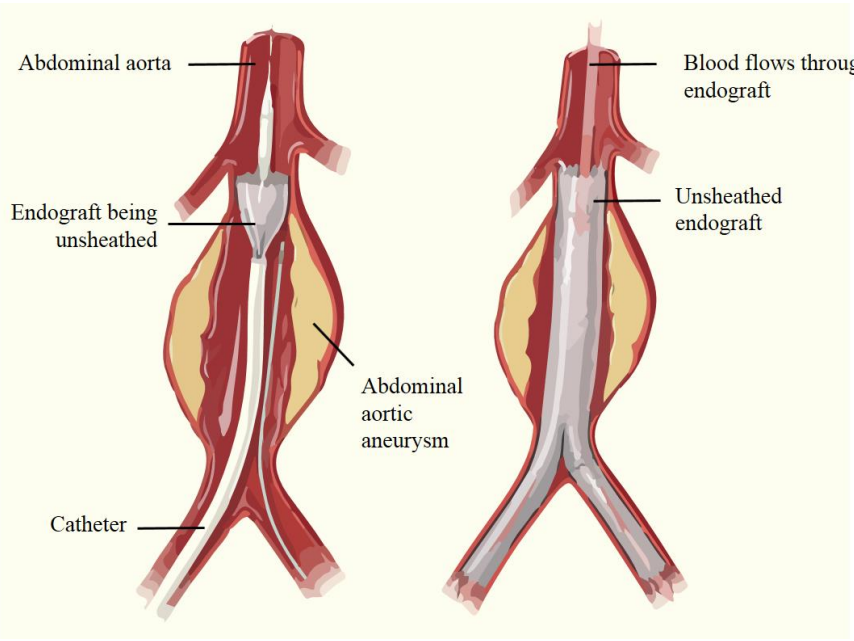

Figure 1.7 Endovascular aortic repair showing the deployment of endograft inside the abdominal aortic aneurysm. (Reproduced with permission from National Institutes of Health)

Compared with open surgery, EVAR is associated with lower operative mortality risk, faster recovery time, and shorter hospital stays [81,82]. The major complications with EVAR include device migration, kinking, occlusion, as well as endoleaks (a persistent blood flow leaking into the aneurysm sac outside the endograft) that can hamper the proper AA exclusion and lead to a state susceptible to secondary rupture [5,83].

1.5.3 Comparative considerations between open surgery and EVAR

There are certain exclusion criteria for open surgery due to its invasive nature, including: advanced age (>70 years), American Society of Anesthesiologists classification of IV or more, New York Heart Association classification (1994) of cardiac function of III/C or more, or dysfunction of other important organ systems (i.e. severe chronic obstructive pulmonary disease, renal or hepatic insufficiency) [84–86].

Although EVAR provides a minimally invasive alternative for these patients, there are several anatomic criteria required for standard EVAR, including: (1) iliofemoral access vessels large enough to allow safe insertion of the device, (2) an aortic neck of adequate length (>15 mm) for endograft fixation, and (3) limited angulation (<60°) between the aorta and aneurysm [87].

Considering the complex anatomy with involvement of important branches, open repair is still the standard of care for the AAs in the ascending thoracic aorta and the aortic arch. By contrast, EVAR is emerging as a preferred initial approach for the descending aorta and abdominal aorta [88–90].

To evaluate the treatment outcomes of open surgery and EVAR, several RCTs have been conducted for a head-to-head comparison. The first and largest RCT is the UK EndoVascular Aneurysm Repair (EVAR)-1 trial [91–94], which started in the United Kingdom from 1999. Similar trials were conducted in Netherlands: the Dutch Randomised Aneurysm Management (DREAM) trial [95–97]. There was also the Open Vs. Endovascular Repair (OVER) trial in the United States [98,99] and the Anevrysme de l'aorte abdominale, Chirurgie versus Endoprothese (ACE) trial in France [100]. A meta-analysis combined all of the RCTs mentioned above and two smaller trials [100], resulting in 1,470 patients being allocated to EVAR and 1,429 being patients allocated to open surgery. The results of short-term (30 days), intermediate-term (up to 2 years)

and long-term (>3 years) were analysed. It was reported that 30-day all-cause mortality was significantly lower with EVAR than open surgery [relative risk (RR) 0.35; 95% CI 0.19-0.64]. However, the significance was gradually lost during follow-up due to secondary sac rupture after EVAR, yielding an RR of 0.78 (95% CI 0.57-1.08) for intermediate-term and 0.99 (95% CI 0.85-1.15) at long-term follow-up. Briefly, in patients with suitable AAA anatomy, EVAR is associated with a 66% reduction in operative mortality while the benefit is lost during long-term follow-up due to an increased re-intervention rate. Given the need for lifelong surveillance after endovascular repair, younger patients with low operative risk may benefit more from open surgery, while older patients and those with high operative risk may benefit more from EVAR.

It should be noted that most of the endografts used in the above RCTs are early-generation endografts while optimised designs have been developed and more commonly used. Although the long-term durability of these later versions of endografts has not been evaluated yet, it is expected that they would be associated with lower rates of complications and reinterventions.

In terms of the selection between open and endovascular techniques, personalised approaches to the patient are recommended by guidelines from major medical and surgical societies, taking into account the patient's age, risk factors for operative morbidity and mortality, anatomic factors, and experience of the surgeon [62,69,101]. In particular, imaging is essential to achieve successful treatment and reduce therapeutic complications. As the deployment of endografts is irreversible during EVAR, precise imaging and thorough assessment of the morphology is crucial in pre-surgical plan. Moreover, post-operative lifelong imaging surveillance is required to monitor late complications including endoleaks, stent migration and rupture. The details of imaging technique will be discussed in Chapter 2.

1.6 Challenges in endovascular aortic repair

As discussed in Section 1.5, EVAR is an alternative for patients who are not suitable for open surgery. However, there are limitations for the application of standard EVARs. In a study with 3,005 patients with AAs, it was estimated that 24% of the AAs were not suitable for standard EVAR, mostly due to a short neck length and an insufficient landing zone [102]. Moreover, side branches of the aorta involved in complex AAs limit the use of standard EVAR, because the

endograft may cover and occlude these branches. The side branches of the aorta include minor branches such as the segmental arteries, and major branches such as the superior mesenteric artery, coeliac artery, and the renal arteries. Occlusion of these vital side branches can lead to severe damage to important organs or even death. For example, spinal cord injury caused by side branch occlusion is the most dreaded potential complication after standard thoracic EVAR, with an overall risk reported to be between 2-10% [103,104].

To preserve the vital side branches in EVAR, two different strategies have been proposed: (1) advanced endograft designs or techniques (Figure 1.8), including fenestrated and branched endografts, as well as the chimney technique; and (2) flow-diverting strategy with uncovered stents harnessing haemodynamic and rheological effects, such as flow-diverting stents and multiple overlapping uncovered stents. The implementations and differences of these strategies are discussed as follows.

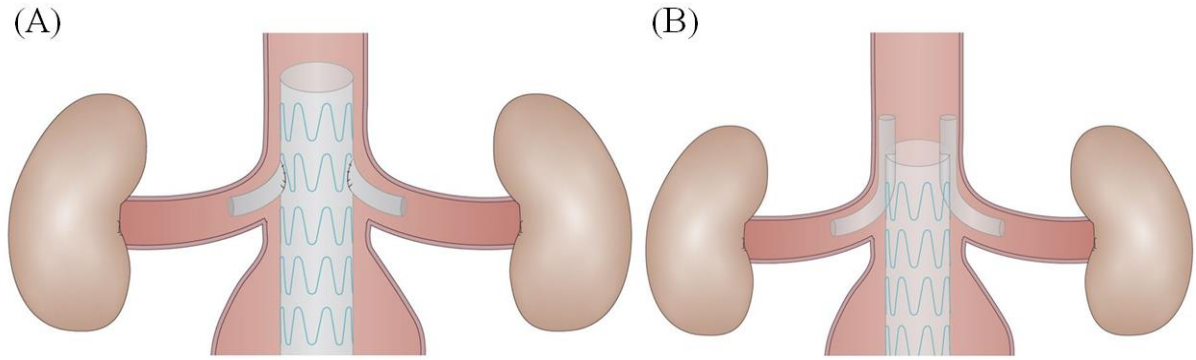

Figure 1.8 Examples of advanced endograft designs and chimney techniques treating juxarenal AAA. **(A)** fenestrated/branched endograft; **(B)** chimney technique. (Adapted from Buck *et al*. [105], with permission from Springer Nature)

1.6.1 Fenestrated/branched endografts and chimney technique

The principle of fenestrated or branched endografts is to integrate additional components and connect to the side branches, so as to preserve the blood supply. The first fenestrated endograft was reported in 1999 [106]. The technology in this area has advanced rapidly [107–114], and the first FDA-approved fenestrated endograft was available in 2012 [115]. The fenestrated endograft is featured by the fenestrations (holes) on the main endograft (Figure 1.9 left), which is

individually customised based on the locations of target arteries from pre-operative imaging. The deployment of the main endograft must be precise to obtain a correct orientation. Smaller alignment stents for branch preservation are inserted to the side branches from the fenestrations, which can keep the patency and prevent the occlusion or stenosis. Fenestrated endovascular repairs have been used primarily to manage juxtarenal AAAs and showed lower operative morbidity and mortality than open surgery [116]. Similar to fenestrated endografts, branched endografts have separate side-arm components to preserve the patency of target vessels (Figure 1.9 right). The cuffs are sutured to the main aortic endograft before intervention, which serve as a docking site for placement of side endografts connected to the main aortic component.

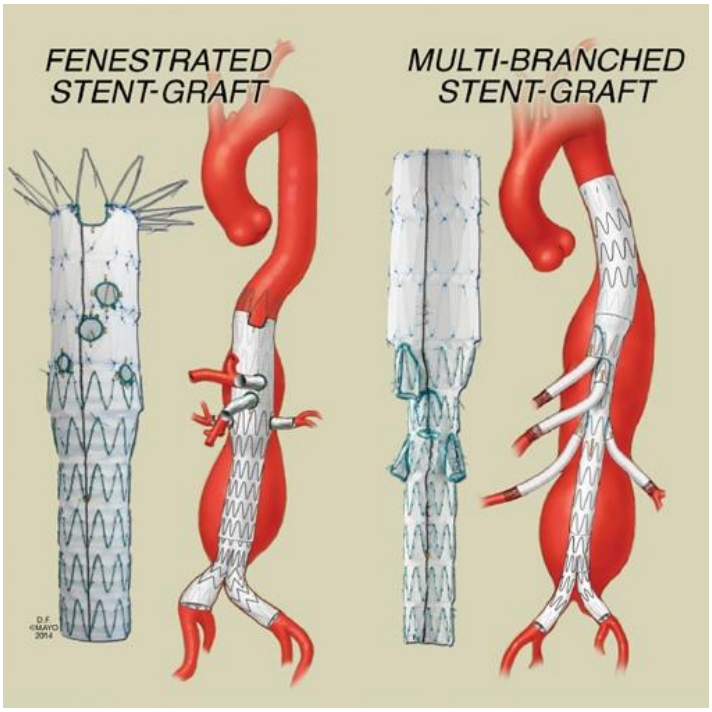

Figure 1.9 An example of fenestrated endograft (left) and branched endograft (right). (Reproduced with permission from Mayo Clinic)

Chimney grafting (Figure 1.8b) is an alternative to the fenestrated/branched endograft with challenging anatomy, which also preserves the perfusion of side branches. Instead of customising the main endograft, the chimney techniques include additional paralleled side endografts, which can be deployed via brachial or axillary access. Thus a conduit (chimney) is formed outside the main graft to preserves flow in the side branches. A systematic review [117]

involving data of 75 patients who had undergone EVAR using the chimney technique (96 chimney grafts used) demonstrated a high technical success rate of 98.9%. During the follow-up ranging from two days to 54 months, three deaths occurred as late complications and three chimney grafts occluded, necessitating two reinterventions [117]. Long term follow-up is not available and FDA approval has not been attained yet.

Although the application of EVAR is extended by the development of fenestrated endografts and the chimney technique, there are still many limitations. Target vessels <4 mm in diameter is a contraindication due to the increased risk of arterial complications [118]. In addition, the number of side branches that can be preserved depends on the branches of endografts (usually <4). Due to the high degree of customisation, it can take up to 12 weeks for manufactured customisation at a high financial cost. Moreover, the complex procedure requiring advanced catheter skills is also a disadvantage.

1.6.2 Flow-diverting strategy

To preserve the side branches in EVAR, a distinct concept called flow-diverting strategy using uncovered stents has been proposed. This concept was first described about two decades ago, when Geremia et al [119] suggested that a low-mesh-porosity metallic bare stent bridging an intracranial aneurysm would lead to lesion occlusion by modulating the flow.

■ Principles

As demonstrated in Figure 1.10, the successful deployment of flow-diverting stents can alter the flow pattern. Due to the rheological nature of blood, a reduction of flow velocity in the AA sac can accelerate the formation of intraluminal thrombus (ILT) [105]. As an attached structural component, thrombus can change the geometry of the sac and therefore the mechanical loading within the aortic wall due to cushion-effect.

The mechanical effect of stent-induced thrombus can be approximated by the Laplace's law (Equation 1.1). The presence of thrombus decreases the luminal diameter D and increases the wall thickness h, resulting in the decrease of stress $\bar{\sigma}$. In 2002, Wang *et al.* showed that ILT changes the distribution of wall stress and reduces the peak wall stress [120]. In that study, four

patient-specific finite element models were analysed and all models showed a significant decrease in the wall stress under the presence of thrombus.

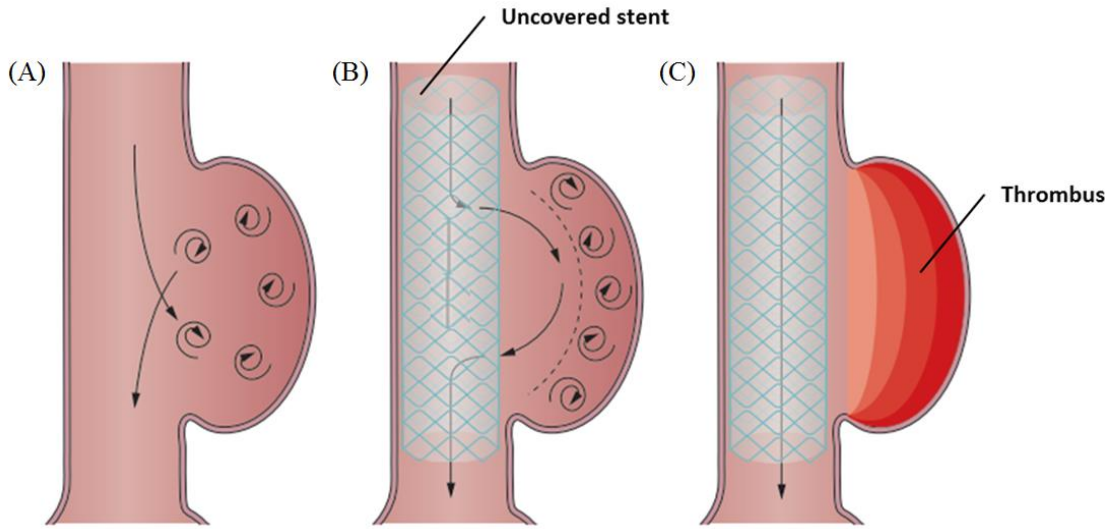

Figure 1.10 The diverting effect of uncovered stents: **(A)** before intervention; **(B)** short-term outcome; **(C)** long-term outcome. (Adapted from Buck *et al.* [105], with permission from Springer Nature).

Compared to endografts in standard EVAR, the concept of flow-diverting stents is based on a totally different mechanism: endografts provide a mechanical barrier between the aneurysm sac and normal blood flow, resulting in a reduced sac pressure immediately and therefore leading to a decreased aneurysm wall tension; but flow-diverting stents modulate the blood flow and promote the formation of thrombus, reducing the wall tension gradually with the thrombus growth. However, the thrombosis and endothelialisation process might take months to reach an effective level. Patients may remain exposed to the risk of AA rupture after the deployment of flow-diverting stents. This makes flow-diverting strategy not suitable for patients in emergency repair with a high risk of rupture.

■ Preliminary application in EVAR

Cardiatis Multilayer Flow Modulator (MFM) (Cardiatis, Isnes, Belgium) is a flow-diverting uncovered stent used in most reported studies [121–124] for managing complex thoracoabdominal AAs. The stent is designed with self-expandable wire mesh interconnected in layers permitting a porosity of 65% (Figure 1.11).

Figure 1.11 A photo of Cardiatis Multilayer Flow Modulator. (Reproduced with permission from Cardiatis)

A nonrandomised trial named the Evaluation of the Safety and Efficacy of the Multilayer Stent (STRATO), reported that MFM appears to be safe and effective in maintaining branch vessel patency [125]. In this small cohort which included 23 patients with a 3-year follow-up, stable aneurysm thrombosis was achieved in 15 of 20 patients at 12 months, 12 of 13 patients at 24 months, and 10 of 11 patients at 36 months. The rate of branch patency was 96% at 12 months (primary patency), 100% at 24 months, and 97% at 36 months. In a recent systematic review of MFM treatment including 171 patients, Hynes *et al.* reported an all-cause survival rate of 97.1% (95% CI, 92.9%-98.9%) at 30 days and 53.7% (95% confidence interval, 46%-61.3%) at 1 year. It was suggested that MFM can be safely utilised in some patients with complex thoracoabdominal pathologies providing that operators adhere to the instructions for use.

However, serious concerns have also been raised by several adverse reports about AAA rupture after MFM implantation [122,126]. As MFM is interconnected and highly deformable, the significant longitudinal shorting and migration from the original target location could lead to insufficient coverage of the aneurysms or misuse of an undersized device. The mechanisms for delayed rupture should be investigated carefully and the instructions for use of MFM should be reviewed before this flow-modulator can be widely disseminated. RCTs, registries, and continued assessment are essential.

1.6.3 Multiple overlapping uncovered stents

Following the flow-diverting principle, Lu *et al.* proposed another implementation using multiple overlapping uncovered stents (MOUS) [85]. The procedure includes the consecutive deployment of multiple uncovered stents, to achieve a lower porosity and better flow-diverting outcomes than a single aortic stent. The stents used are closed-cell, self-expandable stents (Sinus-XL stent, OptiMed, Ettlingen, Germany), providing strong fixation to landing zone, as shown in Figure 1.12.

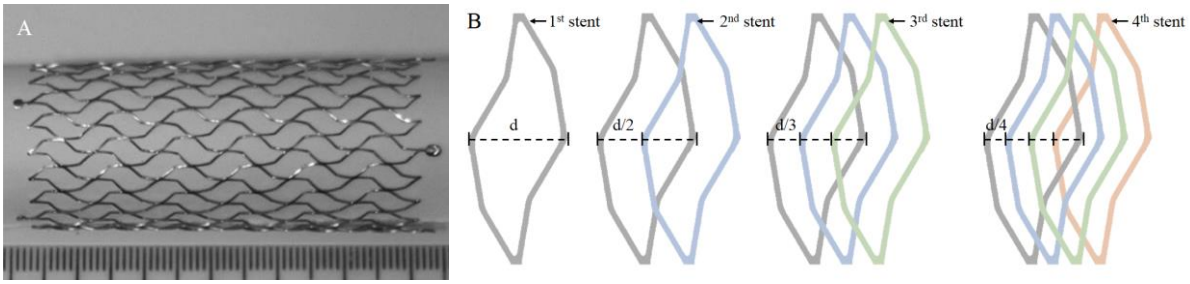

Figure 1.12 A photo of Sinus-XL stent and the schematic representation of the uniform overlapping pattern. **(A)** A photo of the aortic stent used in the MOUS technique; **(B)** The unit cell representation of the uniform overlapping pattern of four stents in different colours.

The diameter of the stents is selected in conformity with the manufacturer's instructions, with 10% to 20% oversizing at the aneurysm neck. To conform to the deformation of the aorta, the MOUS technique is currently limited to the treatment of descending TAAs and AAAs. The advantages of MOUS includes: commercially available stents without customisation, flexible porosity controlled by the number of stent deployment, and firm fixation to the aortic wall.

A pilot study of the MOUS procedure has been performed in a cohort of 42 patients who were judged neither suitable for open surgery nor standard EVAR. Encouraging short-term and mid-term outcomes have been reported [85,127]. On average, 3.3 stents were deployed for each patient in the MOUS procedure and the technical success rate was 40/42 (96%). During an average follow-up period of 20.9±9.0 months, a significant shrinkage of mean aneurysm diameter (from 53.4 mm to 48.8 mm, $P<0.001$) and a significant increased sac thrombosis ratio (from 18% to 94%, $P<0.001$) were observed. The patency of side branches was evaluated from the pre-operative and follow-up CTA imaging. It was reported that the majority of side branches

(74/76 (97%) major visceral branches, 237/244 (97%) minor segmental arteries) maintained their patency after stenting. The long-term follow-up is still ongoing.

Although the short-term and mid-term outcomes of MOUS are encouraging, several important questions need to be addressed. Currently, the number of stents that should be deployed depends on the experience of the operator, while the optimised choice for a specific patient needs to be explored. Moreover, uncertainty during the deployment may result in different overlapping patterns of the multiple stents and their influence on the flow-diverting outcome is not clear. Furthermore, the increased structural loading in the loading zone induced by multiple stents deployment may cause wall damage that has not been assessed comprehensively.

Mechanics theory plays an important role in the success of MOUS. Firstly, the material strength of the aortic wall is essential for the aneurysm rupture, which can be quantified by biomechanical testing. Secondly, biomechanics provides a framework to investigate the interaction between stents, blood flow and the aortic wall. In particular, imaged-based computational analysis provides a comprehensive assessment for personalised pre-surgical plan, which can be used to perform virtual MOUS deployment, visualise the flow-diverting effects and predict possible treatment outcome.

1.7 Summary

Formation of AAs is a complex and chronic process that results from the interaction of genetic and environmental factors. The progression of AA is a consequence of structural degeneration associated with multiple processes including proteolytic degradation, inflammation response, and tissue remodelling. These biochemical processes break the biomechanical balance between the structural loading and aortic wall structure. The elective repair of an aneurysm is based on the assessment of rupture risk compared to repair risk. EVAR is emerging as a preferred approach for suitable anatomies due to its minimally invasive nature. To solve the challenges of side branch involvement, fenestrated/branched endografts and the chimney technique have been proposed, while their application is limited by high costs and complex procedures. New therapeutic techniques with flow-diverting strategies have been proposed. The MOUS

procedure is an emerging technique with an encouraging clinical outcome in preliminary experiences. To achieve an improved outcome, several questions surrounding MOUS procedure remain unclear. They can be investigated by biomechanical methodologies.

Aim of the study

This dissertation seeks to investigate the mechanical behaviour of AA, characterise the interaction between the aorta and vascular stents, and provide a comprehensive assessment of the MOUS technique based on image-based biomechanical analysis.

Structure of the thesis

In Chapter 2, *in vivo* imaging techniques with their applications in clinical management and biomechanical modelling are discussed. In Chapter 3, the general methods of biomechanical modelling are introduced. In Chapter 4, the mechanical behaviours of AAs are characterised by uniaxial material tests. A Bayesian framework is proposed for material constants identification, and correlated to the microstructure of tissue fibre network. In the Chapter 5, biomechanical modelling of MOUS deployment is performed based on patient-specific images, and the mechanism of MOUS-induced flow modulation is investigated. In Chapter 6, the effects of cross-stent structure of MOUS are further investigated through parameter studies. In Chapter 7, the pathological effect of structural stress concentration induced by implanted device is further studied in rabbit models. In Chapter 8, the general conclusions and future directions are discussed.

Chapter 2 Imaging of aortic aneurysms

The rapid development of imaging techniques has facilitated *in vivo* high-resolution evaluation of the vascular system, and revolutionised the clinical management of aortic aneurysms. High-quality images of the AAs are of crucial importance for pre-surgical planning, intraoperative deployment, and follow-up assessment. In this chapter, commonly used vascular imaging techniques including anatomical and functional imaging, as well as their applications are discussed.

2.1 Overview of imaging techniques

Medical imaging techniques provide an *in vivo* visual representation of tissue and organs within the body for clinical assessment. In general, medical imaging techniques include anatomical imaging and functional imaging, according to the information they provide:

Anatomical imaging. These techniques usually provide two-dimensional (2D) or three-dimensional (3D) information on the geometry of tissues and dynamic changes in geometry with time. The morphology of the aortic vasculature with side branches is essential in both pre-surgical planning of EVAR and follow-up surveillance. In addition, the structural information of tissue components within the aortic wall is of great importance for the assessment of aneurysm progression, such as calcification and intraluminal thrombus. The most frequently used anatomical imaging for AAs include computerised tomography (CT), magnetic resonance imaging (MRI) and ultrasound.

Functional imaging. These techniques provide information related to physiology of living organisms. In contrast to anatomical imaging, functional imaging reveals physiological activities, usually by employing biomarkers. The biomarkers interact with target tissues and generate signals, which reflect the biological function and can be detected by the imaging

system. The most common molecular imaging technique used for AAs is positron emission tomography (PET), which can be used to reflect inflammation. Other modalities, including advanced MRI and ultrasound can also be used for functional purposes.

2.2 X-ray imaging

Since the discovery of X-rays by Rontgen in 1895, X-ray imaging has been widely used for medical diagnosis. The basic imaging system involves production of X-rays from a tube, passage of these X-rays through the target, and detection of their attenuation. At present, several types of X-ray imaging techniques have been well established.

2.2.1 Conventional radiography

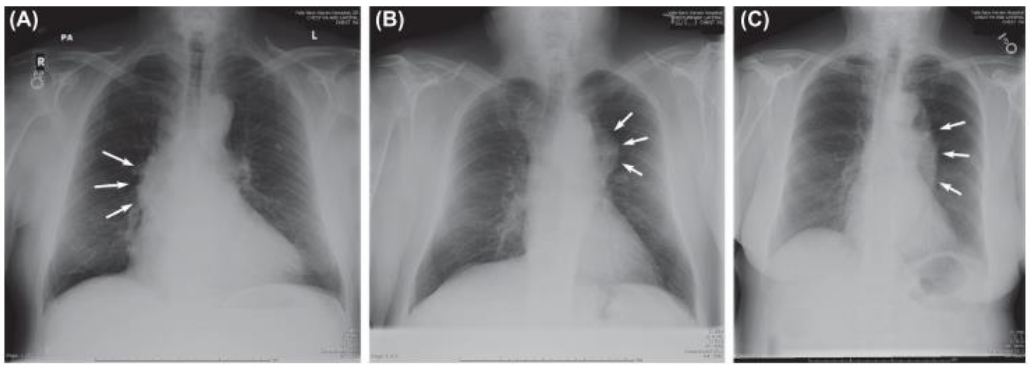

Figure 2.1 TAAs diagnosed by chest plain X-rays. **(A)** Ascending; **(B)** Arch; **(C)** Descending. (Reproduced from Damberg *et al*. [52] with permission from Elsevier)

Conventional radiography (also called plain X-rays) accounts for 75% of medical imaging examinations [128]. Plain X-rays are 2D projection images made by an x-ray beam passing through and absorbed by various tissues in the body. Four basic densities are visible on plain X-rays: air, fat, water (blood and soft tissue) and bone [129]. A chest radiography can be used to examine the contours of the aorta because of the contrast between the air-filled lungs and the fluid-filled aorta. As shown in Figure 2.1, the abnormalities of thoracic aortic aneurysms can be observed on conventional radiography, however lacking of many details.

The advantages of conventional radiography include low costs, wide availability and short imaging time which is particularly useful for emergency diagnoses. However, it is neither

sufficient to make an accurate diagnosis or exclude aortic pathology, nor does it offer sufficient anatomical details for therapeutic planning [52]. Another drawback of conventional radiography is the exposure to ionizing radiation (0.1 mSv for chest and 0.7 for abdominal radiographs) [130].

2.2.2 Computerised tomography

Computerised tomography (CT) is accomplished by passing a rotating fan beam of X-rays through the patient. The raw 2D cross-sectional images are acquired from thousands of projection angles, which are reconstructed using filtered back projections [131]. The collection of 2D slices enables production of a 3D volume, with each voxel assigned a grayscale value representing the local attenuation coefficient. The X-ray attenuation is quantified by Hounsfield Units (HU), named after Sir Godfrey N. Hounsfield for his pioneering work in the development of CT. The type of tissue can be inferred by the range of HU values, which provide more contrast beyond the four basic densities on conventional radiography. The HU values of the four common tissues prior to intravenous contrast is listed below (Table 2.1). Moreover, the 3D imaging volume provide more anatomical information for precise assessment of the aortic morphology.

Table 2.1 Typical HU values for different tissues.

Substance	Hounsfield units (HU)
Air	-1,000
Fat	-100
Water	0
Muscle/soft tissue	+40
Contrast	+130
Bone	+1,000

On early CT machines, vascular imaging was limited due to slow acquisition time. The X-ray tube must finish a complete rotation to obtain a single slice before the table was moved incrementally for next slice. Until early 1990s, the development of helical scanning techniques and multi-detector row technology revolutionised the role of CT in vascular imaging [132,133]. Slip-ring technology allows for the continuous rotation of the X-ray tube, and multiple detector

rows allow the simultaneous acquisition in a single rotation [134]. The more detector rows used, the shorter imaging time and the less amount of intravenous contrast medias are required. A modern multi-detector CT machine can complete vascular interrogation from the aortic arch to the foot in less than 30 s [135]. The helically acquired data can be reconstructed into traditional reformatted planes (Figure 2.2). Computerised tomographic angiography (CTA) is the contrast-enhanced CT acquired after intravenously injecting contrast medias, to achieve a high radiodensity within the blood vessels. CTA normally consists of multiple imaging phases, including a pre-contrast image series and at least one contrast-enhanced series.

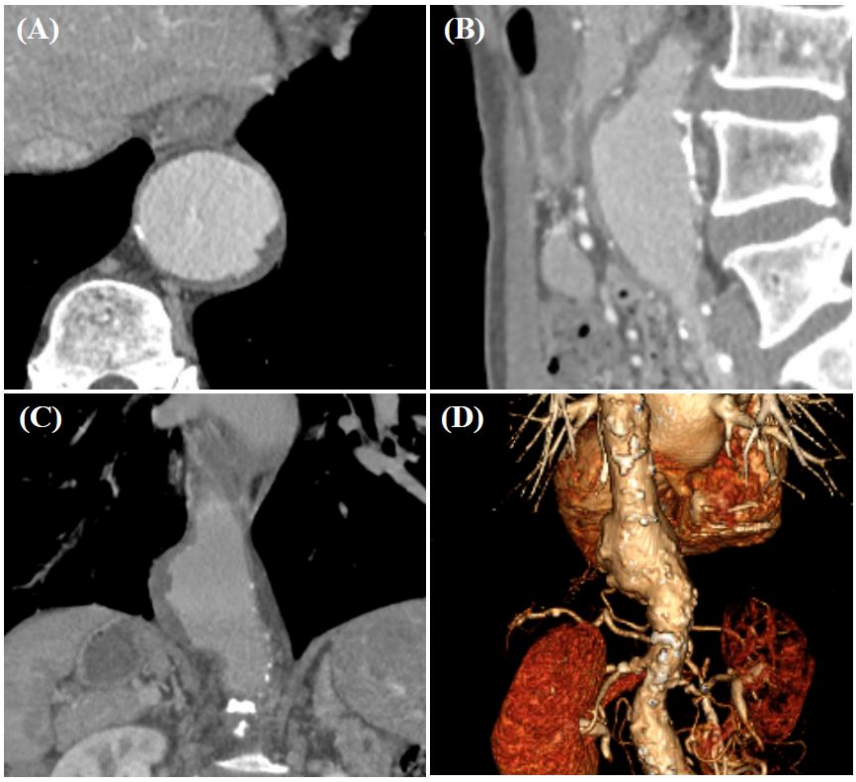

Figure 2.2 CTA imaging of an AAA: **(A)** Axial view; **(B)** Sagittal view; **(C)** Coronal view; **(D)** 3D rendering. The aortic lumen is contrast-enhanced while the intensities of intraluminal thrombus and aortic wall are similar without a clear border.

The advantages of CT for evaluating AAs include the short imaging time and detailed 3D anatomic information, allowing for accurate measurement of aneurysm diameters and evaluation of whole vessel morphology. For EVAR, a precise morphological assessment is vital in both pre-operative planning and follow-up surveillance, which has been extensively investigated based on CT images, including: aneurysm diameter [136–138], length [139–141], tortuosity

[142,143] and volume [144–146]. In addition, calcification with high HU values can be segmented and assessed [147–149], which alters the stiffness of aortic wall significantly. The main disadvantages of CT are the radiation burden (about 10-100 times more than conventional radiography) and use of potentially nephrotoxic contrast medias in CTA [150]. Other limitations include weak soft-tissue contrast making intraluminal thrombus segmentation difficult, and the susceptibility to blooming artefacts from calcium [151].

2.2.3 Digital Subtraction Angiography

Digital subtraction angiography is an X-ray fluoroscopy technique that is used to visualise the vasculature by masking the background tissues with digital subtraction [129]. A catheter is inserted from the entry point (usually the femoral artery) and delivered into the targeted blood vessel for the injection of iodinated contrast. A series of 2D X-ray projections are acquired during the injection. The initial image without contrast is called the mask, which is digitally subtracted from later images with contrast. Therefore, only the contrast-enhanced vasculature is left in images (Figure 2.3). Compared to non-digital angiography, DSA provides superior contrast resolution with lower doses of intravenous contrast in dynamic imaging.

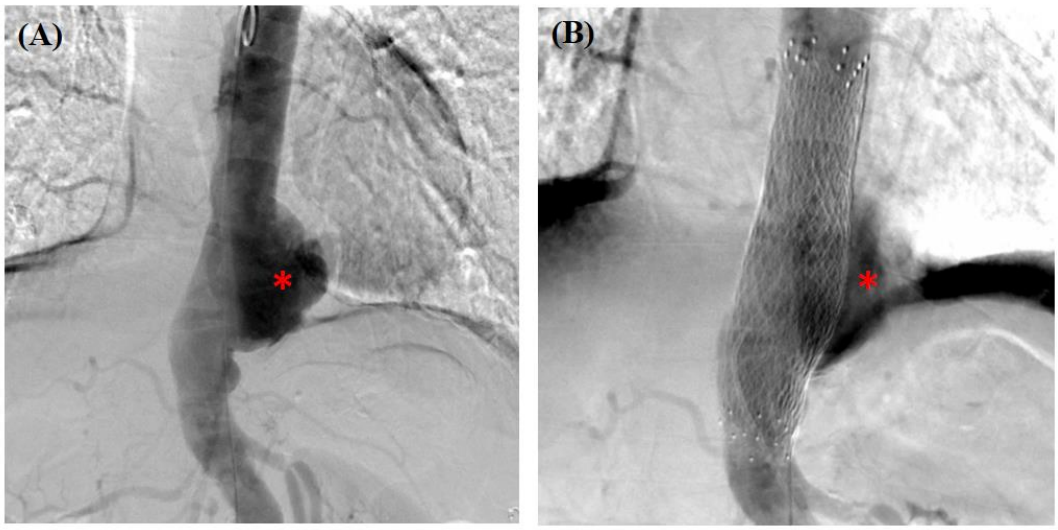

Figure 2.3 DSA image of a thoracoabdominal aortic aneurysms before **(A)** and after **(B)** the deployment of MOUS.

The features of image magnification and real-time subtraction make DSA suitable for simultaneous EVAR. The intervention procedure of EVAR can be guided and monitored by

DSA. The contrast change in the aneurysm sac is related to flow conditions, which can be used to indirectly assess aneurysm occlusion or the flow-diverting outcome [152–154]. Although DSA can visualise the aorta with side branches, it has some major drawbacks. Since angiography only visualises the blood flow without the wall components, the actual vessel and aneurysm sizes may be underestimated, due to the presence of thrombus which is masked out in the subtraction. Moreover, DSA is an invasive procedure with exposure to iodinated contrast, which is related to complications such as arterial puncture and potential nephrotoxicity of the contrast medias. For those reasons, the primary role of DSA in pre-operative scan has been replaced by CT and MRI [150].

2.3 Ultrasound imaging

Differing from X-ray techniques, ultrasound imaging uses high-frequency sound waves (typically 2-18 MHz) without ionizing radiation [155]. The transducer is the equipment to send out and receive the ultrasound waves, which transmit through and are reflected by internal structures of the body. The returning sound waves are categorised according to their intensity (referred to echogenicity) and reflection time.

2.3.1 Ultrasonography

Clinical ultrasonography (US) is a 2D imaging technique, reconstructed in real-time as the transducer moves across the body surface. Three-dimensional ultrasound images can be obtained by sequential collection of 2D images [156]. The echogenicity of tissues varies greatly and result in different brightness, which can be used to distinguish the structures on the reconstructed images. In B-mode US, the aorta appears anechoic with hyperechoic walls [157]. A rapid assessment of the aortic morphology from different planes can be achieved by rotating the orientations of the transducer. Ultrasound does not work well in imaging thoracic aorta due to the large chest cavity. Therefore, it is mainly used to screen the abdominal aorta. An example of abdominal US is shown in Figure 2.4. The diameter of aorta can be measured on cross-sectional planes to identify AAs.

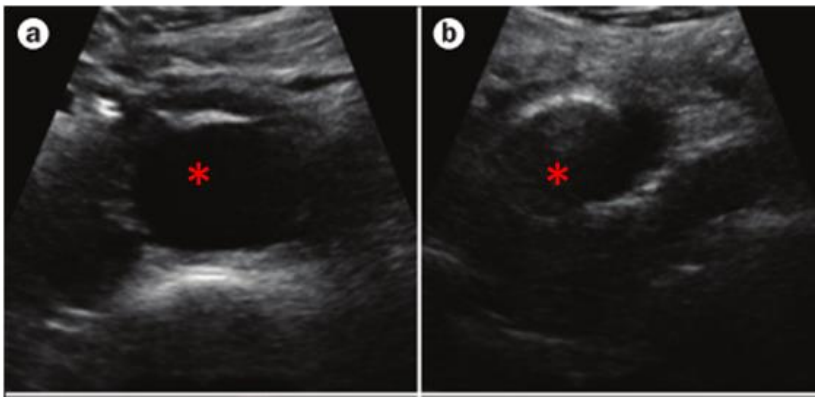

Figure 2.4 Ultrasonography showing a transverse view of the distal aorta. (Reproduced from Buck *et al*. [105], with permission from Springer Nature)

US is a non-invasive and inexpensive technique of high sensitivity and specificity, without ionizing radiation [158]. However, the images are operator-dependent and provide less accuracy in measurement. The pathological findings on ultrasound should be further evaluated on more accurate anatomical modalities such as CT and MRI.

2.3.2 Doppler ultrasound

Doppler ultrasound can detect the motion of fluids based on the Doppler shift, which is a change in the frequency of the returning echo as it encounters a moving structure. With the information from the Doppler shift, images can be generated to visualise the speed and direction of the blood flow (Figure 2.5).

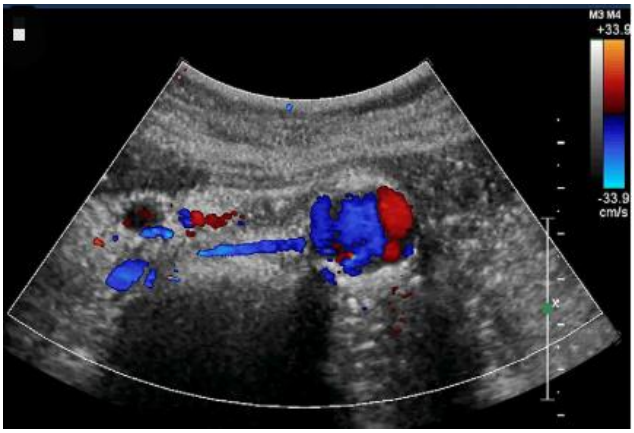

Figure 2.5 An aortic aneurysm is characterised by swirling flow on Colour Doppler ultrasound. (Reproduced from Prager *et al*. [157] with permission from Springer Nature)

Typical display formats include the time-velocity waveform form at an individual location, and a 2D real-time colour visualisation of the blood flow with velocity encoded. Doppler ultrasound is usually combined with traditional US providing the structural information, which is called duplex ultrasound. Doppler ultrasound is particularly useful in vascular imaging, providing a rapid and overall assessment of the blood flow condition. The duplex ultrasound can also be used for follow-up surveillance of EVAR, which helps monitor the aneurysm size and characterise the endoleak [159]. The limitations include the aliasing noise and the poorer temporal resolution, especially at increased depths.

2.3.3 Intravascular ultrasound

Intravascular ultrasound (IVUS) is a recent development which provides a 360° cross-sectional view of the vessel wall (Figure 2.6), using a specially designed catheter with a miniaturised ultrasound probe attached to the distal end.

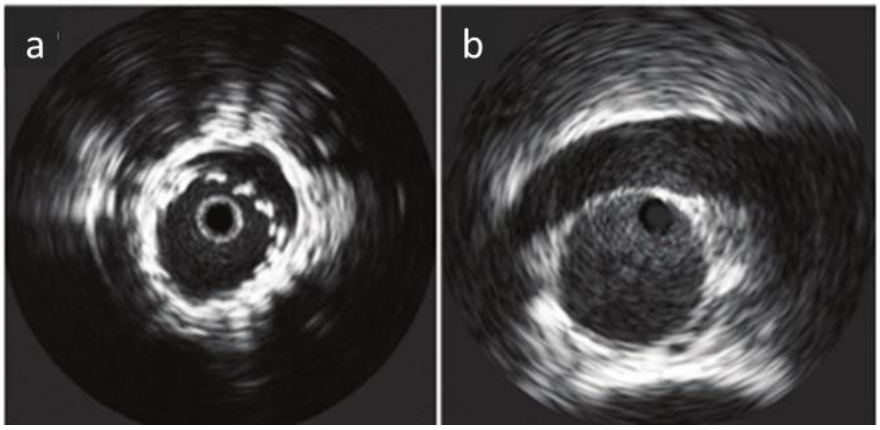

Figure 2.6 IVUS cross-sectional imaging demonstrating a stent graft in AAA. (Reproduced from Buck *et al*. [105], with permission from Springer Nature)

Since no exogenous contrast is required, IVUS can be used in patients with renal insufficiency. Another advantage of IVUS is that the aortic diameter can be evaluated accurately in real time, which can be used to estimate aortic compliance [160]. However, IVUS is susceptible to operator-dependent error and the probe is required to be at the centre of lumen for accurate measurement, while it is increasingly difficult for the aorta with large diameter and tortuosity. Currently it still remains a costly and invasive procedure which is primarily used for research purposes [161].

2.4 Magnetic resonance imaging

MRI allows image the body by utilising a strong magnetic field (modern clinical machines function at 1.5-3.0 Tesla (T)) and radiofrequency (RF) pulses [162,163]. The protons (or certain other nuclei) within patients are the primary source of signals. The net magnetization of protons can be deflected by the application of RF pulse, followed by a magnetic recovery process which emits signals. The spatial information can be encoded to the emitted signals by the design of RF pulses, and reconstructed to images via Fourier transforms [164]. The magnetic recovery process after an RF pulse has two components: a longitudinal relaxation (T_1 relaxation) and a transverse relaxation (T_2 relaxation). Accordingly, the recovery times are termed as T_1 and T_2 relaxation times, which characterise environments of protons and can be used to generate imaging contrast. The imaging contrast can be altered either by changing the properties of tissues (such as intravenous injection of Gadolinium-based media), or by acquisition protocols with RF sequence design highlighting different characteristics of tissues (such as black-blood technique). A wide spectrum of MRIs has been developed for different purposes, including the aortic wall imaging and magnetic resonance angiography (MRA).

2.4.1 Aortic wall imaging

MRI provides excellent soft-tissue contrast of the aortic wall, due to its intrinsic MR properties. In general, clinical MRI can be classified into two basic types – T_1-weighted and T_2-weighted images, highlighting different relaxation times. Example T_1- and T_2-weighted MRIs of aortic aneurysm wall from three different types of specimen are shown in Figure 2.8, along with their photos and CTA. MRI offers a significant advantage to CTA for characterising the morphological appearance of intraluminal thrombus [165], which can be integrated into the assessment of the aneurysm progression [166] and complications after EVAR [167].

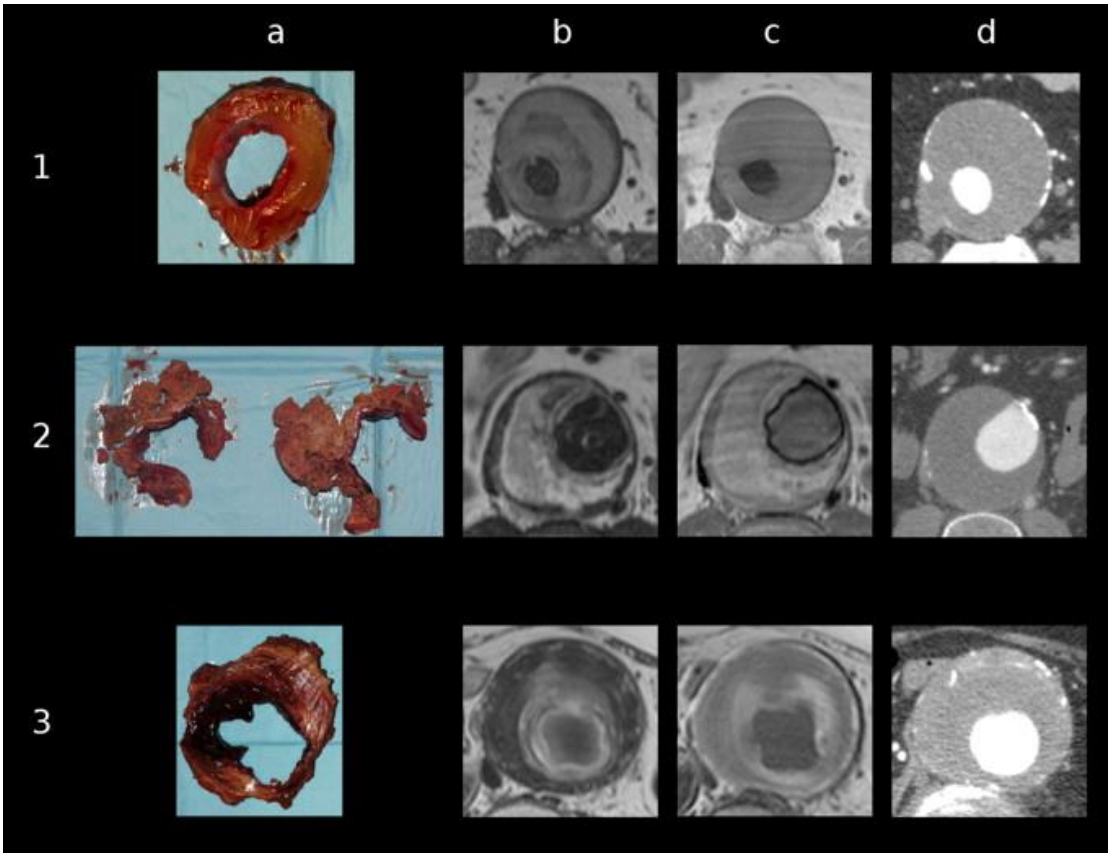

Figure 2.7 Illustration of the specimen categories and their appearance on MRI and CTA. **(a)** Photography, **(b)** T_2-weighted image, **(c)** T_1-weighted image, **(d)** CTA image. The specimen include different types of intraluminal thrombus with different apperances on MRIs. Type 1: organised thrombus (homogeneously low signal on both T_1- and T_2-weighted images); Type 2: unorganised thrombus (high signal on both T_1- and T_2-weighted images); Type 3: partially organzied thrombus (imhomogeneous signal with hyperintense areas on both T1- and T2-weighted images). (Reproduced from De La Motte *et al.* [168], with permission from Elsevier)

Black-blood (also called dark-blood) imaging is a technique to suppress blood signals [169]. This technique is particularly useful in wall imaging by applying double inversion recovery fast spin echo (FSE) sequences with electrocardiographic (ECG)-gating[170]. This technique provides contrast between mural morphology and the luminal signal-void, which is useful to depict suspected mural pathology such as intraluminal thrombus. FSE T_1-weighted images can be used to provide accurate AA diameter measurements and to demonstrate the composition of the aortic wall (Figure 2.8, right) [171–173], providing more structural information than contrast-enhanced CT (Figure 2.8, left). FSE T_2-weighted images can be used to characterise oedema which may be visualised as a hyperintense intramural signal [170]. To reduce the relatively long

acquisition time, some novel black-blood imaging techniques without ECG-gating are being developed including modified k-space reconstruction schemes and 3D high-spatial-resolution FSE sequences [174].

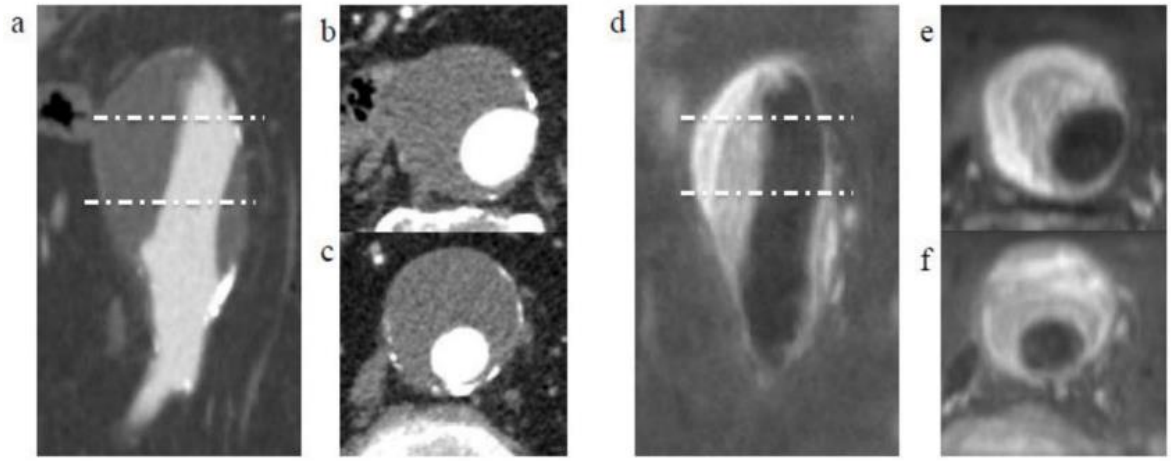

Figure 2.8 Comparison of CTA images (left) and FSE T_1-weighted images (right) in an AAA patients with intraluminal thrombus (ILT). Coronal **(a, d)** and two axial slices **(b-c, e-f)** at identical locations are shown. (Reproduced from Zhu *et al*. [171], with permission from Elsevier)

In addition, paramagnetic contrast medias can be used to characterise the perfusion properties of wall components. Gradient-echo T_1-weighted sequences with fat saturation technique are often employed to assess the enhancement of aneurysm wall, which is related to hypervascularity, suggesting the presence of inflammation [175,176].

2.4.2 Magnetic resonance angiography

The use of MRI in angiography is termed MRA. Unenhanced MRA was first introduced into clinical application more than 30 years ago [177]. However, in early stages, the imaging time was long and image quality was low associated with artefacts. The clinical use of MRA became more popular after the introduction of gadolinium-based contrast medias and the subsequent development of contrast-enhanced magnetic resonance angiography (CE-MRA) [178].

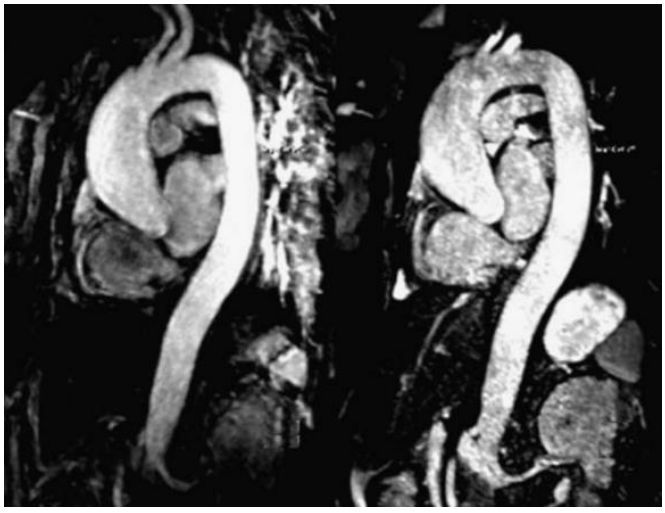

Figure 2.9 MR images in a 59-year-old patient suffering from aneurysm of the aorta root obtained with CE-MRA (left) and unenhanced MRA (right) sequence. (Reproduced from Xu *et al*. [179], with permission from John Wiley & Sons)

■ Contrast-enhanced MRA

Three-dimensional CE-MRA is acquired in a manner similar with CTA. The strong paramagnetic properties of gadolinium-based contrast media can shorten the T_1 relaxation time and consequently produce enhanced intravascular signal (Figure 2.9 left). CE-MRA is typically performed using a rapid 3D T_1-weighted spoiled gradient-echo sequence with short repetition and echo time [178]. Different acquisition modes are available: the single-phase method that captures vascular images at a single time point; the time-resolved method that repeatedly acquire images as the contrast agent passes through the vasculature. Similarly to the DSA technique, image quality of MRA can be improved by image subtraction, where a pre-contrast image is subtracted from the later images. The application of higher-field strength (i.e., 3.0T versus 1.5T) MRI enables higher signal-to-noise ratio (SNR), which allows for higher spatial resolution, faster acquisition time, and less dose of contrast medias [180–182]. Ultra-high-field (7T) MRA has been recently tested as a useful tool for microvascular imaging and functional angiography, although further studies are needed to assess its clinical feasibility and safety [183].

The advantages of CE-MRA include intrinsically high SNR, high spatial resolution, and relative freedom from flow-related artefacts. Due to the excellent imaging quality and high speed of acquisition, CE-MRA has been widely used in routine clinical practice. However, multiple studies have raised safety concerns on gadolinium-based contrast medias in the last

decade. In 2006, Grobner described the link of nephrogenic systemic fibrosis with high dose of gadolinium (Gd) in patients with renal dysfunction [184]. Since 2014, a number of publications also reported Gd deposition in the brain after administration of gadolinium-based contrast medias [185–187]. In 2017, the European Medicine Agency released a report restricting the use of certain contrast medias due to safety concerns [188]. Systematic studies to further delineate Gd-induced symptoms are needed [189].

■ Unenhanced Magnetic Resonance Angiography

Unenhanced MRA is a type of MRA without the injection of contrast medias (Figure 2.9 right). Although CE-MRA is widely regarded superior to unenhanced MRA for the diagnosis of vascular disease, in terms of imaging speed, accuracy and robustness, there has been a renewed interest in unenhanced MRA [190]. Several factors contributed to the renaissance, including the aforementioned safety concerns regarding contrast medias, improvements in MR hardware, and advances in sequences design. In contrast to CE-MRA, unenhanced MRA techniques are entirely based on the MR properties of flowing blood, such as its intrinsic relaxation times, time-of-flight (TOF) effects, and spin-phase effects [191]. Several different types of unenhanced MRA have been established:

Time-of-flight (TOF) MRA: TOF-MRA refers to a category of unenhanced MRA using TOF effects with a flow-related enhancement [169]. The advantages of TOF MRA include widespread availability on commercial MRI machines, and good opacification of arteries containing rapid or continuous flow[191].

Phase-contrast (PC) MRA: PC-MRA exploits the spin-phase effects, referred to the changes in precession angle (phase) of protons when moving within a gradient [192]. One major advantage of PC-MRA is that the phase can be used to quantify the 3D velocity field of blood flow, which provides functional information of the vasculature [193].

Steady-state Free Precession (SSFP) MRA: SSFP-MRA is emerging as an important method for unenhanced MRA of the chest and abdomen, which utilises the inherent T_1/T_2 ratio of blood [194,195]. The advantages of SSFP-MRA include its fast, high SNR readout with a high spatial resolution, and its ability to depict vessels containing very slow or stationary blood.

Fast Spin Echo (FSE) MRA: FSE-MRA (or called fresh blood imaging, FBI) is a technique to obtain an arteriogram by subtraction of systolic from the diastolic images [191]. The advantages of the FSE MRA include relatively short imaging time, sensitivity to slow flow, and less susceptible to field heterogeneities[191].

TOF-MRA and PC-MRA were the two most commonly used unenhanced MRA techniques while several novel methods have become more popular [196]. Briefly, the primary benefit of unenhanced MRA is its non-invasiveness without the exposure to ionised irradiation or exogenous contrast medias [169]. Another advantage of unenhanced MRA is that the angiograms can be repeated in the case of technical error, which is not immediately permissible in CE-MRA. The main limitation of unenhanced MRA is the long acquisition time and artefacts in regions with complex blood flow, which is being improved by emerging techniques.

2.5 Positron emission tomography

PET uses radiolabelled molecules to create 3D tomographic images of biological processes *in vivo* [197,198]. As a nuclear medicine imaging technique, PET is based on the detection of two photons emitted by the patient after administration of a radiolabel tracer. The image parameters measure the concentration of the tracers in the tissue. To reflect a wide variety of physiological and pathological processes at a molecular level, different isotopes (such as ^{18}F, ^{11}C, ^{13}N, ^{15}O) can be used to label compounds, including enzymes, receptor ligands, and neurotransmitters [199].

PET imaging was developed in mid-1970s, and has made major improvements in both diagnostic performance and practicality. Many standalone PET imaging systems have been replaced by hybrid systems such as PET-CT or PET-MR [200,201], which fuse PET with anatomical imaging to offer structural details and more accurate reconstruction. In routine clinical practice, the vast majority of PET studies are performed using fluorodeoxyglucose (^{18}F-FDG) which reflects glucose metabolism.

2.5.1 ^{18}F-FDG PET

^{18}F-FDG is a glucose analogue, which enters cells using the same transporter as glucose [197]. Once inside the cell, ^{18}F-FDG is phosphorylated into ^{18}F-FDG-6-phosphate which cannot be further metabolised or released and is thus trapped within cells. ^{18}F-FDG PET can be used to image inflammation as glucose is the primary energy source for inflammatory cells such as macrophages [202]. In previous studies, ^{18}F-FDG demonstrates a high sensitivity for the detection of activated macrophages in PET [203]. Therefore ^{18}F-FDG PET could be potentially used to monitor inflammatory changes of the aorta, which might be linked to the development of AA [204] (Figure 2.10).

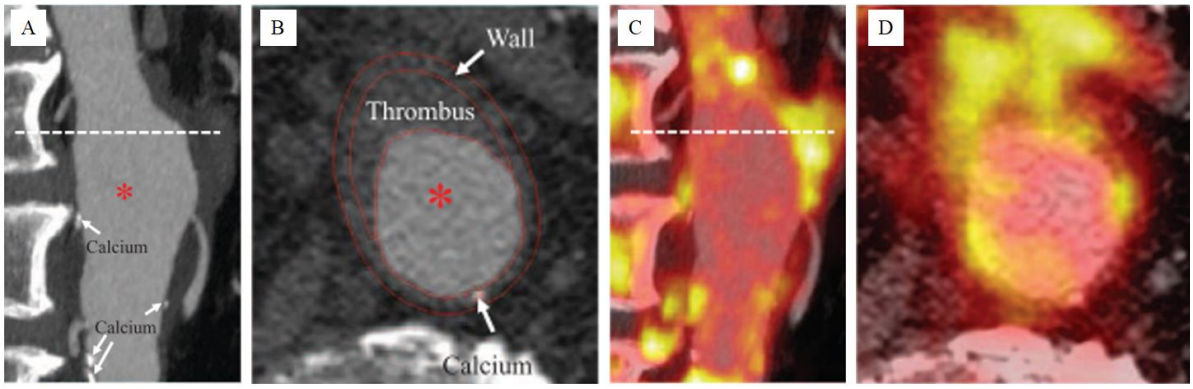

Figure 2.10 In vivo PET-CT images of an abdominal aortic aneurysm: **(A)** contrast-enhanced CT, sagittal view; **(B)** 18F-FDG PET, sagittal view; **(C)** contrast-enhanced CT, transverse view; **(D)** 18F-FDG PET, transverse view. (Adapted from Huang *et al.* [205], with permission from Wolters Kluwer Health, Inc.)

2.5.2 Integrin $\alpha_V\beta_3$ PET

Integrin $\alpha_V\beta_3$ is a cell-surface adhesion receptor identified as a marker of angiogenesis, as it is up-regulated in vascular endothelial cells by angiogenesis [206]. It has also been shown that vascular macrophages express high levels of integrin $\alpha_V\beta_3$. Arg-Gly-Asp (RGD) is an extensively studied short amino acid sequence binder to $\alpha_V\beta_3$, and radiolabelled RGD such as ^{18}F-labeled RGD agent (^{18}F-FPPRGD$_2$) can be used for PET imaging [207]. This technique has potential for clinical molecular imaging of AAs to quantify the inflammation and neoangiogenesis [38].

2.6 Clinical application

According to Clinical Practice Guidelines of the European Society [150], appropriate imaging modalities should be employed under different scenarios for different purposes.

2.6.1 Aneurysm screening

Diagnosis of AAs rely on aortic imaging to confirm the presence of the aneurysm [62,208]. AAs are normally asymptomatic and are usually incidentally found after imaging studies such as chest X-rays and transabdominal ultrasound [209–214], which should be further evaluated using cross-sectional imaging such as CT and MRI.

The guideline recommends chest radiography screening for first-degree relatives of patients with familial TAA [208], while ultrasound is recommended for screening AAAs in the population [215]. The utility of ultrasound has been validated in the large RCTs of AAA screening, with a sensitivity of 95-100% and a specificity of nearly 100% [216,217]. One-time screening with ultrasound for AAA has been shown to be effective in reducing AAA-related mortality and AAA rupture in men over 65 years [218–221]. In the United Kingdom, an ultrasound screening is offered to 65-year-old men, among whom diagnosed aneurysms are referred to a vascular surgeon for further management.

2.6.2 Aneurysm surveillance

Several randomised trials of intervention versus surveillance for small AAs (3.0 to 5.5 cm diameter) have shown no benefit from early intervention, as summarised in a recent systematic review [222]. Therefore, patients with small AAs are suggested to undergo periodic imaging to assess AA growth. For AAA surveillance, ultrasound is the optimal imaging technique due to its sufficient accuracy and no irradiation. The recommended surveillance schedule depends on the disease history while the optimal frequency has not been defined by RCTs [223]. For TAA surveillance, CT and MRI are recommended, ideally performed with contrast for accurate measurement. MRI has advantages to minimise patient's radiation exposure during long-term

surveillance, particularly in younger individuals, where accumulated potential cancer risk from repeated imaging is important [208].

2.6.3 Pre-operative assessment

A thorough assessment of the aneurysm morphology is essential for the selection of appropriate endografts and pre-surgical plans. Three-dimensional angiography with high resolution is required to characterise the full extent of the aneurysm, assess the relationship to key branches, identify anomalous anatomy, and evaluate the adverse factors (such as excessive calcification) and surgery risks. Because of excellent image quality, relatively non-invasive nature and lower cost, CTA is the current standard for pre-operative AA assessment [150]. However, MRA is emerging as a preferred alternative which provides the same details as CTA, and offer more information of the blood flow and aortic wall by advanced sequences as mention in Section 2.4.2 [62]. In addition, PET has the potential to visualise and quantify the inflammatory response within the aneurysm wall, which is of clinical significance for risk evaluation [204].

2.6.4 Endovascular aneurysm repair

For EVAR, the fluoroscopic guidance is of great importance to deliver the catheter and to deploy endografts at the planned sites. DSA is recommended due to its real-time feature and dynamic imaging without the requirement of reconstruction. Novel methods that fuse pre-operative imaging (such as CTA, MRA and ultrasound) with intraoperative fluoroscopy have been developed to provide 3D information with less dose of irradiation [224,225].

2.6.5 EVAR follow-up

The long-term efficacy of EVAR remains to be evaluated and subsequent lifelong imaging surveillance is currently required to monitor for late complications, which include endoleaks, aneurysm sac enlargement or rupture, migration or loss of integrity of the endograft [62]. Spiral CTA has demonstrated advantages as the best imaging technique for endograft surveillance after EVAR [226,227]. It is accurate for diameter measurement, the detection of endoleaks and other device-related complications [228,229]. Duplex ultrasound is suggested as an alternative to

CTA in follow-up surveillance of AAA [230], to avoid ionising radiation or exposure to contrast media. In a recent meta-analysis evaluating surveillance outcomes after EVAR [231], MRI was reported to have a higher detection rate of endoleaks than CTA. However, the limitations of MRI in EVAR follow-up is the difficulty of evaluating device integrity due to artefact, and contraindication for stainless-steel-based grafts.

Chapter 3 Biomechanical analysis[†]

This dissertation sought to provide a comprehensive assessment of the MOUS technique from a biomechanical perspective. Resected human samples are tested *in vitro* to characterise the material behaviour of aneurysm tissue, and image-based computational analyses are performed to investigate the interaction between the blood flow, stents and aortic wall. This chapter therefore describes the framework and methods used in the biomechanical modelling, including the basic mechanical concepts, experimental tests and computational simulations.

3.1 Description of internal deformation and forces

Since Fung *et al.* introduced finite deformation theory in 1960s, a comprehensive framework of continuum mechanics has been established to investigate the behaviour of arteries. In this theory, the arterial tissue is assumed as a continuum body, which deforms in a 3D space subject to loadings. The principal task is to model the internal deformation and forces within the vessel wall under external loadings.

- **Displacement**

When the body is in the reference state (undeformed configuration), a material particle occupies a place whose coordinate is **X**. At time *t*, the body deforms to the current state (deformed configuration), and the original material particle moves to a place with an updated coordinate **x**, as shown in Figure 3.1. The deformation history of the body can be described by the time-dependent deformation field

$$\mathbf{x} = \mathbf{x}(\mathbf{X}, t) \tag{3.1}$$

[†]More details on the concepts of stress, strain, constitutive law and the detailed finite element procedure can be found in Bathe Klaus-Jürgen, Finite element procedures, 2006.

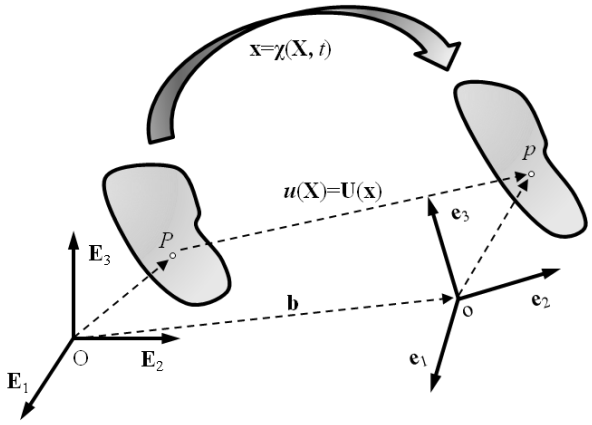

Figure 3.1 Schematic drawing of the motion of a continuum body.

The field functions of displacement of the material particle **X** at time *t* is expressed as

$$\mathbf{u}(\mathbf{X}, t) = \mathbf{x}(\mathbf{X}, t) - \mathbf{X} \tag{3.2}$$

■ **Deformation gradient**

Consider two nearby material particles *P* and *Q*. The vector *d***X** connects the places occupied by *P* with coordinate **X** and *Q* with coordinate **X**+*d***X** in the reference state (Figure 3.2).

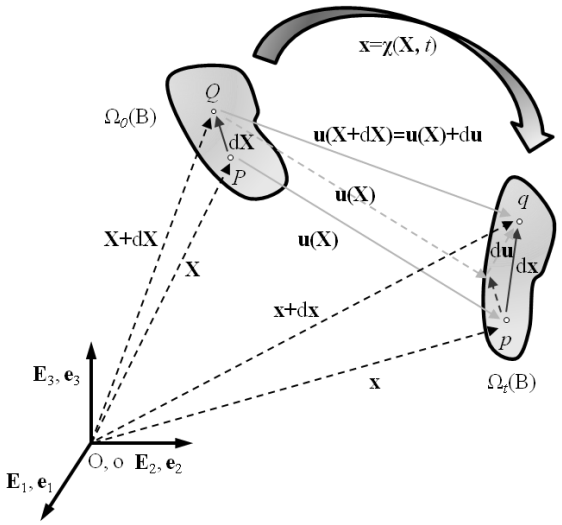

Figure 3.2 Schematic drawing of the deformation (right) of a continuum body.

At time *t*, the two material particles move to new coordinates with **x**(**X**,*t*) and **x**(**X**+*d***X**, *t*), which are two ends of a vector *d***x**

$$d\mathbf{x} = \mathbf{x}(\mathbf{X} + d\mathbf{X}, t) - \mathbf{x}(\mathbf{X}, t) \tag{3.3}$$

Recall the one-order Taylor expansion of the function **x**(**X**, *t*) near **X** at time *t*

$$\mathbf{x}(\mathbf{X} + d\mathbf{X}, t) = \mathbf{x}(\mathbf{X}, t) + \boldsymbol{\nabla}_{\boldsymbol{X}}\mathbf{x}(\mathbf{X}, t)d\mathbf{X} \tag{3.4}$$

If the displacement is continuous and *d***X** is infinitesimal, above Taylor expansion is accurate. Therefore, the Equation (1.4) can be rewritten as

$$\begin{gathered} d\mathbf{x} = \boldsymbol{\nabla}_{\boldsymbol{X}}\mathbf{x}(\mathbf{X}, t)d\mathbf{X} = \mathbf{F}d\mathbf{X} \\ F_{iK} = \frac{\partial x_i(\mathbf{X}, t)}{\partial X_K} \end{gathered} \tag{3.5}$$

where **F** is called the deformation gradient tensor, the linear map from *d***X** in the reference state to *d***x** in the current state. Similar to the deformation gradient tensor, the displacement gradient tensor **H** can be defined by

$$\begin{gathered} d\mathbf{u} = d\mathbf{x} - d\mathbf{X} = (\mathbf{F} - \mathbf{I})d\mathbf{X} = \mathbf{H}d\mathbf{X} \\ \mathbf{H} = \mathbf{F} - \mathbf{I} \\ H_{iK} = \frac{\partial x_i(\mathbf{X}, t)}{\partial X_K} - \delta_{iK} \end{gathered} \tag{3.6}$$

where δ_{iK} is the Kronecker delta, defined as $\delta_{iK} = 1$ when $i = K$, $\delta_{iK} = 0$ when $i \neq K$.

■ **Strain**

The strain is a normalised measure of deformation, which evaluates how much a given displacement differs locally from a rigid body displacement. Consider an infinitesimal line element *d***X** in the reference state, the original length is

$$l_X^2 = d\mathbf{X} \cdot d\mathbf{X} \tag{3.7}$$

After the deformation onto *d***x**, the length in the current state is

$$l_x^2 = d\mathbf{x} \cdot d\mathbf{x} = \mathbf{F}d\mathbf{X} \cdot \mathbf{F}d\mathbf{X} = d\mathbf{X}\mathbf{F}^{\mathbf{T}}\mathbf{F}d\mathbf{X} = d\mathbf{X} \cdot \mathbf{C} \cdot d\mathbf{X} \tag{3.8}$$

where **C** is called the right Cauchy-Green deformation tensor, defined as

$$\mathbf{C} \coloneqq \mathbf{F}^{\mathbf{T}} \cdot \mathbf{F} \tag{3.9}$$

Therefore, the change of element length is characterised by **C**. A spectral decomposition can be performed over **C**:

$$\mathbf{C} = \sum_{i=1}^{3} \lambda_i^2 \, \mathbf{N}_i \otimes \mathbf{N}_i \tag{3.10}$$

where λ_i $(i = 1,2,3)$ are the three principal stretches, with corresponding principal directions $\mathbf{N}_i$ $(i = 1,2,3)$. Invariants of **C** are defined as

$$\begin{aligned} I_1^C &\coloneqq \mathrm{tr}(\mathbf{C}) = \lambda_1^2 + \lambda_2^2 + \lambda_3^2 \\ I_2^C &\coloneqq \frac{1}{2}[\mathrm{tr}(\mathbf{C})^2 - \mathrm{tr}(\mathbf{C^2})] = \lambda_1^2\lambda_2^2 + \lambda_2^2\lambda_3^2 + \lambda_3^2\lambda_1^2 \\ I_3^C &\coloneqq \det(\mathbf{C}) = \lambda_1^2\lambda_2^2\lambda_3^2 = J^2 \end{aligned} \tag{3.11}$$

which are useful for the expression of strain energy density function (SEDF). Recall the Equation 1.8, the right Cauchy-Green deformation tensor C can be expressed in terms of the displacement gradient **H**:

$$\mathbf{C} = \mathbf{H}^{\mathbf{T}} + \mathbf{H} + \mathbf{H}^{\mathbf{T}}\mathbf{H} + \mathbf{I} \tag{3.12}$$

There are different types of strain tensors to characterise the local deformation for different purposes. One of such strains for large deformation is the Lagrangian finite strain tensor, defined as

$$\mathbf{E} = \frac{1}{2}(\mathbf{C} - \mathbf{I}) = \frac{1}{2}(\mathbf{H}^{\mathbf{T}} + \mathbf{H} + \mathbf{H}^{\mathbf{T}}\mathbf{H}) \tag{3.13}$$

E is a measure of the difference between **C** and unit tensor **I**.

Although the vessel wall undergoes big deformation, it is useful to understand the relationship between the displacement and strain under small deformation, which is fundamental to non-linear analysis. The small-strain approximation assumes $H_{iK} << 1$, therefore the quadratic term $\mathbf{H}^{\mathbf{T}}\mathbf{H}$ can be neglected in Equation 1.14, and the Lagrangian finite strain tensor **E** can be simplified to the small strain tensor $\boldsymbol{\varepsilon}$:

$$\boldsymbol{\varepsilon} = \frac{1}{2}(\mathbf{H}^{\mathbf{T}} + \mathbf{H})$$
$$\varepsilon_{ij} = \frac{1}{2}\left(\frac{\partial u_i}{\partial X_i} + \frac{\partial u_j}{\partial X_i}\right) \tag{3.14}$$

In brief, **C** (in the case of small deformation, **ε**) is the strain tensor describing the local deformation of the continuum body.

■ **Stress**

The concept of stress is to measure the internal forces existing in a deformed body. Image a cut plane inside the body and examine the force acting on the cut surface, as shown in Figure 3.3A. The limiting value of the force per unit area is called the stress vector or surface traction. In simple loading situations such as uni-axial tensile or simple shear test, the stress state within the body is uniform and therefore can be described by a single vector (Figure 3.3B&C).

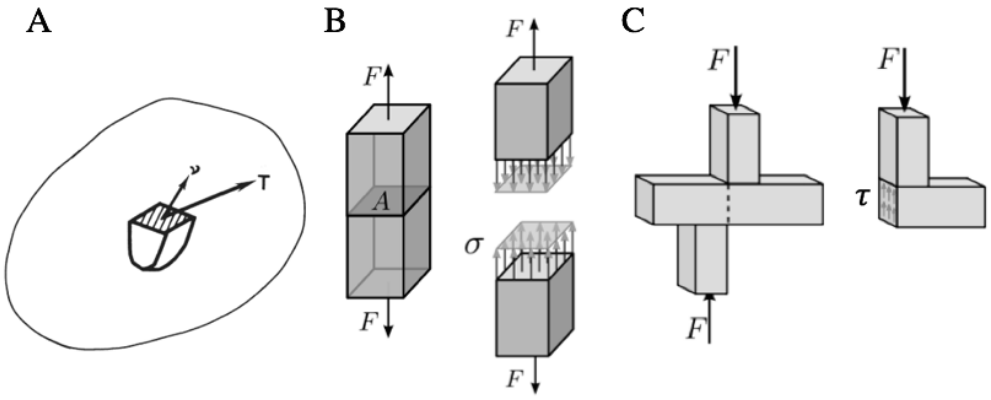

Figure 3.3 Schematic drawing of stress: **(A)** stress vector **T** on a cut surface with normal vector **ν (B)** normal stress vector **σ (C)** simple shear stress vector **τ**.

In the example of a straight rod under uni-axial tension, the normal stress vector **σ** can be obtained by dividing the force **F** with the cross-sectional area **A**. The direction is perpendicular to the cut plane. Similarly, the shear stress vector can be calculated by dividing the shear force with the cross-sectional area, while the direction is parallel to the cut plane.

However, under physiological conditions, a complex stress state exists within vessel wall. The magnitude and direction of local stress vector depend on the normal direction of the cut plane, and also vary at different locations. A higher order tensor is introduced to describe the stress

state, named Cauchy stress tensor. The Cauchy stress tensor $\boldsymbol{\sigma}$ can be expressed in terms of nine components σ_{ij} $(i,j = 1,2,3)$ on an orthonormal basis [$\mathbf{e}_1$, $\mathbf{e}_2$, $\mathbf{e}_3$] (Figure 3.4 left):

$$\boldsymbol{\sigma} = \sigma_{ij} = \begin{bmatrix} \sigma_{11} & \sigma_{12} & \sigma_{13} \\ \sigma_{21} & \sigma_{22} & \sigma_{23} \\ \sigma_{31} & \sigma_{32} & \sigma_{33} \end{bmatrix} \tag{3.15}$$

where σ_{ij} represents the stress component acting on a plane normal to the x_i-axis and along the direction of the x_j-axis. The stress tensor completely defines the stress state at a point inside the deformed body: according to the Cauchy's stress theorem, the stress vector $\mathbf{T}^{(\mathbf{n})}$ on an arbitrary cut plane with normal direction $\mathbf{n}$ can be obtained from the stress tensor (Figure 3.4 right) :

$$\mathbf{T}^{(\mathbf{n})} = \mathbf{n} \cdot \boldsymbol{\sigma} \tag{3.16}$$

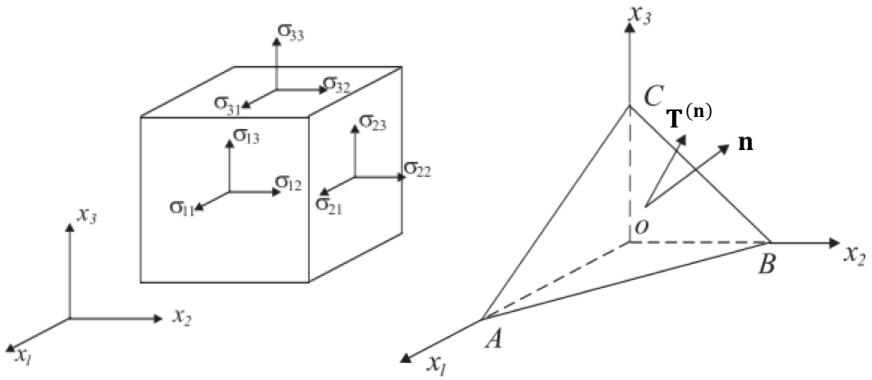

Figure 3.4 Schematic drawing of stress tensor: the components of stress tensor (left) and the stress vector $\mathbf{T}^{(\mathbf{n})}$ on an arbitrary direction $\mathbf{n}$ (right)

Similar to strain tensor, three principal normal stress σ_i $(i = 1,2,3)$ and their corresponding principle directions $\mathbf{N}_i$ $(i = 1,2,3)$ can be derived from the stress tensor, by solving the eigenvalue equation:

$$\mathbf{N} \cdot \boldsymbol{\sigma} = \sigma \mathbf{N} \tag{3.17}$$

The principle normal stresses can be used to calculate the effective stress (also called von Mises stress), which is defined as

$$\sigma_e = \sqrt{\frac{1}{2}[(\sigma_1 - \sigma_2)^2 + (\sigma_2 - \sigma_3)^2 + (\sigma_3 - \sigma_1)^2]} \tag{3.18}$$

In this dissertation, the effective stress is used to estimate the overall stress level within the vessel.

3.2 Constitutive law for arteries

Constitutive law, the relationship connecting strain/deformation and stress/force, is used to describe the inherent material properties. Typical engineering materials (e.g. steel and aluminium) usually exhibit linear and elastic properties, as reflected by a linear stress-strain curve (Figure 3.5 left). In contrast, arterial tissues often exhibit nonlinear behaviour due to their composite structures as discussed in Section 1.2 (Figure 3.5 right).

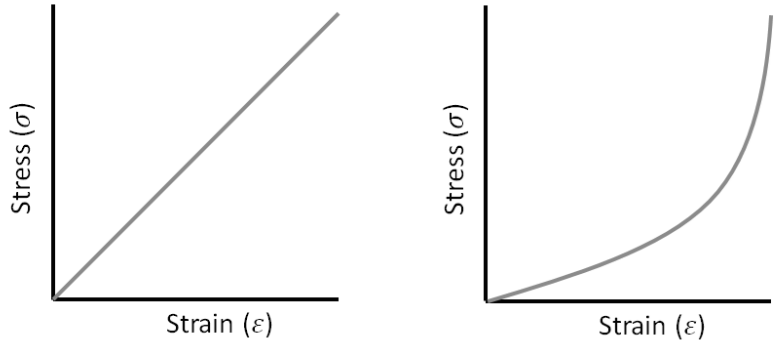

Figure 3.5 Schematic strain-stress curve of linear metal material (left) and non-linear biological soft tissue (right).

■ Hyperelasticity

Hyperelasticity is one type of non-linear elastic model which is commonly used to characterise the mechanical behaviour of biological tissues. Hyperelastic materials are truly elastic in the way that if external loadings are applied and removed later, the material returns to its original configuration without any energy loss. Therefore, a scalar-valued function can be defined as the energy stored within a unit volume due to deformation, which is called SEDF:

$$W = W(\mathbf{C}) = \bar{W}(\mathbf{F}^{\mathrm{T}} \cdot \mathbf{F}) \tag{3.19}$$

As discussed in Section 1.3, the aorta is composed of three layers with reinforced fibres, which are anisotropic at the microscopic level. However, it is difficult to image the fibre structure *in vivo* due to the limited resolution of current imaging techniques. In this dissertation, the biological tissues are assumed to be isotropic materials. The principle of material frame indifference of an isotropic material leads to the conclusion that SEDF can be expressed in terms of the principle stretches or the invariants of **C**:

$$W = \widetilde{W}(\lambda_1, \lambda_2, \lambda_3) = \widehat{W}(I_1, I_2, I_3) \tag{3.20}$$

The Cauchy stress tensor **σ** can be obtained from the derivative of SEDF with respect to the right Cauchy-Green deformation tensor **C**:

$$\boldsymbol{\sigma} = 2\mathbf{F} \cdot \frac{\partial W}{\partial \mathbf{C}} \cdot \mathbf{F}^{\mathrm{T}} \tag{3.21}$$

Accordingly, the principle normal stress can be expressed as

$$\sigma_i = \lambda_i \frac{\partial \widetilde{W}}{\partial \lambda_i} \tag{3.22}$$

■ **Modified Mooney-Rivlin model**

Different SEDFs have been developed to characterise hyperelastic materials. The modified Mooney-Rivlin model was initially proposed to model industrial materials such as rubber, and later was introduced into biomechanics to characterise the material behaviour of arteries. This phenomenon-based model has the capacity of capturing the linear response in lower stretch and non-linear response in higher stretch, and also showed excellent numerical stability for computational simulation. The SEDF of this model is expressed as

$$\widehat{W} = C_1(\bar{I}_1 - 3) + D_1\left[e^{D_2(\bar{I}_1 - 3)} - 1\right] + \kappa(J - 1) \tag{3.23}$$

where $J = det(\mathbf{F}) = \lambda_1\lambda_2\lambda_3$, $\bar{I}_1 = J^{-\frac{2}{3}}(\lambda_1^2 + \lambda_2^2 + \lambda_3^2)$, C_1, D_1 and D_2 are material constants, κ is the hydrostatic pressure as a Lagrangian multiplier to enforce the incompressibility (J=1). Considering Equation (1.23) and (1.24), the relationship between principle stress and the principle stretches is expressed as

$$\sigma_i = \lambda_i \left(\frac{\partial \widehat{W}}{\partial I_1} \frac{\partial I_1}{\partial \lambda_i} + \frac{\partial \widehat{W}}{\partial J} \frac{\partial J}{\partial \lambda_i} \right) = 2\lambda_i^2 \left[c_1 + D_1 D_2 e^{D_2(\bar{I}_1 - 3)} \right] + \kappa \ (i = 1,2,3) \tag{3.24}$$

where the hydrostatic pressure κ is determined by the boundary conditions.

3.3 Uniaxial tensile test

To determine the material constants, material tests on the tissue samples are required. The most common experimental method is the uniaxial tensile test with simple boundary conditions. Displacement loadings are exerted at two ends of the tissue strips, and the traction is measured to obtain the stress-strain relationship for estimation of material constants. The details of the equipment and experimental procedure are described in Chapter 4. This section gives the theoretical formula of the stress-stretch curve in uniaxial tensile tests. Considering the isotropy and incompressibility, the principle stretches under uniaxial test are expressed as

$$\lambda_1 = \lambda_{11} = \lambda, \qquad \lambda_2 = \lambda_3 = \frac{1}{\lambda_1} = \frac{1}{\sqrt{\lambda}} \tag{3.25}$$

where λ is the measured axial Cauchy stretch. As the sample is under uni-axial tensile stress, the principle stresses are expressed as

$$\sigma_1 = \sigma_{11} = \sigma, \qquad \sigma_2 = 0, \qquad \sigma_3 = 0 \tag{3.26}$$

where σ is the measured axial stress and the direction of σ_1 and λ_1 is the axial direction. Recall the Equation (1.25), the measured stress-stretch relationship can be expressed as

$$\sigma = \sigma_1 - \sigma_3 = 2\left(\lambda^2 - \frac{1}{\lambda}\right)\left[c_1 + D_1 D_2 e^{(\lambda^2 + \frac{2}{\lambda} - 3)} \right] \tag{3.27}$$

The ordinary least square (OLS) method is often used to fit experimental data to Equation (1.25) to determine the material constants c_1, D_1 and D_2, by minimising the cost function

$$\Psi(c_1, D_1, D_2) = \sum_{j=1}^{N} \left(\sigma^{j*} - \sigma^{j} \right)^2 \tag{3.28}$$

where N is the number of experimental data points, σ^{j*} is the j^{th} directly measured stress value and σ^{j} is the fitted value at the j^{th} stretch level. Due to the non-linearity of the cost function, the fitting result is usually not unique which limits the physical interpretation of the material constants. In Chapter 4, we introduce the Bayesian framework to infer the material constants to solve this challenge.

3.4 Description of fluid dynamics of blood flow

In fluid dynamics, a field approach is commonly used to describe the flow by Eulerian description. The individual fluid particle is not identified or tracked. Instead, a fixed control volume is defined and flow-related parameters are described as field functions within the control volume.

■ **Velocity field**

A fluid is unable to retain an unsupported shape, and will flow to take up the shape of the container. Similar to the role of displacement in the solid analysis, velocity is a fundamental variable in the fluid analysis. The field of flow is described by the velocity vector field

$$\mathbf{v} = \mathbf{v}(\mathbf{X}, t) = \mathbf{i}\, u(x, y, z, t) \; + \; \mathbf{j}\, (x, y, z, t) \; + \; \mathbf{k}\, w(x, y, z, t) \tag{3.29}$$

where u, v, w are the velocity components along the basis vectors **i**, **j** and **k**, respectively.

■ **Strain rate**

The strain rate tensor **e** describes the rate of change of the deformation in the neighbourhood of a certain point (Figure 3.6), which can be defined as the derivative of the strain tensor with respect to time

$$\begin{aligned} \mathbf{e} &= \frac{\partial \boldsymbol{\varepsilon}}{\partial t} = \frac{1}{2}(\boldsymbol{\nabla}\mathbf{v} + \mathbf{v}\boldsymbol{\nabla}) \\ e_{ij} &= \frac{1}{2}\left(\frac{\partial v_i}{\partial x_j} + \frac{\partial v_j}{\partial x_i}\right) \end{aligned} \tag{3.30}$$

Note that Equation (3.25) is similar to Equation (3.15), where the displacement in strain tensor is replaced by velocity in the strain rate tensor. Therefore, their geometric interpretations are also similar: each diagonal term is the rate of stretching per unit in the direction of the corresponding basis vector, and the off-diagonal term is the rate of angular deformation which is called the rate of shear strain.

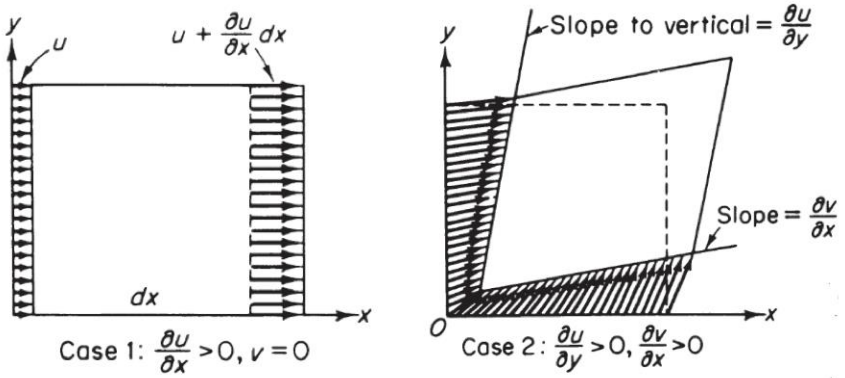

Figure 3.6 Velocity gradients and interpretation of rate of strain tensor components: diagonal terms (left) and off-diagonal terms (right). (Adapted from Fung [232], with permission from Springer Nature)

■ **Stress**

As a continuum model, the stress state at any point in the fluid domain can be described by a second order stress tensor $\boldsymbol{\sigma}$, the same to Equation 3.16. The diagonal terms are the normal stress components and the off-diagonal terms are the shear stress components.

$$\boldsymbol{\sigma} = \sigma_{ij} = \begin{bmatrix} \sigma_{11} & \sigma_{12} & \sigma_{13} \\ \sigma_{21} & \sigma_{22} & \sigma_{23} \\ \sigma_{31} & \sigma_{32} & \sigma_{33} \end{bmatrix} \tag{3.31}$$

$$\boldsymbol{\sigma} = -p\mathbf{I} + \boldsymbol{\tau}$$

The stress tensor of fluid is usually written as the sum of a hydrostatic component $-p\mathbf{I}$ (called hydrostatic pressure tensor where p is the pressure) and a deviatoric component $\boldsymbol{\tau}$ (called viscous stress tensor).

■ **Viscosity**

The viscosity μ is an intrinsic property of a fluid, which connects the strain rate and stress within the fluid domain, similar to the role of elasticity in solid analysis. To illustrate this, consider two parallel plates each of cross-sectional arear A with fluid of viscosity μ (Figure 3.7). The relationship between viscous shear stress τ and shear rate $\partial u/\partial y$ for flow in the x-direction is given as

$$\tau = \mu \frac{\partial u}{\partial y} \tag{3.32}$$

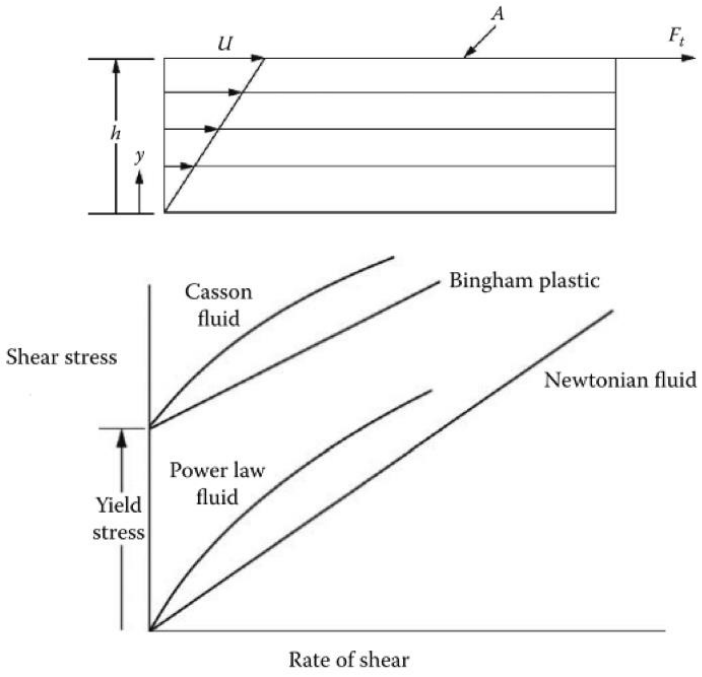

Figure 3.7 Fluid subjected to simple shearing stress (top) and different types of viscosity (bottom).

The coefficient μ in the Equation (1.32) is known as the dynamic viscosity. If the viscosity is constant where shear stress increase linearly with shear rate (Figure 3.7), the fluid is known as a Newtonian fluid. Any fluid which does not have a linear stress-shear rate behaviour is called non-Newtonian, including Bingham plastic fluids, shear thinning fluids and shear thickening fluids. The viscosity of blood depends on the protein concentration of the plasma, the deformability of the blood cells, and the tendency of the blood cells to aggregate. In general, the viscosity increases when the shear strain rate decreases. Although the whole blood is non-Newtonian, it is permissible to use Newtonian constitutive model to simplify the analysis. From

experiments [233], the shear strain rate of blood within human aorta exceeds 100 sec^{-1}, so that the viscosity of blood may be regarded as a constant about 3.5 cP in aorta. The non-Newtonian effect is less important near the vessel wall compared to the centreline of the aorta because of higher strain rate. In this dissertation, the Newtonian fluid model for blood flow is assumed for the computational analysis.

3.5 Haemodynamic variables on the wall

As discussed in Section 1.4, the abnormal haemodynamics could trigger pathological remodelling of the aortic wall. Several haemodyamicvariables defined on the vessel wall have been demonstrated to be related to the development of aortic aneurysm formation and the thrombosis process.

- **Wall Shear Stress**

WSS is the shear force from blood flow that is exerted on the surface of endothelium cells. WSS is the stress vector tangential to the wall surface and varies with time, which can be obtained from the stress tensor $\boldsymbol{\sigma}$:

$$\boldsymbol{\tau}_{\mathbf{w}}(\mathbf{X}, t) = \mathbf{n}(\mathbf{X}) \cdot \boldsymbol{\sigma}(\mathbf{X}, t) \cdot \mathbf{n}(\mathbf{X}) \tag{3.33}$$

where $\mathbf{n}$ is the normal direction of vessel wall. The time-averaged wall shear stress (TAWSS) is calculated by integrating WSS magnitude over the cardiac cycle:

$$\text{TAWSS} = \frac{1}{T}\int_0^T |\boldsymbol{\tau}_{\mathbf{w}}| dt \tag{3.34}$$

- **OSI**

Oscillatory shear index (OSI) is a dimensionless metric which characterises whether the WSS vector is aligned with the TAWSS vector throughout the cardiac cycle, defined as:

$$\text{OSI} = \frac{1}{2}\left(1 - \frac{\left|\int_0^T \boldsymbol{\tau}_{\mathbf{w}}\, dt\right|}{\int_0^T |\boldsymbol{\tau}_{\mathbf{w}}| dt}\right) \tag{3.35}$$

The OSI is greater than zero if there is some direction change during the flow cycle, and the maximum value is 0.5 in the case of pure oscillatory flow without any net forward flow.

- **RRT**

Relative residence time (RRT) at a specific site is inversely proportional to the distance that a particle at that site travels during a single cardiac cycle, defined as

$$\mathrm{RRT}\sim\left(\frac{1-2\times OSI}{T}\int_0^T|\boldsymbol{\tau}_{\mathbf{w}}|dt\right)^{-1} \tag{3.36}$$

The expression on the right is used as the indicator of RRT to represent the average amount of time that a particle spent in a specific region.

3.6 Finite element analysis

In theory, based on detailed information about morphology, constitutive law and boundary conditions, the mechanical variables can be calculated by solving mathematical equations. However, due to the complex geometry of biological structures, non-linear material properties of biological tissues, as well as the complex governing equations, it is not feasible to find an analytical solution to the patient-specific problem. Instead, as a popular numerical technique, finite element method (FEM) can be used to find approximate solutions to partial differential and integral equations. If certain basic numerical requirements and standards of practice are satisfied, the solution from the finite element analysis (FEA) estimates the exact physical solution. As a general method, FEM can be used for both structural solid analysis and fluid analysis.

3.6.1 Solid Analysis

In solid mechanics, the mathematical equations include governing equations, constitutive law and boundary conditions that are written in differential forms and with the tensor notation:

$$\begin{aligned} &\Omega: && \nabla \cdot \boldsymbol{\sigma} + \rho \mathbf{b} = \rho \mathbf{a} \\ & && \boldsymbol{\sigma} = 2\mathbf{F} \cdot \frac{\partial W}{\partial \mathbf{C}} \cdot \mathbf{F}^{\mathrm{T}} \\ &S_u: && \mathbf{u} = \bar{\mathbf{u}} \\ &S_t: && \boldsymbol{\sigma} \cdot \mathbf{n} = \mathbf{T} \end{aligned} \tag{3.37}$$

where $\boldsymbol{\sigma}$ is the Cauchy stress tensor; $\mathbf{b}$ is the body force per unit mass; ρ is the density; $\mathbf{a}$ is the acceleration; $\mathbf{F}$ is the deformation gradient; $\mathbf{C}$ is the stiffness tensor; $\mathbf{u}$ is the displacement; $\bar{\mathbf{u}}$ is the prescribed displacement on boundary surface S_u; $\mathbf{T}$ is the prescribed traction on boundary surface S_t and $\mathbf{n}$ is the normal direction. The detailed constitutive equation and boundary conditions in this study are described in Chapter 4.

When performing solids analysis using FEM, the continuum (e.g. stent) is divided into a finite number of discrete regions, named elements. The mechanical variable (such as displacement, strain and stress) at any point within the continuum are interpolated with values at the nodes of these elements. An approximate solution of the entire continuum is solved from the assembly of the individual elements. Usually, the displacements of nodes are taken as fundamental unknown quantities. From the displacements, the strains are evaluated by taking the appropriate derivatives. The material properties provide the necessary basis for computing stress from these strains. Through FEM, the differential equations on continuous fields can be finally transformed to algebraic equations of discrete nodal quantities which can be solved efficiently. FEA is a reliable and efficient technique that a detailed stress analysis is required prior to approval of a new stent design by the regulatory agencies such as the U.S. Food and Drug Administration [234].

3.6.2 Fluid Analysis

The motion of a continuous fluid medium is governed by Navier–Stokes equations. Under the assumptions of incompressible and Newtonian fluid, the governing equations of blood flow can be expressed in non-conservative forms for mass and momentum, respectively:

$$\begin{aligned} \frac{\partial \rho}{\partial t} + \rho \boldsymbol{\nabla} \cdot \mathbf{v} &= 0 \\ \rho \frac{\partial \mathbf{v}}{\partial t} + \rho \mathbf{v} \cdot \boldsymbol{\nabla} \mathbf{v} - \boldsymbol{\nabla} \cdot \boldsymbol{\tau} &= \mathbf{0} \\ \mathbf{e} &= \frac{1}{2}(\boldsymbol{\nabla} \mathbf{v} + \mathbf{v} \boldsymbol{\nabla}) \\ \boldsymbol{\sigma} &= -p\mathbf{I} + 2\mu\mathbf{e} \end{aligned} \tag{3-38}$$

where t is the time, ρ is the constant density, $\mathbf{v}$ is the velocity vector, μ is the dynamic viscosity constant, $\mathbf{e}$ is the strain rate tensor, $\boldsymbol{\sigma}$ is the stress tensor. The solve these equations, appropriate boundary conditions are applied, which are discussed in Chapter 4.

For the FEM implementation in computational fluid dynamics (CFD), the flow domain is discretised into a set of small fluid elements. Similar to structural analysis, the equations are written into an appropriate form for each element, and the set of resulting algebraic equations for the whole domain are solved numerically. As numerical details of this method are mathematically sophisticated and are not the main focus of this dissertation, further information can be found in related textbooks [235].

3.7 Image-based biomechanical modelling

Although detailed morphology of an aneurysm can be obtained by means of advanced imaging techniques, *in vivo* measurements of the mechanical environment are not available yet. Image-based FEA provides a non-invasive method to estimate the flow field and the deformation of aorta, which helps to predict the geometry and the biomechanical environment after EVAR. In industrial application of FEA, the computational model is usually generated from computer-aided design software with standard geometry. Instead, models in biomechanical application come from *in vivo* images with complex geometry. Extra consideration and processing are required, as discussed below:

- **Pre-processing of medical images**

Clinical images are commonly stored in the DICOM file format, with 3D image volumes in greyscale values. As images may be generated from different machines with different

parameters (e.g. resolution, contrast injection and orientation), the first step is to standardise the images, including processes of denoising, co-registration, resampling, and normalisation.

- **Image segmentation**

To extract the morphological information, the segmentation is performed to delineate the region of interest (ROI). The segmentation can be manually done by experienced radiologists or semi-automated by computer-aided algorithms such as thresholding and region growing. In recent years, the rapid development of machine learning algorithms makes the fully-automatic segmentation possible, given enough training data with manual annotations.

- **Pre-shrinkage**

Typically, the computational start shape in FEM solid simulation is stress-free. However, because the model was extracted from *in vivo* images, the aneurysm shape is pre-deformed under physiological loadings including blood pressure and axial stretch. Therefore, a shrinkage process should be applied to obtain the loading-free configuration. In mathematics, given the deformed shape and applied loading, the load-free configuration can be obtained by solving an inverse problem, which is time-consuming[236]. An approximate method was proposed by Raghavan[237] motivated by the observation that patterns in displacement field for a given AAA are strikingly consistent under all physiological pressure. The basic principle is to recover the stress-free shape by subtracting the displacement caused by blood pressure from the *in vivo* shape.

Chapter 4 Material properties of arterial tissues[†]

This chapter investigates the material behaviour of arterial tissues by uniaxial tensile material tests. A framework of Bayesian inference is proposed to estimate the material constants from the experimental data, which are further correlated to the microstructural fibre architecture on histological images. The material properties are compared among aortic aneurysm, normal aorta and atherosclerotic plaque. The experimental results of AAs in this chapter provide the material constants in constitutive equations for following computational analyses of this dissertation.

4.1 Introduction

Cardiovascular diseases (CVD) are the No.1 killer and responsible for an estimated 31% of all deaths worldwide [238]. About 80% of all CVD deaths are due to heart attacks and strokes [239], which are induced by atherosclerotic plaques. AAs, occurring in approximately 8% of men aged >65 [240], are another common cause of CVD deaths, with the mortality after aneurysm rupture being ~90% [241]. In current clinical practice, luminal stenosis and maximum wall diameter are the only validated risk assessment criteria for atherosclerotic disease and aneurysm, respectively. However, such size-based criteria showed only limited sensitivity and specificity [66,242–244]. Therefore, there is a clear need for novel risk-stratification biomarkers to estimate the risks of atherosclerosis and aneurysm in the hope of improving patient outcomes.

[†] The author of this dissertation carried out all of the work described in this chapter unless specified otherwise. The material test and histological analysis of eight aneurysms were performed together with Aziz Tokgoz from Department of Radiology, University of Cambridge. The other material tests of arterial tissues were performed by Dr Zhongzhao Teng from Department of Radiology, University of Cambridge. The main content of this chapter has been included in

1. **Wang S**, Tokgoz A, Huang Y, Zhang Y, Feng J, Sastry P, Sun C, Figg N, Lu Q, Sutcliffe MPF, Teng Z, Gillard JH. Bayesian inference-based estimation of normal aortic, aneurysmal and atherosclerotic tissue mechanical properties: from material testing, modelling to histology. *IEEE Transactions on Biomedical Engineering*, 2018.

Under physiological conditions, both types of lesion are subject to mechanical loading due to dynamic blood pressure and flow. It has been shown that mechanical loading within the arterial tissue structure has an association with biological activities within the lesion [56,205,245–247], which can promote its development [248–250], leading to both progression and rupture. Accurate characterisation of mechanical properties of atherosclerotic and aneurysmal tissues is required for reliable prediction of mechanical loading in the lesion structure. A reliable prediction process should follow the steps of: (1) direct measurement of tissue stress-stretch [251]; (2) carefully selected SEDF [252]; and (3) determination of material constants in SEDF with an optimisation method to minimise the objective function, which describes the difference between the predicted and measured stress-stretch curves. Several SEDFs have been used to characterize the tissue material, such as neo-Hookean [253–256], one-term Ogden [257], two-term Ogden [258–261], Yeoh [262,263], five-parameter Mooney-Rivlin [264,265], Demiray [266–268], and modified Mooney-Rivlin SEDF [269–271].

It is challenging to obtain a robust estimation of material constants in these SEDFs with traditional least squares methods, which often converge to a local minimum of the objective function in a narrow region around the initial guesses. This yields different sets of constants that can all fit the experimental data well. Although these distinct sets of material constants can lead to very similar stress predictions [252], it is inappropriate to characterise the tissue mechanical behaviour by using regressed material constants, whose values are highly dependent on their initial guesses. In other words, it is incorrect to assign a physical meaning to these regressed constants.

In this study, Bayesian inference was used to estimate the probability of each material constant across a wide range and the expectation was used to characterise the material constants for each tissue strip. This approach avoids non-uniqueness of parameter estimation associated with the least squares method. The capability of the determined material constants to differentiate tissues from normal aorta, carotid atherosclerotic plaque and AAs were assessed and the association between determined material constants and fibre architectures in the tissue was explored.

4.2 Materials and methods

4.2.1 Tissue collection and preparation

In this study, stress-stretch curves from direct uniaxial material tests with 8 normal aortas [272], 19 AAs [272] and 21 carotid atherosclerotic plaques [251] were collected from previous studies, except for 8 aneurysms. The eight aneurysmal samples (seven males, age 63.3±11.7 years) were collected from the Papworth Cambridge University Hospital during open surgical repair. The protocol was approved by the local ethics committee and written informed consent was obtained from all patients. Details of patient demographics and tissue preparation except for the eight from Papworth Hospital have been described in two previous studies [251,272]. The overall patient demographics are listed in Table 4.1.

Table 4.1 Patient demographics.

	Normal aorta	**Aortic aneurysm**	**Carotid atherosclerotic plaques**
Male, n (%)	7 (87.5)	16 (84.2)	18 (85.7)
Age, (Mean±SD)	34.1 ± 7.8	61.2 ± 7.3	68.2 ± 7.4

Samples were banked in liquid nitrogen for <4 months prior to testing. Cryoprotectant solution (20% dimethylsulfoxide (DMSO) in 5% human albumin solution) added to a final concentration of 10% DMSO was utilised to prevent ice crystals from damaging the tissue. Prior to testing, the samples were immersed in phosphate buffered saline and defrosted in a 37ºC tissue bath. The intact aneurysm rings were cut and open using a scalpel, and further dissected by a tweezer into three layers including intima, media and adventitia. Approximately 10 rectangle tissue strips of 1-2 mm width were obtained, both longitudinal (the axial direction) and perpendicular (the circumferential direction) to the blood flow, as shown in Figure 4.1.

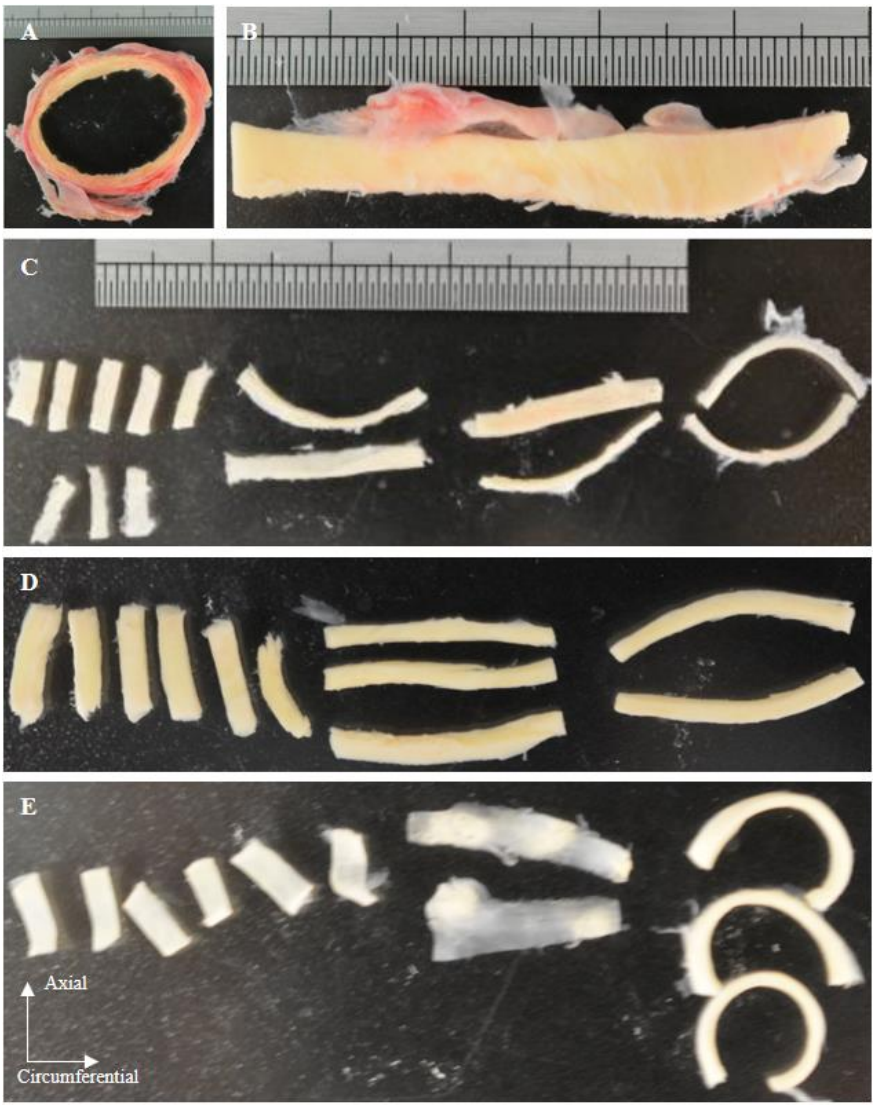

Figure 4.1 A representative sample of aortic aneurysm. **(A)** The intact arterial ring; **(B)** Cut and opened arterial tissue; **(C)** Adventitia tissue strips; **(D)** Media tissue strips; **(E)** Intima tissue strips.

4.2.2 Uniaxial tensile testing

An in-house designed tester comprised of a stepper motor (Miniature Steel Linear Stages, Newport Corporation, USA), a load cell (custom designed), a camera (PixeLink PL-B776U 3.1 MP USB2 Colour Camera, PixeLINK, Canada) and a controlling system developed in LabVIEW 2011 (National Instruments, USA) were used to perform the uniaxial extension test (Figure 4.2 A). The position resolution of the stepper motor was 0.1 μm; the precision of the

load cell was 0.0005 N and the image size of each image frame is 2,048×1,536 pixels, with an 80×60 mm^2 field of view. The tissue strip was mounted on the tester using modified 6-cm straight haemostatic clamps (Shanghai Medical Instruments (Group) Ltd., Corp. China). The clamped section of each end was 1-1.5 mm.

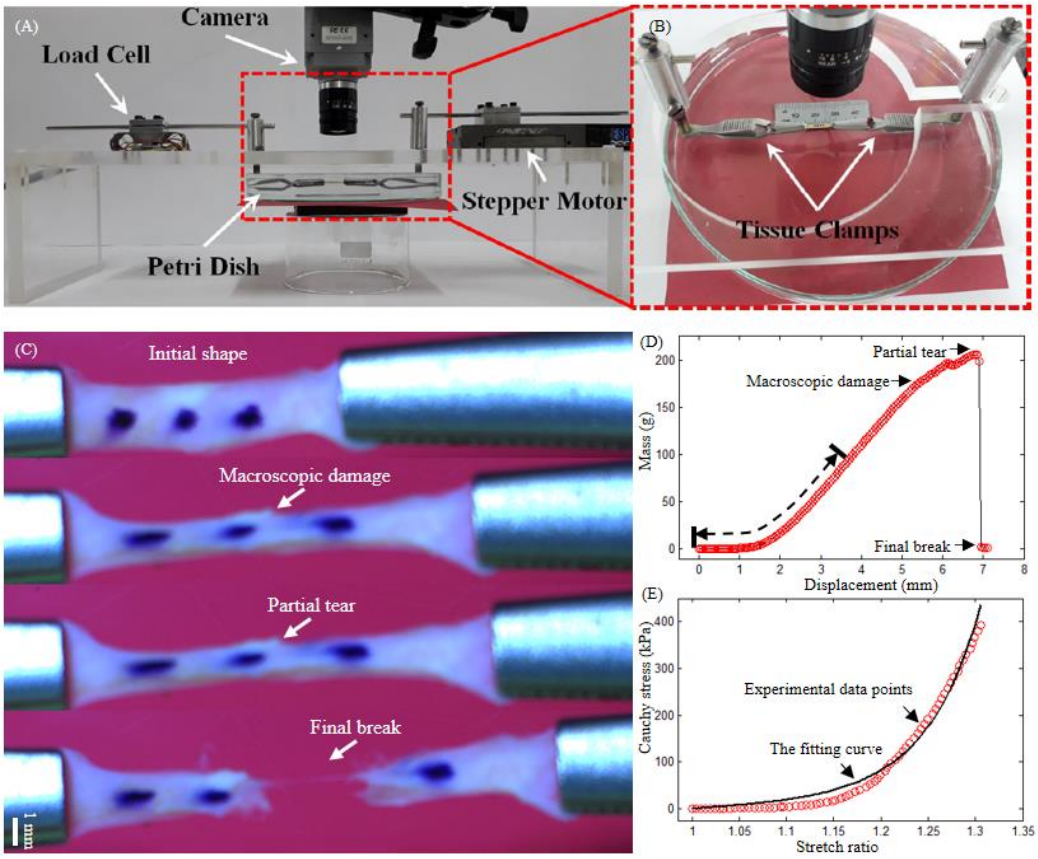

Figure 4.2 Overview of the testing equipment and an example of the testing process. **(A)** Different parts of the testing equipment; **(B)** Captured region of the camera; **(C)** An aneurysmal media strip at different stages of stretching; **(D)** The mass-displacement curve recorded during stretching and the unsmoothed steps along the curve representing tissue damage due to stretching; **(E)** The converted stress-stretch data points where stress≤400 kPa and the corresponding fitted curve.

After five preconditioning cycles (by moving one of the clamps 2.5% of the total distance between the two clamp ends at a speed of 0.05 mm/s), the testing was performed with a speed of 0.01 mm/s immersed in a tissue bath with 37ºC saline solution. Black ink markers were placed on the surface to trace the local displacement (Figure 4.2C). Testing was stopped when the tissue strip failed under the applied strain. The centre of each marker was identified and the

local stretch ratio was calculated from the distance between the marker centres. The Cauchy stress was converted from the measured force signal using the strip thickness, the width at rest and the stretch ratio with the assumption of incompressibility (Figure 4.2E).

4.2.3 Strain energy density function

As introduced in Section 3.2, the modified Mooney-Rivlin SEDF was used to characterise the mechanical behaviour of the tissue strips based on the consideration of material stability [252]. Recall the Equation (3.27), the Cauchy stress σ_{11} along the tensile direction is express as

$$\sigma_{11}(\lambda) = 2\left(\lambda^2 - \frac{1}{\lambda}\right)\left[C_1 + D_1 D_2 e^{D_2\left(\lambda^2 + \frac{2}{\lambda} - 3\right)}\right] \tag{4.1}$$

in which λ is the stretch ratio.

4.2.4 Ordinary least square fitting method

The ordinary least square (OLS) fitting method was used to determine the material constants in Equation (4.1) by finding the local minimum of the objective function around the initial guess of (C_{10}, D_{10}, D_{20}),

$$S(C_1, D_1, D_2) = \sum_{k=1}^{N}\left[\sigma_{11k}^{p} - \sigma_{11k}^{m}\right]^2 \tag{4.2}$$

in which N is the number of data points, $\sigma_{11k}^{p}$and σ_{11k}^{m} are the kth predicted and measured Cauchy stresses, respectively. All material constants were constrained to be positive to avoid any unphysical phenomenon. Relative error was used to assess the fitting quality,

$$\gamma = \frac{\sum_{i=k}^{N}\left|\sigma_{11k}^{p} - \sigma_{11k}^{m}\right|}{\sum_{i=k}^{N}\left|\sigma_{11k}^{m}\right|} \times 100\% \tag{4.3}$$

4.2.5 Bayesian inference framework

In the Bayesian inference, all unknown parameters are treated as random variables $\boldsymbol{\theta}$. Given the experimental data $\mathcal{D}$, its aim is to estimate the conditional distribution of unknown parameters $p(\boldsymbol{\theta}|\mathcal{D})$, which is referred as the posterior distribution (*posterior*). First a prior distribution (*prior*) $p(\boldsymbol{\theta})$ is assumed to represent the prior knowledge about unknown parameters. The prior distribution can be adapted from previous studies and/or from experts' opinions. If there is no established prior distribution for a problem, a non-informative *prior* can be applied using the Principle of Maximal Entropy.

An appropriate noise model and chosen constitutive equations are used to derive the likelihood function (*likelihood*) $p(\mathcal{D}|\boldsymbol{\theta})$. The *posterior* can be calculated by linking the *prior* and the *likelihood* using Bayes' theorem,

$$p(\boldsymbol{\theta}|\mathcal{D}) = \frac{p(\boldsymbol{\theta}) \times p(\mathcal{D}|\boldsymbol{\theta})}{p(\mathcal{D})} \tag{4.4}$$

The denominator of Equation (4.4) is a constant referred to as the probability of the evidence (*evidence*) and given by,

$$p(\mathcal{D}) = \int p(\boldsymbol{\theta}) \times p(\mathcal{D}|\boldsymbol{\theta}) d\boldsymbol{\theta} \tag{4.5}$$

The multi-dimensional integral in Equation (4.5) is generally difficult to evaluate. If the unknown parameters are the only ones of interest, Equation (4.5) can be rewritten as,

$$p(\boldsymbol{\theta}|\mathcal{D}) \propto p(\boldsymbol{\theta}) \times p(\mathcal{D}|\boldsymbol{\theta}) \tag{4.6}$$

Sampling methods, e.g., Markov Chain Monte Carlo (MCMC), can be applied to explore the *posterior* without explicitly computing the *evidence* (Equation (4.6)). The strategy is to draw samples from a distribution similar to the *posterior* by using effective sampling methods. More details about Bayesian inference and different sampling methods can be found in references [273–275].

When Bayesian inference is used to estimate the material constants in Equation (4.1), a Gaussian noise model is introduced for the uncertainty, hoping that $\sigma_{11k}^{p}(\lambda)$ equals to $\sigma_{11k}^{m}(\lambda)$,

$$\sigma_{11}(\lambda) = 2\left(\lambda^2 - \frac{1}{\lambda}\right)\left[C_1 + D_1 D_2 e^{D_2\left(\lambda^2+\frac{2}{\lambda}-3\right)}\right] + \mathcal{N}(0, \varepsilon^2) \tag{4.7}$$

in which $\mathcal{N}(0, \varepsilon^2)$ is the Gaussian noise with zero mean and variance ε^2. Therefore, the likelihood function can be written as,

$$p(\mathcal{D}|C_1, D_1, D_2, \varepsilon) = \prod_{k=1}^{N} \mathcal{N}\left(\sigma_{11k}^{p} - \sigma_{11k}^{m}|0, \varepsilon^2\right) \tag{4.8}$$

In this study, the *prior* for C_1, D_1, D_2 and ε were assumed to be uniform distributions with ranges of [0, 5000 kPa], [0, 5000 kPa], [0, 5000 kPa] and [0, 5000 kPa], respectively. The sensitivity to the *prior* was tested. The MCMC with Gibbs sampling method was implemented in the software WinBUGS (MRC Biostatistics Unit, University of Cambridge) to estimate the posterior distribution of the parameters, i.e. $p(\boldsymbol{\theta}|\mathcal{D})$. The mean and standard deviation of the *posterior* was calculated for further analyses amongst tissues from different types of lesions and distinct morphological component.

4.2.6 Quantitative histological analysis

Twenty-four tissue strips adjacent to those used for mechanical testing from the 8 aneurysmal samples (3 strips from each sample), which were collected from Papworth Hospital were submitted for histological examination. Following a standard processing procedure, 4-μm tissue slices in were stained with Verhoeff–van Gieson (EVG) and Picrosirius Red (PSR) to visualise the elastin and collagen contents. Elastin appears dark in EVG stain, and collagen appears red in Sirius Red stain. Elastin and collagen percentage of each tissue slice, as well as the fibre dispersion (κ; a parameter describing the scatter of fibre orientations), and fibre waviness (ω) were quantified using an in-house designed MATLAB-based (MathWorks, Inc.) software, as described in the appedix at the end of this chapter. The software was optimised by using an expert pathologist to assess the results. In this study, the area percentage of elastin (= *area with elastin/area of ROI; ROI stands for region of interest*) and collagen (= *area with collagen/area of ROI*), κ, and ω were used to characterise the fibre architecture in the structure.

Perfectly parallel fibres correspond to κ=0 and an even scatter of fibre orientations has κ=1/3. Smaller values of ω correspond to wavier fibres, and ω=1 indicates straight fibres.

4.2.7 Statistical analysis

The correlation between the percentage of collagens and the estimated material constants was assessed using Spearman correlation test. In this study, multiple samples were from a single tissue piece and the linear mixed effect model was constructed to assess the difference of parameters from different tissue types, considering both random and fixed effect. The statistical analysis was performed in MATLAB (MathWorks, Inc.). A significant difference was assumed if p<0.05.

4.3 Results

In this study, stress-stretch curves from 312 tissue strips in the circumferential direction (perpendicular to the direction of blood flow) were analysed using both OLS and Bayesian inference. In detail, the curves were from 15 media and 15 adventitial strips of 8 normal aortas; 28 adventitial, 36 media, 8 thickened intima and 27 thrombus strips of 19 aortic aneurysms; 65 media, 59 fibrous cap (FC), 38 lipid, and 21 intraplaque haemorrhage/thrombus (IPH/T) strips of 21 carotid atherosclerotic plaques.

4.3.1 Case study on material constants' uniformity

Figure 4.3 provides a representative example showing the fitted results using OLS fitting method and Bayesian inference. The determined material constants were dependent on initial guesses when OLS method was used. In the cases shown in Figure 4.3, when the initial guesses of (1, 1, 1) and (10, 10, 10) were used, the fitting results were very different (Table 4.2). A certain choice of initial guesses, e.g., (100, 100, 100), might lead to a poor regression (Figure 4.3). It is therefore inappropriate to use material constants determined by OLS to characterise the mechanical properties of arterial tissues. On the contrary, based on Bayesian inference, the determined material constants showed little changes (<5%) when the *prior* ranges of C_1, D_1 and D_2 all increased ten times from [0, 1000] to [0, 10000].

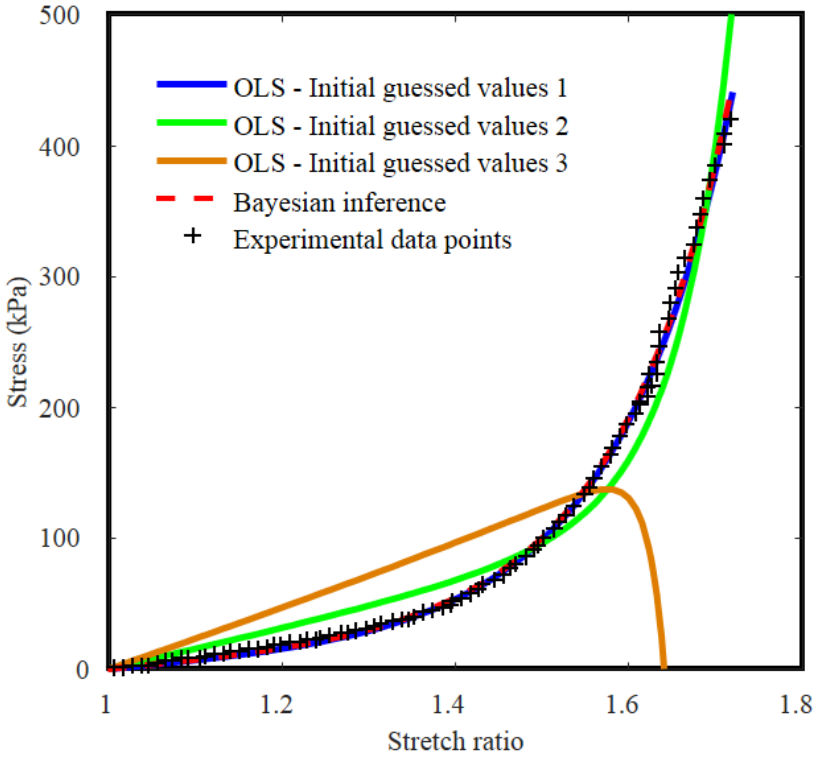

Figure 4.3 A representative example showing the fitted results using ordinary least square (OLS) method and Bayesian inference (initially guessed values 1 of (C_1, D_1, D_2) are (1, 1, 1), values 2 are (10, 10, 10), and values 3 are (100, 100, 100); the detailed fitted results are listed in Table 1; the experimental data were acquired from a media strip of a normal aorta).

Table 4.2 Representative regressions using the ordinary method with different initial values and Bayesian inference procedure with different *prior* ranges.

Fitting Method	C_1 **(kPa)**	D_1 **(kPa)**	D_2	γ
OLS - Initial values (1, 1, 1)	2.19	4.00	2.12	3.3%
OLS - Initial values (10, 10, 10)	25.56	0.04	5.27	15.1%
OLS - Initial values (100, 100, 100)	39.10	2.65×10^{-8}	19.92	444.5%
OLS - Initial values (0, 1, 0)	6.17	2.84	2.31	3.1%
Bayesian inference (*Prior* [0, 1000])	3.11	3.72	2.16	3.3%
Bayesian inference (*Prior* [0, 5000])	3.26	3.67	2.17	3.3%
Bayesian inference (*Prior* [0, 10000])	3.20	3.68	2.17	3.3%

In general, if the initially guessed value is properly chosen, OLS can fit the experimental data well. The fitting quality γ was 8.5% [6.0, 12.1] (Median [Interquartile range]), which is slightly better than that of the Bayesian inference-based estimation (8.8% [6.0, 12.3], p<0.0001).

4.3.2 Bayesian inference-based material constants of different tissues

The values of C_1, D_1 and D_2 for each type of tissue are provided in Figure 4.4 (the outliers that are out of 1.75 quartile range were not shown) with actual values listed in Table 4.3. In normal aorta, the media and adventitia have comparable C_1 , D_1 and D_2 (p=0.18, 0.33, and 0.14, respectively). Samples from the aortic aneurysm, media and thickened intima showed a comparable C_1 (p=0.50), which is higher than that in either adventitia or thrombus (p<0.05). Adventitia has the lowest value of D_1 (p<0.005); intima has the highest value of D_1 (p<0.01), but is comparable with the one of thrombus (p=0.21). Media has the highest D_2 value compared with adventitia, thickened intima and thrombus (p<0.05); and thrombus has the lowest value of D_2 (p<0.05), but is comparable with that of intima (p=0.29).

Table 4.3 Bayesian inference-based estimations for different types of tissues (Median [Interquartile range])

		C_1 (kPa)	D_1 (kPa)	D_2	γ (%)
Normal aorta	Media	4.53 [0.88, 10.84]	3.68 [1.19, 9.21]	2.53 [1.74, 4.29]	3.3 [2.3, 4.5]
	Adventitia	1.04 [0.60, 3.46]	1.46 [0.75, 6.51]	3.57 [3.12, 5.26]	9.8 [5.5, 13.6]
Aneurysm	Media	1.81 [0.83, 6.31]	2.33 [0.79, 4.02]	16.77 [9.12, 25.71]	11.8 [8.8, 14.7]
	Adventitia	0.96 [0.30, 2.88]	0.79 [0.56, 3.40]	8.04 [5.60, 12.13]	12.0 [7.2, 14.8]
	Intima	3.27 [0.74, 20.91]	7.98 [3.82, 21.42]	6.05 [3.04, 10.44]	7.9 [5.6, 11.5]
	Thrombus	0.46 [0.12, 1.17]	5.34 [1.66, 9.90]	2.80 [0.59, 10.77]	8.3 [7.2, 14.1]
Atherosclerosis	Media	3.34 [1.44, 9.60]	2.27 [1.45, 3.62]	21.78 [16.16, 35.24]	7.7 [6.6, 9.6]
	FC	4.87 [2.50, 12.33]	2.21 [1.26, 4.16]	28.06 [17.95, 44.17]	9.2 [7.0, 11.5]
	Lipid	1.48 [0.71, 5.62]	1.40 [0.28, 4.15]	10.07 [6.42, 23.66]	8.4 [5.9, 11.4]
	IPH/T	0.79 [0.18, 1.47]	1.17 [0.44, 2.20]	10.58 [5.45, 13.63]	10.8 [8.2, 18.4]

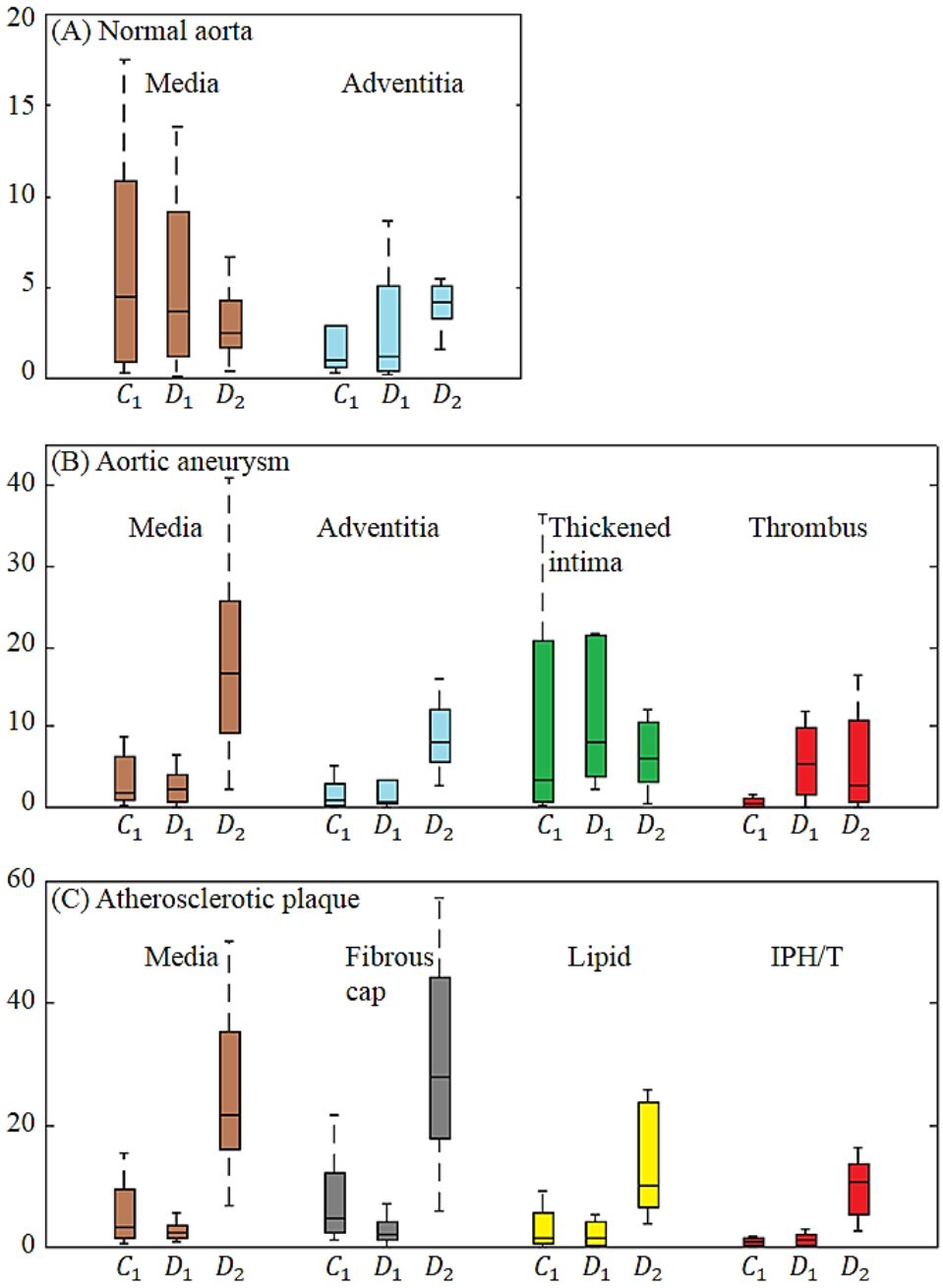

Figure 4.4 The visualisation of (C_1, D_1, D_2) of different tissue strips from different types of samples (A: tissue strips of media and adventitia from normal aortas; B: tissue strips of media, adventitia, thickened intima and thrombus from aortic aneurysms; C: tissues strips of media, fibrous cap, lipid and intraplaque haemorrhage/thrombus from carotid atherosclerotic plaques; Unit of C_1 and D_1 is kPa and D_2 is dimensionless).

In carotid atherosclerotic plaques, the media and FC have a comparable C_1 (p=0.33), higher than those of lipid and IPH/T (p<0.05). Compared with IPH/T, C_1 value of lipid is higher (p=0.03). The value of D_1 for media, FC and lipid is comparable (p>0.05), and IPH/T has the lowest value of D_1 compared with media and FC (p<0.01), but is comparable with that of lipid (p=0.87). Both media and FC have a comparable D_2 (p=0.33), as do lipid and IPH/T (p=0.39); both media and FC have a significantly higher D_2 than either lipid or IPH/T (p<0.005).

The media is the only common tissue in all three types of samples. The C_1 values of media from normal aorta, aortic aneurysm and carotid atherosclerotic plaque are comparable (p>0.05), as is D_1 (p>0.05). However, D_2 has the capacity to differentiate all three types of tissue. The value of D_2 for the media from both aneurysm and plaque is significantly larger than that from normal aorta (p<0.0001), and the D_2 value of media from plaque is much larger than that from aneurysm (p=0.022).

4.3.3 Material constants, elastin and collagen contents and architectures

A tissue strip adjacent to the one used for the mechanical testing of each layer from each of the eight aneurysm samples from Papworth Hospital were submitted for histological examination, to investigate the elastin and collagen in the tissue microstructure (Figure.4.5 and Figure 4.6).

As shown in Figure 4.7A, the area percentage of elastin in both thickened intima and media is higher than the adventitia (an example is shown in Figure 4.5), and thickened intima has the lowest area percentage of collagen (Figure 4.7B), followed by media, where the adventitia has the highest area percentage of collagen (an example is shown in Figure.4.6). The difference in elastin content in these three layers (Figure 4.7A) is consistent with the difference of C_1 value as listed in Table 4.3.

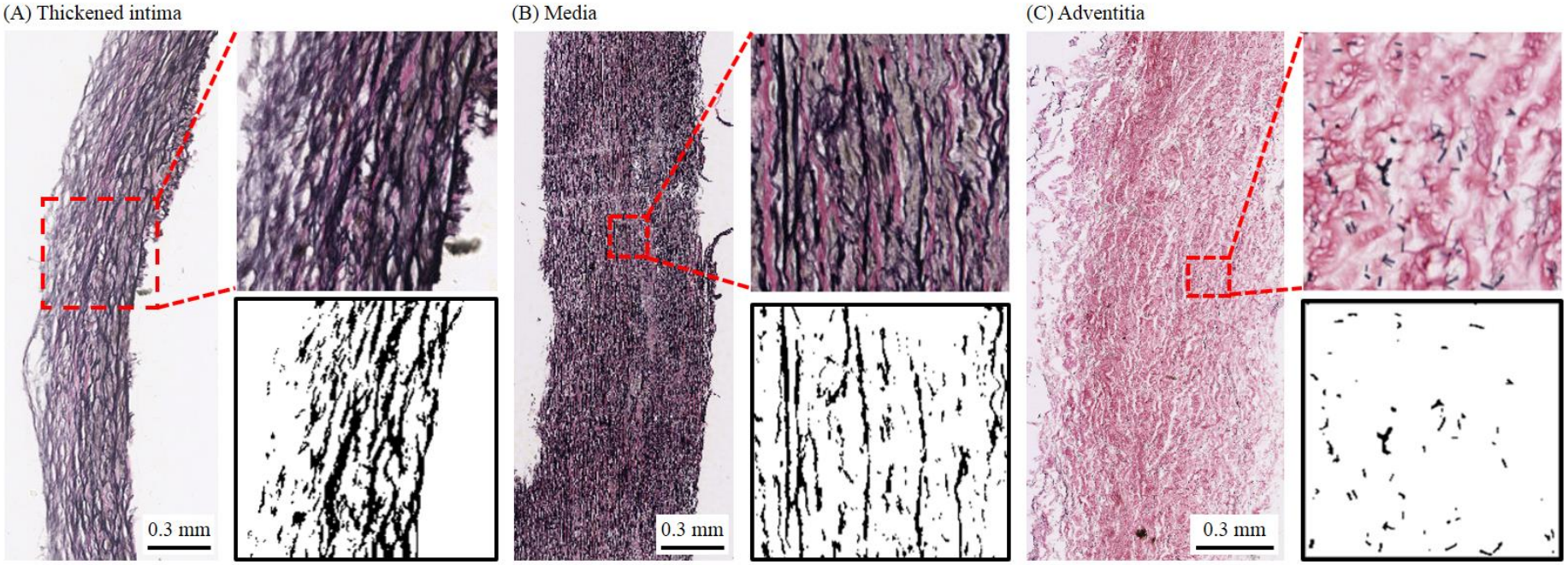

Figure 4.5 Representative EVG stained images showing the distribution of elastin in the thickened intima, media and adventitia of an aortic aneurysm (The elastin contents are segmented in black. The adventitia has much less elastin fibres than either the thickened intima or media.)

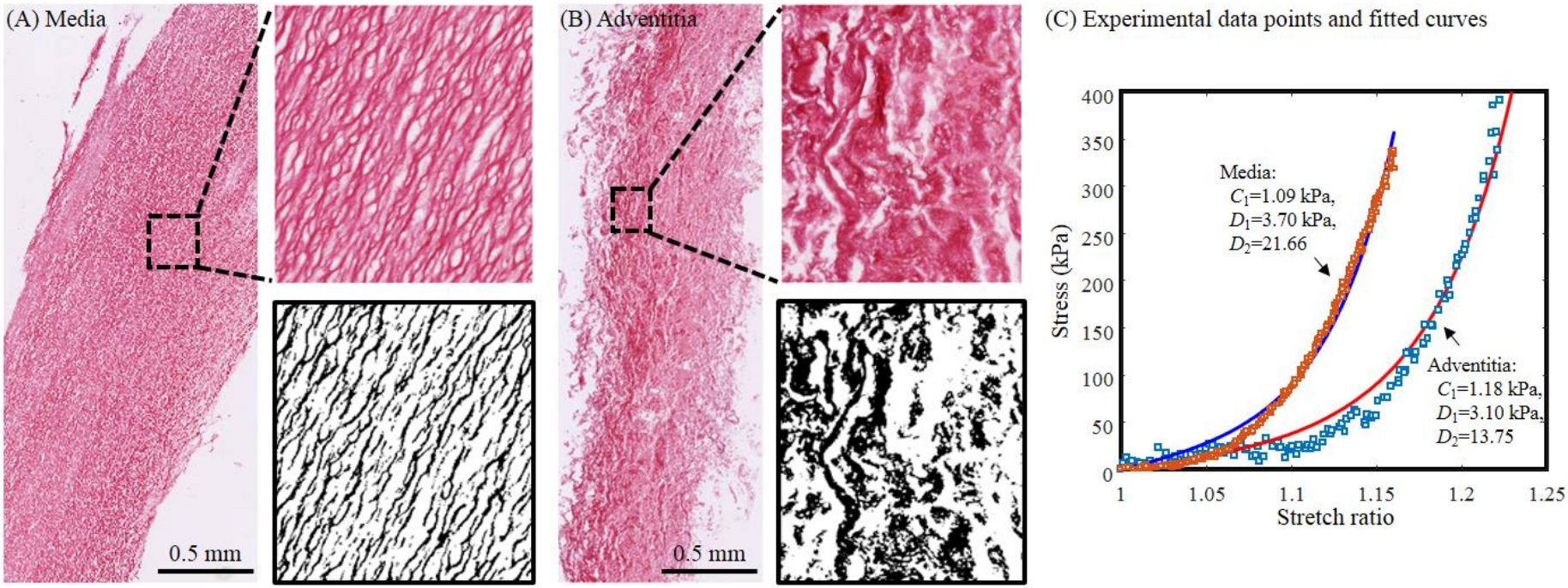

Figure 4.6 Representative Sirius Red stained images showing the collagen fibres in the media and adventitia of an aortic aneurysm. (The collagen contents are segmented in black. Collagen fibres in the adventitia (B) is much wavier than those in the media (A). C: the stress-stretch curves of the tissue strips are shown in A and B.)

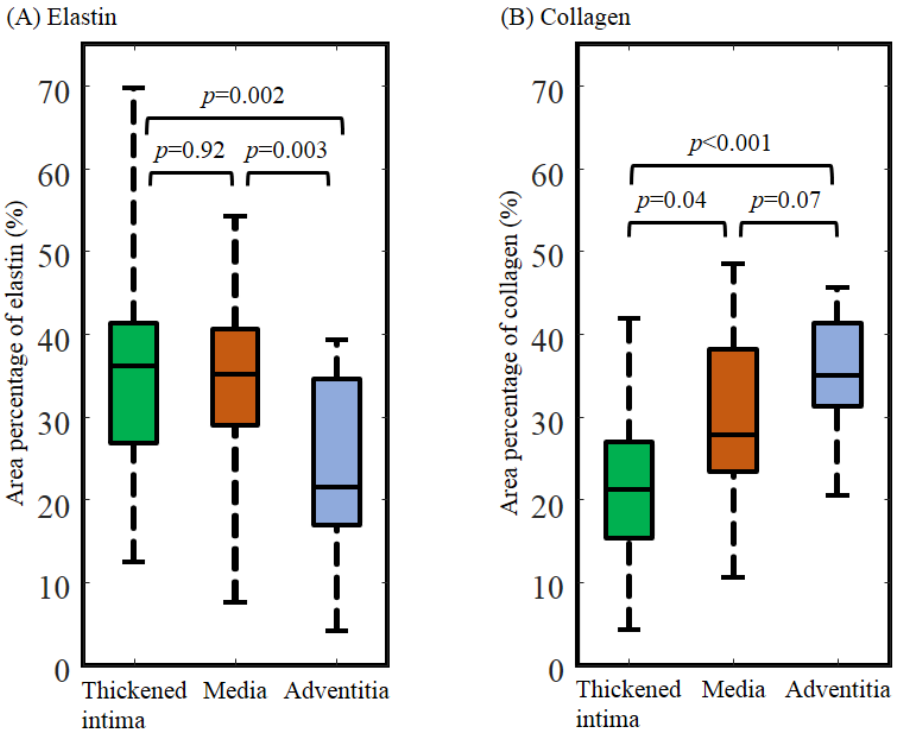

Figure 4.7 Comparison of area percentage of elastin and collagen contents in the thickened intima, media and adventitia from eight aortic aneurysms.

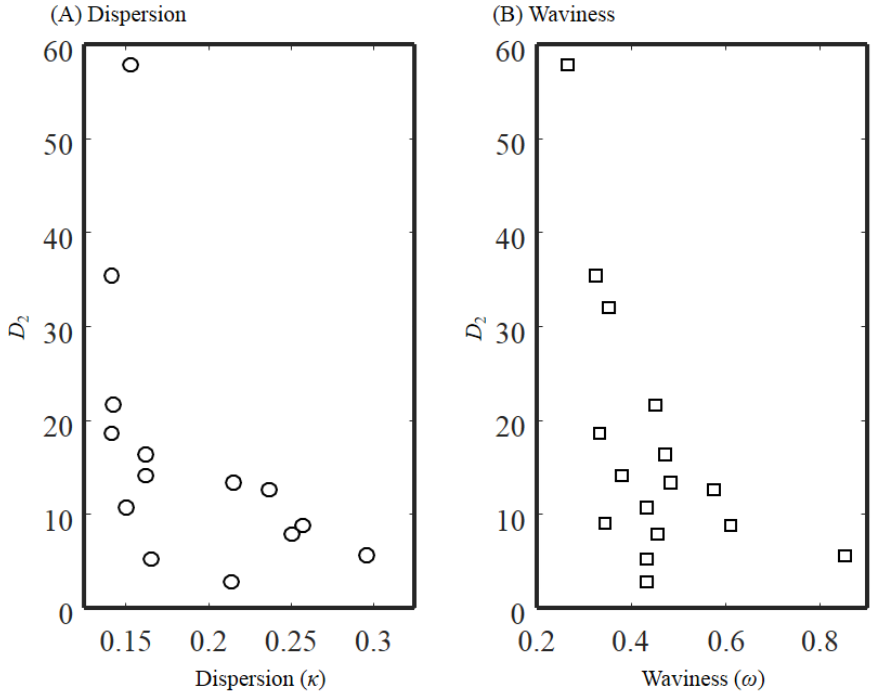

Figure 4.8 The association between collagen fibre dispersion (κ) and waviness (ω) and D_2.

Elastin fibres in the thickened intima and media are mostly well organised and straight while those in the adventitia are more fragmented (Figure.4.5). Similarly, the collagen fibres in the thickened intima and media are straight with a preferred direction, while in the adventitia, the collagen fibres are wavier and more disorganised. Compared with the media, the collagen fibre dispersion, κ, is much bigger (0.14 [0.13, 0.15] vs 0.23 [0.19, 0.25], p=0.008), and the waviness, ω, is higher in the adventitia (0.07 [0.09, 0.12] vs 0.16 [0.15, 0.18], p=0.008). When κ, ω, D_1 and D_2 of media and adventitia were pooled, κ was inversely associated with D_2 (ρ=-0.61, p=0.014) and ω was positively associated with D_2 (ρ=0.73, p=0.002) (Figure 4.7); but no association was found between D_1 and κ or ω.

4.4 Discussion

Bayesian inference estimates the distribution of material parameters in the constitutive model rather than finding their point-based estimations. It is used in this study to avoid the sensitivity to initial guesses when the OLS method is used, allowing characterisation of the tissue through comparison of material constants. The obtained results indicate that C_1 , D_1 and D_2 were tissue type dependent. In particular, D_2 is the most sensitive parameter in differentiating tissues of distinct arterial layers from a single type of sample, or of the same layer between different type of samples; and D_2 is also associated with tissue architectures, e.g., fibre dispersion and waviness. In general, atherosclerotic tissues have the largest D_2 values, followed by those from aneurysms and then normal aortas.

The proper choice of both SEDF and material constants is important for material stability and numerical convergence in computational studies that aim to predict stress distribution within the lesion [252,276]. The robustness of the SEDF is reflected by its ability to reproduce several modes of deformation, including, but not limited to uniaxial, biaxial and pure shear deformation [17]. In this study, stress-stretch data from uniaxial testing was used, since it is nearly impossible to perform biaxial and pure shear testing with atherosclerotic tissues, because of their non-homogeneity and irregularity. Regarding the material constants of the SEDF, using constraints on their values can make the SEDF convex to achieve material stability to a particular extent [277]. Although a wide search with multiple initial guesses might alleviate the

sensitivity of material constants to the initial guess, an exhausted try is not possible and moreover, different sets of material constants may all have a satisfactory regression. For example, the initial guess of (1, 1, 1) and (0, 1, 0) can both fit the experimental data points shown in Figure 4.3 well, but with very different material constants, in particular, C_1 and D_1 (Table 4.2). The employment of Bayesian inference-based approach can eliminate such dependency.

The material constants, C_1 , D_1 and D_2 contribute differently to the stress when the tissue strip is subject to stretching as shown in Equation 4.7. Taking the results in Figure 4.3 as an example, when λ=1.2, the term with C_1 contributes 21.2% to the total stress and the term with D_1 and D_2 contributes the rest; when λ=1.6, the proportion from the term with C_1 decreases to 6.3%, and that from D_1 and D_2 increases to 93.7%. The change of each constant also has a distinct effect on the calculated stress. Figure 4.9 shows the stress-stretch curves when C_1(=3.26 kPa), D_1(=3.67 kPa) and D_2(=2.17) decrease by 50% and increase by 50% in intervals of 10%.

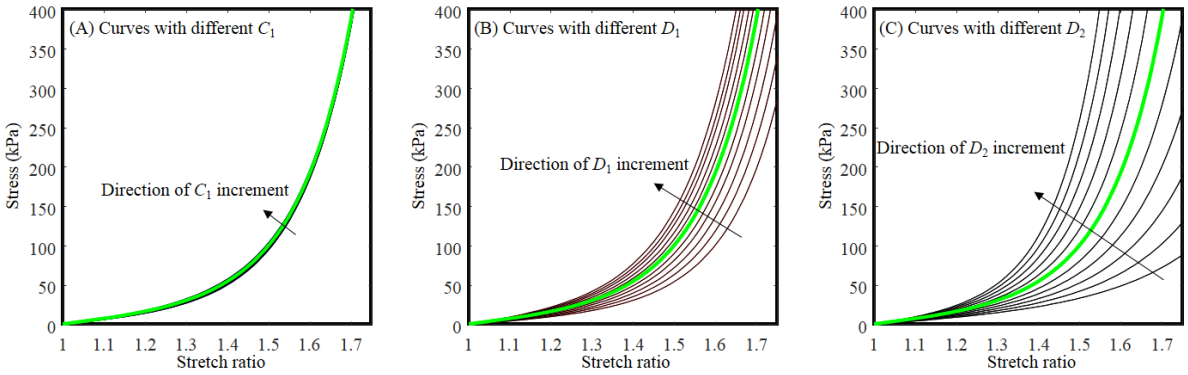

Figure 4.9 The change of stress-stretch curves with the change of C_1, D_1, and D_2 (all constants decrease and increase 50% from the baseline of (3.26, 3.67, 2.17) which are from the case shown in Figure 4.3).

It can be seen that the change in curve is insensitive to the change of C_1, more prominent with changes in D_1, and very profound with changes in D_2. The quantitative relationship between the stress change and the change of constants can be found through individual partial derivative,

$$\frac{\partial \sigma_{11}(\lambda)}{\partial C_1} = 2\left(\lambda^2 - \frac{1}{\lambda}\right)$$

$$\frac{\partial \sigma_{11}(\lambda)}{\partial D_1} = 2\left(\lambda^2 - \frac{1}{\lambda}\right) D_2 e^{D_2\left(\lambda^2 + \frac{2}{\lambda} - 3\right)} \tag{4.9}$$

$$\frac{\partial \sigma_{11}(\lambda)}{\partial D_2} = 2D_1\left(\lambda^2 - \frac{1}{\lambda}\right)\left[1 + D_2\left(\lambda^2 + \frac{2}{\lambda} - 3\right)\right] e^{D_2\left(\lambda^2 + \frac{2}{\lambda} - 3\right)}$$

The extracellular matrix components, specifically the mixture of elastin and collagen in the vessel wall, determine the passive mechanical properties of large arteries. C_1, D_1 and D_2 might be used to characterise their mechanical behaviour under physiological and pathological conditions. In an unloaded healthy artery, both elastin and collagen appear undulated and wavy, where they straighten as the artery begins to bear load [278]. Elastin is mostly straight at physiological pressures [278]. Upon involvement of C_1, the term in Equation (4.1) may reflect this procedure. In contrast to the elastin, less than 10% of the collagen fibres are straight and load-bearing at physiological pressures [13]. As the pressure increases, more collagen fibres become load-bearing and their stiffness limits arterial distension, providing the classical nonlinear behaviour observed in arterial mechanics [279]. This is characterised by the term in Equation (4.1) with D_1 and D_2 involvement, particularly, D_2 dominates the rate of increase in stress. Elastin and collagen fibres can be degraded by several members of the matrix MMP family. Increased expression of MMP-1 and MMP-9, for example, have been reported in aneurysms, which are characterised by fragmentation of both elastin and collagen fibres [280], where the increased expression of MMP-2 is localised to the sites of fragmentation in the elastic lamellae [281]. These pathological changes lead to a stiffer artery, that is, stress increases quicker during stretching. The bigger D_2 value of aneurysmal and atherosclerotic tissues can be the consequence of these pathological changes.

Of note, the modified Mooney-Rivlin SEDF is a phenomenological approximation of the material behaviour. Information from microstructure was not used, and therefore material parameters C_1 , D_1 and D_2 can only loosely link to the fibre architecture. Moreover, the exponential term describing the toe region in the stress-stretch curve is oversimplified and unbounded, allowing the tangential stiffness to rise infinitely with increasing stretch. Such limitations can be overcome by employing a more microstructurally informed model, which

takes gradual recruitment of collagen fibres into consideration [282–284]. In their stress-free state, the collagen fibres rest in a crimped configuration with waviness following a right-skewed distribution [285,286]. As a result, the likelihood of collagen fibres becoming newly recruited follows a Gamma distribution,

$$\Gamma(\bar{I}_1; \alpha, \beta) = \frac{\beta^{\alpha}(\bar{I}_1 - 3)^{\alpha-1} e^{-\beta(\bar{I}_1-3)}}{\Gamma(\alpha)} \tag{4.10}$$

where Γ_{α} is a complete Gamma function, and α and β are the shape and rate parameters. Both parameters relate to the microstructure of the tissue, with $\alpha\beta^{-1}$ and $\alpha\beta^{-2}$ being the expectation and variance of $\bar{I}_1 - 3$ at which the collagen fibres become recruited. Integrating this probability density function gives the cumulative likelihood of collagen fibres contributing to stiffness. Thus, SEDF at a given stretch level can be obtained as follows,

$$W = C_1(\bar{I}_1 - 3) + D_1 \int_0^{\bar{I}_1} \Gamma(x;\ \alpha, \beta) dx \tag{4.11}$$

where C_1 and D_1 reflect the contribution (incorporating fibre stiffness, alignment and relative volume fraction) of elastin and collagen fibres, respectively. Such a formulation offers more flexibility in fitting and better insights into the mechanical response [283,284], however the whole fitting procedure is much more complicated than either OLS or Bayesian inference-based estimations. Given that phenomenological models already lead to comparable goodness of fit [49], we conducted the present study using modified Mooney-Rivlin models for conciseness.

The obtained estimations listed in Table 4.3 can serve as *priors* for future studies to improve the accuracy of the estimation. Despite the interesting findings, limitations exist in this study: (1) the stress-stretch curve used in this study was from uniaxial tests and modified Mooney-Rivlin SEDF is an isotropic model, so that the anisotropy was not considered. The anisotropic SEDF considering microstructures can be found in studies by Holzapfel et al [9]; (2) the EVG and Sirius Red stains were used to visualise the gross elastin and collagen architectures and pathological features, e.g., inflammation, was not considered and might affect tissue mechanical properties and therefore the value of C_1, D_1 and D_2; and (3) the modified Mooney-Rivlin SEDF usually can fit the whole stress-stretch curve of the normal aorta well, but not for

all tissue strips of aneurysm and atherosclerotic plaque, in particular, in the region with a low stretch level.

4.5 Conclusion

Bayesian inference-based estimation robustly determines material constants in the modified Mooney-Rivlin SEDF and these constants can reflect the inherent physiological and pathological features of the tissue structure. The parameters from the experiments can be used for biomechanical simulation of arterial tissues.

Chapter 5 Image-based finite element analysis of multiple overlapping uncovered stents: a patient-specific study[†]

In this chapter, a patient-specific MOUS procedure is reproduced *in silico* through computational analysis based on pre-operative CTA images. The interaction between the stents and the aortic wall, as well as the flow-diverting effect, are investigated. The influence of multiple stents on the local mechanical environment is assessed.

5.1 Introduction

The flow diverter has been designed to induce thrombosis within intracranial aneurysm by altering blood flow [287–289]. The underlying mechanism is thought to be related to the formation of mural thrombus, increasing the effective wall thickness and decreasing the lumen radius. This reduces the aneurysm wall tension resulting in a lower risk of arterial rupture [290]. The primary aim of such a diverter is to treat intracranial lesions that are not effectively managed by traditional approaches, including coil embolization, conventional high porosity stents and coils, parent artery occlusion and neurosurgical procedures, e.g., aneurysm clipping, resection and bypass. Further technical developments have improved the cure rate with lower complication rates. This technique has transformed the management of intracranial aneurysms and has become the preferred treatment option for large or giant wide-necked lesions [291].

[†] Part of the content in this chapter has been published in

1. **Wang, S.**, Y. Zhang, J. Feng, Y. Huang, A. Tokgoz, U. Sadat, J. H. Gillard, Q. Lu, and Z. Teng. Influence of overlapping pattern of multiple overlapping uncovered stents on the local mechanical environment: A patient-specific parameter study. *J. Biomech.*, 2017.

The attractive advantages of this technology is its minimally invasive nature and the capacity to keep long-term patency of side branches [292]. Encouraged by the success of flow diverter in treating intracranial aneurysms, researchers have attempted to use a similar strategy to manage complex aortic aneurysms by using MOUS. However, controversial findings were reported due to the differences in the haemodynamic environment and lesion size between intracranial and aortic aneurysms. Aneurysm expansion and rupture after uncovered metal stent deployment [121,122,124] and longitudinal shortening of stents have been reported [293], while promising outcomes were also documented [294,295]. This implies that there is a need for refined patient selection and further comprehensive studies to identify the key factors affecting the outcome of MOUS.

This study is designed to quantify the MOUS deployment induced changes of local haemodynamic environment, including the flow velocity and rate in the sac and side branches, wall shear stress, oscillatory shear index, relative residence time and pressure in the sac and structural stress in the landing zone, by performing patient-specific FEA. The obtained results will help understand the mechanism of failure and success in different patient cohorts, and provide a framework to estimate the biomechanical environment for pre-surgical plan.

5.2 Materials and methods

5.2.1 The patient

The patient involved in the analysis is from the previously reported cohort [294,295]. This study was approved by the review board of Changhai Hospital, Shanghai, China. The patient was a 68-year old male with a complex thoracoabdominal aortic aneurysm (maximum diameter was 70.1 mm) (Figure 5.1). His medical history included pulmonary function impairment, grade II hypertension (146/92 mmHg) and coronary artery disease that had been previously treated by stenting. Given his multiple comorbid conditions and the risk of spinal cord ischaemia (at the level of T11-L1) and occlusion of coeliac arteries after stent-grafting, the patient was judged unfit for either open surgery or traditional endovascular aortic repair by the multidisciplinary surgical team consisting of vascular surgeons, cardio-thoracic surgeons, and anaesthetists. The

MOUS strategy was therefore explained to the patient, who gave written informed consent for the procedure. Closed-cell, self-expandable and uncovered sinus-XL stents from OptiMed (Ettlingen, Germany) were used.

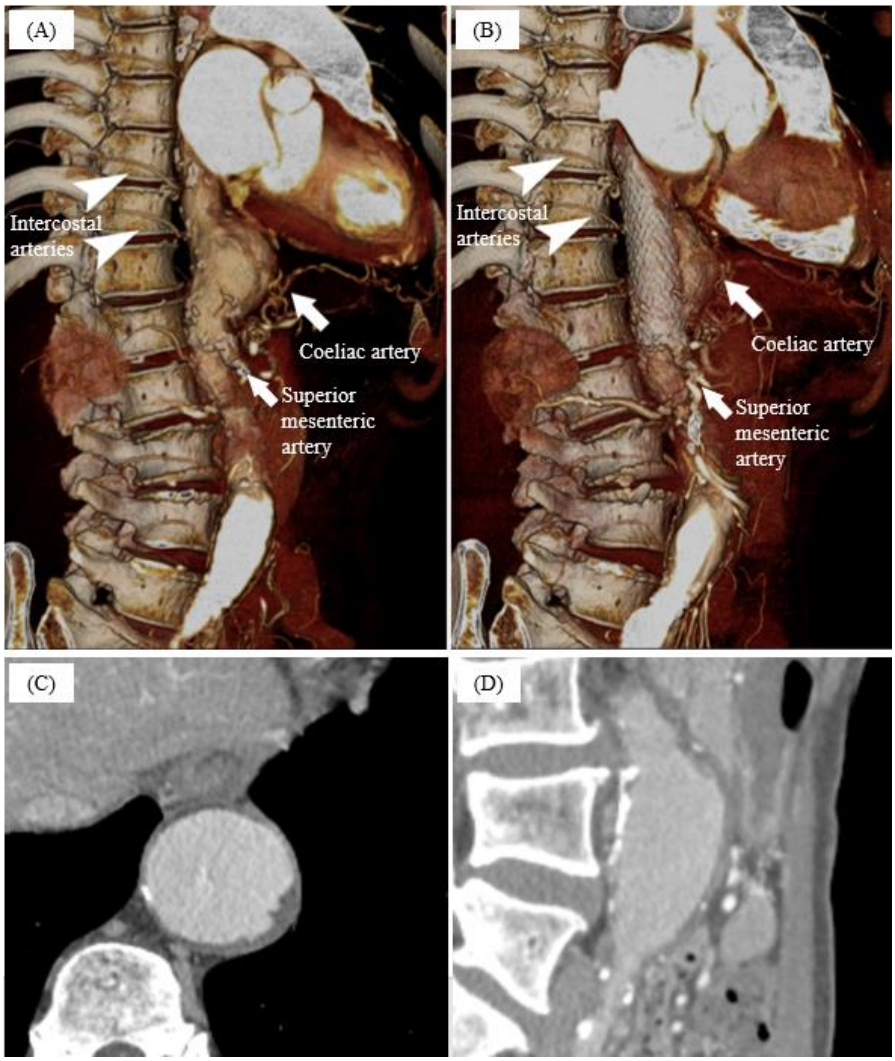

Figure 5.1 The configuration of a complex aortic aneurysm with vital branches involvement. **(A)** 3D rendering of the lesion configuration before stent deployment; **(B)** 3D rendering of the configuration after 4-layer stents deployment; **(C)** A 2D axial slice; **(D)** A 2D sagittal slice.

5.2.2 Stent reconstruction

The diameter and length of the uncovered stents deployed in this patient were 28 mm and 100 mm, respectively (Figure 5.2A). The geometry of the bare metal stent was reconstructed

according to the parameters provided by the supplier in Creo2.0 (PTC, Needham, USA) (Figure 5.2B) and exported to ICEM for meshing (Figure 5.2C). A single stent was meshed with 119,592 hexahedron elements. The typical length of each element was approximately 0.15 mm. The same stent mesh was duplicated four times, generating the overall mesh of 4-stent MOUS.

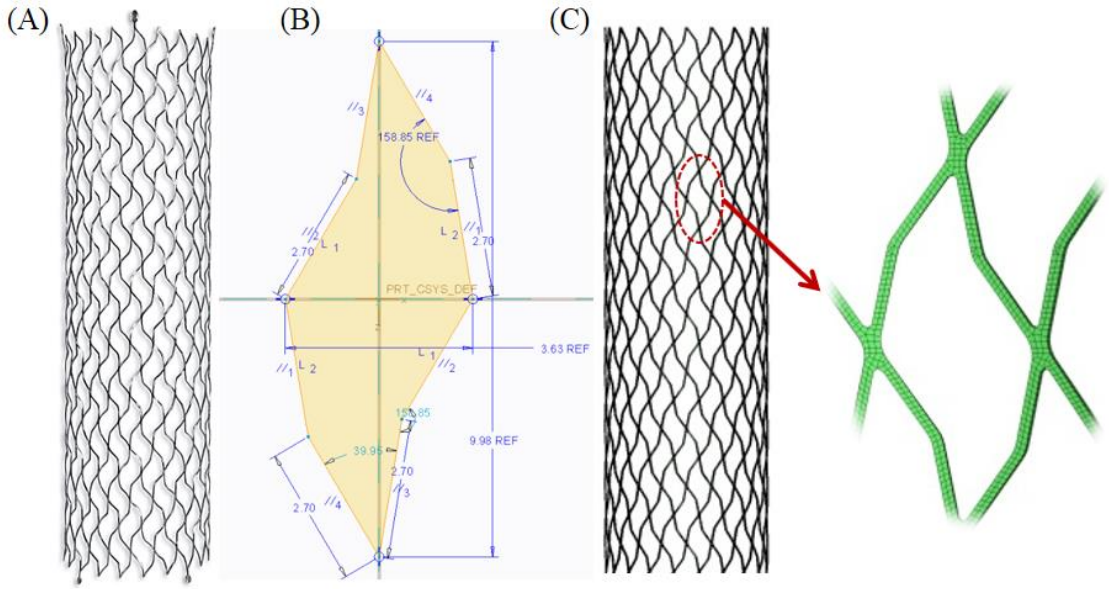

Figure 5.2 Reconstruction of the uncovered stents. **(A)** A photo of the stent product; **(B)** The geometry of the stent cell annotated with the measurements in CAD software; **(C)** Reconstructed stent model meshed with 3D hexahedral elements.

5.2.3 Patient-specific aneurysm reconstruction

Image Segmentation

Segmentation was performed based on the pre-operative contrast-enhanced CTA images to identify aortic wall, calcium and thrombus using an in-house program developed in MATLAB R2016a (The MathWorks, Inc., USA). The surrounding tissues and organs, e.g., spine and liver, were not considered. In this study, the CTA resolution was 0.683×0.683×0.8 mm^3, the aortic wall thickness was about 2.5 mm and the diameters of visible sub-branches ranged from 2.9 mm to 6.0 mm, and the wall thickness of sub-branches was about 1.0 mm. To reduce the effect of smoothing operation during the 3D geometry reconstruction, CTA images were resampled with a voxel size of 0.1×0.1×0.1 mm^3. The model reconstruction included the aorta

reconstruction and sub-branches reconstruction. Firstly, the resampled CTA images were imported into an in-house MATLAB platform (Figure 5.3) to semi-automatically segment aortic lumen, calcium and aortic wall by trained operators [205].

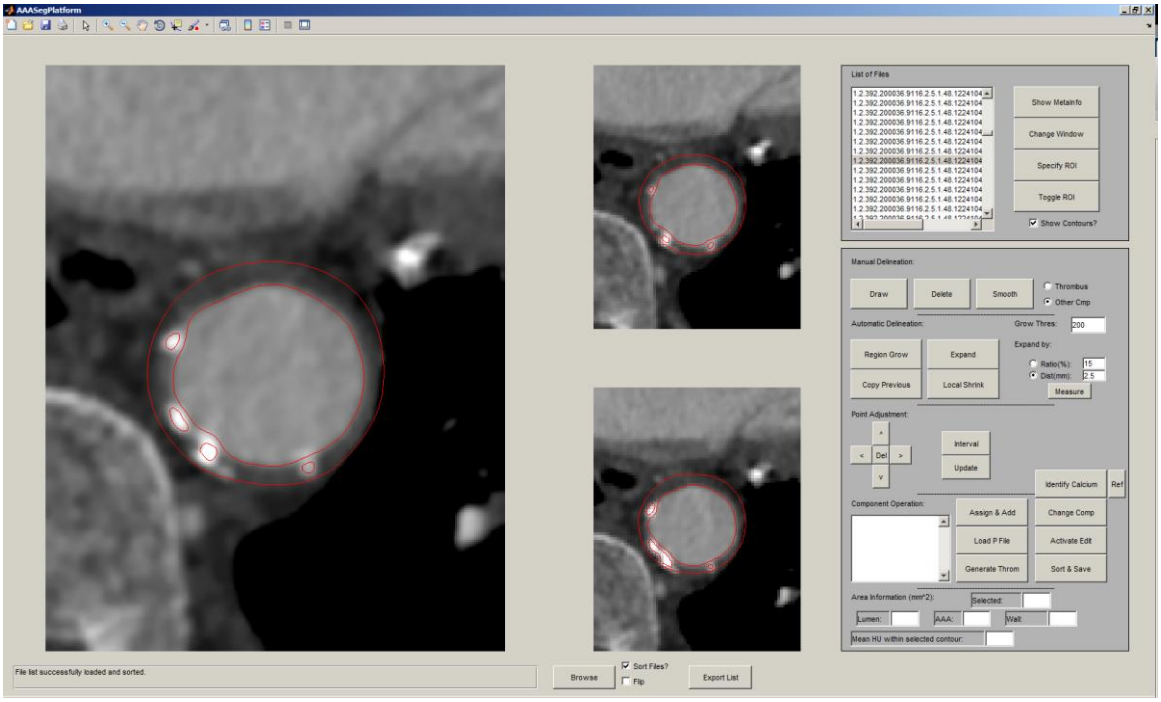

Figure 5.3 Graphical User Interface of the AAA segmentation platform. The contours of the lumen, calcium and aortic wall are annotated in red on axial slices. Adjacent slices are displayed on the middle panel for context reference. Segmentation tools are displayed on the right panel, including the options of region grow, threshold and contour smoothing.

The segmented contour information was translated into a voxel-based label map then output to 3D Slicer (http://www.slicer.org). The lumens of sub-branches were segmented using threshold algorithm and a uniform wall thickness of 1 mm for all sub-branches was applied by dilating the lumen label map. The voxel-based label maps of aortic components and sub-branches were then merged by Boolean operation and smoothed using the Gaussian Filter (Figure 5.4A).

Surface Processing and 3D Meshing

After completion of the final voxel-based label maps, the surfaces of each object were generated using fast marching method in 3D Slicer and imported to VMTK (http://www.vmtk.org/), followed by smoothing with Taubin's algorithm [296]. Finally, surfaces

of inlet and outlet of AAA and the outlet of each sub-branch were clipped (Figure 5.4B) and extended 15 times of the local diameter to eliminate the inlet and outlet effect.

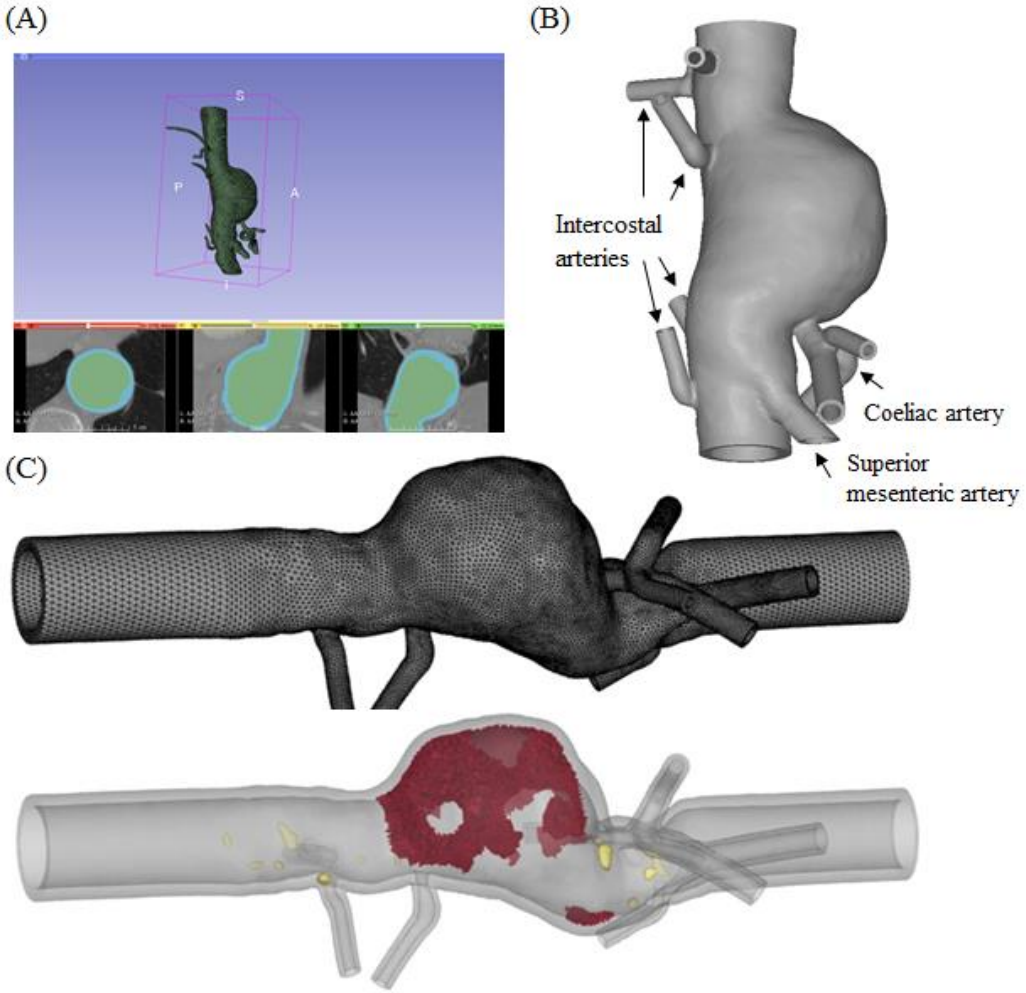

Figure 5.4 Surface processing and meshing of the aneruysm. **(A)** The 3D rendering (top panel) and cross-sectional views (bottom panel) of the lumen with side branches, where lumen is green and the aortic wall is blue. **(B)** Clipped and smoothed surfaces generated from voxel label map. **(C)** 3D meshing of the aortic wall and components after adding straight extension, where aortic wall is coloured in grey, thrombus in red and calcium in yellow.

3D volumes enclosed by these surfaces were generated, and tetrahedron meshing was made based on local geometry curvature in ICEM (ANSYS Inc., USA) (Figure 5.4C). The ILT was first considered as part of aortic wall in the meshing procedure and further assigned to a separate element group. The distance to the outer wall surface was calculated for each element within the aortic wall. The average thickness of the aorta was assumed as 2.5 mm, and any

element with a distance above 2.5 mm was assigned to the ILT group. For the baseline model (without any stent), 409,357 tetrahedron elements were generated for the solid part of the aneurysm model.

5.2.4 Finite element analysis

In this study, a one-way fluid-structure interaction (FSI) analysis was performed to re-predict the mechanical conditions before and after the deployment of the stents, to investigate the influence of stent deployment on critical mechanical conditions within the aneurysmal structure and blood flow in the sac and side branches. Detailed processes for the cases with stents deployment can be found in the flowchart shown in Figure 5.5.

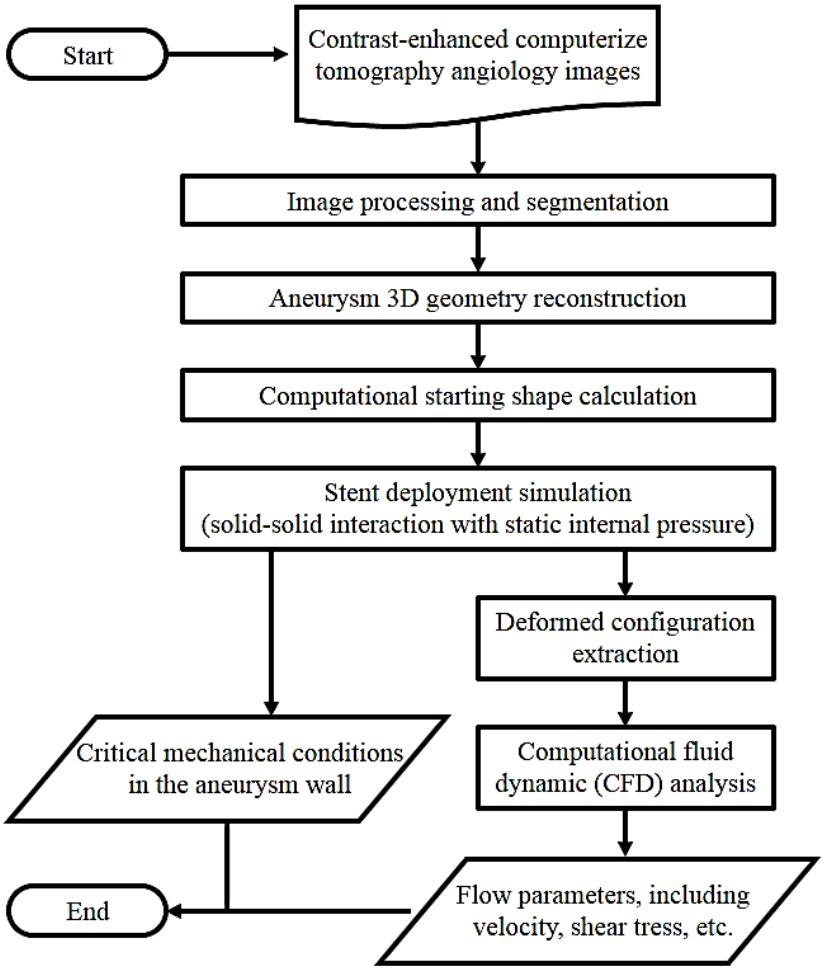

Figure 5.5 The workflow chart of the one-way fluid-structure interaction analysis.

Virtual stent deployment

Since the CTA images were acquired under pressurised condition, an inverse procedure with a pressure level of 110 mmHg (patient's mean blood pressure) and axial stretch 2.5% at both ends was followed to obtain the computational starting shape [237]. Each stent was assumed to be a linear material with Young's modulus and Poison's ratio of 75 GPa and 0.333, respectively. As discussed in Chapter 4, the modified Mooney-Rivlin model was used to describe the material properties of the aortic wall, thrombus and calcium. The material constants are adopted from the previous experimental results of AAA [272,297]: aortic wall, C_1=0.07 kPa, D_1=6.54 kPa and D_2=5.88; thrombus, C_1=0.24 kPa, D_1=8.69 kPa and D_2=0.61; and calcium, C_1=1.147×10^5 kPa, D_1= 7.673×10^4 kPa, and D_2=2.838×10^{-8}.

A static blood pressure of 110 mmHg was applied on the luminal surface and an axial stretch of 2.5% was prescribed at both aortic ends to restore the in-vivo configuration. The stents' surface and lumen surface were defined as contact surfaces. Steps mimicking the deployment were as follows: (1) a gradually increased concentrated force from 0 to 350 N was applied at both ends of the stent along its axial direction to shrink the stent; (2) a rigid body displacement was prescribed to deliver the stents into the lumen to the target location, which were identified by the locations of radio-opaque markers on the post-operative CTA imaging; (3) the stent was released by gradually decreasing the concentrated force to 0. Multiple stents were deployed sequentially controlled by the phase-shifted time functions.

Different degree of freedom (DOF) fixity policies were adopted to eliminate rigid displacements where appropriate for different parts. The displacement of both ends of the extended aorta was specified to maintain the axial stretch ratio, and the circumferential rotation of nodes on these two ends was not allowed. For each side branch, all DOFs at the end were fixed except for the local radial displacement. For stents, circumferential rotation and axial displacement at the proximal (close to the heart) were not allowed, while there was no constriction for the other end. The virtual deployment simulation was performed using ADINA 9.0 in the implicit statics mode with the consideration of large strain and large displacement. An auto time step technique was used for the consideration of convergence. Finally, averaged and peak von Mises stress was extracted under the 99.5% criterion as the indicator of structural stress in the wall.

Computational fluid dynamic simulation of blood flow before and after stent deployment

The deformed lumen and struts surface after deployment were extracted to form the fluid domain (there was no struts surface before deployment). The stent struts in direct contact with the aortic wall were masked out to reduce computational costs. Then the fluid domain was imported into ICEM CFD (ANSYS Inc., USA) and meshed using the Octree method with tetrahedral elements. The thickness of the boundary layer was estimated to be 1.4 mm considering the Womersley number of about 18.2 in this study. Three prism thin boundary layers were therefore generated for a fine calculation in the region near the lumen surface with the first layer thickness being 0.4 mm and the third layer 0.8 mm [298,299]. In total, the fluid domain without stents was meshed with 80,562 tetrahedral and 175,691 prism elements; a single stent with 518,988 tetrahedral and 99,037 prism elements; two stents with 832,072 tetrahedral and 105,722 prism elements; three stents with 943,176 tetrahedral elements and 114,642 prism elements; and four stents with 1,004,782 tetrahedral elements and 126,128 prism elements.

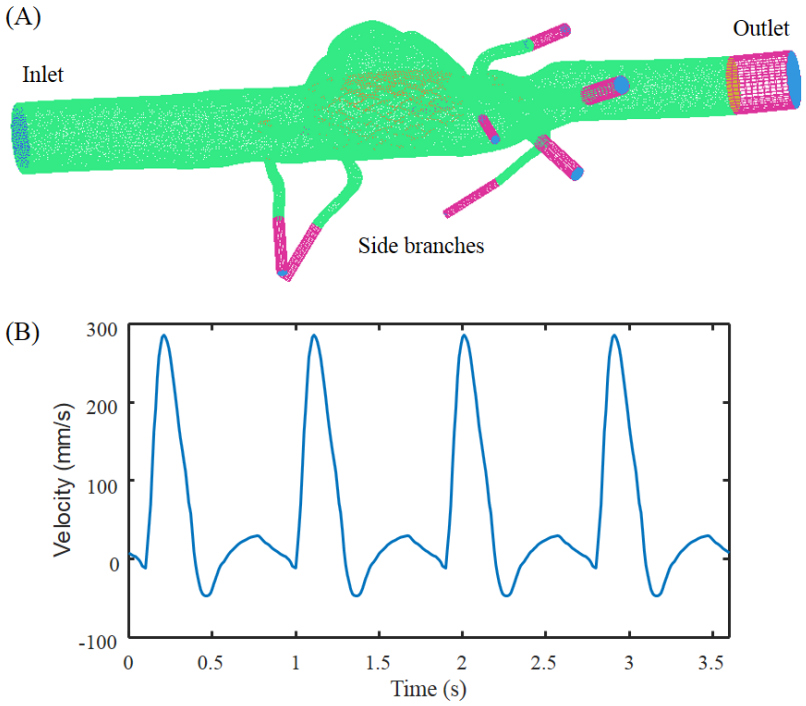

Figure 5.6 The computational model for haemodynamic simulation. **(A)** The fluid domain was meshed with tetrahedron and prism elements after 4-stent MOUS deployment. Impendence units were added at the aortic outlet and ends of the side branches (pink). **(B)** The 'plug' velocity waveform was applied at the inlet over 4 cardiac cycles.

A ‘plug’ velocity profile with a mean velocity of 66.7 mm/s, peak velocity 284 mm/s and period of 0.9 s was adopted from measurements by Olufsen et al. [300] as the loading condition at the aortic inlet (Figure 5.6B). At the outlets, a resistant unit was added at each outlet to mimic the afterload of the downstream circulation bed [301]. The resistance of each unit was determined by the following steps: (1) a CFD simulation without resistance units was performed by assigning discharge ratio of each outlet according to Murray’s Law [302] and a pressure profile was applied at the outlet of the aorta; and (2) extract computed pressure at the outlet of each side branch and calculate the resistance by, *resistance = (mean pressure)/(mean flow rate)*.

The blood was assumed to be incompressible and Newtonian with a density of 1.06 g/cm^3 and a constant viscosity of 0.035 poise, and the flow to be transient laminar. The Newton-Raphson iteration method was used for each time step with a convergence criterion for the relative residual of 0.001. Simulation was performed over 4 cardiac cycles. Results of the last cycle were extracted for analysis where the flow was fully developed.

WSS [303,304], OSI [304] and RRT [305,306] have been widely suggested to be associated with atherosclerosis and aneurysm development and their clinical presentations. With this consideration, apart from flow velocity and rate, these parameters were also used to quantify the flow pattern modulated by the stent deployment. The calculation of these variables on the vessel wall were implemented using Equation (3.33-35), as discussed in Section 3.5. RRT was normalised ($\overline{\mathrm{RRT}}$) by the average value in the case before deployment at the proximal disease-free region where the flow was fully developed.

5.3 Results

Nine side branches were located around the diseased region, including 7 intercostal arteries, superior mesenteric artery and the coeliac artery (Figure 5.4 B). Two intercostal arteries were ignored in this study due to their small size. The diameter at the proximal and distal were 25 mm and 20 mm, respectively. In total, 4 uncovered stents were deployed in clinical treatment for this patient. After 12-month follow-up, one of the intercostal arteries was occluded and all others remained patency. The thrombus rate increased from 30% at the baseline to 97%, while the maximum aneurysm diameter decreased from 70.1 mm to 62.5 mm.

5.3.1 Overall porosity of MOUS

The deployment of multiple stents resulted in a periodic overlapping pattern. The 3D geometry of MOUS was projected to the outer cylinder surface, to quantify the porosity. A unit cell of the projection result was extracted (Figure 5.7A), and the overall porosity of MOUS was calculated as the relative area ratio of stent struts to the unit cell.

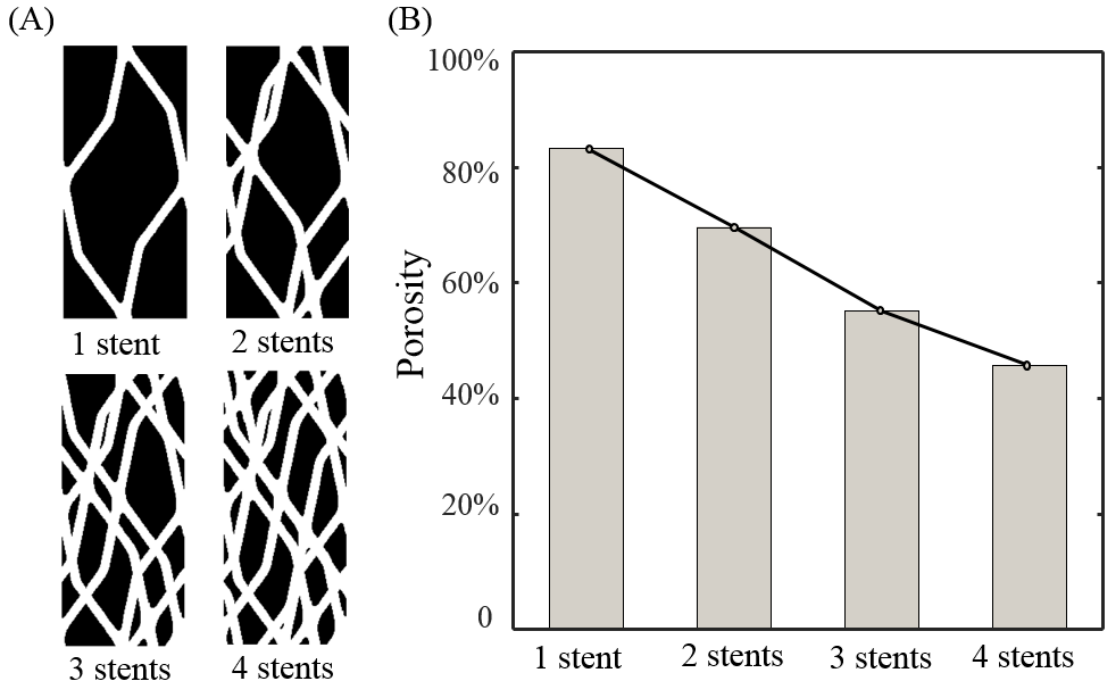

Figure 5.7 Overall porosity of MOUS after stents deployment. **(A)** Unit cell representation of the projection of one stent, two stents, three stents and four stents; **(B)** The corresponding porosity calculated from the relative area ratio of the stent struts.

The porosity of one single stent is 83%, which means a single stent covered 17% area of the corresponding cylinder surface. The subsequently deployed stents overlapped with previously deployed stents and decreased the overall porosity (Figure 5.7B). Under the overlapping pattern reconstructed from the post-operative CTA imaging, the 2nd, 3rd and 4th stents reduced the porosity to 69%, 56% and 46%, respectively. As more stents were deployed, the subsequent stent induced less reduction of the MOUS porosity, which was expected due to more overlapping coverage with previously deployed stents.

5.3.2 Structural stress concentration induced by multiple stents

Right after the first stent was deployed, the aneurysm configuration changed immediately due to the solid-solid interaction (Figure 5.9 A&B), and the structural stress increased accordingly depending on the location. The change of stress of the representative node at different regions was shown in Figure 5.8. At points in direct contact with the stent struts, particularly in the landing zone, the stress level could increase over 5 times (Node B&D, Figure 5.8). The stress increased more gently in the non-contact points, e.g., the stress could be doubled in the non-contact landing zone (Node A, Figure 5.8); however, stress in the sac remained nearly unchanged (Node C, Figure 5.8).

When subsequent stents were deployed, the configuration remained nearly unchanged (Figure 5.9). The stress level in different regions however changed differently; regions in contact with stent struts experienced a much higher stress increase than the non-contact regions. In summary, the peak stress around the diseased region could increase 12 times from 143 kPa to 1718 kPa after 4 stents were deployed and such stress elevation was only observed in the landing zone, not in the aneurysm sac.

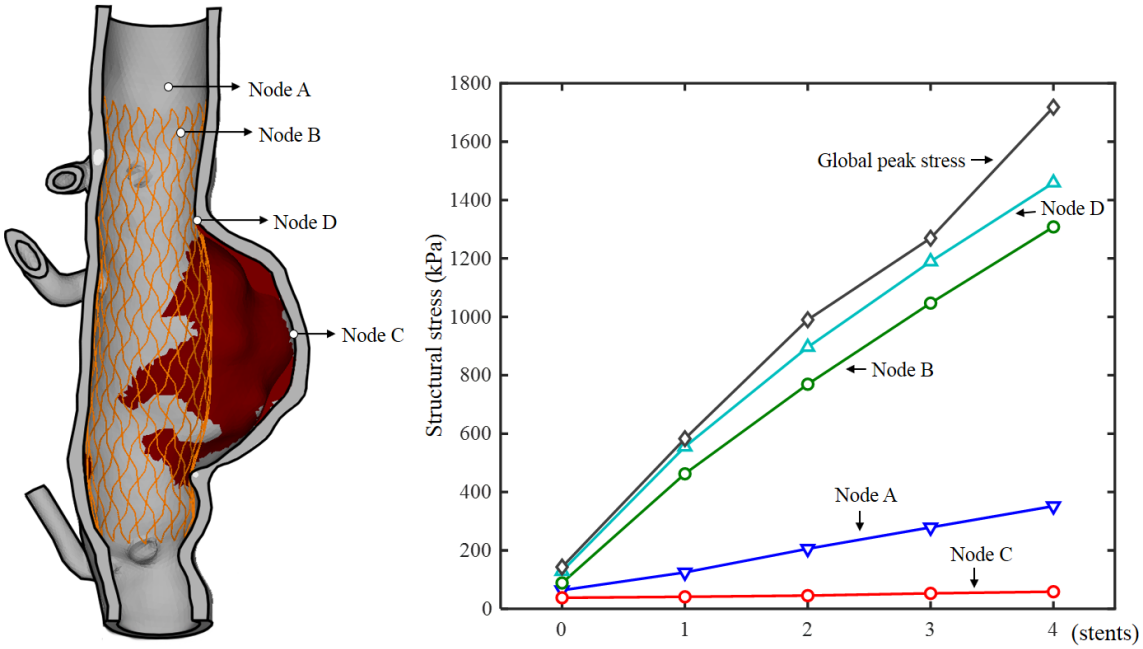

Figure 5.8 Structural stress level at different location changed after MOUS deployment.

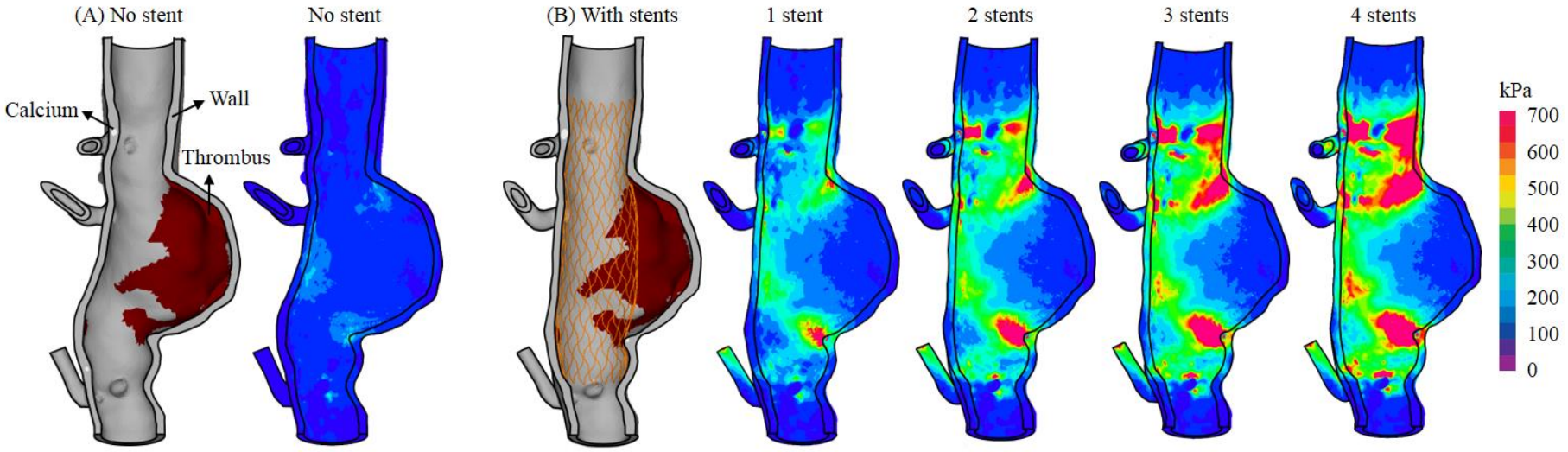

Figure 5.9 Band plots of effective stress within the wall before and after stents deployment. **(A)** The configuration and effective stress under static mean blood pressure before stent deployment; **(B)** The aneurysm configuration after one stent deployment, followed by effective stress after the deployment of the 2nd, 3rd and 4th stent).

5.3.3 Flow velocity, WSS, OSI, RRT and pressure modulation by MOUS

In general, the flow velocity inside the aneurysm sac was much slower than that in the main arterial lumen (Figure 5.11). After the deployment of the MOUS, the flow pattern in the sac was modulated significantly, resulting in the reduction of flow velocity (Figure 5.10).

After the 1st stent was deployed, the mean sac time-averaged velocity decreased from 39.8 mm/s to 25.3 mm/s (36.4% reduction). The deployment of 2nd, 3rd and 4th stents further reduced the velocity to 20.2 mm/s (49.3% reduction), 16.0 mm/s (59.8% reduction) and 14.8 mm/s (62.8% reduction), respectively. Similar to the change of overall porosity (Figure 5.7B), additional velocity reduction induced by the subsequent stent decreased after more stents deployed. In this patient-specific simulation, the 4-stent MOUS only induced about 3% further reduction of the original sac-averaged velocity, compared to the 3-stent MOUS.

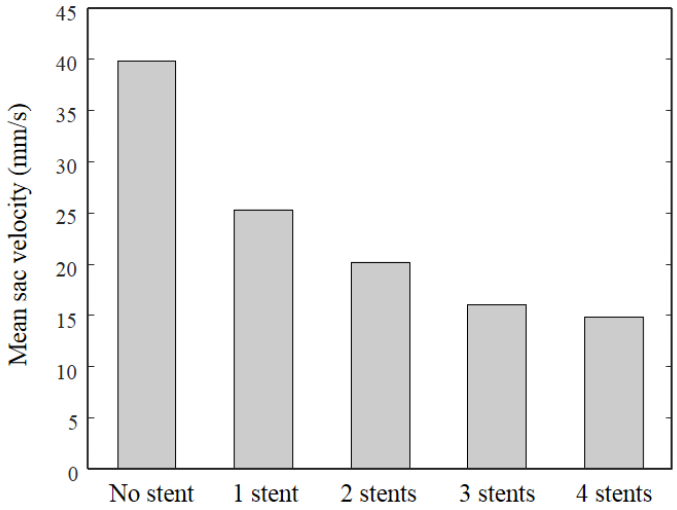

Figure 5.10 The change of mean sac time-averaged velocity before and after multiple stents deployment.

Associated with changes of flow velocity, other haemodyamic parameters, including TAWSS, OSI and RRT, changed accordingly (Figure 5.12). The mean TAWSS on the sac wall decreased from 0.19 Pa to 0.15 Pa when the 1st stent was deployed, and further decreased to 0.13 Pa after subsequent stents were deployed. The flow became more disturbed after the 1st stent was deployed as OSI increased from 0.18 to 0.30, and the deployment of the subsequent stents further increased OSI to 0.40 (2nd stent), 0.44 (3rd stent) and 0.44 (4th stent).

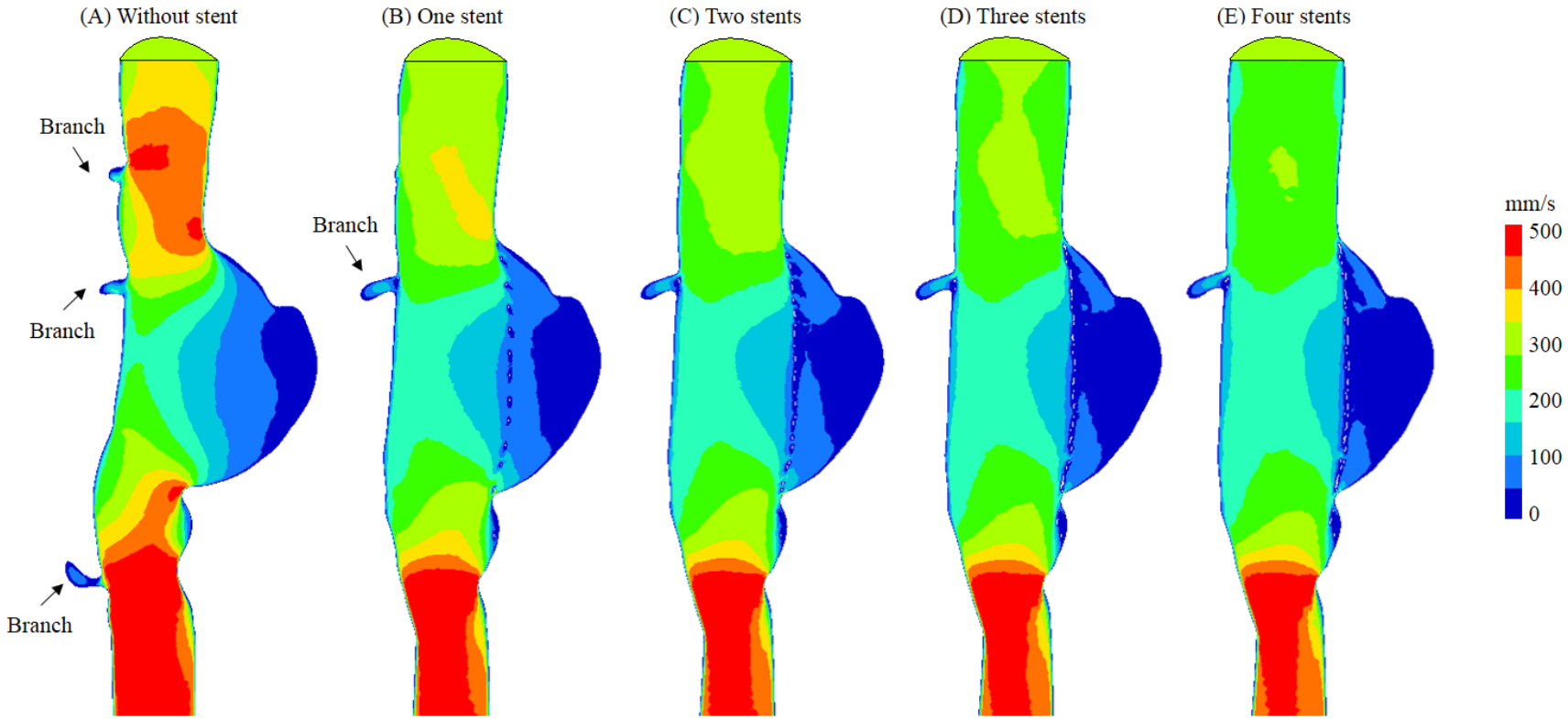

Figure 5.11 Cross-sectional band plot of blood velocity at systole **(A)** Band plot of velocity without stent deployment; **(B)** One stent deployment; **(C)** two stents deployment; **(D)** three stents deployment; **(E)** four stents deployment.

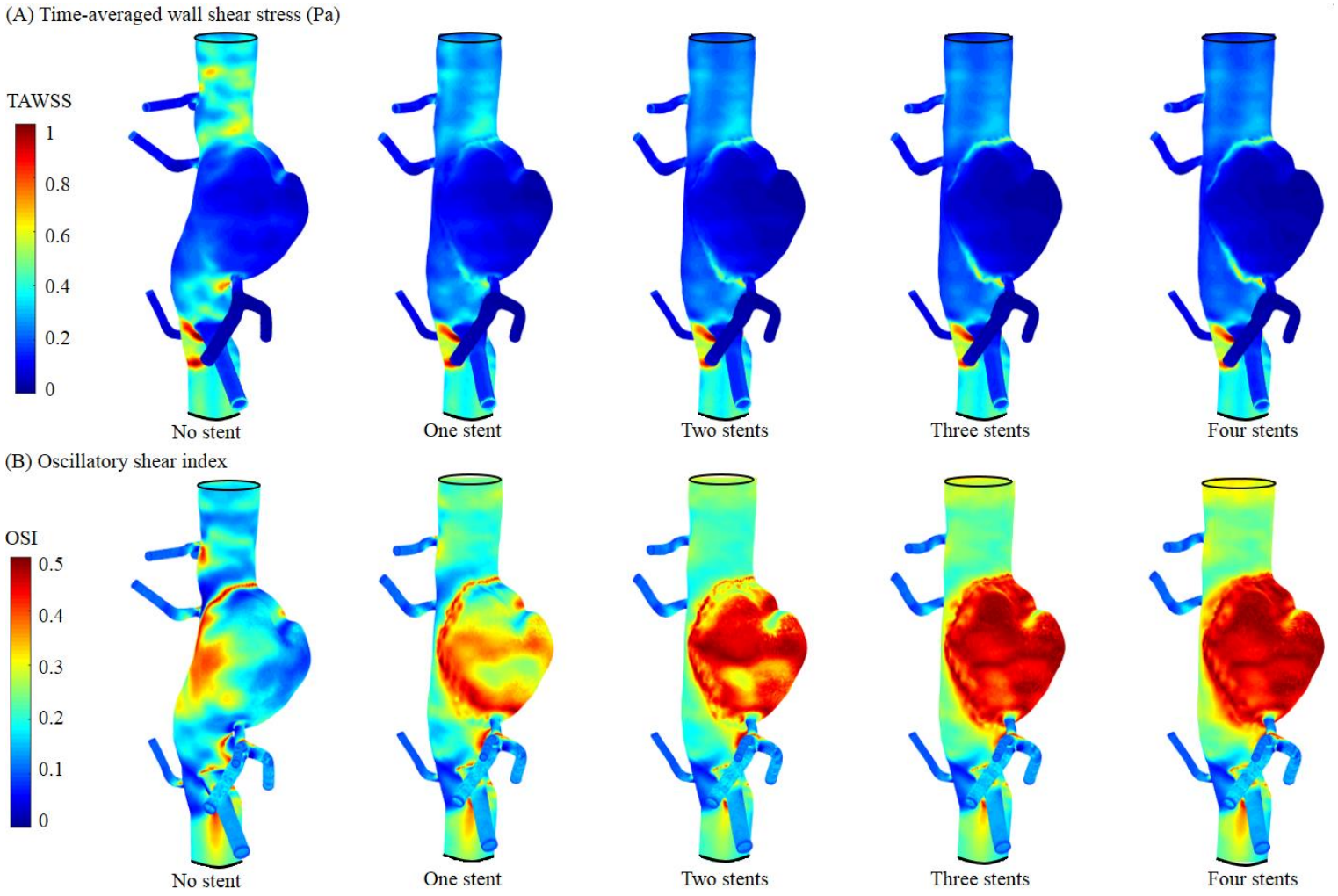
(A) Time-averaged wall shear stress (Pa)
TAWSS
1
0.8
0.6
0.4
0.2
0
No stent
One stent
Two stents
Three stents
Four stents
(B) Oscillatory shear index
OSI
0.5
0.4
0.3
0.2
0.1
0
No stent
One stent
Two stents
Three stents
Four stents

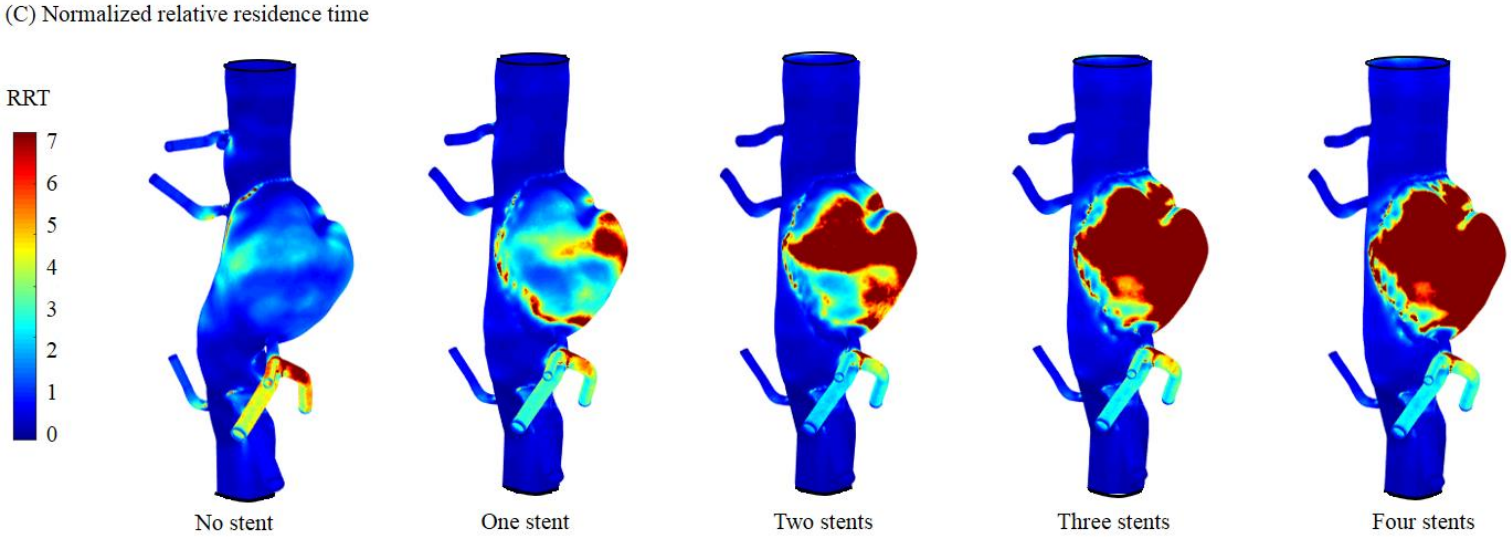

Figure 5.12 Band plots of haemodynamic variables on the lumen wall before and after multiple stents deployment: **(A)** Time-averaged wall shear stress; **(B)** Oscillatory shear index; and **(C)** Normalised relative residence time.

RRT at the proximal disease-free region where the flow fully developed was 8.5 Pa^{-1}, and changed to be 8.4 Pa^{-1} after the first stent was deployed, while remained the same after subsequent stents deployment. When the first stent was deployed, the mean $\overline{RRT}$ on the sac wall increased from 1.29 to 3.13; it further increased to 4.90 (2^{nd} stent), 17.78 (3^{rd} stent) and 18.80 (4^{th} stent). The mean time-averaged pressure in the sac decreased by 2.4% after the first stent was deployed, and decreased further by 4.2% (2^{nd} stent), 5.4% (3^{rd} stent) and 5.6% (4^{th} stent) when the subsequent stents were deployed.

5.3.4 Flow rate in side branches

Keeping the side branch patency is one of the advantages of MOUS system. For this patient, only 1 of the intercostal arteries was lost after 1 year. Total flow rate of side branches was 6.0% of the whole flow rate. After stent deployment, the flow rate in each side branch changed differently depending on many factors, e.g., the location and relative position to the struts (Table 5.1).

Table 5.1 Comparison of time-averaged flow rate in each side branch before and after MOUS deployment. (Unit: ×10-3ml/s; CA: coeliac artery; SMA: superior mesenteric artery; other side branches were intercostal arteries)

Side branch	No stent	1-stent	2-stent	3-stent	4-stent
1†	111	119	120	119	118
2†	119	117	113	110	109
3†	116	122	117	115	115
4	60	54	52	50	51
5†	79	74	76	75	73
CA	172	161	156	150	151
SMA	574	578	572	570	569

† The orifice of these side branches was partially covered by the stent strut.

For this patient, CA originated from the sac and SMA originated right below the sac (Figure 5.1). After the first stent was deployed, the flow rate decreased 6.4% in CA and increased slightly in SMA. Further decrease in both CA and SMA was observed after subsequent stents were deployed. In general, the flow rate change after the 4-stent MOUS deployment was less than 20% compared with the case before stent deployment.

5.4 Discussion

To the authors' best knowledge, this is the first comprehensive study assessing the mechanical environments in both wall structure and fluid domains modulated by the MOUS system.

The results obtained from this study indicate that MOUS introduce high structural stress concentrations around the diseased region. For a clear understanding of the change of stress with the number of stents deployed, the change of stress of a representative node was shown in Figure 5.8. In the landing zone, the stress increased with the number of stents deployed, while the stress level in the sac remained nearly constant. Further analysis indicated that either averaged stress or peak stress in different regions with stent contact increased similarly with the number of stents deployed (Figure 5.13). These two parameters remained nearly unchanged in regions away from stent struts, e.g., zone I (above or below the landing zone) and V (sac) in Figure 5.13. Elevated stress concentrations in the landing zone might have undesirable effects such as continued aneurysmal degeneration of the aortic wall. Long-term follow-up data is therefore required to assess this.

The MOUS system decreased the flow velocity (Figure 5.11) and WSS (Figure 5.12A) in the sac, while increased OSI and RRT (Figure 5.12B&C). These results were in agreement with previous findings using CFD analysis with idealised geometry [290,307]. Due to the rheological nature of blood, slow flow velocity increases its viscosity which is the primary driving force of thrombus formation and growth [308]. In addition, low WSS promotes the adherence of discoid platelets contributing to the formation of thrombus [308]. The developed thrombus appears to protect against aneurysm rupture through a 'cushioning' effect that reduces wall stress [120,309]. However, such thrombus development may take time. In addition, MOUS system does not significantly reduce the blood pressure in the sac and thus structural stress in the sac wall

(Figures 5.8 and 5.9). This technique therefore might not be suitable for lesions judged in a high risk of near-future rupture. On the other hand, the formation of thrombus might not be always protective in the long term. Inflammatory content might infiltrate the aneurysm wall beneath thrombus [310] and thick thrombus might lead to local hypoxia and neovascularization [311]. Such pathological effects might weaken the vessel wall leading to aneurysm expansion [312].

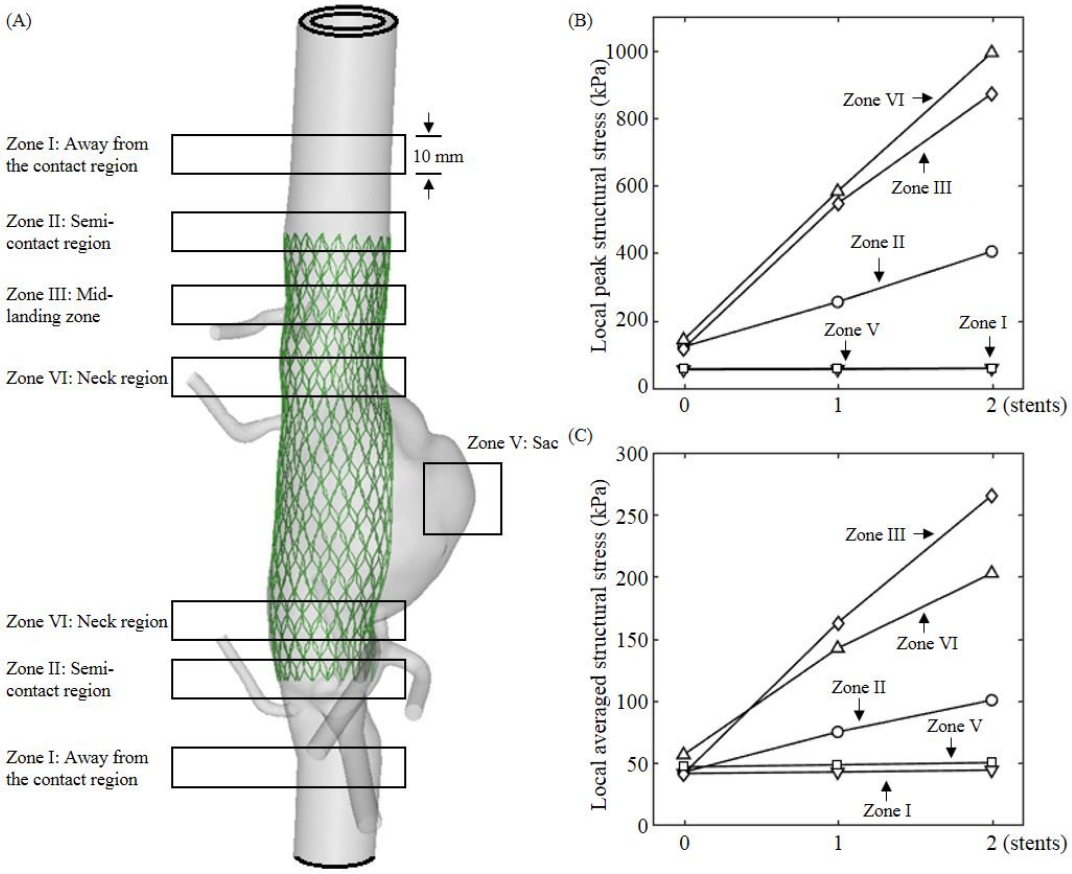

Figure 5.13 The change of peak stress and averaged stress in different regions with the number of stents deployed. **(A)** The definition of different zones; **(B)** The change of peak stress in different zones with the number of stents deployed; **(C)** The change of averaged stress in different zone with the number of stents deployed.

It is clear that one of the key functions of MOUS is to reduce the blood velocity and to increase RRT in the sac, promoting the formation and development of thrombus. The MOUS porosity has been identified as the main factor determining the velocity reduction associated with subsequent thrombosis, and literature suggested that optimal effect might be achieved with a

porosity of 50-70% [313–316]. The mesh porosity is 83% for a single stent used in this study, and MOUS resulted in a lower overall porosity. It is obvious that the velocity further reduces with the number of stents deployed, while the marginal velocity reduction is decreasing. Furthermore, more stents introduce higher structural stress concentrations in the landing zone (Figure 5.8). Two or three stents should be an optimal option considering the trade-off between velocity reduction and stress concentration. As demonstrated in this study, after two stents were deployed, the mean sac velocity reduced by nearly 50% and the peak structural stress was about 1000kPa. If a third stent was added, the porosity might reduce to 56%, and the peak structural stress increased to about 1300kPa. According to direct material tests, the ultimate material strength of aneurysmal tissues was in a range of 500-2000kPa [245,272,317–321].

Another key function of MOUS is to maintain the blood flow into side branches. The flow velocity in the side branch is determined by branch diameter, location, local configuration and the relative position with stent struts; predicting the flow rate in each side branch is difficult. However, according to the results obtained from the FEA (Table 5.1), there was subtle flow reduction for most of side branches, despite some side branches were partially covered by the stent strut. This finding explained the clinical observation that 311/320 side branches remained patency in 40 patients in a mean follow-up period of 21 months [295].

In order to capture the temporal change of blood flow and obtain a stable result for an accurate calculation of flow parameters, e.g., OSI and $\overline{\mathrm{RRT}}$, the time step has to be sufficiently small and simulation cycles should be enough. However, the finer time step or the more simulation cycles, the higher computational cost. In this study, the time step was set to be 9 milliseconds (ms). When the time step increased to be 18 ms or decreased to be 4.5 ms, the difference in flow parameter calculation was negligible, e.g., for the case with 1-stent, the OSI difference was less than 2% and the peak velocity different was less than 2.5%. Moreover, the result at the 4th cycle was extracted for analysis as the difference between the 3rd and 4th cycles was very small, e.g., the difference in peak velocity was less than 0.5%. Furthermore, in this study, blood was assumed to be Newtonian. This may introduce over-/under-estimation for flow parameters, e.g., WSS. An increase in mean WSS was observed in non-Newtonian fluid model compared to Newtonian model for a matched flow waveform [322]. Perktold et al. reported WSS magnitude

difference only on the order of 10% between two models in carotid artery [323], but the difference in WSS could be up to 26.7% in AAAs [324].

Despite the interesting findings, several limitations exist in the present study: (1) a one-way rather than fully coupled FSI analysis was performed (Figure 5.5) to re-predict the mechanical environment in this study. Due to the complexity in the geometry, interactions among aneurysmal wall, stents and blood flow, the non-linearity in material properties and governing equations, as well as big deformations, it is nearly impossible to perform a fully coupled FSI analysis using current numerical methodologies. However, it has been demonstrated that a one-way FSI yielded a small deviation in predicting structural stress and flow parameters compared with those obtained from a fully coupled FSI in the carotid artery with atherosclerotic disease [325]; (2) tissue components, including wall, calcium and thrombus, were assumed to be piece-wise homogenous and the inhomogeneity in each component was not considered; (3) The empirical Reynolds number for the transition to turbulence in pipe flow is 2000-2300. In this study, the Reynolds number was estimated to range from 532 to 2,256 when the mean and the peak velocity of 66.67 mm/s and 284 mm/s were considered. The ignorance of turbulence in this study should be reasonable. However turbulent flow might exist locally in the fluid domain [298]; (4) The flow discharged ratio into different side branches estimated from Murray's Law might not reflect the real situation in diseased vasculature (5) residual stress that might exist in the aneurysmal wall was not considered.

5.5 Conclusion

In conclusion, the MOUS system may induce high structural stress concentrations in the landing zone, which increased linearly with the number of stents; MOUS system decreased the mean flow velocity and WSS, increased OSI and RRT in the sac, while maintained the blood supply to side branches; it had very little effect in pressure reduction in the sac. FEA based on pre-operative images could be used to predict the biomechanical environment and flow-diverting outcome, which could aid surgeons in the decision of the optimal number of stents for personalised MOUS configuration.

Chapter 6 Influence of cross-stent structures: parameter studies of multiple overlapping uncovered stents[†]

The uncertainty during the deployment of multiple stents may lead to different configurations of MOUS, while their influence on the treatment outcome remains unclear. This chapter conducts a series of parameter studies on the influence of cross-stent structures, including 2D overlapping patterns and 3D multi-layer structures.

6.1 Introduction

The principle of treating aneurysms with a flow-diverting strategy is to modulate the blood flow, which promotes the thrombosis and shrinkage of the aneurysm sac [85,105,326]. Porosity has been identified as a key factor for the intracranial flow-diverters in previous experimental and computational studies [313–316]. As an off-shelf implementation, MOUS are based on the sequential deployment of multiple stents, to achieve an efficient porosity [85,127]. Different overlapping patterns could be generated from the uncertainty of deployment process, resulting in different cross-stent structures. The successful experience of treating giant intracranial aneurysms with overlapping stents have been described in a few clinical case reports [327–329]. Several *in vivo* and *in vitro* studies reported the improved efficacy of overlapping intracranial stents on flow modulation [330–333]. Previous computational studies also found the stent-in-stent

[†] Part of the content in this chapter has been included in
1. **Wang, S.**, Y. Zhang, J. Feng, Y. Huang, A. Tokgoz, U. Sadat, J. H. Gillard, Q. Lu, and Z. Teng. Influence of overlapping pattern of multiple overlapping uncovered stents on the local mechanical environment: A patient-specific parameter study. *J. Biomech.*, 2017.
2. **Wang, S.**, Y. Zhang, J. Feng, Y. Huang, A. Tokgoz, U. Sadat, J. H. Gillard, Q. Lu, and Z. Teng. Influence of cross-stent structure and optimised design of multiple overlapping uncovered stents. (In preparation).

technique promotes haemodynamic stasis in intracranial aneurysms [332,334,335]. Most of previous studies focused on the haemodynamic comparison among different stents [331,334,335], however, a comprehensive study of the overlapping pattern is lacking. As an emerging area, only a few studies have investigated the application of MOUS in aortic aneurysms [336,337], which reported the flow modulation in the ideal models. The robustness of MOUS and influence of overlapping patterns are of great importance in clinical practice, which remains unknown yet.

The study was designed to investigate the cross-stent structures after the deployment of MOUS, and their influence on the local biomechanical environment including both haemodyamic change inside the aneurysm and structural stress within the diseased wall.

6.2 Materials and methods

6.2.1 Patient-specific FEA of MOUS

In this study, the same thoracoabdominal aortic aneurysm model was reconstructed from pre-operative CTA images in Chapter 5 (Figure 5.1). The procedure of one-way FSI simulation was followed, where the fluid analysis was performed after the virtual deployment of stents, as described in Section 5.2 (Figure 5.5). The first stent was delivered to the real location as identified on the post-operative CTA image, while the delivered location of other stents were set different in the parameter studies, as described below. The structural stress and haemodynamic variables were calculated and compared, including sac-averaged flow velocity, pressure, TAWSS, OSI and RRT.

6.2.2 2D overlapping patterns

A parameter study of 2D overlapping patterns was performed in a 2-stent MOUS system. Once the first stent was deployed, the delivered position of the second stent before deployment was controlled by two parameters: the circumferentially overlapping angle, θ, and the normalised axial overlapping displacement, D. The stent has a periodic configuration with $\theta = 18°$ in the circumferential direction and one cell unit in the axial direction. We therefore performed simulations with θ being 0º-15º with an interval of 3º, to investigate the influence of different

overlapping angles in the circumferential direction (Figure 6.1). The parameter study on the axial displacement of -1 to 1 cell unit with an interval of 0.25 was also performed, to investigate the different overlapping patterns in the axial direction (Figure 6.2). For comparison, we also investigated the case without any stent and with only one stent.

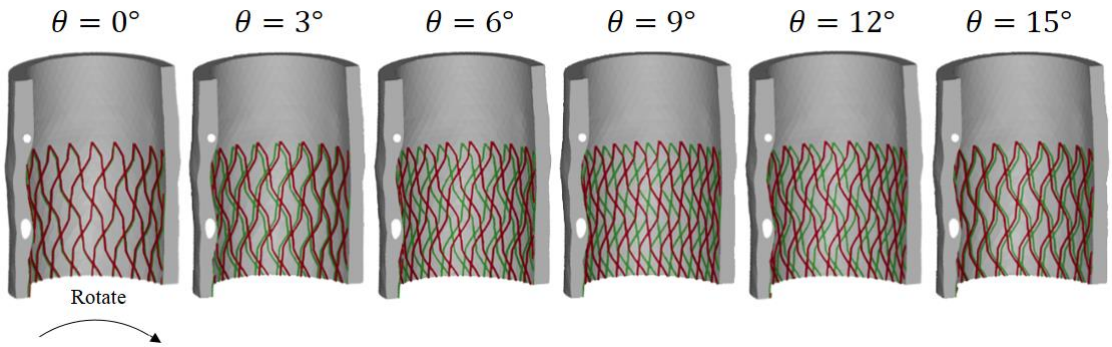

Figure 6.1 The local view of two stents with different overlapping patterns in the circumferential direction. The 1st stent is in green and the 2nd stent is in red. θ is the relative circumferential angle in the clockwise direction.

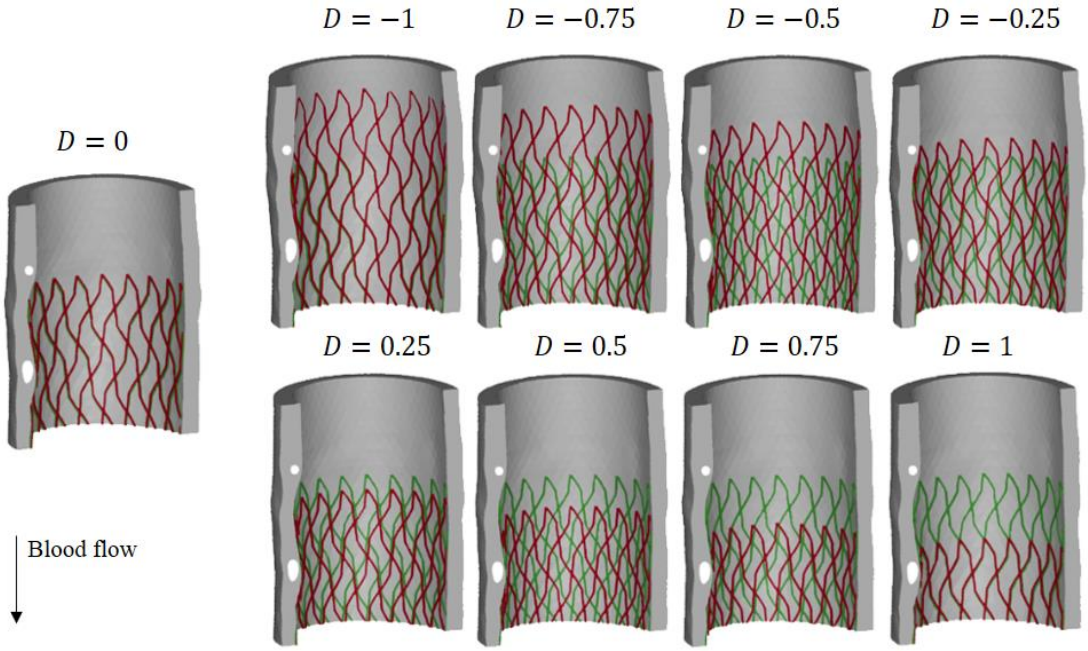

Figure 6.2 The local view of two stents with different overlapping patterns in the axial direction. The 1st stent is in green and the 2nd stent is in red. D is the relative axial displacement normalised by the cell length, along the blood flow direction.

6.2.3 Monte Carlo Method

As shown in Section 5.3.7, the overall porosity of the MOUS can be estimated from the geometry projection to the outer cylinder surface. Given the parameters of the relative circumferential angles and axial displacements for each stent, the overall porosity of MOUS can be determined. If the deployment processes of N stents are assumed independent and random, the overall porosity can be expressed as

$$\begin{gathered} p = p(\theta_1, D_1, \theta_2, D_2, \dots, \theta_N, D_N) \\ \theta_1 = 0, D_1 = 0 \\ \theta_k \sim U[0,18°], \qquad D_k \sim U[-1,1], \qquad k = 2,3,\dots,N \end{gathered} \tag{6.1}$$

where θ_k and D_k are circumferential angle and normalised axial displacement of the kth stent, respectively. $U[a,b]$ is a uniform distribution between a and b. The parameters of the 1st stent were set to 0, as the reference configuration for relative circumferential angles and axial displacements of subsequent stents. The irregular cell shape of the stent (Figure 5.2B) makes an analytical expression and analysis of the porosity function infeasible. Instead, the Monte Carlo method can be used to estimate the probability distribution of MOUS porosity after deployment, by repeated sampling of the porosity function. In this study, the porosity function p was sampled independently for 1,000,000 times for the deployment of 2-stent, 3-stent and 4-stent MOUS, respectively.

6.2.4 3D multi-layer structure

In addition to 2D overlapping patterns, the deployment of multiple stents also generates 3D structures (Figure 6.3A&B). To investigate the influence of multi-layer structures, a compact model with a single layer was built for comparison (Figure 6.3C): the geometry of each stent was projected outwards to the surface of the first stent, after the virtual deployment of a MOUS system. MOUS had the same overall porosity as the corresponding compact model, while the multi-layer structure was transformed into a single layer. The 2-stent, 3-stent and 4-stent compact models were generated based on deployed geometry during patient-specific simulation, as discussed in Chapter 5. Then the compact models were imported to ICEM

(ANSYS Inc., USA) for fluid domain meshing. The flow-diverting outcomes were compared between MOUS and compact models.

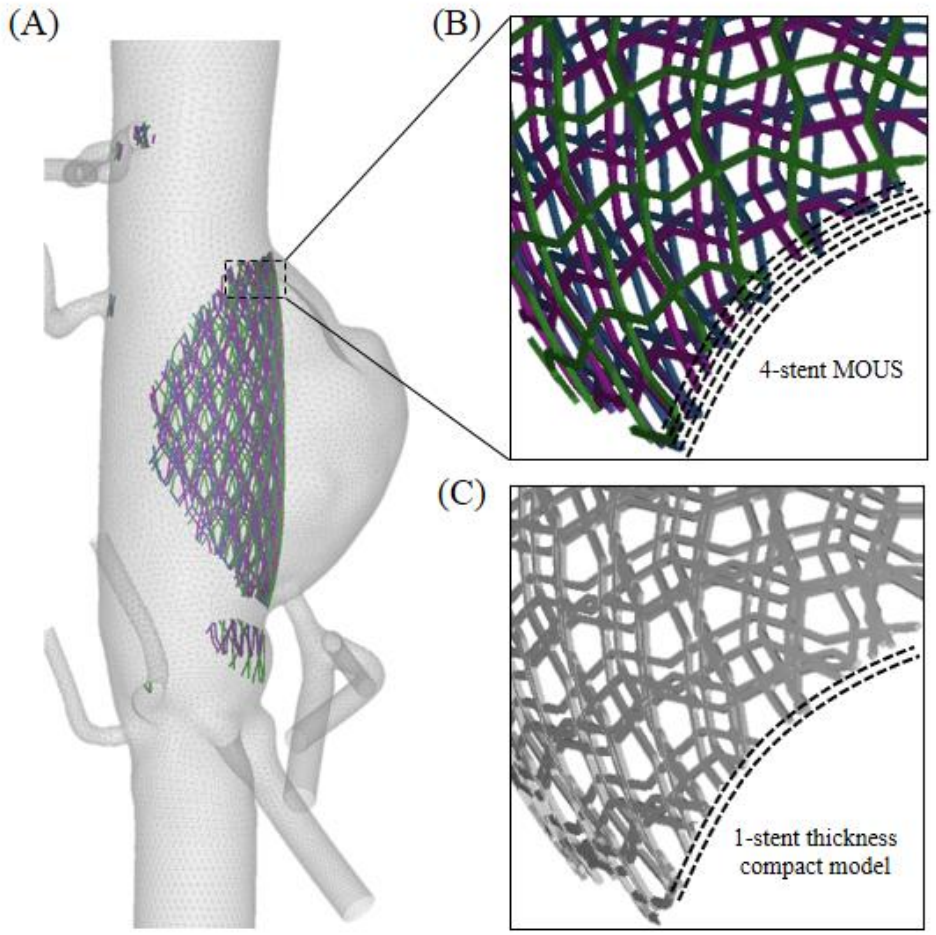

Figure 6.3 The 3D structure of a 4-stent MOUS and the corresponding compact model. **(A)** The configuration of MOUS and lumen surface after the deployment of 4 stents. The four layers of stents were in different colours, while stent struts in contact of the lumen wall were masked out. **(B)** The local view of MOUS configuration. **(C)** The local view of corresponding compact model.

A virtual deployment of the compact model of 4-stent MOUS was simulated by the similar procedure as described in Section 5.2.4. However, only contact pairs between the stents and the lumen wall were active while cross-stent contact pairs were inactive. This modified contact setting eliminated the internal interaction between stents and simulated an artificially 'merged' single-layer stent.

6.3 Results

6.3.1 Uncertainty of MOUS porosity

The probability density functions (PDF) of MOUS porosity with different number of stents were estimated from Monto Carlo simulation results, as demonstrated in Figure 6.4.

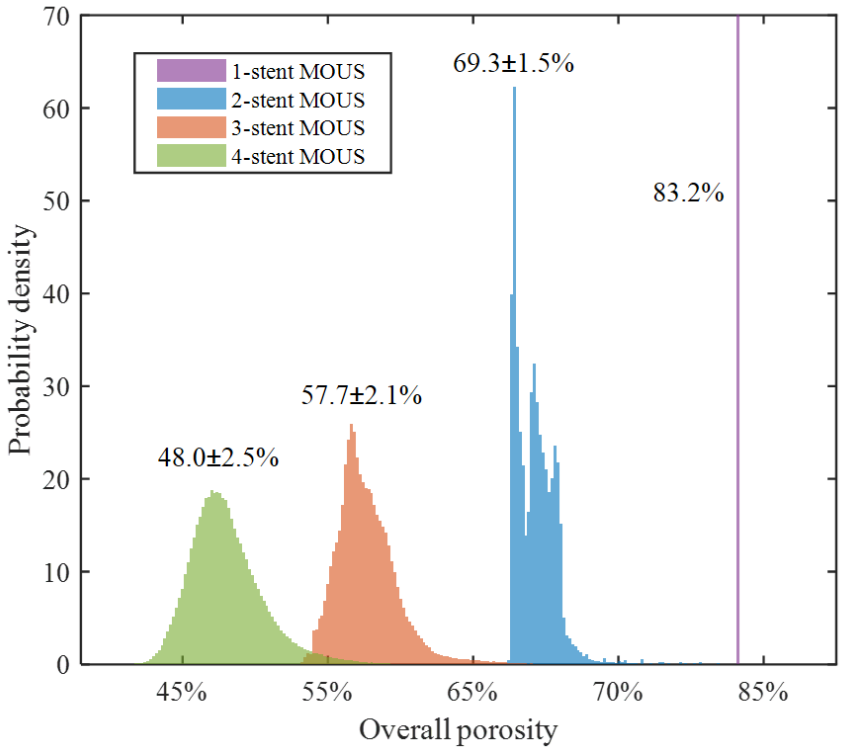

Figure 6.4 The probability density functions of MOUS porosity under random deployments. Mean ± standard deviation of sampling results from the Monto Carlo simulation are annotated for MOUS with different number of stents.

The porosity of 1-stent MOUS is 83.2%, which was reduced by subsequently deployed stents. The porosity (mean±SD) of MOUS from random deployment was 69.3±1.5%, 57.7±2.1% and 48.0±2.1% for 2-stent, 3-stent and 4-stent MOUS, respectively. For the parameter study of overlapping patterns, the porosity among different circumferential angles (Figure 6.5A) and axial displacements (Figure 6.5B) were similar (68.72%-69.51%), except for the cases with complete stents struts alignment (θ = 0º, 18º; D = -1,0,1).

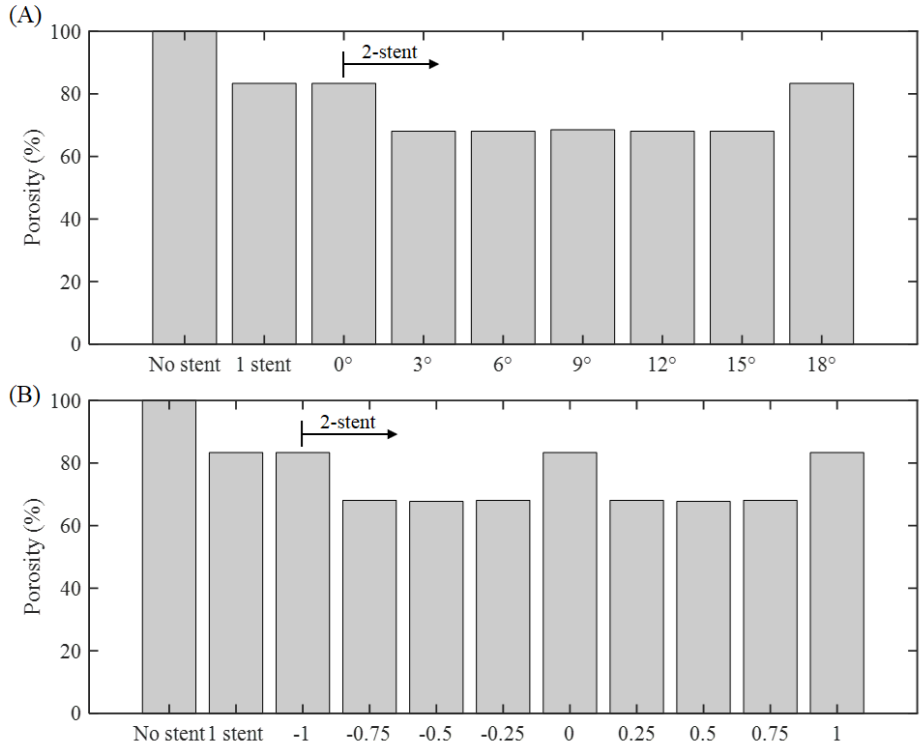

Figure 6.5 The overall porosity of no stent, 1-stent and 2-stent MOUS under different overlapping patterns. **(A)** With different circumferential angles; **(B)** With different axial displacements.

6.3.2 Influence of 2D overlapping patterns

Structural stress within the aortic wall

The different circumferential and axial overlapping patterns (Figure 6.1 & Figure 6.2) seem to have very little impact on the stress level in different regions (Figure 6.6). The stress variation was less than 2.5% when the two stents overlapped with each other in different circumferential angles (θ changed from 0º to 18º, Figure 6.6A). When the second stent moved along the axial direction (D changed from -1 to 1, Figure 6.6B), significant stress decreases (~20%) were observed in the margin of the proximal landing zone (Figure 6.6B), but not in other regions. In general, the variation of peak stress around the diseased region was less than 5%, and stress level in the sac remained nearly unchanged when the stents were overlapped differently (Figure 6.6).

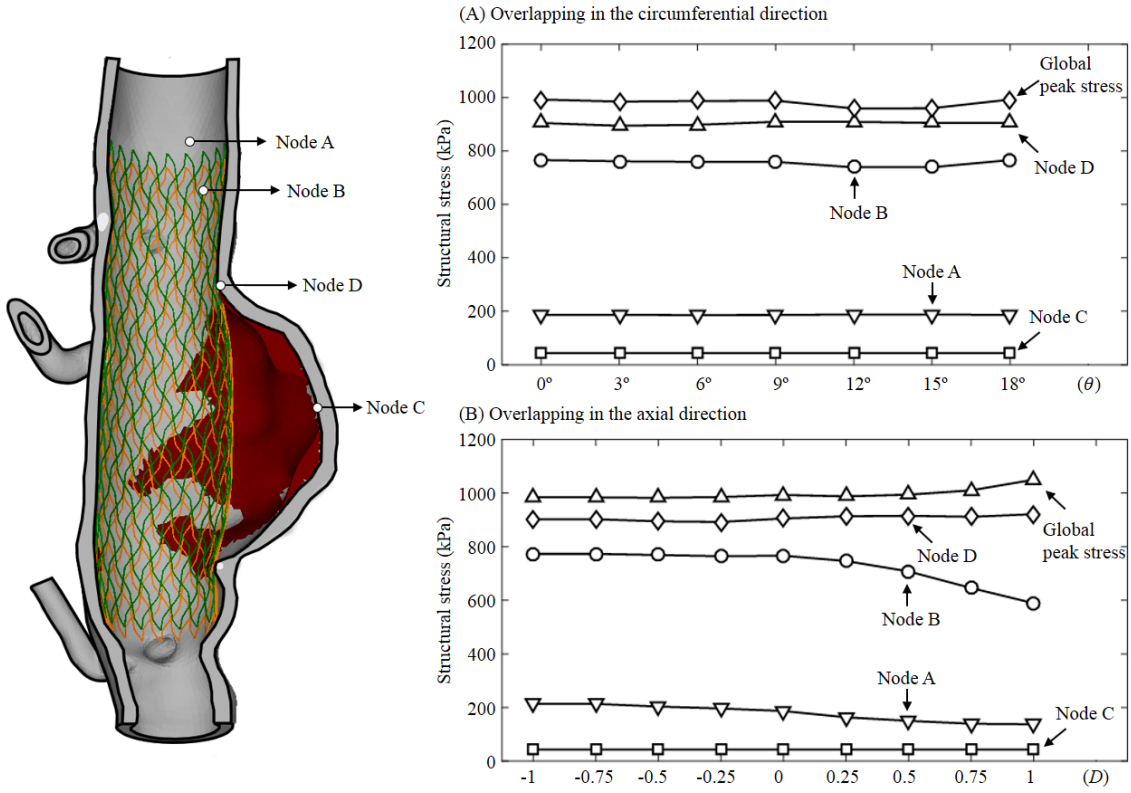

Figure 6.6 Structural stress level of a representative node in different location changed when two stents were overlapped differently in the circumferential **(A)** and axial **(B)** direction.

Flow-diverting outcome

After the first stent was deployed, the mean sac time-averaged velocity decreased from 39.8 mm/s to 25.3 mm/s (36.4% reduction). The deployment of the second stent further reduced the mean sac time-averaged velocity. However, the reduction depended on the overlapping parameters in both circumferential and axial direction (Figure 6.7D&E). When cells of the two stents completely aligned with each other, e.g. the cases of θ being 0° and 18°, and D being -1, 0 and 1, the further mean velocity reduction by the 2nd stent was ~10% (25.3 mm/s vs. 23.3±0.3 mm/s). As long as there was separation between struts in the two stents, the further mean velocity reduction was prominent with further ~20% decrease (25.3 mm/s vs. 20.2±0.3 mm/s). Compared with the value before stent deployment, the mean sac velocity could be reduced by 49.1%±0.7% under conditions with struts separation.

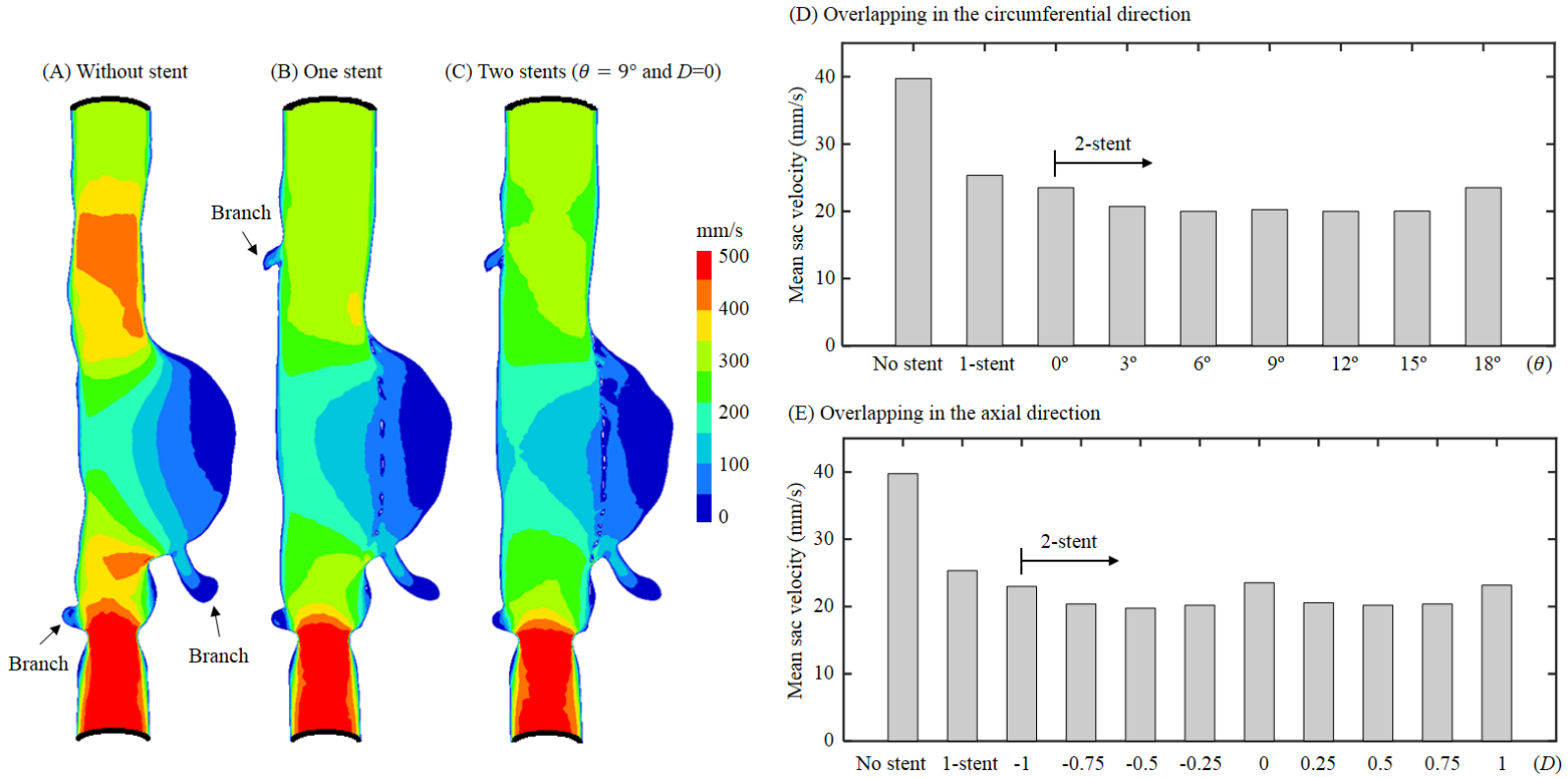

Figure 6.7 Influence of the 2D overlapping pattern on the velocity reduction inside the aneurysm sac. Band plot of velocity without stent deployment **(A)**; one stent deployment **(B)**; and two stents deployment **(C)** at systole. The change of mean sac time-averaged velocity before and after two-stent MOUS deployment with different overlapping patterns in circumferential direction **(D)** and in axial direction **(E)**.

The mean time-averaged pressure in the sac decreased by 2.4% after the first stent was deployed and decreased by 5.1±0.9% when the second stent was deployed. Difference in stents overlapping had very minor influence on the pressure reduction.

Also, the different 2D overlapping patterns had a little influence (~5%) on both mean TAWSS and OSI on the sac wall (Table 6.1). RRT at the proximal disease-free region where the flow fully developed was 8.5 Pa^{-1}, changed to be 8.4 Pa^{-1} after the first stent was deployed and remained the same after the second deployment. When the first stent was deployed, $\overline{RRT}$ in the sac increased from 1.29 to 3.13; it further increased to 4.90±0.75 after the second one was deployed; and the elevation (5.36±0.33) would be more prominent if the cases with complete stent cell alignment were excluded (Table 6.1).

Table 6.1 Comparison of mean TAWSS, OSI, $\overline{RRT}$ on the aneurysm sac after the deployment of 2-stent MOUS with different overlapping patterns.

Variables		**Overlapping parameters**								
	***θ* (º)**	**0**	**3**	**6**	**9**	**12**	**15**	**18**		
TAWSS (Pa)		0.14	0.14	0.13	0.13	0.13	0.13	0.14		
OSI		0.32	0.34	0.35	0.35	0.35	0.35	0.32		
$\overline{\mathbf{RRT}}$		3.81	4.92	5.55	5.40	5.61	5.57	3.81		
	D	**-1**	**-0.75**	**-0.5**	**-0.25**	**0**	**0.25**	**0.5**	**0.75**	**1**
TAWSS (Pa)		0.14	0.13	0.14	0.13	0.14	0.14	0.13	0.14	0.14
OSI		0.32	0.35	0.36	0.35	0.32	0.34	0.35	0.35	0.32
$\overline{\mathbf{RRT}}$		4.03	5.09	6.09	5.24	3.81	5.06	5.24	5.18	4.04

The flow rates in side branches after the deployment of 2-stent MOUS under different overlapping patterns were listed in Table 6.2. The change of flow rate in the distal side branches (CA and SMA) were more prominent in the cases of large axial displacement (*D*=0.75 and D =1) than other overlapping patterns, because the orifices became partially covered by the 2nd

stent. In general, the variation of flow rates in side branches is little (~1%) under different overlapping patterns.

Table 6.2 Comparison of time-averaged flow rate in each side branch after the deployment of 2-stent MOUS with different overlapping patterns. (Unit: $\times 10^{-3}$ml/s; CA: coeliac artery; SMA: superior mesenteric artery; other side branches were intercostal arteries)

Side branch	**Overlapping parameters**								
	***θ* (º)**	**0**	**3**	**6**	**9**	**12**	**15**	**18**	
1†		120	121	120	120	122	122	120	
2†		113	113	113	115	115	115	113	
3†		117	120	119	118	118	118	117	
4		52	53	52	52	52	53	52	
5†		76	75	78	77	77	75	76	
CA		156	157	156	157	157	157	156	
SMA		572	574	568	574	573	573	572	
	D	**-1**	**-0.75**	**-0.5**	**-0.25**	**0**	**0.25**	**0.5**	**0.75**	**1**
1†		120	121	120	121	120	121	121	118	119
2†		112	110	112	112	113	112	112	112	107
3†		116	117	118	118	117	115	118	114	115
4		52	53	52	52	52	51	52	50	49
5†		76	75	73	73	76	74	73	68	70
CA		156	156	158	157	156	156	157	154	151
SMA		566	565	574	574	572	569	574	561	550

† The orifice of these side branches was partially covered by the stent strut.

6.3.3 Influence of 3D cross-stent structures

Flow-diverting outcome

The flow-diverting outcome after patient-specific virtual deployment of 1-stent, 2-stent, 3-stent and 4-stent MOUS have been reported in Section 5.3.3. Similar to the multi-layer MOUS, the single-layer compact models modulated the flow pattern and decreasing the flow velocity inside the aneurysm sac (Figure 6.8). After the deployment of 2-stent MOUS, the mean sac-averaged velocity decreased from 39.8 mm/s to 20.2 mm/s, and the corresponding 2-stent compact model yield a similar mean velocity of 19.9 mm/s (Figure 6.8C). Compared to MOUS, the compact models led to slightly better performance (~5%) in flow velocity reduction (15.2 vs. 16.0 mm/s for 3 stents, 13.7 vs 14.8 mm/s for 4 stents) (Figure 6.8C).

In terms of the haemodynamics variables on the aneurysm wall (e.g. TAWSS, OSI and $\overline{RRT}$), little difference (<5%) was observed between MOUS and compact models, as shown in Table 6.3. The mean time-averaged pressure in the sac between MOUS and corresponding compact models were equivalent (relative difference <1%).

Table 6.3 Comparison of haemodyamicvariables averaged on the aneurysm wall, between MOUS and corresponding compact models.

Variables	**2-stent**		**3-stent**		**4-stent**	
	MOUS	Compact model	MOUS	Compact model	MOUS	Compact model
TAWSS (Pa)	0.14	0.14	0.13	0.13	0.13	0.12
OSI	0.40	0.40	0.44	0.43	0.44	0.44
$\overline{\mathbf{RRT}}$	4.90	4.82	17.77	17.79	18.80	18.91

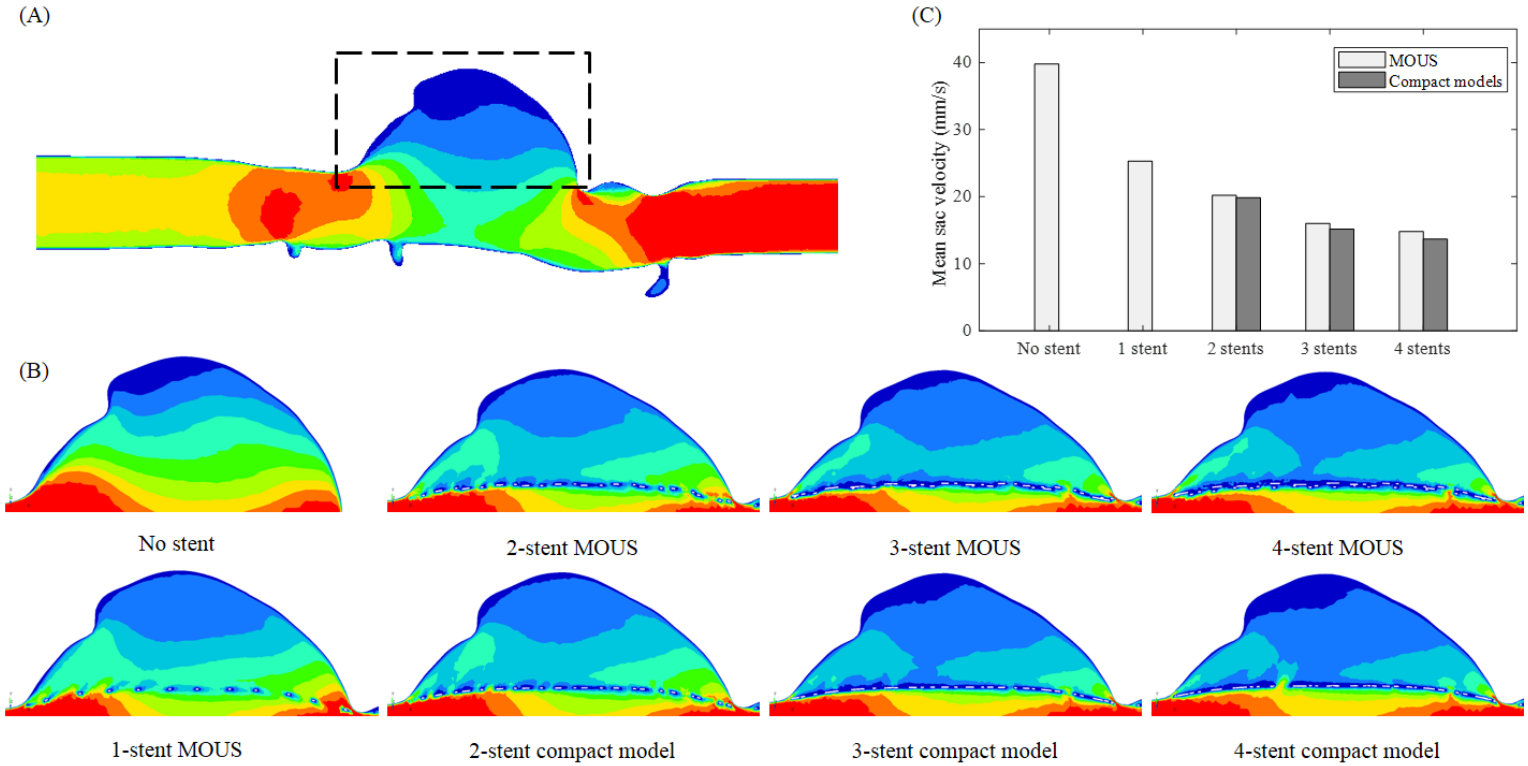

Figure 6.8 Comparison of velocity reduction between the MOUS and compact models. **(A)** Cross-sectional band plot of velocity without stent deployment at systole; **(B)** The local view of the flow velocity in the aneurysm sac before and after the deployment of the MOUS and corresponding compact models; **(C)** Comparison of the mean sac velocity between MOUS and corresponding compact models.

Structural stress within aortic wall

The structural stress level within the aortic wall after the deployment of corresponding compact models was lower than with MOUS, while varied on the different locations (Figure 6.9). In this study, the 2-stent compact model induced a peak structural stress about 14% lower than 2-stent MOUS, while the structural stress level within the sac wall (Figure 6.9, Node C) was about 6% lower. Similarly, after the virtual deployment of 3-stents compact models, the peak structural stress and sac wall stress were about 12% and 18% lower than MOUS, respectively. The 4-stent compact model reduced the peak stress level about 14%, and 23% in the sac wall, compared to the 4-stent MOUS.

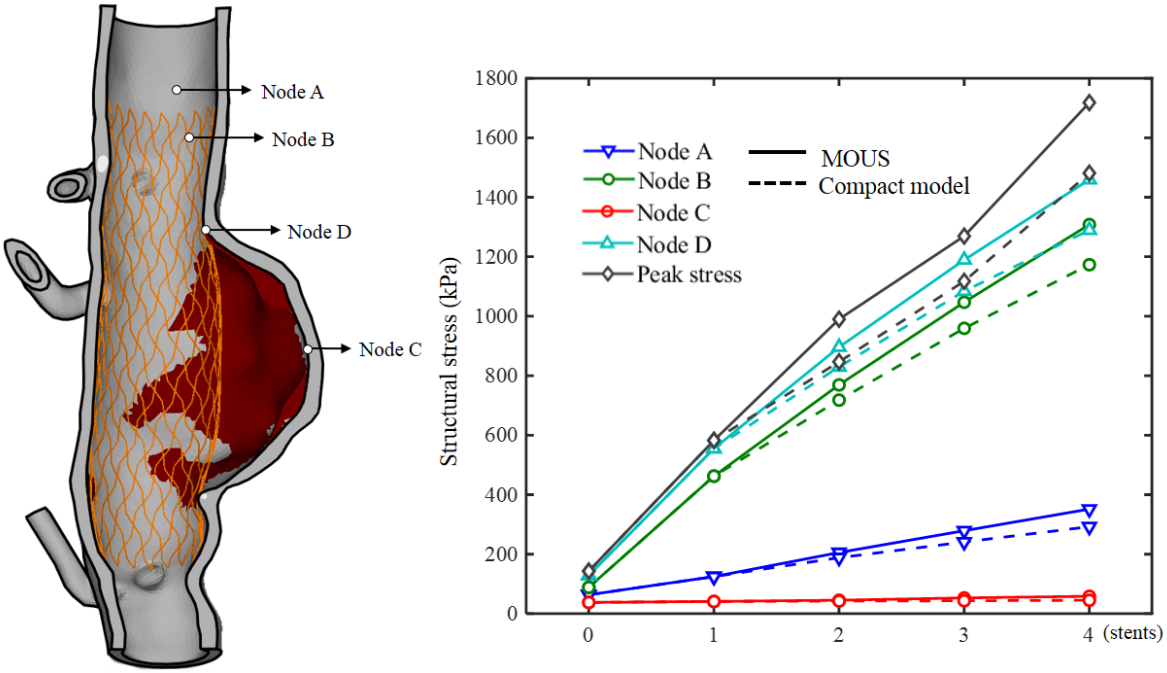

Figure 6.9 Comparison of structural stress level at different location after the deployment of MOUS and corresponding compact models, with different number of stents. The results of 4 different nodes are plotted in different colours, where MOUS is plotted with solid line and compact models are plotted with dash line.

6.4 Discussion

As discussed in Chapter 5, the overall porosity was considered as a key factor of the flow-diverting outcome [313–316]. The low-porosity MOUS induces significant flow velocity reduction inside the aneurysm sac and increased RRT on the sac wall, which promotes the formation and development of thrombus [295]. The Monte Carlo simulation evaluated the uncertainty of the overall porosity of MOUS under random deployment (Figure 6.4). In average, the second stent reduced the porosity by 14% (from 69.3% to 83.2%), while the third and fourth stent led to a further reduction of overall porosity by 12% and 9%, respectively. The less reduction induced by the third and fourth stent was expected, as overlapping coverage between stents struts increased. Overlapping pattern has an influence on the overall porosity of MOUS (Figure 6.4), while the variation was small for most cases (standard deviation of PDF < 2.5%). In rare cases where the subsequent stent was aligned completely to previously deployed stents, the overall porosity remains the same.

The parameter study of two-stent MOUS demonstrated the limited influence of 2D overlapping patterns on flow-diverting outcome. Apart from the cases with complete cells alignment (θ being 0º and 18º; and D being -1, 0 and 1), porosity (68.1±0.002%) varied very little with the change of θ or D. Despite of the difference in the resultant cell shape, different θ or D (except the cases of complete alignment) induced a negligible change in the velocity (Figure 6.7), pressure, OSI and RRT in the sac, which could be attributed to the fact that flow modulated by the stent strut was limited in a narrow region around the strut. Moreover, the difference in overlapping pattern also had limited influence on the stress concentration around the diseased region (Figure 6.6). These findings suggest that endovascular surgeries using MOUS can be performed with less attention to the overlapping pattern as the chance to achieve a complete cell alignment is low.

Interestingly, the 3D multi-layer MOUS did not show better performance on the flow-diverting outcome compared to the corresponding single-layer structure (Table 6.3). Instead, a further velocity reduction (~5%) was observed in the 3-stent and 4-stent compact models than MOUS (Figure 6.9). This could be explained by the elimination of 3D ‘tunnels’ across the dimension

of thickness, during the projection of multiple layers to single-layer structure, which reduced the effective porosity.

The structural stress concentrations within landing zones after MOUS deployment might have undesirable effects, such as continued aneurysmal degeneration of the aortic wall [56,57]. One case of aneurysm recurrence was observed in this cohort, which might be related to the structural stress concentrations. As demonstrated in Figure 6.10, the TAA was managed with a 4-stent MOUS and the aneurysm sac was thrombosed in 1 month. The aneurysm disappeared on 1-month and 12-month follow-up CTA (Figure 6.10B&C), however, recurrence near the proximal landing zone was observed on the 36-month follow-up images (Figure 6.10D).

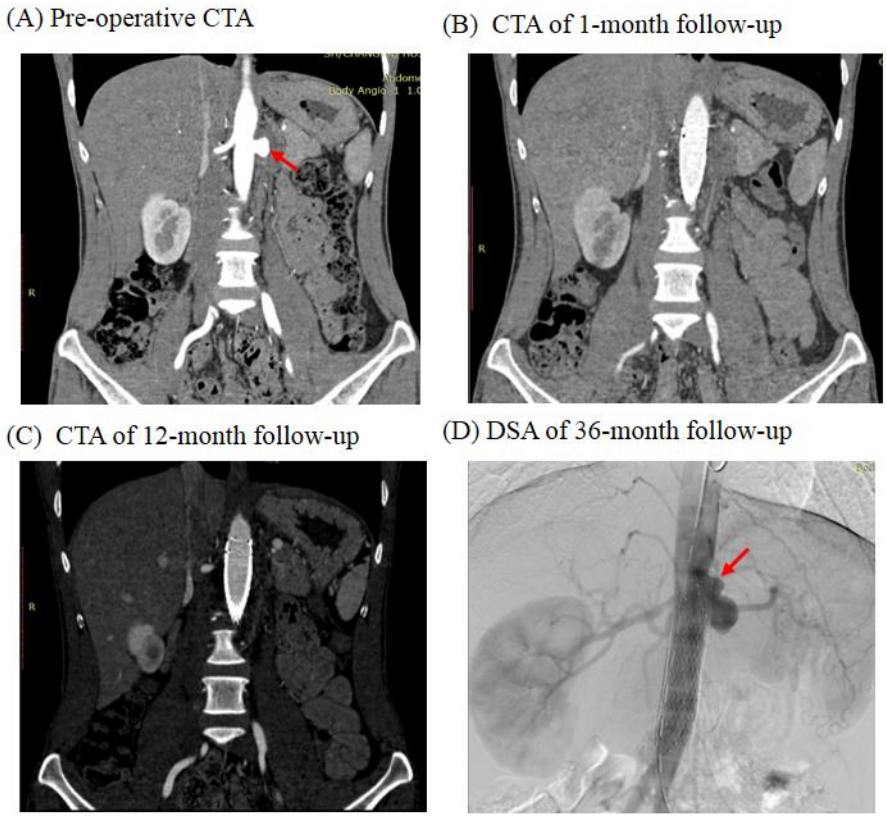

Figure 6.10 An example of aneurysm recurrence near the landing zone after MOUS treatment. **(A)** TAA identified on pre-operative CTA; **(B)** Full occlusion of aneurysm after 1 month; **(C)** Full occlusion of aneurysm after 12 months; **(D)** Recurrence of an aneurysm near the proximal landing zone.

To improve treatment outcome, the number of stents used for MOUS should be decided by considering the trade-off between the flow-modulation and the structural stress concentrations. The advanced imaging modalities such as PET have the potential to evaluate inflammation in the aorta and the risk of high stress concentrations [338].

On the other hand, a better design of the stents used for the MOUS procedure is desirable to reduce the stress concertation. By comparing multi-layer MOUS to the single-layer compact model (Figure 6.9), it was observed that the artificially 'merged' structure could reduce the stress concentrations by more than 10%, while keeping equivalent flow-diverting outcome. This suggests that, the use of less number of stents with lower porosity could reduce the MOUS-induced structural stress concentrations, providing similar overall porosity. The material and size of the stents could also be optimised, to provide more compliance and achieve better conformity to the aorta. However, the stent should provide efficient fixation to the landing zones, avoiding the longitudinal shortening and displacement of stent which has been reported with aneurysm expansion and rupture [121,122,124].

Despite these interesting findings, several limitations exist in the present study: (1) The limitations of patient-specific simulation as discussed in Chapter 5; (2) Considering the computational costs, only 16 representative overlapping patterns were investigated in the parameter study of 2-stent MOUS. However, it should be reasonable to infer the result of more complex overlapping patterns from the representative overlapping patterns.

6.5 Conclusion

In conclusion, porosity is the dominant factor for the flow-diverting outcome while cross-stent structures had limited influence. Better stent design with lower porosity and more material compliance might help reduce the structural stress concentrations and related adverse outcome.

Chapter 7 Pathological effects of high structural stress concentrations[†]

As discussed in Chapter 6, MOUS may induce local high structural stress concentration within the landing zone, which might be related to adverse clinical outcomes. However, the correlation has not been validated in experiments. There was an animal study performed by our research group which studied the feasibility of creating atherosclerosis in rabbit models by collars. Similar to stents, the collars would induce high stress concentrations and trigger pathological remodelling of the arterial wall. In this chapter, a retrospective analysis of previous animal experiments was perform to investigates the pathological effects of abnormal environment induced by implanted device.

7.1 Introduction

Cardiovascular diseases (CVD) are the leading cause of death and disability worldwide [238]. Atherosclerosis and aneurysms are the two most common forms of CVD, both of which share predisposing risk factors and exhibit similar inflammatory cell infiltrates at lesion sites [4]. Under physiological conditions, arterial walls are subject to mechanical loading, which is considered important during the formation and development of these diseases [249,339]. Mechanical loads can be classified into vascular structural stress (VSS) due to arterial expansion driven by blood pressure, and wall shear stress (WSS) acting on the lumen surface due to blood flow.

[†] The author of this dissertation carried out all of the work described in this chapter unless specified otherwise. The animal experiments were performed by Dr Joseph Bird from Department of Radiology, University of Cambridge. The MRI segmentation and biomechanical model reconstruction were performed by Dr Zhongzhao Teng from Department of Radiology, University of Cambridge.

Blood flow at sites with bifurcation or bend is disturbed due to the irregular luminal geometry, leading to alterations in both the magnitude and direction of WSS. The association between supraphysiological WSS and the malfunctioning of endothelial cells, and therefore the initialisation and development of CVD has been extensively studied [249].

Endothelial cells are actually subject to both WSS and VSS, while other cells within the extracellular matrix are subject to VSS only. The magnitude of VSS is much higher than that of WSS (100-1000 kPa vs. 0.01-0.10 kPa) [340]. VSS is a complex mechanical stress state that acts in circumferential, axial and radial directions within the arterial wall, causing structural deformation of individual cells. VSMCs are capable of sensing pulsatile stretch through multiple mechanisms and transduce it into intracellular signals, resulting in the modulations of gene expression and cellular functions, such as proliferation, apoptosis, migration and remodelling [341,342]. High VSS is also correlated with both increased MMP expression [343] and macrophage accumulation [344], which are associated with structural degradation of ECM. The role of VSS in atherogenesis was proposed more than half a century ago based on the fact that atherosclerosis is found in arteries and not in veins, and it is likely to develop at ostia of branches where high VSS concentration occurs [345,346]. Experimental studies in rabbits showed that reduction of arterial intramural stress inhibited atherosclerosis [347,348].

The deployment of stents will change the local geometry of lesion regions, as well as alter the biomechanical environment. Foreign body stent placement might lead to endothelium injury and inflammatory response, triggering pathological remodelling of the arterial wall [349]. Most of previous studies focused on the role of WSS [350–352], while the role of VSS has been least explored [353].

In this study, constrictions were created in rabbit carotid arteries by implantation of collars. *In vivo* MRI was performed to visualise the configuration and to reconstruct the 3D geometry. FSI analyses were performed to quantify both WSS and VSS near the constrictions. Histopathological stains were used to visualise the plaque distribution and the local inflammatory status. The association between WSS, VSS and presence of plaque is reported.

7.2 Materials and methods

7.2.1 Rabbit treatment protocol

This study was performed according to Home Office animal welfare guidelines and had approval from the local ethics committee. Nine New Zealand White rabbits were put on a high fat diet that comprised of 0.3% cholesterol and 4.7% palm oil in standard rabbit chow for 16 weeks. Drinking water was available all the time. A non-occlusive, silastic collar (ARK Therapeutics, Finland) was implanted on the left common carotid artery (CCA) after the animals had been on the high fat diet for two weeks (Figure 7.1A). The collar had two narrow points constricting to 2 mm external diameter (Figure 7.2A) and produced a partial occlusion of the artery. The proximal constriction was named Constriction 1# and the distal constriction was named Constriction 2#.

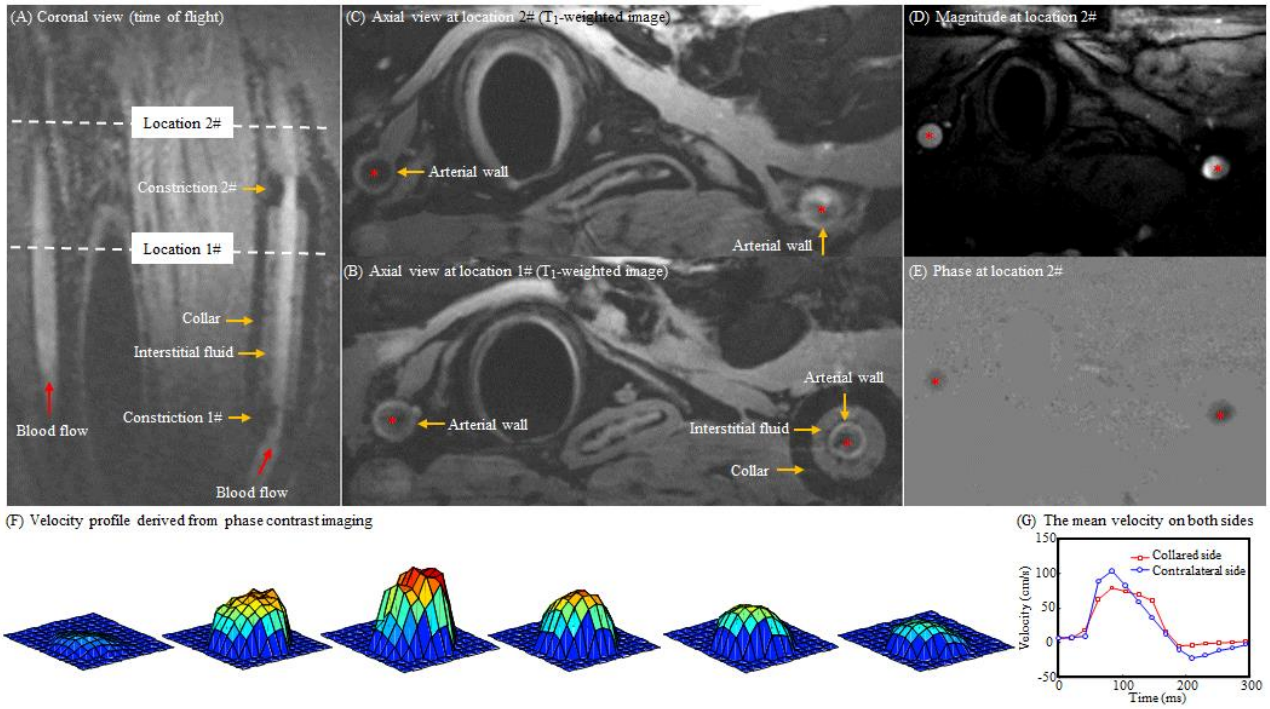

Figure 7.1 *In vivo* magnetic resonance imaging showing rabbit carotid arteries with and without collar and corresponding blood velocity measurements. **(A)** Time of flight (TOF) image showing both arteries on the coronal plane; **(B)&(C)**: T_1-weighted image showing both arteries in the transverse plane at the location between two constrictions and above the Constriction 2#; **(D)&(E)**: The magnitude and phase images obtained from phase contrast imaging; **(F)** The blood velocity profile on the collared side with a 20-ms interval between each frame; (**G)** The mean velocity on both sides.

The collar was placed carefully using standard veterinary surgical and aseptic techniques. The right CCA was exposed at the same time during the operation but without collar deployment. Rabbit health status was assessed by serological analysis and body weight. Blood cholesterol, high density lipoprotein (HDL), low density lipoprotein (LDL) and triglyceride levels were measured to monitor the dietary intake of cholesterol and lipids.

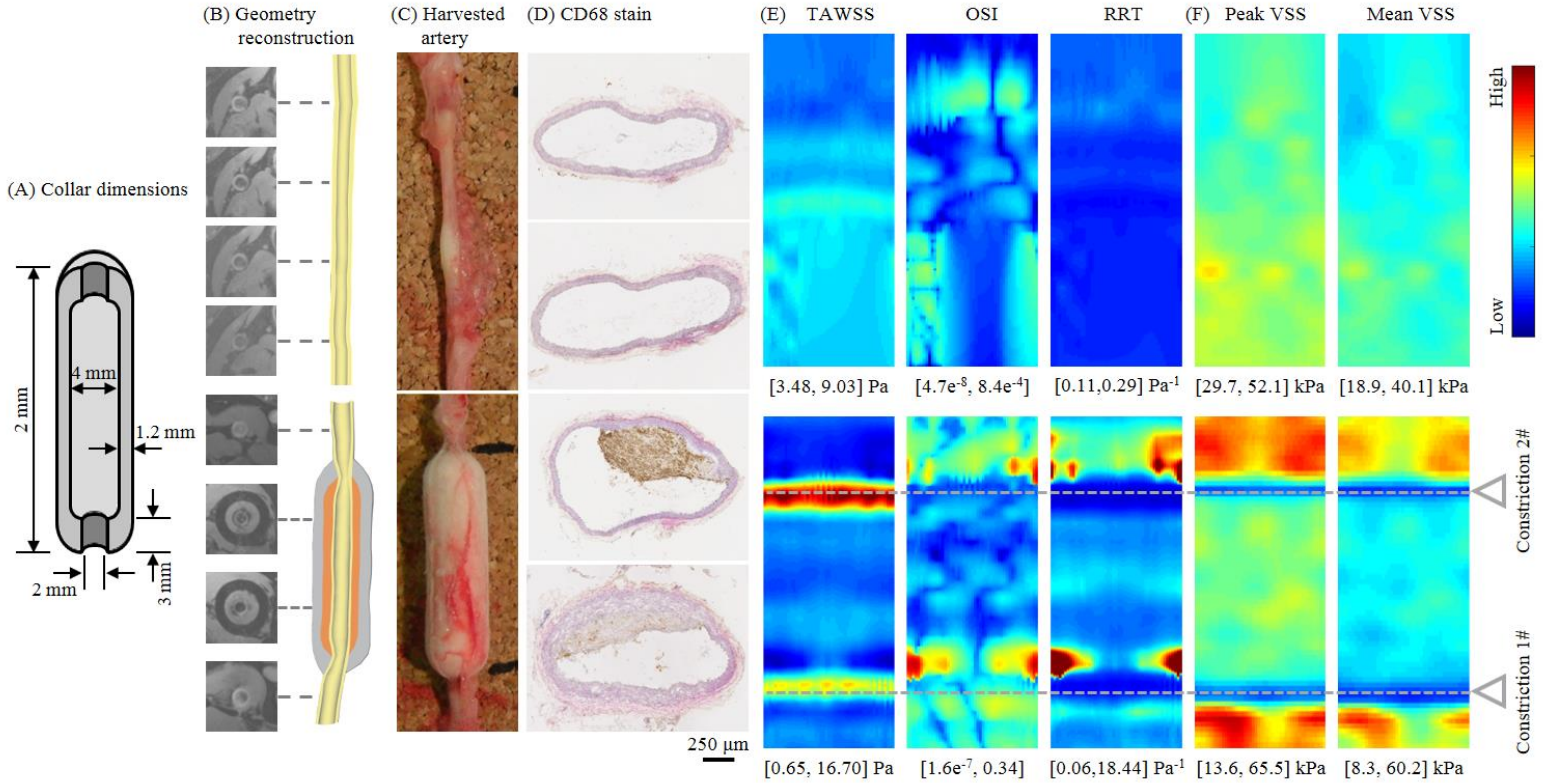

Figure 7.2 Reconstructed 3D geometry based on baseline MR images, images of arteries removed from the animals and corresponding Cluster of Differentiation 68 (CD68) stain, and calculated flow parameters and mechanical loading within the structure. **(A)** Schematic drawing showing the collar geometry and dimension; **(B)** MR-based 3D geometry reconstruction; **(C)** Artery with collar and the corresponding contralateral artery; **(D)** CD68 stain showing macrophages in brown; **(E)** Expanded view of TAWSS, OSI and RRT; **(F)** Peak VSS and Mean VSS in the artery wall.

7.2.2 Magnetic resonance imaging

MR imaging was performed on bilateral carotid arteries of all rabbits three days after implantation of collars with bespoke 3D time of flight (Figure 7.1A), T_1-weighted spin echo (Figure 7.1B&C), T_{2*}-weighted gradient echo and phase contrast (Figure 7.1D&E) sequences to visualise carotid artery structure and measure blood flow velocity (Figure 7.1F&G). The imaging was performed on a Bruker 4.7T system with a surface coil (Bruker 25-mm coil) with ECG-gating. The silastic does not produce any MR signal and the collar therefore appeared hypointense in both T_1-weighted and T_2^*-weighted images. Following implantation, the void within the collar became filled with interstitial fluid (Figure 7.1A&B) which was hyperintensed in both T_1-weighted and T_2^*-weighted images. The 3D TOF was performed with 0.3 mm isotropic resolution. T_1-weighted and T_2^*-weighted imaging were performed with a through plane resolution of 2.0 mm and an in-plane resolution of 0.13mm.

7.2.3 Fluid-structure interaction analysis

The lumen, outer wall, collar and interstitial fluid were identified manually with reviewing TOF, T_1-weighted and T_2*-weighted images using VascularView (Tenoke Ltd., Cambridge, UK). The 3D geometry was reconstructed and meshed using hexahedral elements.

Determination of computational starting shape

Since images were acquired at the pressurised condition with axial stretch [354], shrinkage was therefore necessary to recover the stretch-free configuration to generate the starting shape for the computational simulation [355]. Axial shrinkage was set to be 15%, which was determined by the ratio of the arterial length before and after harvesting. The blood pressure (78-116 mmHg) and waveform were adopted from previous reports [356,357]. Considering the constriction from the collar, radial shrinkages were different among the regions beyond the constrictions, at the constrictions and between the constrictions. The shrinkage for each section was determined such that when pressurised with mean blood pressure, the configuration matched with the one obtained from *in vivo* imaging. The radial shrinkage was 10.2±0.7%, 0.1±0.2%, 0.2±0.2% for each of the three sections, respectively.

Fluid-structure interaction analysis

After the shrinkage amounts were determined, the arterial lumen and outer wall contours and the slice thicknesses were updated accordingly. 3D geometry was reconstructed based on the updated configuration and meshed using hexahedral elements (Figure 2B). The Young modulus of silastic collar is 2.05 MPa and the Poisson's ratio is 0.35 as provided by the manufacturer. The arterial wall was assumed as a hyperelastic material and characterised by the modified Mooney-Rivlin model, and the material constants were fitted from previously reported experimental data [358]. The interstitial fluid between the artery and collar was modelled as an incompressible gel with material constants set to be one-tenth of intraplaque haemorrhage (C_1=0.02 kPa, D_1=0.43 kPa and D_2=0.53) [359]. The volume enclosed by the arterial lumen surface was defined as fluid domain, which was similarly meshed by hexahedral elements.

Blood flow was assumed to be laminar, Newtonian, viscous, and incompressible. Incompressible Navier-Stokes equations with arbitrary Lagrangian-Eulerian formulation were used as the governing equations,

$$\rho_b \frac{\partial \boldsymbol{u}}{\partial t} + \left[\left(\left(\boldsymbol{u} - \boldsymbol{u}_g\right) \cdot \nabla\right)\boldsymbol{u}\right] = -\partial p + \mu \partial^2 \boldsymbol{u}, \quad \nabla \cdot \boldsymbol{u} = 0 \tag{7.1}$$

with loading conditions,

$$p|_{inlet} = p_{in}(t), \quad p|_{outlet} = p_{out}(t) \tag{7.2}$$

where $\boldsymbol{u}$ is the flow velocity, $\boldsymbol{u}_g$ is the mesh velocity, p is the pressure, and μ and ρ_b stand for the blood viscosity and density, respectively. The motion of the arterial wall, collar and interstitial fluid was governed by,

$$\rho_w v_{i,tt} = \sigma_{ij,j} \quad i,j = 1,2,3; \text{ sum over } j \tag{7.3}$$

with boundary condition,

$$\sigma_{ij,j} \cdot n_j\big|_{outter\ wall} = 0 \tag{7.4}$$

in which $\boldsymbol{v}$ is the displacement vector, $\boldsymbol{\sigma}$ is the stress tensor, and t denotes time. There was no relative displacement between collar, interstitial fluid and the arterial outer wall. No-slip condition between the flow-vessel interfaces was set as

$$\boldsymbol{u}|_{\Gamma} = \left.\frac{\partial \boldsymbol{v}}{\partial t}\right|_{\Gamma} \tag{7.5}$$

and interaction actions between the fluid and solid was governed by

$$\sigma_{ij}^{f} \cdot n_j\big|_{\Gamma} = \sigma_{ij}^{s} \cdot n_j\big|_{\Gamma} \tag{7.6}$$

where Γ represents the inner wall of the vessel and the superscripts; *f* and *s*, stand for fluid part and solid part, respectively.

The fully coupled FSI models were solved in ADINA 9.2.3 (ADINA R&D Inc.). It uses unstructured finite element methods for both fluid and solid models with nonlinear incremental iterative procedures. The governing finite element equations for both solid and fluid models are solved by the Newton-Raphson iteration method. The energy convergence criterion was used for solid domain during equilibrium iterations, with the relative energy tolerance being 0.05 and relative force and moment tolerance being 0.01. For the fluid domain, the relative tolerances for velocities, pressure and displacements were set to be 0.06 for controlling the equilibrium. Both the displacements and velocities at the fluid-structure interface and the forces on the structure were checked for convergence. Relative displacement/velocity and force tolerances were both set to be 0.06. The $p_{out}(t)$ was adjusted such that the difference between the simulated flow rate and the one measured by phase contrast MR was less than 5%. Details of the models and methods are given by Bathe [235].

Mechanical parameters for analysis

In this study, effective stress was used to characterise the critical mechanical conditions within the arterial wall structure. WSS, OSI and RRT were used to characterise the haemodynamic environment, which have been widely suggested to be associated with atherosclerosis initialisation and development [303–306].

7.2.4 Immunohistochemical processing and analysis

All nine rabbits were sacrificed at the end of 16-week diet period. Carotid arteries on both sides of each animal were collected (Figure 7.2C). Implanted collars were carefully removed and constriction points were marked. Following the standard immunohistochemical procedure, 5-

μm slices were made for Haematoxylin and Eosin (H&E) and Cluster of Differentiation 68 (CD68) stains, from three different regions: 1) Proximal: proximal to the Constriction #1 with a 1-mm gap on the collared side; 2) Distal: distal to the Constriction #2 with a 1-mm gap on the collared side; 3) Contralateral: similar levels on the contralateral side. Each histological slide was scanned and digitised using NanoZoomer (Hamamatsu Photonics, Hamamatsu, Japan) at x40 mode.

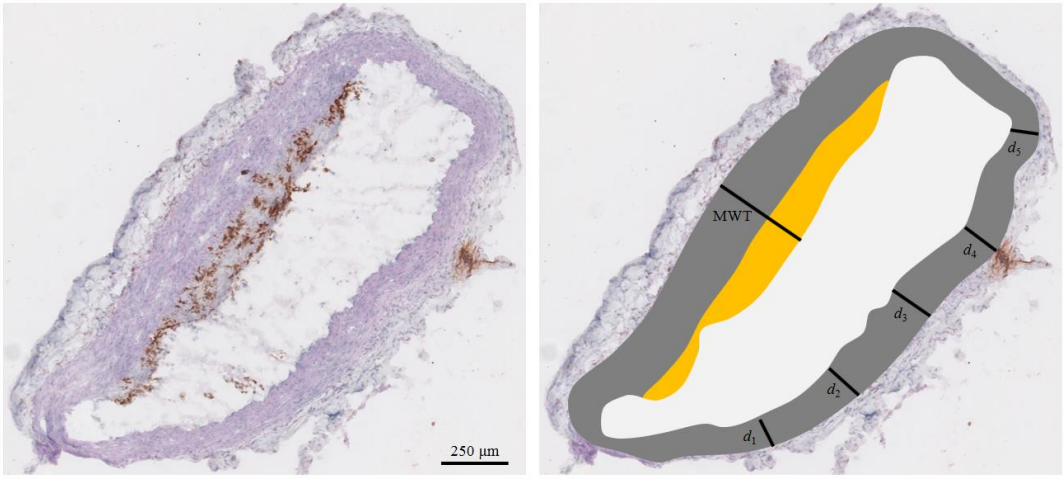

Figure 7.3 A representative image showing wall and plaque segmentation (area marked in yellow showing the region with plaque and the one in grey is wall; MWT is the maximum wall thickness and MTH=(d_1+d_2+d_3+d_4+d_5)/5 is the mean wall thickness of the healthy section)

An in-house software developed in Matlab 2018a (The Mathworks, Inc., MA, USA) was used to perform quantitative histological analysis. Each CD68 image was processed with a semi-automatic support vector machine classifier [360] to segment and detect macrophages. Density of macrophage within the arterial walls were quantified from the segmentation results. Segmentation parameters of the classifier were optimised with the help of Ms Nichola Figg, who has more than 15 years of experience in histopathological analysis of diseased arterial tissues. Moreover, plaque area ratio (PAR), maximum wall thickness (MWT) and the mean thickness of healthy (disease free) section (MTH) were measured manually in NDP Reviewer (Hamamatsu Photonics, Hamamatsu, Japan) (Figure 7.3). PAR is defined as the ratio between area in yellow (plaque) and the wall (area in grey and yellow). MWT is the largest thickness

along the lumen and MTH is defined as the mean value of five sampling points d_1, d_2, d_3, d_4, and d_5, as shown in Figure 7.3.

7.2.5 Statistical analysis

The normality was assessed by Shapiro Wilk test. The difference in plaque characteristics and mechanical variables at different regions were evaluated by Wilcoxon signed rank test. The correlations between plaque characteristics and mechanical variables were assessed using Spearman correlation test. The statistical analysis was performed in MATLAB (MathWorks, Inc.). A significant difference was assumed if $p<0.05$.

7.3 Results

The final weights, triglycerides, total cholesterol, LDL and HDL levels at the end of 16-week high fat diet were listed in Table 7.1. The stenosis caused by the collar at Constriction #1 was 30.4±11.6% and 34.8±12.2% at Constriction #2. No significant difference was found between the two constrictions (p=0.324).

Table 7.1 Weight and cholesterol levels after 16-week high fat diet

Weight (kg)	5.04±0.20
Total cholesterol (mmol/L)	1.525±0.465
LDL (mmol/L)	0.525±0.222
HDL (mmol/L)	0.665±0.157
Triglycerides (mmol/L)	0.675±0.310

7.3.1 Location-dependent histological features

Presence of plaque was defined as plaque area ratio exceeding 5%. From the histological slides, 15 plaques were found on the collared sides, eight from regions proximal to Constriction 1# and seven from regions distal to Constriction 2#. In comparison, only five plaques were found on the contralateral sides (p=0.003).

Plaques on the collared side either proximal to Constriction 1# or distal to Constriction 2# tended to be bigger and more inflammatory than those on the contralateral side, with higher plaque area ratio (PAR), maximum wall thickness (MWT), mean thickness of healthy section (MTH) and density of macrophages (Figure 7.4). Plaques proximal to Constriction 1# were bigger than those distal to Constriction 2#, while with a similar level of inflammatory burden (Figure 7.4).

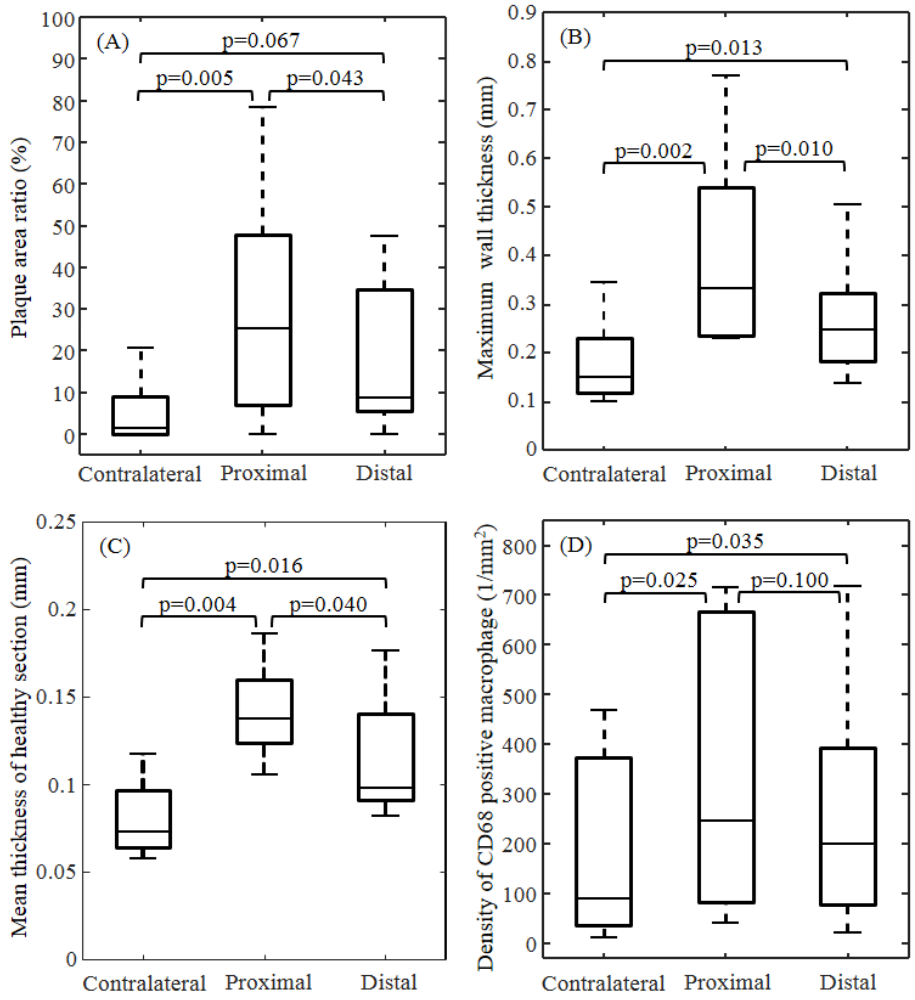

Figure 7.4 The comparison of plaque morphological and inflammatory features at different location. **(A)** Plaque area ratio (PAR); **(B)** Maximum wall thickness (MWT); **(C)** Mean wall thickness of the healthy section (MTH); and **(D)** The density of CD68-positive macrophage.

7.3.2 Location-dependent mechanical characteristics

A representative case showing mechanical parameters on the collared side and corresponding contralateral side was illustrated in Figure 7.2E&F. The lumen surface was opened and mapped to a plain surface for visualisation. Quantitative comparison of the mechanical variables among different regions corresponding to the histological sites was demonstrated in Figure 7.5.

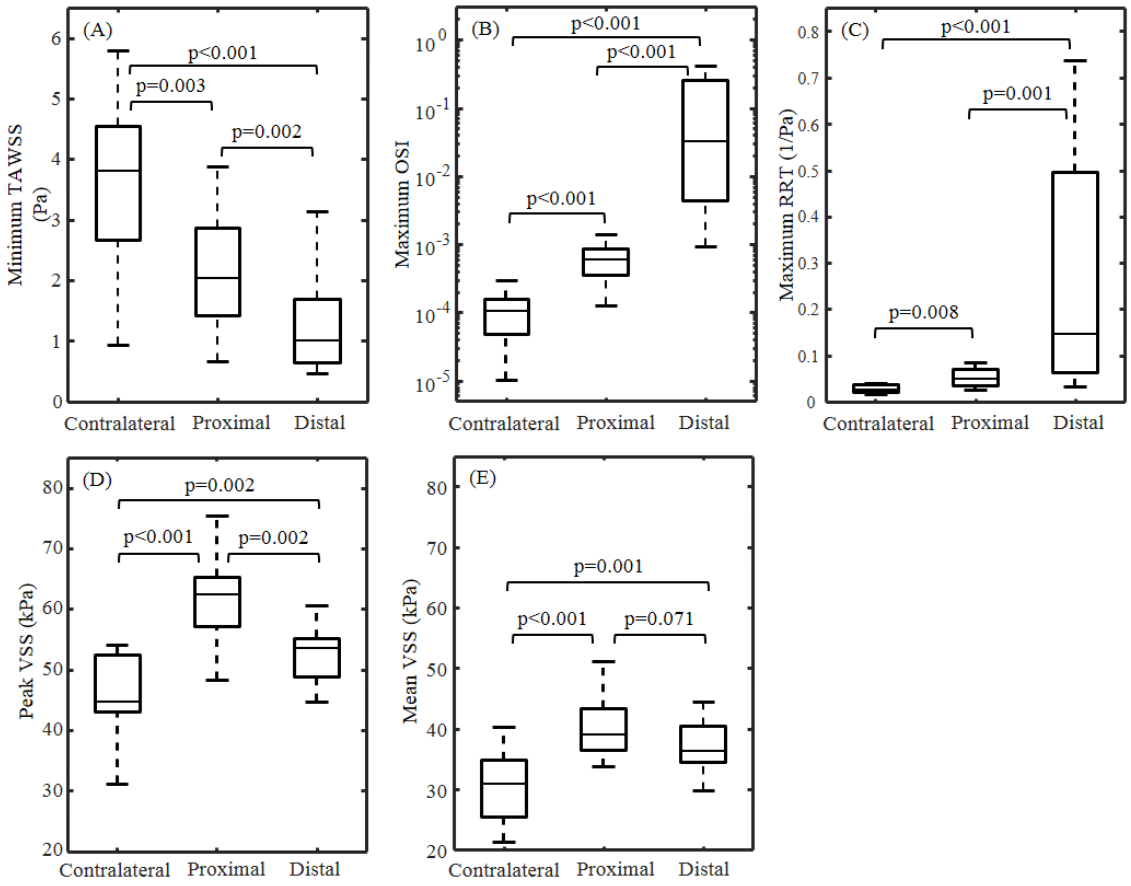

Figure 7.5 The comparison of mechanical parameters among different regions. **(A)** Minimum time averaged wall shear stress (TAWSS); **(B)** Maximum oscillatory shear index (OSI); **(C)** Maximum relative residence time (RRT); **(D)** Peak vessel structural stress (VSS) during one cardiac cycle; **(E)** Mean VSS.

Flow variables

As shown in Figure 7.2E, flow parameters during one cardiac cycle, including TAWSS, OSI and RRT were all location-dependent. TAWSS was highest at the constriction points due to their narrowest dimension and it was lowest in the expanding region right after each constriction. The distributions of OSI and RRT were similar. Both of them were lowest at the sites with constriction, and highest in the expanding region right after each constriction. The values of WSS, OSI and RRT in the region proximal to Constriction 1# and in the middle region between the two constrictions were moderate.

The minimum TAWSS, and maximum OSI and RRT in the region proximal to the Constriction 1#, distal to Constriction 2# and on the contralateral side were quantitatively compared in Figure 7.5A-C. Minimum TAWSS in the region proximal to Constriction 1# was significantly higher than the one in the region distal to Constriction 2#. Both maximum OSI and RRT in the region proximal to Constriction 1# were significantly lower than the two in the region distal to Constriction 2#. The highest minimum TAWSS, and lowest maximum OSI and RRT appeared on the contralateral side.

Structural stress within arterial wall

The vessel structural stress was shown in Figure 7.2F. VSS is dependent on location (x, y, z) and time (t), that is, VSS=VSS(x, y, z, t). In this study, it was transformed into cylindrical coordinate system (r, θ, z). Both peak and mean values were used to characterise the structural loading, that is,

$$\begin{aligned} \text{Peak VSS} &= \max_{t}\left\{\max_{r}[\text{VSS}(r,\theta,z,t)]\right\} \\ \text{Mean VSS} &= \operatorname{mean}_{t}\left\{\max_{r}[\text{VSS}(r,\theta,z,t)]\right\} \end{aligned} \tag{7.7}$$

As shown in Figure 7.2F, both of Peak VSS and mean VSS were lowest between the sites of constriction and highest near the constriction points. Arteries on the contralateral had the lowest Peak VSS and Mean VSS. In the quantitative analysis of the three regions, these two structural stress reached their highest level in the region proximal to Constriction 1#, while Peak VSS and Mean VSS were moderate in the other two regions (Figure 5D&E).

7.3.3 Relations between local mechanical parameters and plaque features

In the region distal to Constriction 2#, both maximum OSI and RRT were associated with PAR significantly with ρ being 0.76 (p=0.040) and 0.81 (p=0.025), respectively. Moreover, both of them were also associated with the density of macrophage with ρ being 0.85 (p=0.012) and 0.83 (p=0.016), respectively. However, minimum TAWSS was not significantly correlated to neither PAR nor macrophage density. None of the flow parameters, including TAWW, OSI and RRT were associated with MWT or MTH. In the region proximal to Constriction 1#, none of the flow parameters were associated with PAR, MWT, MWH, or macrophage density.

On the contrary, Peak VSS was associated with PAR, MWT and macrophage density with ρ being 0.88 (p=0.003), 0.72 (p=0.037), and 0.70 (p=0.043), respectively. Mean VSS was associated with PAR and macrophage density with ρ being 0.80 (p=0.014) and 0.75 (p=0.025), respectively. However, none of the Peak VSS and Mean VSS were associated with any plaque feature in the region distal to Constriction 2#.

7.4 Discussion

To the authors' best knowledge, this is the first study to quantify the association between local mechanical loadings, including both WSS and VSS, and morphological and inflammatory features of atherosclerotic plaques, by deploying collars on rabbit carotid arteries to create two constrictions. Atherosclerotic plaques were found in the regions proximal to Constriction 1# and distal to Constriction 2#. Traditional WSS hypothesis could well explain the appearance of plaque in the region distal to Constriction 2# due to the turbulent flow. However, it failed for those found in the region proximal to Constriction 1#, where TAWSS was higher, and OSI and RRT were lower. Regression analysis demonstrated that high VSS associated well with lesion found in the region proximal to Constriction 1# (Figure 7.6). This study implied that both WSS and VSS could initialise atherosclerosis.

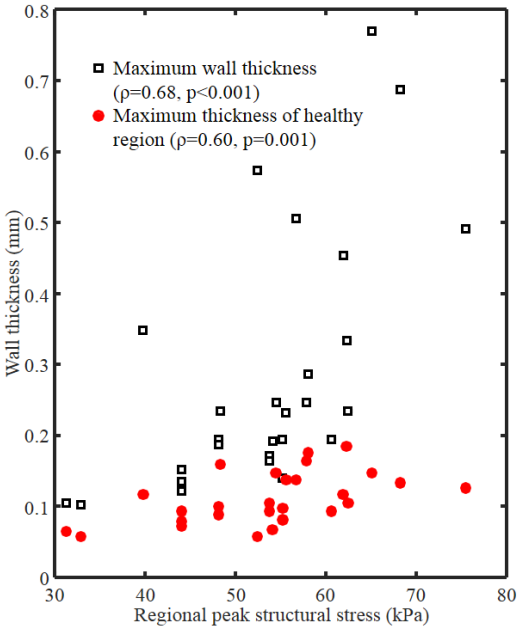

Figure 7.6 Wall thickness of both diseased and healthy section was associated with local vessel structural stress.

It has been reported that arteries tend to maintain a certain stress level within the wall by adjusting its thickness according to local intramural blood pressure [361,362]. Following this principle and Laplace's law (stress×thickness=pressure×radius), increased stress will stimulate wall thickening when pressure and radius remain constant, which is confirmed by this animal study. As shown in Figure 7.6 that VSS correlated very well with local wall thickness either at the location with plaque or free of plaque.

In general, previous studies on the biomechanics of atherosclerosis focused largely on the pathological effects of abnormal flow environment on the vascular physiology. In contrast, there is a lack of comprehensive studies aimed to understand the effects of structural stresses and stretches on the pathophysiology of the vessel wall. The preferable appearance of atherosclerotic plaque at the location with bifurcation or bend has been thought to be mainly due to malfunctioned WSS. However, high VSS also appears in these locations. Only fluid-structure interaction analysis can quantify WSS and VSS simultaneously. However, due to irregular wall geometry at these locations, nonlinear material properties and large deformations, it is challenging to obtain a successful FSI simulation due to convergence.

Perhaps this is one of the main reasons that major efforts have been spent on seeking the pathological impact of WSS, while the role of VSS has been ignored.

The physiological stretch of the vessel wall ranges between 5-10%, while high magnitudes of stretches more than 20% are considered pathological[363]. Physiological stretch is beneficial for regulating the normal cellular processes such as angiogenesis[364,365], cell proliferation[366] and extracellular matrix (ECM) remodelling[367]. In contrast, pathological stretches as observed in hypertension, could activate pathways leading to CVD. Although hypertension is often associated with excessive levels of WSS, it is also equally responsible for elevated levels of structural stress, particularly at arterial regions with a highly tortuous shape and at bifurcations [368]. Increased structural loadings are known to cause phenotypic adaptations in vascular smooth muscle cells that transform them to dedifferentiated states [341,349,369]. This indicates that, structural loading has the capacity to modulate gene expression, as well as various functions of the VSMCs, such as proliferation, survival and ECM remodelling [339]. *In vivo* experiments also demonstrated the role of pathological stretch in endothelial dysfunction and cell apoptosis[370]. Abnormal levels of stretch is known to promote expression of inflammatory genes, such as inducible nitric oxide synthase (iNOS) [371]. Pathological stretch was reported to promote pro-inflammatory response by cytokines (IL-8, IL-6) [372] and MCP-1[373], resulting in the accumulation of inflammatory cells. It was also reported that pathological stretch could disturb the integrity of ECM by activating macrophage cells to produce MMPs such as MMP-1, MMP-3 and MMP-9 [371,374,375].

Despite interesting finding in this study, there are several limitations: (1) The MRI sequences were susceptible to flow artefacts, which may induce error on the geometry reconstruction; (2) The FSI analysis did not consider residual stress within the arterial wall, which might overestimate the structural stress; (3) The computational model did not consider the biological reaction to the collar, which might also contribute to the inflammatory response.

7.5 Conclusion

In conclusion, this animal study confirmed the pathological role of structural stress induced by implanted device, which is associated with the arterial wall remodelling and inflammatory

response. Therefore, structural analysis is important for a comprehensive assessment of the biomechanical environment after the deployment of endovascular devices.

Chapter 8 Conclusion

The pathological development of AA is a chronic and multifactorial process, characterised by the structural degradation of ECM within the aortic wall. The microstructural changes lead to weakening material properties, associated with an increased risk of AA rupture. The stretch-stress curves from experimental tests can be parameterised into material constants of the hyperelastic model. Bayesian inference framework provides a robust estimation of these coefficients, reflecting the characteristics of tissue fibre network. The experimental results provide essential constitutive relations for a reliable assessment of the biomechanical factors.

Image-based FEA provides a non-invasive method to simulate the virtual deployment of MOUS and predict the flow modulation, which is useful for understanding the mechanism of MOUS and making personalised pre-surgical plans. The MOUS provides an efficiently-low porosity, which modulates the flow patterns in the aneurysm, promoting the aneurysm thrombosis and shrinkage. The patency of side branches is preserved, as the stent struts coverage has minimal effects on the flow rate. The flow-diverting outcome is dominated by the overall porosity, while the various overlapping patterns have limited influence, providing a robust performance of MOUS. However, structural stress concentrations appear within the landing zones after the deployment of multiple stents. The elevated structural loading might lead to inflammatory response within the aortic wall, along with adverse pathological effects. Computational analysis showed that a more compact design of MOUS could reduce the structural stress concentrations, which provides insight into the design optimisation of next generation MOUS. More investigations and long-term follow-up are essential before this novel technique can be widely applied into clinical practice.

8.1 Limitations

Despite the interesting findings presented in this dissertation, there remains a few limitations that merit discussion.

In the material tests, the uniaxial loading was applied, while biaxial loading conditions are more realistic in physiological conditions [285,376,377]. However, useful information can be still obtained from uniaxial tests with appropriate data interpretation [378]. The modified Mooney-Rivlin SEDF is an isotropic model, where the microstructure was not explicitly included. The information of fibre distribution can be integrated into the SEDF with additional terms [379].

The aneurysm model was reconstructed from CTA images, where the border between thrombus and vessel wall was not clear. A more accurate model could be established from MRA images with better soft-tissue contrast. In the computational analysis, the virtual deployment of MOUS was simulated in a quasi-static style followed by the CFD with fixed wall conditions. The residual stress was not considered as it cannot be measured using current non-invasive approaches [380]. The dynamic motion of stents after the deployment was not considered due to heavy computational cost. Flow rate waveform at the aortic inlet is adapted from literature, which could be replaced with patient-specific assessment, by *in vivo* measurement from Doppler ultrasound or PC-MRA [157,381]. The patient-specific simulation and parameter studies were based on a representative aneurysm model. The findings should be further validated in more patient-specific models using the developed framework.

8.2 Potential future directions

Future work should focus on addressing the limitations mentioned above, as well as translating the image-based biomechanical analysis into clinical practice.

The Bayesian framework can be extended to compare the performance of different constitutive models in describing the experimental data, and select the most suitable model [273]. This provides more flexibility and accuracy in modelling different types of diseased tissue. Given a large amount of samples, Bayesian hierarchical modelling can be used to describe the change

of mechanical behaviour during the disease process [382]. This could provide a tool to evaluate the uncertainty of material property and the influence on biomechanical analysis at a population level.

In addition to the pre-surgical planning, image-based biomechanical analysis could be also applied to real-time assessment during the intervention. The contrast concentration on the DSA images provides the information of the flow field, which has the potential to assess the haemodynamic environment within the aneurysm [383–385]. This could help surgeons to optimise the surgical plan using the real-time assessment.

Considering the possible structural stress concentrations within landing zones, the design optimisation is an essential step before MOUS is widely used. More compliant stents with better conformity to the aortic geometry should be preferred. On the other hand, the possible fretting corrosion between the struts of overlapping stents should be investigated, since it may enhance the incidence of stent rupture [114,386,387].

Appendix

Histology segmentation

A semi-automatic MATLAB platform was developed to segment the collagen and elastin fibres on PSR stained and EVG stained images respectively. The histology slice was scanned using a NanoZoomer (Hamamatsu Photonics, Japan) and digitalised to RGB images for segmentation. First, a ROI was manually drawn and the pixels outside the ROI were removed. Then the cropped image was transformed into L-a-b colour space. A threshold was automatically selected to remove the white background by applying the Otsu's method on the lightness channel [388,389]. Next, the threshold for segmenting collagen from PSR stained image was chosen by applying the Otsu's method on the green–red channel. The threshold for segmenting elastin from EVG stained image was chosen by applying the Otsu's method on the green channel. An example of collagen segmentation by using the platform was demonstrated in Figure 4.10.

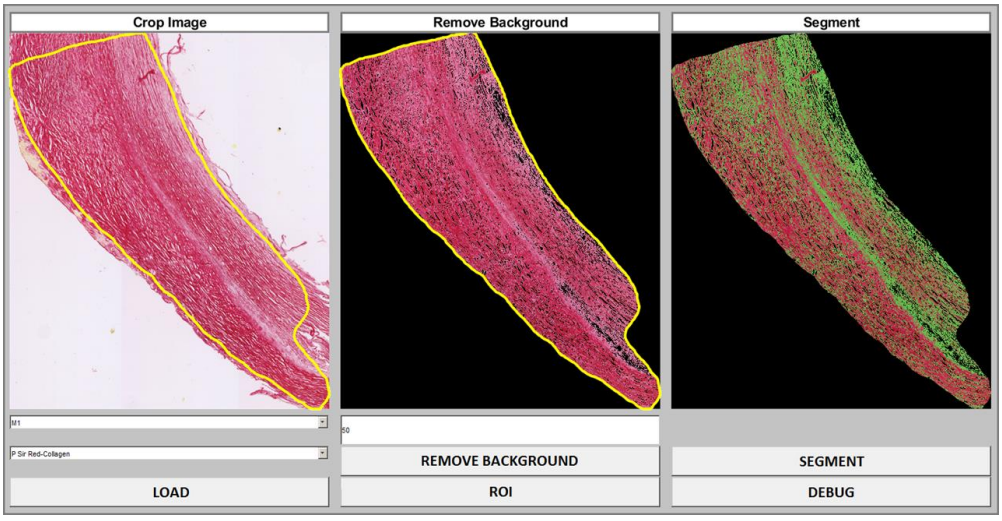

Figure S1 The semi-automatic MATLAB platform that was used to compute the densities of all microstructural components. Left is the raw image with a yellow ROI drawn manually. Middle is the image after removing the white background. Right is the image with a green label masking the background tissue.

The automatically segmented results of both PSR and EVG stained images were reviewed by NF, who has over 15 years of experience in histological analysis of diseased arterial tissues.

Quantification of component percentages

Based on above segmented results, the component percentage of each slice was computed as:

$$Component\ Area\ Percent = \frac{Number\ of\ Component\ Pixels}{Number\ of\ Pixels\ in\ the\ Tissue\ Region} \times 100\%$$

Quantification of waviness and dispersion of collagen fibres

Based on the segmented results from the PSR stained image, the waviness and dispersion were computed. Considering the heterogeneous distribution of collagen fibres, 16 square patches with 0.18 mm (200 pixels) in length were independently and randomly drawn in the ROI. The final waviness (ω) and dispersion (κ) of the overall image was computed as the average of results from the 16 patches. For each square patch, each disconnected collagen fibre was first recognised from the segmented mask.

The major axis length and perimeter of each fibre was calculated using the function *Regionprops* in Matlab. The waviness of each fibre is computed as:

$$Waviness\ = \frac{Perimeter}{2\ \times Major\ axis\ length} - 1$$

The dispersion of collagen fibres was computed by using the previously proposed algorithm[390]. The distribution of the collagen fibre orientations were characterised with the 2D planar form of the transversely isotropic and π-periodic von Misses distribution [391–393]. The von Misses distribution with a probability density function of orientation, $\rho(\theta)$ was assumed:

$$\rho(\theta) = 4\sqrt{\frac{b}{2\pi}\frac{\exp[b(\cos(2\theta)+1)]}{\mathrm{erfi}(\sqrt{2b})}}$$

where b is the concentration parameter and $\mathrm{erfi}(x)$ is the imaginary form of the error function, which were fitted from the orientations . The dispersion parameter κ was computed as:

$$\kappa = \frac{1}{4}\int_0^{180} \rho(\theta) sin^3\theta d\theta$$

The values of κ are between and including 0 and 1/3, where 0 means an isotropic distribution and 1/3 means a uniform distribution.

References

1. Antoniou, G. A., Antoniou, A. I., Antoniou, S. A. & Lazarides, M. K. A historical perspective of medical terminology of aortic aneurysm. *J. Vasc. Surg.* **54,** 1527–1528 (2011).
2. Johnston, K. W. *et al.* Suggested standards for reporting on arterial aneurysms. Subcommittee on Reporting Standards for Arterial Aneurysms, Ad Hoc Committee on Reporting Standards, Society for Vascular Surgery and North American Chapter, International Society for Cardiovascular. *J. Vasc. Surg. Off. Publ. Soc. Vasc. Surg. [and] Int. Soc. Cardiovasc. Surgery, North Am. Chapter* **13,** 452–458 (1991).
3. Pande, R. L. & Beckman, J. A. in *Vascular Medicine: A Companion to Braunwald's Heart Disease* (2012).
4. Seki, A. & Fishbein, M. C. *Cardiovascular pathology*. (2016).
5. Sakalihasan, N., Limet, R. & Defawe, O. D. Abdominal aortic aneurysm. *Lancet* **365,** 1577–89 (2005).
6. Benjamin, E. J. *et al.* Heart Disease and Stroke Statistics-2018 Update: A Report From the American Heart Association. *Circulation* **137,** e67–e492 (2018).
7. Global Burden of Disease Collaborative Network. Global Burden of Disease Study 2016 (GBD 2016). (2017). at <http://ghdx.healthdata.org/gbd-results-tool?params=gbd-api-2016-permalink/2bc7a572b39ce165b58d1d23a0114f58>
8. Zipes, D. P., Libby, P., Bonow, R. O., Mann, D. L. & Tomaselli, G. F. *Braunwald's Heart Disease E-Book: A Textbook of Cardiovascular Medicine*. (Elsevier Health Sciences, 2018).
9. Gasser, T. C., Ogden, R. W. & Holzapfel, G. a. Hyperelastic modelling of arterial layers with distributed collagen fibre orientations. *J. R. Soc. Interface* **3,** 15–35 (2006).
10. Collins, J. A., Munoz, J. V., Patel, T. R., Loukas, M. & Tubbs, R. S. The anatomy of the aging aorta. *Clin. Anat.* **27,** 463–466 (2014).
11. Shadwick, R. E. Mechanical design in arteries. *J. Exp. Biol.* **202,** 3305–13 (1999).
12. Greenwald, S. E., Moore, J. E., Rachev, A., Kane, T. P. & Meister, J. J. Experimental investigation of the distribution of residual strains in the artery wall. *J. Biomech. Eng.* **119,** 438–44 (1997).
13. Armentano, R. L. *et al.* Assessment of elastin and collagen contribution to aortic elasticity in conscious dogs. *Am. J. Physiol.* **260,** H1870-7 (1991).
14. Wolinsky, H. & Glagov, S. Comparison of abdominal and thoracic aortic medial structure in mammals. Deviation of man from the usual pattern. *Circ. Res.* **25,** 677–86 (1969).
15. Mitchell, G. F. *et al.* Changes in Arterial Stiffness and Wave Reflection With Advancing Age in Healthy Men and Women: The Framingham Heart Study. *Hypertension* **43,** 1239–1245 (2004).
16. O'Rourke, M. F. & Nichols, W. W. Aortic diameter, aortic stiffness, and wave reflection increase with age and isolated systolic hypertension. *Hypertension* **45,** 652–658 (2005).
17. Kohara, K. *et al.* Radial augmentation index: A useful and easily obtainable parameter for vascular aging. *Am. J. Hypertens.* **18,** 11–14 (2005).
18. Hickson, S. S. *et al.* The relationship of age with regional aortic stiffness and diameter. *JACC Cardiovasc. Imaging* **3,** 1247–1255 (2010).
19. Fritze, O. *et al.* Age-Related Changes in the Elastic Tissue of the Human Aorta. *J. Vasc. Res.* **49,** 77–86 (2012).
20. Campa, J. S., Greenhalgh, R. M. & Powell, J. T. Elastin degradation in abdominal aortic aneurysms. *Atherosclerosis* **65,** 13–21 (1987).
21. Cohen, J. R., Mandell, C., Chang, J. B. & Wise, L. Elastin metabolism of the infrarenal aorta. *J. Vasc. Surg.* **7,** 210–4 (1988).
22. Carmo, M. *et al.* Alteration of elastin, collagen and their cross-links in abdominal aortic aneurysms. *Eur. J. Vasc. Endovasc. Surg.* **23,** 543–9 (2002).

23. López-Candales, A. *et al.* Decreased vascular smooth muscle cell density in medial degeneration of human abdominal aortic aneurysms. *Am. J. Pathol.* **150,** 993–1007 (1997).
24. Absi, T. S. *et al.* Altered patterns of gene expression distinguishing ascending aortic aneurysms from abdominal aortic aneurysms: Complementary DNA expression profiling in the molecular characterization of aortic disease. *J. Thorac. Cardiovasc. Surg.* **126,** 344–357 (2003).
25. Visse, R. & Nagase, H. Matrix metalloproteinases and tissue inhibitors of metalloproteinases: Structure, function, and biochemistry. *Circ. Res.* **92,** 827–839 (2003).
26. Newman, K. M. *et al.* Matrix metalloproteinases in abdominal aortic aneurysm: characterization, purification, and their possible sources. *Connect. Tissue Res.* (1994).
27. Vine, N. & Powell, J. T. Metalloproteinases in degenerative aortic disease. *Clin. Sci.* **81,** 233–239 (1991).
28. Herron, G. S. *et al.* Connective tissue proteinases and inhibitors in abdominal aortic aneurysms. Involvement of the vasa vasorum in the pathogenesis of aortic aneurysms. *Arterioscler. Thromb. a J. Vasc. Biol.* **11,** 1667–77 (1991).
29. Davis, V. *et al.* Matrix metalloproteinase-2 production and its binding to the matrix are increased in abdominal aortic aneurysms. *Arterioscler. Thromb. Vasc. Biol.* **18,** 1625–33 (1998).
30. McMillan, W. D., Patterson, B. K., Keen, R. R. & Pearce, W. H. In situ localization and quantification of seventy-two-kilodalton type IV collagenase in aneurysmal, occlusive, and normal aorta. *J. Vasc. Surg.* **22,** 295–305 (1995).
31. Longo, G. M. *et al.* Matrix metalloproteinases 2 and 9 work in concert to produce aortic aneurysms. *J. Clin. Invest.* **110,** 625–32 (2002).
32. Petersen, E., Wågberg, F. & Ängquist, K. A. Proteolysis of the abdominal aortic aneurysm wall and the association with rupture. *Eur. J. Vasc. Endovasc. Surg.* **23,** 153–157 (2002).
33. Wilson, W. R. W. *et al.* Elevated plasma MMP1 and MMP9 are associated with abdominal aortic aneurysm rupture. *Eur. J. Vasc. Endovasc. Surg.* **35,** 580–4 (2008).
34. Defawe, O. D. *et al.* TIMP-2 and PAI-1 mRNA levels are lower in aneurysmal as compared to athero-occlusive abdominal aortas. *Cardiovasc. Res.* **60,** 205–13 (2003).
35. Rajagopalan, S., Meng, X. P., Ramasamy, S., Harrison, D. G. & Galis, Z. S. Reactive oxygen species produced by macrophage-derived foam cells regulate the activity of vascular matrix metalloproteinases in vitro. Implications for atherosclerotic plaque stability. *J. Clin. Invest.* **98,** 2572–9 (1996).
36. Liu, P., Sun, M. & Sader, S. Matrix metalloproteinases in cardiovascular disease. *Can. J. Cardiol.* **22 Suppl B,** 25B–30B (2006).
37. Dodd, B. R. & Spence, R. A. Doxycycline inhibition of abdominal aortic aneurysm growth: a systematic review of the literature. *Curr. Vasc. Pharmacol.* **9,** 471–8 (2011).
38. Brangsch, J. *et al.* Molecular Imaging of Abdominal Aortic Aneurysms. *Trends Mol. Med.* **23,** 150–164 (2017).
39. Libby, P. Inflammation in atherosclerosis. *Nature* **420,** 868–74 (2002).
40. Rose, A. G. & Dent, D. M. Inflammatory variant of abdominal atherosclerotic aneurysm. *Arch. Pathol. Lab. Med.* **105,** 409–13 (1981).
41. Satta, J. *et al.* Chronic inflammation and elastin degradation in abdominal aortic aneurysm disease: an immunohistochemical and electron microscopic study. *Eur. J. Vasc. Endovasc. Surg.* **15,** 313–9 (1998).
42. Golledge, A. L. V, Walker, P., Norman, P. E. & Golledge, J. A systematic review of studies examining inflammation associated cytokines in human abdominal aortic aneurysm samples. *Dis. Markers* **26,** 181–8 (2009).
43. Hellenthal, F. A. M. V. I., Buurman, W. A., Wodzig, W. K. W. H. & Schurink, G. W. H. Biomarkers of abdominal aortic aneurysm progression. Part 2: inflammation. *Nat. Rev. Cardiol.* **6,** 543–52 (2009).
44. Truijers, M., Kurvers, H. a J. M., Bredie, S. J. H., Oyen, W. J. G. & Blankensteijn, J. D. In vivo imaging of abdominal aortic aneurysms: increased FDG uptake suggests inflammation in the aneurysm wall. *J. Endovasc. Ther.* **15,** 462–7 (2008).
45. Treska, V. *et al.* Inflammation in the wall of abdominal aortic aneurysm and its role in the symptomatology of aneurysm. *Cytokines. Cell. Mol. Ther.* **7,** 91–7 (2002).
46. MacSweeney, S. T. R., Powell, J. T. & Greenhalgh, R. M. Pathogenesis of abdominal aortic aneurysm. *Br. J. Surg.* **81,** 935–41 (1994).

47. He, C. M. & Roach, M. R. The composition and mechanical properties of abdominal aortic aneurysms. *J. Vasc. Surg. Off. Publ. Soc. Vasc. Surg. [and] Int. Soc. Cardiovasc. Surgery, North Am. Chapter* **20,** 6–13 (1994).
48. Dobrin, P. B. & Mrkvicka, R. Failure of elastin or collagen as possible critical connective tissue alterations underlying aneurysmal dilatation. *Cardiovasc. Surg.* **2,** 484–8 (1994).
49. Boussel, L. *et al.* Aneurysm growth occurs at region of low wall shear stress: Patient-specific correlation of hemodynamics and growth in a longitudinal study. *Stroke* **39,** 2997–3002 (2008).
50. Tronc, F. *et al.* Role of matrix metalloproteinases in blood flow-induced arterial enlargement: interaction with NO. *Arter. Thromb Vasc Biol* **20,** E120-6 (2000).
51. Groenendijk, B. C. W. *et al.* Changes in shear stress-related gene expression after experimentally altered venous return in the chicken embryo. *Circ. Res.* **96,** 1291–1298 (2005).
52. Damberg, A., Ziganshin, B. A. & Elefteriades, J. A. in *New Approaches to Aortic Diseases from Valve to Abdominal Bifurcation* 129–131 (Elsevier, 2018).
53. Biasetti, J., Spazzini, P. G., Swedenborg, J. & Gasser, T. C. An integrated fluid-chemical model toward modeling the formation of intra-luminal thrombus in abdominal aortic aneurysms. *Front. Physiol.* **3,** 266 (2012).
54. Biasetti, J., Hussain, F. & Gasser, T. C. Blood flow and coherent vortices in the normal and aneurysmatic aortas: a fluid dynamical approach to intra-luminal thrombus formation. *J. R. Soc. Interface* **8,** 1449–1461 (2011).
55. Fung, Y. C. *Biomechanics:Motion, Flow, Stress, and Growth*. *Journal of Applied Mechanics* **60,** (Springer New York, 1990).
56. Asanuma, K., Magid, R., Johnson, C., Nerem, R. M. & Galis, Z. S. Uniaxial strain upregulates matrix-degrading enzymes produced by human vascular smooth muscle cells. *Am. J. Physiol. - Hear. Circ. Physiol.* **284,** H1778–H1784 (2003).
57. Ruddy, J. M. *et al.* Differential effects of mechanical and biological stimuli on matrix metalloproteinase promoter activation in the thoracic aorta. *Circulation* **120,** S262-8 (2009).
58. Krettek, A., Sukhova, G. K. & Libby, P. Elastogenesis in human arterial disease: a role for macrophages in disordered elastin synthesis. *Arterioscler. Thromb. Vasc. Biol.* **23,** 582–7 (2003).
59. Vorp, D. A. & Vande Geest, J. P. Biomechanical determinants of abdominal aortic aneurysm rupture. *Arterioscler. Thromb. Vasc. Biol.* **25,** 1558–1566 (2005).
60. Brewster, D. C. *et al.* Guidelines for the treatment of abdominal aortic aneurysms. Report of a subcommittee of the Joint Council of the American Association for Vascular Surgery and Society for Vascular Surgery. *J. Vasc. Surg.* **37,** 1106–17 (2003).
61. Elefteriades, J. A. Indications for aortic replacement. *J. Thorac. Cardiovasc. Surg.* **140,** S5–S9 (2010).
62. Erbel, R. *et al.* 2014 ESC guidelines on the diagnosis and treatment of aortic diseases. *Eur. Heart J.* **35,** 2873–2926 (2014).
63. United Kingdom EVAR Trial Investigators *et al.* Endovascular repair of aortic aneurysm in patients physically ineligible for open repair. *N. Engl. J. Med.* **362,** 1872–80 (2010).
64. Ouriel, K., Clair, D. G., Kent, K. C., Zarins, C. K. & Positive Impact of Endovascular Options for treating Aneurysms Early (PIVOTAL) Investigators. Endovascular repair compared with surveillance for patients with small abdominal aortic aneurysms. *J. Vasc. Surg.* **51,** 1081–7 (2010).
65. Cao, P. *et al.* Comparison of surveillance versus aortic endografting for small aneurysm repair (CAESAR): results from a randomised trial. *Eur. J. Vasc. Endovasc. Surg.* **41,** 13–25 (2011).
66. Lederle, F. A. *et al.* Immediate repair compared with surveillance of small abdominal aortic aneurysms. *N. Engl. J. Med.* **346,** 1437–44 (2002).
67. Mortality results for randomised controlled trial of early elective surgery or ultrasonographic surveillance for small abdominal aortic aneurysms. The UK Small Aneurysm Trial Participants. *Lancet (London, England)* **352,** 1649–55 (1998).
68. Davis, F. M., Rateri, D. L. & Daugherty, A. Mechanisms of aortic aneurysm formation: translating preclinical studies into clinical therapies. *Heart* **100,** 1498–1505 (2014).
69. Chaikof, E. L. *et al.* The care of patients with an abdominal aortic aneurysm: the Society for Vascular Surgery practice guidelines. *J. Vasc. Surg.* **50,** S2-49 (2009).
70. Kiru, G., Bicknell, C., Falaschetti, E., Powell, J. & Poulter, N. An evaluation of the effect of an angiotensin-converting enzyme inhibitor on the growth rate of small abdominal aortic aneurysms: a randomised placebo-controlled trial (AARDVARK). *Health Technol. Assess.* **20,** 1–180 (2016).

71. Dubost, C., Allary, M. & Oeconomos, N. Resection of an aneurysm of the abdominal aorta: reestablishment of the continuity by a preserved human arterial graft, with result after five months. *AMA. Arch. Surg.* **64,** 405–8 (1952).
72. Kannan, R. Y., Salacinski, H. J., Butler, P. E., Hamilton, G. & Seifalian, A. M. Current status of prosthetic bypass grafts: a review. *J. Biomed. Mater. Res. B. Appl. Biomater.* **74,** 570–81 (2005).
73. Kapadia, M. R., Popowich, D. A. & Kibbe, M. R. Modified prosthetic vascular conduits. *Circulation* **117,** 1873–82 (2008).
74. John F Eidt. Open surgical repair of abdominal aortic aneurysm. *UpToDate Inc.* (2018). at <http://www.uptodate.com>
75. Drury, D., Michaels, J. a., Jones, L. & Ayiku, L. Systematic review of recent evidence for the safety and efficacy of elective endovascular repair in the management of infrarenal abdominal aortic aneurysm. *Br. J. Surg.* **92,** 937–946 (2005).
76. Dick, F. *et al.* Endovascular suitability and outcome after open surgery for ruptured abdominal aortic aneurysm. *Br. J. Surg.* **99,** 940–7 (2012).
77. Bhattacharya, V. & Stansby, G. *Postgraduate Vascular Surgery: The Candidate's Guide to the FRCS*. (Cambridge University Press, 2011).
78. Volodos', N. L., Shekhanin, V. E., Karpovich, I. P., Troian, V. I. & Gur'ev, I. A. *A self-fixing synthetic blood vessel endoprosthesis*. *Vestnik khirurgii imeni I. I. Grekova* **137,** 123–125 (1986).
79. Parodi, J. C., Palmaz, J. C. & Barone, H. D. Transfemoral intraluminal graft implantation for abdominal aortic aneurysms. *Ann. Vasc. Surg.* **5,** 491–499 (1991).
80. Eisenack, M., Umscheid, T., Tessarek, J., Torsello, G. F. & Torsello, G. B. Percutaneous endovascular aortic aneurysm repair: a prospective evaluation of safety, efficiency, and risk factors. *J. Endovasc. Ther.* **16,** 708–713 (2009).
81. Schermerhorn, M. L. *et al.* Endovascular vs. Open Repair of Abdominal Aortic Aneurysms in the Medicare Population. *N. Engl. J. Med.* **358,** 464–474 (2008).
82. Epstein, D. *et al.* Long-term cost-effectiveness analysis of endovascular versus open repair for abdominal aortic aneurysm based on four randomized clinical trials. *Br. J. Surg.* **101,** 623–31 (2014).
83. Schumacher, H., Eckstein, H. H., Kallinowski, F. & Allenberg, J. R. Morphometry and classification in abdominal aortic aneurysms: patient selection for endovascular and open surgery. *Journal of endovascular surgery : the official journal of the International Society for Endovascular Surgery* **4,** 39–44 (1997).
84. Rampoldi, V. *et al.* Simple risk models to predict surgical mortality in acute type A aortic dissection: the International Registry of Acute Aortic Dissection score. *Ann. Thorac. Surg.* **83,** 55–61 (2007).
85. Zhang, Y. *et al.* Management of complicated aortic aneurysms using multiple overlapping uncovered stents: mid-term outcome from a cohort study. *Medicine (Baltimore).* **93,** e209 (2014).
86. Lu, Q. *et al.* Endovascular repair of ascending aortic dissection: A novel treatment option for patients judged unfit for direct surgical repair. *J. Am. Coll. Cardiol.* **61,** 1917–1924 (2013).
87. Eliason, J. L. & Upchurch, G. R. Endovascular abdominal aortic aneurysm repair. *Circulation* **117,** 1738–1744 (2008).
88. Abraha, I., Romagnoli, C., Montedori, A. & Cirocchi, R. Thoracic stent graft versus surgery for thoracic aneurysm. *Cochrane database Syst. Rev.* CD006796 (2013).
89. Cheng, D. *et al.* Endovascular aortic repair versus open surgical repair for descending thoracic aortic disease a systematic review and meta-analysis of comparative studies. *J. Am. Coll. Cardiol.* **55,** 986–1001 (2010).
90. Walsh, S. R. *et al.* Endovascular stenting versus open surgery for thoracic aortic disease: systematic review and meta-analysis of perioperative results. *J. Vasc. Surg.* **47,** 1094–1098 (2008).
91. Greenhalgh, R. M. *et al.* Comparison of endovascular aneurysm repair with open repair in patients with abdominal aortic aneurysm (EVAR trial 1), 30-day operative mortality results: randomised controlled trial. *Lancet (London, England)* **364,** 843–8 (2004).
92. United Kingdom EVAR Trial Investigators. Endovascular versus open repair of abdominal aortic aneurysm. *N. Engl. J. Med.* **362,** 1863–71 (2010).
93. Patel, R., Sweeting, M. J., Powell, J. T. & Greenhalgh, R. M. Endovascular versus open repair of abdominal aortic aneurysm in 15-years' follow-up of the UK endovascular aneurysm repair trial 1 (EVAR trial 1): a randomised controlled trial. *Lancet* **388,** 2366–2374 (2016).

94. EVAR trial participants. Endovascular aneurysm repair versus open repair in patients with abdominal aortic aneurysm (EVAR trial 1): randomised controlled trial. *Lancet (London, England)* **365,** 2179–86 (2005).
95. De Bruin, J. L. *et al.* Long-term outcome of open or endovascular repair of abdominal aortic aneurysm. *N. Engl. J. Med.* **362,** 1881–9 (2010).
96. Blankensteijn, J. D. *et al.* Two-year outcomes after conventional or endovascular repair of abdominal aortic aneurysms. *N. Engl. J. Med.* **352,** 2398–405 (2005).
97. Prinssen, M. *et al.* A randomized trial comparing conventional and endovascular repair of abdominal aortic aneurysms. *N. Engl. J. Med.* **351,** 1607–18 (2004).
98. Lederle, F. A. *et al.* Long-term comparison of endovascular and open repair of abdominal aortic aneurysm. *N. Engl. J. Med.* **367,** 1988–97 (2012).
99. Lederle, F. A. *et al.* Outcomes following endovascular vs open repair of abdominal aortic aneurysm: a randomized trial. *JAMA* **302,** 1535–42 (2009).
100. Becquemin, J.-P. *et al.* A randomized controlled trial of endovascular aneurysm repair versus open surgery for abdominal aortic aneurysms in low- to moderate-risk patients. *J. Vasc. Surg.* **53,** 1167–1173.e1 (2011).
101. Hirsch, A. T. *et al.* ACC/AHA 2005 Practice Guidelines for the management of patients with peripheral arterial disease (lower extremity, renal, mesenteric, and abdominal aortic): a collaborative report from the American Association for Vascular Surgery/Society for Vascular Sur. *Circulation* **113,** e463-654 (2006).
102. Keefer, A., Hislop, S., Singh, M. J., Gillespie, D. & Illig, K. A. The influence of aneurysm size on anatomic suitability for endovascular repair. *J. Vasc. Surg.* **52,** 873–7 (2010).
103. Etz, D. C. *et al.* Spinal cord ischemia in open and endovascular thoracoabdominal aortic aneurysm repair: new concepts. *J. Cardiovasc. Surg. (Torino).* **55,** 159–68 (2014).
104. Acher, C., Acher, C. W., Marks, E. & Wynn, M. Intraoperative neuroprotective interventions prevent spinal cord ischemia and injury in thoracic endovascular aortic repair. *J. Vasc. Surg.* **63,** 1458–65 (2016).
105. Buck, D. B., van Herwaarden, J. a, Schermerhorn, M. L. & Moll, F. L. Endovascular treatment of abdominal aortic aneurysms. *Nat. Rev. Cardiol.* **11,** 112–23 (2014).
106. Faruqi, R. M. *et al.* Endovascular repair of abdominal aortic aneurysm using a pararenal fenestrated stent-graft. *Journal of endovascular surgery : the official journal of the International Society for Endovascular Surgery* **6,** 354–358 (1999).
107. Bicknell, C. D. *et al.* Treatment of Complex Aneurysmal Disease with Fenestrated and Branched Stent Grafts. *Eur. J. Vasc. Endovasc. Surg.* **37,** 175–181 (2009).
108. Ziegler, P., Avgerinos, E. D., Umscheid, T., Perdikides, T. & Stelter, W. J. Fenestrated endografting for aortic aneurysm repair: a 7-year experience. *J. Endovasc. Ther.* **14,** 609–18 (2007).
109. Verhoeven, E. L. G. *et al.* Fenestrated stent grafting for short-necked and juxtarenal abdominal aortic aneurysm: an 8-year single-centre experience. *Eur. J. Vasc. Endovasc. Surg.* **39,** 529–36 (2010).
110. O'Neill, S. *et al.* A prospective analysis of fenestrated endovascular grafting: intermediate-term outcomes. *Eur. J. Vasc. Endovasc. Surg.* **32,** 115–23 (2006).
111. Greenberg, R. K., Haulon, S., O'Neill, S., Lyden, S. & Ouriel, K. Primary endovascular repair of juxtarenal aneurysms with fenestrated endovascular grafting. *Eur. J. Vasc. Endovasc. Surg.* **27,** 484–91 (2004).
112. Amiot, S. *et al.* Fenestrated endovascular grafting: the French multicentre experience. *Eur. J. Vasc. Endovasc. Surg.* **39,** 537–44 (2010).
113. Greenberg, R. K. *et al.* Intermediate results of a United States multicenter trial of fenestrated endograft repair for juxtarenal abdominal aortic aneurysms. *J. Vasc. Surg.* **50,** 730–737.e1 (2009).
114. Tambyraja, A. L. *et al.* Fenestrated aortic endografts for juxtarenal aortic aneurysm: medium term outcomes. *Eur. J. Vasc. Endovasc. Surg.* **42,** 54–8 (2011).
115. Administration, U. F. and D. Medical devices: device approvals and clearances. (2012). at <http://www.fda.gov/MedicalDevices/>
116. Katsargyris, A., Oikonomou, K., Klonaris, C., Töpel, I. & Verhoeven, E. L. G. Comparison of outcomes with open, fenestrated, and chimney graft repair of juxtarenal aneurysms: are we ready for a paradigm shift? *J. Endovasc. Ther.* **20,** 159–69 (2013).

117. Tolenaar, J. L. *et al.* The chimney graft, a systematic review. *Annals of Vascular Surgery* **26,** 1030–1038 (2012).
118. Moore, R., Hinojosa, C. a., O'Neill, S., Mastracci, T. M. & Cinà, C. S. Fenestrated endovascular grafts for juxtarenal aortic aneurysms: A step by step technical approach. *Catheter. Cardiovasc. Interv.* **69,** 554–571 (2007).
119. Geremia, G. & Haklin, M. Embolization of experimentally created aneurysms with a laser-activated detachable coil device. *Am. J. Neuroradiol.* **36,** 1223–1231 (1994).
120. Wang, D. H. J., Makaroun, M. S., Webster, M. W. & Vorp, D. a. Effect of intraluminal thrombus on wall stress in patient-specific models of abdominal aortic aneurysm. *J. Vasc. Surg. Off. Publ. Soc. Vasc. Surg. [and] Int. Soc. Cardiovasc. Surgery, North Am. Chapter* **36,** 598–604 (2002).
121. Debing, E., Aerden, D., Gallala, S., Vandenbroucke, F. & Van Den Brande, P. Stenting complex aorta aneurysms with the cardiatis multilayer flow modulator: First impressions. *European Journal of Vascular and Endovascular Surgery* **47,** 604–608 (2014).
122. Sultan, S., Hynes, N. & Sultan, M. When not to implant the multilayer flow modulator: lessons learned from application outside the indications for use in patients with thoracoabdominal pathologies. *J. Endovasc. Ther.* **21,** 96–112 (2014).
123. Ruffino, M. A. & Rabbia, C. TCT-5 Efficacy of Cardiatis Multilayer Flow Modulator in Peripheral and Visceral Aneurysms Repair: Italian Multicenter Registry Results at One Year Follow Up. *J. Am. Coll. Cardiol.* **60,** B1–B2 (2012).
124. Lazaris, A. M., Maheras, A. N. & Vasdekis, S. N. A multilayer stent in the aorta may not seal the aneurysm, thereby leading to rupture. *J. Vasc. Surg.* **56,** 829–31 (2012).
125. Ibrahim, W. *et al.* Early and midterm outcome of Multilayer Flow Modulator stent for complex aortic aneurysm treatment in Germany. *J. Vasc. Surg.* **68,** 956–964 (2018).
126. Lazaris, A. M., Maheras, A. N. & Vasdekis, S. N. A multilayer stent in the aorta may not seal the aneurysm, thereby leading to rupture. *J. Vasc. Surg.* **56,** 829–831 (2012).
127. Zhang, Y. X. *et al.* Endovascular management of pararenal aortic aneurysms with multiple overlapping uncovered stents. *J. Vasc. Surg.* **58,** 616–623 (2013).
128. Mettler, F. A. *Essentials of Radiology*. (Elsevier Health Sciences, 2013).
129. Sugawara, E. & Nikaido, H. *Radiology Fundamentals*. **58,** (Springer International Publishing, 2015).
130. Mettler, F. A., Huda, W., Yoshizumi, T. T. & Mahesh, M. Effective Doses in Radiology and Diagnostic Nuclear Medicine: A Catalog. *Radiology* **248,** 254–263 (2008).
131. Chang, L.-T. A Method for Attenuation Correction in Radionuclide Computed Tomography. *IEEE Trans. Nucl. Sci.* **25,** 638–643 (1978).
132. Weg, N., Scheer, M. R. & Gabor, M. P. Liver lesions: improved detection with dual-detector-array CT and routine 2.5-mm thin collimation. *Radiology* **209,** 417–26 (1998).
133. Dillon, E. H., van Leeuwen, M. S., Fernandez, M. A. & Mali, W. P. Spiral CT angiography. *AJR. Am. J. Roentgenol.* **160,** 1273–8 (1993).
134. Rubin, G. D. *et al.* Aorta and Iliac Arteries: Single versus Multiple Detector-Row Helical CT Angiography. *Radiology* **215,** 670–676 (2000).
135. Upchurch Jr, G. R. & Criado, E. *Aortic Aneurysms*. (Humana Press, 2009).
136. Diehm, N. *et al.* Automated software supported versus manual aorto-iliac diameter measurements in CT angiography of patients with abdominal aortic aneurysms: assessment of inter- and intraobserver variation. *Vasa.* **34,** 255–61 (2005).
137. Parker, M. V. *et al.* What imaging studies are necessary for abdominal aortic endograft sizing? A prospective blinded study using conventional computed tomography, aortography, and three-dimensional computed tomography. *J. Vasc. Surg.* **41,** 199–205 (2005).
138. Velazquez, O. C. *et al.* Decreased use of iliac extensions and reduced graft junctions with software-assisted centerline measurements in selection of endograft components for endovascular aneurysm repair. *J. Vasc. Surg.* **40,** 222–7 (2004).
139. Wolf, Y. G. *et al.* Changes in aneurysm volume after endovascular repair of abdominal aortic aneurysm. *J. Vasc. Surg.* **36,** 305–9 (2002).
140. Chaikof, E. L. *et al.* Identifying and grading factors that modify the outcome of endovascular aortic aneurysm repair. *J. Vasc. Surg.* **35,** 1061–6 (2002).

141. Wever, J. J., Blankensteijn, J. D., Broeders, I. A. M. . & Eikelboom, B. C. Length measurements of the aorta after endovascular abdominal aortic aneurysm repair. *Eur. J. Vasc. Endovasc. Surg.* **18,** 481–6 (1999).
142. Tillich, M. *et al.* Iliac arterial injuries after endovascular repair of abdominal aortic aneurysms: correlation with iliac curvature and diameter. *Radiology* **219,** 129–36 (2001).
143. Beebe, H. G. & Kritpracha, B. Computed tomography scanning for endograft planning: evolving toward three-dimensional, single source imaging. *Semin. Vasc. Surg.* **17,** 126–34 (2004).
144. Wever, J. J., Blankensteijn, J. D., Th M Mali, W. P. & Eikelboom, B. C. Maximal aneurysm diameter follow-up is inadequate after endovascular abdominal aortic aneurysm repair. *Eur. J. Vasc. Endovasc. Surg.* **20,** 177–82 (2000).
145. Prinssen, M., Verhoeven, E. L. G., Verhagen, H. J. M. & Blankensteijn, J. D. Decision-making in follow-up after endovascular aneurysm repair based on diameter and volume measurements: a blinded comparison. *Eur. J. Vasc. Endovasc. Surg.* **26,** 184–7 (2003).
146. Chaikof, E. L. *et al.* Reporting standards for endovascular aortic aneurysm repair. *J. Vasc. Surg.* **35,** 1048–60 (2002).
147. Jayalath, R. W., Jackson, P. & Golledge, J. Quantification of abdominal aortic calcification on CT. *Arterioscler. Thromb. Vasc. Biol.* **26,** 429–30 (2006).
148. Bowden, D. J., Aitken, S. R. I., Wilkinson, I. B. & Dixon, A. K. Interobserver variability in the measurement of abdominal aortic calcification using unenhanced CT. *Br. J. Radiol.* **82,** 69–72 (2009).
149. Jayalath, R. W., Mangan, S. H. & Golledge, J. Aortic Calcification. *Eur. J. Vasc. Endovasc. Surg.* **30,** 476–488 (2005).
150. Moll, F. L. *et al.* Management of abdominal aortic aneurysms clinical practice guidelines of the European society for vascular surgery. *Eur. J. Vasc. Endovasc. Surg.* **41,** (2011).
151. Esposito, A., Silvia, R., Papa, M. & Maschio, A. Del. *Thoraco-Abdominal Aorta*. *Thoraco-Abdominal Aorta* (Springer Milan, 2011).
152. Sadasivan, C. *et al.* Angiographic assessment of the performance of flow divertors to treat cerebral aneurysms. *Conf. Proc. ... Annu. Int. Conf. IEEE Eng. Med. Biol. Soc. IEEE Eng. Med. Biol. Soc. Annu. Conf.* **1,** 3210–3 (2006).
153. Kwan, E. S. K., Hall, A. & Enzmann, D. R. Quantitative analysis of intracranial circulation using rapid-sequence DSA. *Am. J. Roentgenol.* **146,** 1239–1245 (1986).
154. Pereira, V. M. *et al.* Quantification of internal carotid artery flow with digital subtraction angiography: validation of an optical flow approach with Doppler ultrasound. *AJNR. Am. J. Neuroradiol.* **35,** 156–63 (2014).
155. Evangelista, A. Imaging aortic aneurysmal disease. *Heart* **100,** 909–915 (2014).
156. Prager, R. W., Ijaz, U. Z., Gee, A. H. & Treece, G. M. Three-dimensional ultrasound imaging. *Proc. Inst. Mech. Eng. Part H J. Eng. Med.* **224,** 193–223 (2010).
157. Battaglia, S., Danesino, G. M., Danesino, V. & Castellani, S. Color Doppler ultrasonography of the abdominal aorta. *J. Ultrasound* **13,** 107–117 (2010).
158. Rudarakanchana, N. & Powell, J. T. Advances in imaging and surveillance of AAA: When, how, how often? *Prog. Cardiovasc. Dis.* **56,** 7–12 (2013).
159. Harrison, G. J. *et al.* Surveillance after EVAR based on duplex ultrasound and abdominal radiography. *Eur. J. Vasc. Endovasc. Surg.* **42,** 187–192 (2011).
160. van Essen, J. a. *et al.* Intravascular ultrasonography allows accurate assessment of abdominal aortic aneurysm: An in vitro validation study. *J. Vasc. Surg.* **27,** 347–353 (1998).
161. Lee, J. T. & White, R. a. Basics of intravascular ultrasound: An essential tool for the endovascular surgeon. *Seminars in Vascular Surgery* **17,** 110–118 (2004).
162. Jacobs, M. A., Ibrahim, T. S. & Ouwerkerk, R. AAPM/RSNA physics tutorials for residents: MR imaging: brief overview and emerging applications. *Radiographics* **27,** 1213–29 (2007).
163. Pooley, R. A. AAPM/RSNA physics tutorial for residents: fundamental physics of MR imaging. *Radiographics* **25,** 1087–99 (2005).
164. Bitar, R. *et al.* MR Pulse Sequences: What Every Radiologist Wants to Know but Is Afraid to Ask. *RadioGraphics* **26,** 513–537 (2006).
165. Castrucci, M. *et al.* Mural thrombi in abdominal aortic aneurysms: MR imaging characterization--useful before endovascular treatment? *Radiology* **197,** 135–9 (1995).

166. Roy, J. *et al.* Bleeding into the intraluminal thrombus in abdominal aortic aneurysms is associated with rupture. *J. Vasc. Surg.* **48,** 1108–13 (2008).
167. Lorelli, D. R. *et al.* Response of plasma matrix metalloproteinase-9 to conventional abdominal aortic aneurysm repair or endovascular exclusion: implications for endoleak. *J. Vasc. Surg.* **35,** 916–22 (2002).
168. De La Motte, L. *et al.* Categorization of aortic aneurysm thrombus morphology by magnetic resonance imaging. *Eur. J. Radiol.* **82,** e544–e549 (2013).
169. Morita, S. *et al.* Unenhanced MR angiography: techniques and clinical applications in patients with chronic kidney disease. *Radiographics* **31,** E13-33 (2011).
170. Simonetti, O. P., Finn, J. P., White, R. D., Laub, G. & Henry, D. A. 'Black blood' T2-weighted inversion-recovery MR imaging of the heart. *Radiology* **199,** 49–57 (1996).
171. Zhu, C. *et al.* Isotropic 3D black blood MRI of abdominal aortic aneurysm wall and intraluminal thrombus. *Magn. Reson. Imaging* **34,** 18–25 (2016).
172. Zhu, C. *et al.* Non-contrast 3D black blood MRI for abdominal aortic aneurysm surveillance: comparison with CT angiography. *Eur. Radiol.* **27,** 1787–1794 (2017).
173. Nguyen, V. L. *et al.* Abdominal aortic aneurysms with high thrombus signal intensity on magnetic resonance imaging are associated with high growth rate. *Eur. J. Vasc. Endovasc. Surg.* **48,** 676–684 (2014).
174. Mihai, G. *et al.* Initial feasibility of a multi-station high resolution three-dimensional dark blood angiography protocol for the assessment of peripheral arterial disease. *J. Magn. Reson. Imaging* **30,** 785–93 (2009).
175. Nastri, M. V *et al.* Gadolinium-enhanced three-dimensional MR angiography of Takayasu arteritis. *Radiographics* **24,** 773–86
176. Richards, J. M. J. *et al.* Abdominal aortic aneurysm growth predicted by uptake of ultrasmall superparamagnetic particles of iron oxide: a pilot study. *Circ. Cardiovasc. Imaging* **4,** 274–81 (2011).
177. Dumoulin, C. L. & Hart, H. R. Magnetic resonance angiography. *Radiology* **161,** 717–20 (1986).
178. Prince, M. R. Gadolinium-enhanced MR aortography. *Radiology* **191,** 155–64 (1994).
179. Xu, J. *et al.* Single breathhold noncontrast thoracic MRA using highly accelerated parallel imaging with a 32-element coil array. *J. Magn. Reson. Imaging* **35,** 963–968 (2012).
180. Barth, M. M., Smith, M. P., Pedrosa, I., Lenkinski, R. E. & Rofsky, N. M. Body MR imaging at 3.0 T: understanding the opportunities and challenges. *Radiographics* **27,** 1445-62; discussion 1462–4
181. Huang, B. Y. & Castillo, M. Neurovascular imaging at 1.5 tesla versus 3.0 tesla. *Magn. Reson. Imaging Clin. N. Am.* **17,** 29–46 (2009).
182. Habibi, R. *et al.* High-spatial-resolution lower extremity MR angiography at 3.0 T: contrast agent dose comparison study. *Radiology* **248,** 680–92 (2008).
183. Park, C.-A., Kang, C.-K., Kim, Y.-B. & Cho, Z.-H. Advances in MR angiography with 7T MRI: From microvascular imaging to functional angiography. *Neuroimage* **168,** 269–278 (2018).
184. Grobner, T. Gadolinium – a specific trigger for the development of nephrogenic fibrosing dermopathy and nephrogenic systemic fibrosis? *Nephrol. Dial. Transplant.* **21,** 1104–1108 (2006).
185. Murata, N. *et al.* Macrocyclic and Other Non-Group 1 Gadolinium Contrast Agents Deposit Low Levels of Gadolinium in Brain and Bone Tissue: Preliminary Results From 9 Patients With Normal Renal Function. *Invest. Radiol.* **51,** 447–53 (2016).
186. Kanda, T. *et al.* Gadolinium-based Contrast Agent Accumulates in the Brain Even in Subjects without Severe Renal Dysfunction: Evaluation of Autopsy Brain Specimens with Inductively Coupled Plasma Mass Spectroscopy. *Radiology* **276,** 228–232 (2015).
187. McDonald, R. J. *et al.* Intracranial Gadolinium Deposition after Contrast-enhanced MR Imaging. *Radiology* **275,** 772–782 (2015).
188. European Medicines Agency. EMA's final opinion confirms restrictions on use of linear gadolinium agents in body scans. (2017). at <http://www.ema.europa.eu/docs/en_GB/document_library/Press_release/2017/07/WC500231829.pdf>
189. Said, Z. H. & Lerakis, S. The role of magnetic resonance angiography in peripheral artery disease. *Curr. Opin. Pharmacol.* **39,** 129–133 (2018).
190. Young, P. & Brinjikji, W. Update on state of the art magnetic resonance angiography techniques. *J. Vasc. Diagnostics* **Volume 3,** 9 (2015).
191. Miyazaki, M. & Lee, V. S. Nonenhanced MR Angiography. *Radiology* **248,** 20–43 (2008).

192. Özsarlak, Ö., Van Goethem, J. W., Maes, M. & Parizel, P. M. MR angiography of the intracranial vessels: technical aspects and clinical applications. *Neuroradiology* **46,** 955–972 (2004).
193. de Haan, M. W. *et al.* Renovascular disease in patients with hypertension: detection with systolic and diastolic gating in three-dimensional, phase-contrast MR angiography. *Radiology* **198,** 449–456 (1996).
194. Scheffler, K. & Lehnhardt, S. Principles and applications of balanced SSFP techniques. *Eur. Radiol.* **13,** 2409–2418 (2003).
195. Fuchs, F., Laub, G. & Othomo, K. TrueFISP—technical considerations and cardiovascular applications. *Eur. J. Radiol.* **46,** 28–32 (2003).
196. Hartung, M. P., Grist, T. M. & François, C. J. Magnetic resonance angiography: current status and future directions. *J. Cardiovasc. Magn. Reson.* **13,** 19 (2011).
197. Sakalihasan, N., Hustinx, R. & Limet, R. Contribution of PET scanning to the evaluation of abdominal aortic aneurysm. *Semin. Vasc. Surg.* **17,** 144–153 (2004).
198. Phelps, M. E. PET: the merging of biology and imaging into molecular imaging. *J. Nucl. Med.* **41,** 661–81 (2000).
199. Gambhir, S. S. Molecular imaging of cancer with positron emission tomography. *Nat. Rev. Cancer* **2,** 683–693 (2002).
200. Beyer, T. *et al.* A combined PET/CT scanner for clinical oncology. *J Nucl Med* **41,** 1369–1379 (2000).
201. Drzezga, A. *et al.* First Clinical Experience with Integrated Whole-Body PET/MR: Comparison to PET/CT in Patients with Oncologic Diagnoses. *J. Nucl. Med.* **53,** 845–855 (2012).
202. English, S. J. *et al.* Increased 18F-FDG Uptake Is Predictive of Rupture in a Novel Rat Abdominal Aortic Aneurysm Rupture Model. *Ann. Surg.* **261,** 395–404 (2015).
203. Sarda-Mantel, L. *et al.* Comparison of 18F-fluoro-deoxy-glucose, 18F-fluoro-methyl-choline, and 18F-DPA714 for positron-emission tomography imaging of leukocyte accumulation in the aortic wall of experimental abdominal aneurysms. *J. Vasc. Surg.* **56,** 765–773 (2012).
204. Jalalzadeh, H. *et al.* Inflammation as a predictor of abdominal aortic aneurysm growth and rupture: a systematic review of imaging biomarkers. *Eur. J. Vasc. Endovasc. Surg.* **52,** 333–42 (2016).
205. Huang, Y. *et al.* High structural stress and presence of intraluminal thrombus predict abdominal aortic aneurysm 18F-FDG uptake: insights from biomechanics. *Circ. Cardiovasc. Imaging* **9,** (2016).
206. Brooks, P., Clark, R. & Cheresh, D. Requirement of vascular integrin alpha v beta 3 for angiogenesis. *Science (80-.).* **264,** 569–571 (1994).
207. Kitagawa, T. *et al.* Integrin-targeted molecular imaging of experimental abdominal aortic aneurysms by 18F-labeled Arg-Gly-Asp positron-emission tomography. *Circ. Cardiovasc. Imaging* **6,** 950–956 (2013).
208. Hiratzka, L. F. *et al.* 2010 ACCF/AHA/AATS/ACR/ASA/SCA/SCAI/SIR/STS/SVM Guidelines for the Diagnosis and Management of Patients With Thoracic Aortic Disease. *J. Am. Coll. Cardiol.* **55,** e27–e129 (2010).
209. Fatimi, S. H., Panni, R. Z. & Ashfaq, A. Incidental finding of a giant aortic root aneurysm and its repair. *J. Pak. Med. Assoc.* **62,** 617–9 (2012).
210. Bicknell, C. D. & Powell, J. T. Thoracic aortic aneurysms. *Br. J. Surg.* **100,** 850–2 (2013).
211. Melville, H. & Costello, J. Significant coincidence. *Emerg. Med. J.* **29,** 414 (2012).
212. Lanitis, S. *et al.* Incidental findings in trauma patients during focused assessment with sonography for trauma. *Am. Surg.* **78,** 366–72 (2012).
213. van Walraven, C. *et al.* The influence of incidental abdominal aortic aneurysm monitoring on patient outcomes. *J. Vasc. Surg.* **54,** 1290–1297.e2 (2011).
214. van Walraven, C. *et al.* Incidence, follow-up, and outcomes of incidental abdominal aortic aneurysms. *J. Vasc. Surg.* **52,** 282-9.e1–2 (2010).
215. Beeman, B. R. *et al.* Duplex ultrasound factors predicting persistent type II endoleak and increasing AAA sac diameter after EVAR. *J. Vasc. Surg.* **52,** 1147–1152 (2010).
216. Wilmink, a B. M., Forshaw, M., Quick, C. R. G., Hubbard, C. S. & Day, N. E. Accuracy of serial screening for abdominal aortic aneurysms by ultrasound. *J. Med. Screen.* **9,** 125–127 (2002).
217. Lederle, F. A. *et al.* Variability in measurement of abdominal aortic aneurysms. Abdominal Aortic Aneurysm Detection and Management Veterans Administration Cooperative Study Group. *J. Vasc. Surg.* **21,** 945–52 (1995).
218. Takagi, H., Goto, S., Matsui, M., Manabe, H. & Umemoto, T. A further meta-analysis of population-based screening for abdominal aortic aneurysm. *J. Vasc. Surg.* **52,** 1103–8 (2010).

219. Ali, M. U. *et al.* Screening for abdominal aortic aneurysm in asymptomatic adults. *J. Vasc. Surg.* **64,** 1855–1868 (2016).
220. Guirguis-Blake, J. M., Beil, T. L., Senger, C. A. & Whitlock, E. P. Ultrasonography screening for abdominal aortic aneurysms: a systematic evidence review for the U.S. Preventive Services Task Force. *Ann. Intern. Med.* **160,** 321–9 (2014).
221. Cosford, P. A. & Leng, G. C. Screening for abdominal aortic aneurysm. *Cochrane database Syst. Rev.* CD002945 (2007).
222. Filardo, G., Powell, J. T., Martinez, M. A.-M. & Ballard, D. J. Surgery for small asymptomatic abdominal aortic aneurysms. *Cochrane database Syst. Rev.* CD001835 (2012).
223. Chaikof, E. L. *et al.* The Society for Vascular Surgery practice guidelines on the care of patients with an abdominal aortic aneurysm. *J. Vasc. Surg.* **67,** 2–77.e2 (2018).
224. Sadek, M. *et al.* Use of preoperative magnetic resonance angiography and the Artis zeego fusion program to minimize contrast during endovascular repair of an iliac artery aneurysm. *Ann. Vasc. Surg.* **28,** 261.e1-261.e5 (2014).
225. Stangenberg, L. *et al.* A novel tool for three-dimensional roadmapping reduces radiation exposure and contrast agent dose in complex endovascular interventions. *J. Vasc. Surg.* **62,** 448–455 (2015).
226. Sun, Z. Helical CT angiography of fenestrated stent grafting of abdominal aortic aneurysms. *Biomed. Imaging Interv. J.* **5,** 1–9 (2009).
227. Rydberg, J. *et al.* Endovascular repair of abdominal aortic aneurysms: assessment with multislice CT. *AJR. Am. J. Roentgenol.* **177,** 607–614 (2001).
228. Sato, D. T. *et al.* Endoleak after aortic stent graft repair: diagnosis by color duplex ultrasound scan versus computed tomography scan. *J. Vasc. Surg.* **28,** 657–63 (1998).
229. McWilliams, R. G. *et al.* Detection of endoleak with enhanced ultrasound imaging: comparison with biphasic computed tomography. *J. Endovasc. Ther.* **9,** 170–9 (2002).
230. Wolf, Y. G. *et al.* Duplex ultrasound scanning versus computed tomographic angiography for postoperative evaluation of endovascular abdominal aortic aneurysm repair. *J. Vasc. Surg.* **32,** 1142–8 (2000).
231. Zaiem, F. *et al.* A systematic review of surveillance after endovascular aortic repair. *J. Vasc. Surg.* **67,** 320–331.e37 (2018).
232. Fung, Y.-C. *Biomechanics: Mechanical Properties of Living Tissues*. (Springer New York, 1993).
233. Fung, Y. C. *Biomechanics*. (Springer New York, 1997).
234. Administration, U. S. F. and D. Non-clinical tests and recommended labeling for intravascular stents and associated delivery systems: guidance for industry and FDA staff. US Department of Health and Human Services. *Food Drug Adm. Cent. Devices Radiol. Heal. January* **13,** (2005).
235. Bathe, K.-J. *Finite element procedures*. (Klaus-Jurgen Bathe, 2006).
236. Gee, M. W., Reeps, C., Eckstein, H. H. & Wall, W. a. Prestressing in finite deformation abdominal aortic aneurysm simulation. *J. Biomech.* **42,** 1732–1739 (2009).
237. Raghavan, M. L., Ma, B. & Fillinger, M. F. Non-invasive determination of zero-pressure geometry of arterial aneurysms. *Ann. Biomed. Eng.* **34,** 1414–1419 (2006).
238. World Health Organization. *World health statistics 2017: monitoring health for the SDGs, Sustainable Development Goals.* (2017).
239. Sugawara, E. & Nikaido, H. Properties of AdeABC and AdeIJK efflux systems of Acinetobacter baumannii compared with those of the AcrAB-TolC system of Escherichia coli. *Antimicrob. Agents Chemother.* **58,** 7250–7 (2014).
240. Nordon, I. M., Hinchliffe, R. J., Loftus, I. M. & Thompson, M. M. Pathophysiology and epidemiology of abdominal aortic aneurysms. *Nat. Rev. Cardiol.* **8,** 92–102 (2011).
241. Pearce, W. H., Zarins, C. K., Bacharach, J. M. & American Heart Association Writing Group 6. Atherosclerotic Peripheral Vascular Disease Symposium II: controversies in abdominal aortic aneurysm repair. *Circulation* **118,** 2860–3 (2008).
242. North American Symptomatic Carotid Endarterectomy Trial Collaborators *et al.* Beneficial effect of carotid endarterectomy in symptomatic patients with high-grade carotid stenosis. *N. Engl. J. Med.* **325,** 445–53 (1991).
243. Nicholls, S. C., Gardner, J. B., Meissner, M. H. & Johansen, H. K. Rupture in small abdominal aortic aneurysms. *J. Vasc. Surg.* (1998).

244. Powell, J. T., Brown, L. C., Greenhalgh, R. M. & Thompson, S. G. The rupture rate of large abdominal aortic aneurysms: is this modified by anatomical suitability for endovascular repair? *Ann. Surg.* **247,** 173–9 (2008).
245. Vallabhaneni, S. R. *et al.* Heterogeneity of tensile strength and matrix metalloproteinase activity in the wall of abdominal aortic aneurysms. *J. Endovasc. Ther.* **11,** 494–502 (2004).
246. Cummins, P. M. *et al.* Cyclic strain-mediated matrix metalloproteinase regulation within the vascular endothelium: a force to be reckoned with. *Am. J. Physiol. Heart Circ. Physiol.* **292,** H28-42 (2007).
247. Maier, A. *et al.* Correlation of biomechanics to tissue reaction in aortic aneurysms assessed by finite elements and [18F]-fluorodeoxyglucose-PET/CT. *Int. j. numer. method. biomed. eng.* **28,** 456–71 (2012).
248. Stevens, R. R. F. *et al.* Biomechanical changes during abdominal aortic aneurysm growth. *PLoS One* **12,** e0187421 (2017).
249. Thondapu, V. *et al.* Basic science for the clinician: Biomechanical stress in coronary atherosclerosis: Emerging insights from computational modelling. *European Heart Journal* (2017).
250. Tuenter, A. *et al.* High shear stress relates to intraplaque haemorrhage in asymptomatic carotid plaques. *Atherosclerosis* **251,** 348–354 (2016).
251. Teng, Z. *et al.* Material properties of components in human carotid atherosclerotic plaques: a uniaxial extension study. *Acta Biomater.* **10,** 5055–5063 (2014).
252. Teng, Z. *et al.* The influence of constitutive law choice used to characterise atherosclerotic tissue material properties on computing stress values in human carotid plaques. *J. Biomech.* **48,** 3912–21 (2015).
253. Lee, R. T., Schoen, F. J., Loree, H. M., Lark, M. W. & Libby, P. Circumferential stress and matrix metalloproteinase 1 in human coronary atherosclerosis. Implications for plaque rupture. *Arterioscler. Thromb. Vasc. Biol.* **16,** 1070–3 (1996).
254. Akyildiz, A. C. *et al.* Effects of intima stiffness and plaque morphology on peak cap stress. *Biomed. Eng. Online* **10,** 25 (2011).
255. Ohayon, J. & Tracqui, P. Computation of adherent cell elasticity for critical cell-bead geometry in magnetic twisting experiments. *Ann. Biomed. Eng.* **33,** 131–41 (2005).
256. Caille, N., Thoumine, O., Tardy, Y. & Meister, J.-J. Contribution of the nucleus to the mechanical properties of endothelial cells. *J. Biomech.* **35,** 177–87 (2002).
257. Barrett, S. R. H., Sutcliffe, M. P. F., Howarth, S., Li, Z.-Y. & Gillard, J. H. Experimental measurement of the mechanical properties of carotid atherothrombotic plaque fibrous cap. *J. Biomech.* **42,** 1650–5 (2009).
258. Li, Z.-Y. *et al.* Stress analysis of carotid plaque rupture based on in vivo high resolution MRI. *J. Biomech.* **39,** 2611–22 (2006).
259. Tang, T. Y. *et al.* Correlation of carotid atheromatous plaque inflammation with biomechanical stress: utility of USPIO enhanced MR imaging and finite element analysis. *Atherosclerosis* **196,** 879–87 (2008).
260. Li, Z.-Y. *et al.* Structural analysis and magnetic resonance imaging predict plaque vulnerability: a study comparing symptomatic and asymptomatic individuals. *J. Vasc. Surg.* **45,** 768–75 (2007).
261. Versluis, A., Bank, A. J. & Douglas, W. H. Fatigue and plaque rupture in myocardial infarction. *J. Biomech.* **39,** 339–47 (2006).
262. Lawlor, M. G., O'Donnell, M. R., O'Connell, B. M. & Walsh, M. T. Experimental determination of circumferential properties of fresh carotid artery plaques. *J. Biomech.* **44,** 1709–15 (2011).
263. Cunnane, E. M., Mulvihill, J. J. E., Barrett, H. E. & Walsh, M. T. Simulation of human atherosclerotic femoral plaque tissue: the influence of plaque material model on numerical results. *Biomed. Eng. Online* **14 Suppl 1,** S7 (2015).
264. Maher, E. *et al.* Tensile and compressive properties of fresh human carotid atherosclerotic plaques. *J. Biomech.* **42,** 2760–7 (2009).
265. Gao, H. & Long, Q. Effects of varied lipid core volume and fibrous cap thickness on stress distribution in carotid arterial plaques. *J. Biomech.* (2008).
266. Kaazempur-Mofrad, M. R. *et al.* Cyclic strain in human carotid bifurcation and its potential correlation to atherogenesis: Idealized and anatomically-realistic models. *J. Eng. Math.* **47,** 299–314 (2003).
267. Chau, A. H. *et al.* Mechanical analysis of atherosclerotic plaques based on optical coherence tomography. *Ann. Biomed. Eng.* **32,** 1494–503 (2004).

268. Delfino, a, Stergiopulos, N., Moore, J. E. & Meister, J. J. Residual strain effects on the stress field in a thick wall finite element model of the human carotid bifurcation. *J. Biomech.* **30,** 777–86 (1997).
269. Tang, D. *et al.* Correlations between carotid plaque progression and mechanical stresses change sign over time: a patient follow up study using MRI and 3D FSI models. *Biomed. Eng. Online* **12,** 105 (2013).
270. Tang, D. *et al.* Sites of rupture in human atherosclerotic carotid plaques are associated with high structural stresses: an in vivo MRI-based 3D fluid-structure interaction study. *Stroke* **40,** 3258–63 (2009).
271. Zhongzhao Teng *et al.* How does juxtaluminal calcium affect critical mechanical conditions in carotid atherosclerotic plaque? An exploratory study. *IEEE Trans. Biomed. Eng.* **61,** 35–40 (2014).
272. Teng, Z. *et al.* Layer- and direction-specific material properties, extreme extensibility and ultimate material strength of human abdominal aorta and aneurysm: a uniaxial extension study. *Ann. Biomed. Eng.* **43,** 2745–59 (2015).
273. Madireddy, S., Sista, B. & Vemaganti, K. Bayesian calibration of hyperelastic constitutive models of soft tissue. *J. Mech. Behav. Biomed. Mater.* **59,** 108–127 (2016).
274. Madireddy, S., Sista, B. & Vemaganti, K. Bayesian calibration of hyperelastic constitutive models of soft tissue. *J. Mech. Behav. Biomed. Mater.* **59,** 108–127 (2016).
275. Doraiswamy, S., Criscione, J. C. & Srinivasa, A. R. A technique for the classification of tissues by combining mechanics based models with Bayesian inference. *Int. J. Eng. Sci.* **106,** 95–109 (2016).
276. Adina. Instability of Two-Term Mooney-Rivlin Model. (2009). at <http://www.adina.com/newsgH48.shtml>
277. Ogden, R. W. in *Biomechanics of Soft Tissue in Cardiovascular Systems* 65–108 (Springer Vienna, 2003).
278. Clark, J. M. & Glagov, S. Transmural organization of the arterial media. The lamellar unit revisited. *Arteriosclerosis* **5,** 19–34 (1985).
279. Wolinsky, H. & Glagove, S. Structural basis for the static mechanical properties of the aortic media. *Circ. Res.* **14,** 400–13 (1964).
280. Tamarina, N. A., McMillan, W. D., Shively, V. P. & Pearce, W. H. Expression of matrix metalloproteinases and their inhibitors in aneurysms and normal aorta. *Surgery* **122,** 264-71; discussion 271–2 (1997).
281. Li, Z., Froehlich, J., Galis, Z. S. & Lakatta, E. G. Increased expression of matrix metalloproteinase-2 in the thickened intima of aged rats. *Hypertens. (Dallas, Tex. 1979)* **33,** 116–23 (1999).
282. Bank, A. J. *et al.* Contribution of collagen, elastin, and smooth muscle to in vivo human brachial artery wall stress and elastic modulus. *Circulation* **94,** 3263–70 (1996).
283. Hill, M. R., Duan, X., Gibson, G. A., Watkins, S. & Robertson, A. M. A theoretical and non-destructive experimental approach for direct inclusion of measured collagen orientation and recruitment into mechanical models of the artery wall. *J. Biomech.* (2012).
284. Sacks, M. S. Incorporation of experimentally-derived fiber orientation into a structural constitutive model for planar collagenous tissues. *J. Biomech. Eng.* (2003).
285. Chen, H. *et al.* Biaxial deformation of collagen and elastin fibers in coronary adventitia. *J. Appl. Physiol.* (2013).
286. Rezakhaniha, R. *et al.* Experimental investigation of collagen waviness and orientation in the arterial adventitia using confocal laser scanning microscopy. *Biomech. Model. Mechanobiol.* (2012).
287. D'Urso, P. I., Lanzino, G., Cloft, H. J. & Kallmes, D. F. Flow diversion for intracranial aneurysms: a review. *Stroke.* **42,** 2363–8 (2011).
288. Mut, F. *et al.* Association between hemodynamic conditions and occlusion times after flow diversion in cerebral aneurysms. *J. Neurointerv. Surg.* **7,** 286–290 (2015).
289. Ouared, R. *et al.* Computational fluid dynamics analysis of flow reduction induced by flow-diverting stents in intracranial aneurysms: A patient-unspecific hemodynamics change perspective. *J. Neurointerv. Surg.* (2016).
290. Zhang, P., Sun, A., Zhan, F., Luan, J. & Deng, X. Hemodynamic study of overlapping bare-metal stents intervention to aortic aneurysm. *J. Biomech.* **47,** 3524–30 (2014).
291. Walcott, B. P., Stapleton, C. J., Choudhri, O. & Patel, A. B. Flow Diversion for the Treatment of Intracranial Aneurysms. *JAMA Neurol.* **73,** 1002–8 (2016).

292. Kallmes, D. F. *et al.* A second-generation, endoluminal, flow-disrupting device for treatment of saccular aneurysms. *Am. J. Neuroradiol.* (2009).
293. Sultan, S. & Hynes, N. One-year results of the multilayer flow modulator stent in the management of thoracoabdominal aortic aneurysms and type B dissections. *J. Endovasc. Ther.* (2013).
294. Zhang, Y. X., Lu, Q. S. & Jing, Z. P. Multilayer stents, a new progress in the endovascular treatment of aneurysms. *Chin. Med. J. (Engl).* **126,** 536–541 (2013).
295. Zhang, Y. *et al.* Management of complicated aortic aneurysms using multiple overlapping uncovered stents: mid-term outcome from a cohort study. *Medicine (Baltimore).* (2014).
296. Taubin, G. Curve and surface smoothing without shrinkage. in *Proceedings of IEEE International Conference on Computer Vision* 852–857 (IEEE Comput. Soc. Press).
297. Ebenstein, D. M., Coughlin, D., Chapman, J., Li, C. & Pruitt, L. A. Nanomechanical properties of calcification, fibrous tissue, and hematoma from atherosclerotic plaques. *J. Biomed. Mater. Res. A* **91,** 1028–37 (2009).
298. Poelma, C., Watton, P. N. & Ventikos, Y. Transitional flow in aneurysms and the computation of haemodynamic parameters. *J. R. Soc. Interface* **12,** 20141394- (2015).
299. Tan, F. P. P. *et al.* Analysis of flow patterns in a patient-specific thoracic aortic aneurysm model. *Comput. Struct.* (2009).
300. Olufsen, M. S. *et al.* Numerical simulation and experimental validation of blood flow in arteries with structured-tree outflow conditions. *Ann. Biomed. Eng.* (2000).
301. Cebral, J. R. *et al.* Aneurysm rupture following treatment with flow-diverting stents: computational hemodynamics analysis of treatment. *AJNR. Am. J. Neuroradiol.* **32,** 27–33 (2011).
302. Murray, C. D. The physiological principle of minimum work: a reply. *J. Gen. Physiol.* **14,** 445 (1931).
303. Caro, C. G., Fitz-Gerald, J. M. & Schroter, R. C. Arterial wall shear and distribution of early atheroma in man. *Nature* **223,** 1159–60 (1969).
304. Kawaguchi, T. *et al.* Distinctive flow pattern of wall shear stress and oscillatory shear index: similarity and dissimilarity in ruptured and unruptured cerebral aneurysm blebs. *J. Neurosurg.* **117,** 774–80 (2012).
305. Himburg, H. A. Spatial comparison between wall shear stress measures and porcine arterial endothelial permeability. *AJP Hear. Circ. Physiol.* (2004).
306. Sugiyama, S. I. *et al.* Relative residence time prolongation in intracranial aneurysms: A possible association with atherosclerosis. *Neurosurgery* **73,** 767–776 (2013).
307. Zhang, P., Liu, X., Sun, A., Fan, Y. & Deng, X. Hemodynamic insight into overlapping bare-metal stents strategy in the treatment of aortic aneurysm. *J. Biomech.* (2015).
308. Nesbitt, W. S. *et al.* A shear gradient-dependent platelet aggregation mechanism drives thrombus formation. *Nat. Med.* **15,** 665–73 (2009).
309. Li, Z. Y. *et al.* Impact of calcification and intraluminal thrombus on the computed wall stresses of abdominal aortic aneurysm. *J. Vasc. Surg.* (2008).
310. Kazi, M. *et al.* Influence of intraluminal thrombus on structural and cellular composition of abdominal aortic aneurysm wall. *J. Vasc. Surg.* **38,** 1283–92 (2003).
311. Vorp, D. A. *et al.* Association of intraluminal thrombus in abdominal aortic aneurysm with local hypoxia and wall weakening. *J. Vasc. Surg.* (2001).
312. Nchimi, A. *et al.* Multimodality imaging assessment of the deleterious role of the intraluminal thrombus on the growth of abdominal aortic aneurysm in a rat model. *Eur. Radiol.* (2016).
313. Augsburger, L. *et al.* Effect of flow diverter porosity on intraaneurysmal blood flow. *Clin. Neuroradiol.* **19,** 204–214 (2009).
314. Liou, T. M. & Li, Y. C. Effects of stent porosity on hemodynamics in a sidewall aneurysm model. *J. Biomech.* **41,** 1174–1183 (2008).
315. Rhee, K., Han, M. H. & Cha, S. H. Changes of flow characteristics by stenting in aneurysm models: Influence of aneurysm geometry and stent porosity. *Ann. Biomed. Eng.* (2002).
316. Sfyroeras, G. S. *et al.* Flow-diverting stents for the treatment of arterial aneurysms. *J. Vasc. Surg.* **56,** 839–46 (2012).
317. Di Martino, E. S. *et al.* Biomechanical properties of ruptured versus electively repaired abdominal aortic aneurysm wall tissue. *J. Vasc. Surg.* (2006).
318. Rectors, T. *et al. Biomechanics of Soft Tissue in Cardiovascular Systems*. (Springer Vienna, 2003).

319. Mohan, D. & Melvin, J. W. Failure properties of passive human aortic tissue. I--uniaxial tension tests. *J. Biomech.* **15,** 887–902 (1982).
320. Reeps, C. *et al.* Measuring and modeling patient-specific distributions of material properties in abdominal aortic aneurysm wall. *Biomech. Model. Mechanobiol.* (2013).
321. Vorp, D. A. *et al.* Effect of aneurysm on the tensile strength and biomechanical behavior of the ascending thoracic aorta. *Ann. Thorac. Surg.* (2003).
322. Dutta, a & Tarbell, J. M. Influence of non-Newtonian behavior of blood on flow in an elastic artery model. *J. Biomech. Eng.* (1996).
323. Perktold, K., Peter, R. O., Resch, M. & Langs, G. Pulsatile non-newtonian blood flow in three-dimensional carotid bifurcation models: a numerical study of flow phenomena under different bifurcation angles. *J. Biomed. Eng.* (1991).
324. Khanafer, K. M., Gadhoke, P., Berguer, R. & Bull, J. L. Modeling pulsatile flow in aortic aneurysms: effect of non-Newtonian properties of blood. *Biorheology* (2006).
325. Huang, Y. *et al.* The influence of computational strategy on prediction of mechanical stress in carotid atherosclerotic plaques: Comparison of 2D structure-only, 3D structure-only, one-way and fully coupled fluid-structure interaction analyses. *J. Biomech.* (2014).
326. Lu, Q., Zhang, Y. & Jing, Z. Reply. *J. Vasc. Surg.* **62,** 269–270 (2015).
327. Cekirge, H. S., Yavuz, K., Geyik, S. & Saatci, I. A novel 'Y' stent flow diversion technique for the endovascular treatment of bifurcation aneurysms without endosaccular coiling. *Am. J. Neuroradiol.* **32,** 1262–1268 (2011).
328. Crowley, R. W., Evans, A. J., Kassell, N. F., Jensen, M. E. & Dumont, A. S. Endovascular treatment of a fusiform basilar artery aneurysm using multiple 'in-stent stents'. Technical note. *J. Neurosurg. Pediatr.* **3,** 496–500 (2009).
329. Bain, M. *et al.* 'Double-barrel' stent reconstruction of a symptomatic fusiform basilar artery aneurysm: Case report. *Neurosurgery* **68,** 1491–1496 (2011).
330. Bouillot, P. *et al.* Particle imaging velocimetry evaluation of intracranial stents in sidewall aneurysm: Hemodynamic transition related to the stent design. *PLoS One* **9,** 1–17 (2014).
331. Roszelle, B. N. *et al.* Flow diverter effect on cerebral aneurysm hemodynamics: an in vitro comparison of telescoping stents and the Pipeline. *Neuroradiology* **55,** 751–8 (2013).
332. Roszelle, B. N. *et al.* In vitro and in silico study of intracranial stent treatments for cerebral aneurysms: effects on perforating vessel flows. *J. Neurointerv. Surg.* **5,** 354–60 (2013).
333. Dai, D. *et al.* Patency of branches after coverage with multiple telescoping flow-diverter devices: an in vivo study in rabbits. *AJNR. Am. J. Neuroradiol.* **33,** 171–4 (2012).
334. Tremmel, M. *et al.* Alteration of intra-aneurysmal hemodynamics for flow diversion using enterprise and vision stents. *World Neurosurg.* **74,** 306–15 (2011).
335. Cantón, G., Levy, D. I., Lasheras, J. C. & Nelson, P. K. Flow changes caused by the sequential placement of stents across the neck of sidewall cerebral aneurysms. *J. Neurosurg.* **103,** 891–902 (2005).
336. Zhang, P., Liu, X., Sun, A., Fan, Y. & Deng, X. Hemodynamic insight into overlapping bare-metal stents strategy in the treatment of aortic aneurysm. *J. Biomech.* **48,** 2041–6 (2015).
337. Zhang, P., Sun, A., Zhan, F., Luan, J. & Deng, X. Hemodynamic study of overlapping bare-metal stents intervention to aortic aneurysm. *J. Biomech.* **47,** 3524–30 (2014).
338. Huang, Y. *et al.* High structural stress and presence of intraluminal thrombus predict abdominal aortic aneurysm 18F-FDG uptake: insights from biomechanics. *Circ. Cardiovasc. Imaging* (2016).
339. Kwak, B. R. *et al.* Biomechanical factors in atherosclerosis: mechanisms and clinical implications. *Eur. Heart J.* **35,** 3013–3020 (2014).
340. Sadat, U., Teng, Z. & Gillard, J. H. Biomechanical structural stresses of atherosclerotic plaques. *Expert Rev. Cardiovasc. Ther.* **8,** 1469–81 (2010).
341. Haga, J. H., Li, Y. S. J. & Chien, S. Molecular basis of the effects of mechanical stretch on vascular smooth muscle cells. *J. Biomech.* **40,** 947–960 (2007).
342. Qiu, J. *et al.* Biomechanical regulation of vascular smooth muscle cell functions: from in vitro to in vivo understanding. *J. R. Soc. Interface* (2014).
343. Wang, B.-W., Chang, H., Lin, S., Kuan, P. & Shyu, K.-G. Induction of matrix metalloproteinases-14 and -2 by cyclical mechanical stretch is mediated by tumor necrosis factor-alpha in cultured human umbilical vein endothelial cells. *Cardiovasc Res* (2003).

344. Hallow, K. M., Taylor, W. R., Rachev, A. & Vito, R. P. Markers of inflammation collocate with increased wall stress in human coronary arterial plaque. *Biomech. Model. Mechanobiol.* (2009).
345. Niimi, H. Role of stress concentration in arterial walls in atherogenesis1. *Biorheology* **16,** 223–230 (1979).
346. De Langen, C. D. The pressure gradient in the arterial wall and the problem of arteriosclerosis. *Cardiologia* **22,** 315–9 (1953).
347. Thubrikar, M. J., Baker, J. W. & Nolan, S. P. Inhibition of atherosclerosis associated with reduction of arterial intramural stress in rabbits. *Arteriosclerosis* (1988).
348. Tropea, B. I. *et al.* Reduction of aortic wall motion inhibits hypertension-mediated experimental atherosclerosis. *Arterioscler. Thromb. Vasc. Biol.* (2000).
349. Chaabane, C., Otsuka, F., Virmani, R. & Bochaton-Piallat, M. L. Biological responses in stented arteries. *Cardiovascular Research* (2013).
350. Fujimoto, M. *et al.* Temporal correlation between wall shear stress and in-stent stenosis after Wingspan stent in swine model. *Am. J. Neuroradiol.* **39,** 994–998 (2014).
351. Hsiao, H.-M., Lee, K.-H., Liao, Y.-C. & Cheng, Y.-C. Cardiovascular stent design and wall shear stress distribution in coronary stented arteries. *Micro Nano Lett.* **7,** 430 (2012).
352. Benard, N., Coisne, D., Donal, E. & Perrault, R. Experimental study of laminar blood flow through an artery treated by a stent implantation: Characterisation of intra-stent wall shear stress. *J. Biomech.* **36,** 991–998 (2003).
353. Jenei, C., Balogh, E., Szabó, G. T., Dézsi, C. A. & Kőszegi, Z. Wall shear stress in the development of in-stent restenosis revisited. A critical review of clinical data on shear stress after intracoronary stent implantation. *Cardiol. J.* **23,** 365–373 (2016).
354. Bergel, D. H. The static elastic properties of the arterial wall. *J. Physiol.* (1961).
355. Huang, Y. *et al.* Non-uniform shrinkage for obtaining computational start shape for in-vivo MRI-based plaque vulnerability assessment. *J. Biomech.* **44,** 2316–2319 (2011).
356. O'Rourke, M. F. From theory into practice: Arterial haemodynamics in clinical hypertension. *Journal of Hypertension* (2002).
357. Kurashina, T. *et al.* A new device for indirect blood pressure measurement in rabbits. *Jpn. Circ. J.* (1994).
358. Williams, C. *et al.* Altered structural and mechanical properties in decellularized rabbit carotid arteries. *Acta Biomater.* **5,** 993–1005 (2009).
359. Teng, Z. *et al.* A uni-extension study on the ultimate material strength and extreme extensibility of atherosclerotic tissue in human carotid plaques. *J. Biomech.* (2015).
360. Cristianini, N. & Shawe-Taylor, J. An Introduction to Support Vector Machines and other kernel based learning methods. *Ai Magazine* (2000).
361. Owens, C. D. Adaptive changes in autogenous vein grafts for arterial reconstruction: Clinical implications. *Journal of Vascular Surgery* (2010).
362. Ren, L. *et al.* Correlation between hypertension and common carotid artery intima-media thickness in rural China: a population-based study. *J. Hum. Hypertens.* **32,** 548–554 (2018).
363. Jufri, N. F., Mohamedali, A., Avolio, A. & Baker, M. S. Mechanical stretch: Physiological and pathological implications for human vascular endothelial cells. *Vasc. Cell* **7,** 1–12 (2015).
364. Zheng, W., Christensen, L. P. & Tomanek, R. J. Differential effects of cyclic and static stretch on coronary microvascular endothelial cell receptors and vasculogenic/angiogenic responses. *Am. J. Physiol. Heart Circ. Physiol.* (2008).
365. Zheng, W., Christensen, L. P. & Tomanek, R. J. Stretch induces upregulation of key tyrosine kinase receptors in microvascular endothelial cells. *Am. J. Physiol. Heart Circ. Physiol.* (2004).
366. Li, W. & Sumpio, B. E. Strain-induced vascular endothelial cell proliferation requires PI3K-dependent mTOR-4E-BP1 signal pathway. *Am. J. Physiol. Heart Circ. Physiol.* (2005).
367. Von Offenberg Sweeney, N. *et al.* Cyclic strain-mediated regulation of endothelial matrix metalloproteinase-2 expression and activity. *Cardiovasc. Res.* (2004).
368. Reed, D., Reed, C., Stemmermann, G. & Hayashi, T. Are aortic aneurysms caused by atherosclerosis? *Circulation* **85,** 205–11 (1992).
369. Shyu, K.-G. Cellular and molecular effects of mechanical stretch on vascular cells and cardiac myocytes. *Clin. Sci. (Lond).* (2009).

370. Kou, B., Zhang, J. & Singer, D. R. J. Effects of cyclic strain on endothelial cell apoptosis and tubulogenesis are dependent on ROS production via NAD(P)H subunit p22phox. *Microvasc. Res.* (2009).
371. McWhorter, F. Y., Davis, C. T. & Liu, W. F. Physical and mechanical regulation of macrophage phenotype and function. *Cell. Mol. Life Sci.* **72,** 1303–16 (2015).
372. Xiong, Y. *et al.* Hypertensive stretch regulates endothelial exocytosis of Weibel-Palade bodies through VEGF receptor 2 signaling pathways. *Cell Res.* (2013).
373. Wagner, A. H. *et al.* Upregulation of glutathione peroxidase offsets stretch-induced proatherogenic gene expression in human endothelial cells. *Arterioscler. Thromb. Vasc. Biol.* (2009).
374. Pugin, J. *et al.* Activation of human macrophages by mechanical ventilation in vitro. *Am. J. Physiol.* **275,** L1040-50 (1998).
375. Wehner, S. *et al.* Mechanical strain and TLR4 synergistically induce cell-specific inflammatory gene expression in intestinal smooth muscle cells and peritoneal macrophages. *Am. J. Physiol. Gastrointest. Liver Physiol.* **299,** G1187-97 (2010).
376. Cavinato, C. *et al.* Biaxial loading of arterial tissues with 3D in situ observations of adventitia fibrous microstructure: A method coupling multi-photon confocal microscopy and bulge inflation test. *J. Mech. Behav. Biomed. Mater.* **74,** 488–498 (2017).
377. Niestrawska, J. A. *et al.* Microstructure and mechanics of healthy and aneurysmatic abdominal aortas: experimental analysis and modelling. *J. R. Soc. Interface* **13,** 20160620 (2016).
378. Holzapfel, G. A. Determination of material models for arterial walls from uniaxial extension tests and histological structure. *J. Theor. Biol.* **238,** 290–302 (2006).
379. Weisbecker, H., Unterberger, M. J. & Holzapfel, G. A. Constitutive modelling of arteries considering fibre recruitment and three-dimensional fibre distribution. *J. R. Soc. Interface* **12,** 20150111–20150111 (2015).
380. Chuong, C. J. & Fung, Y. C. On Residual Stresses in Arteries. *J. Biomech. Eng.* (1986).
381. Koktzoglou, I., Lim, R. P., Flanagan, O. & Edelman, R. R. in *Basic Principles of Cardiovascular MRI* **35,** 297–314 (Springer International Publishing, 2015).
382. Goldstein, H., Browne, W. & Rasbash, J. Multilevel modelling of medical data. *Stat. Med.* (2002).
383. Pereira, V. M. *et al.* A DSA-based method using contrast-motion estimation for the assessment of the intra-aneurysmal flow changes induced by flow-diverter stents. *AJNR. Am. J. Neuroradiol.* **34,** 808–15 (2013).
384. Jou, L. Der & Mawad, M. E. Analysis of intra-aneurysmal flow for cerebral aneurysms with cerebral angiography. *Am. J. Neuroradiol.* **33,** 1679–1684 (2012).
385. Benz, T. *et al.* A Fourier-based approach to the angiographic assessment of flow diverter efficacy in the treatment of cerebral aneurysms. *IEEE Trans. Med. Imaging* **33,** 1788–802 (2014).
386. Kapnisis, K. K. *et al.* Stent overlapping and geometric curvature influence the structural integrity and surface characteristics of coronary nitinol stents. *J. Mech. Behav. Biomed. Mater.* **20,** 227–236 (2013).
387. Auricchio, F., Constantinescu, A., Conti, M. & Scalet, G. Fatigue of Metallic Stents: From Clinical Evidence to Computational Analysis. *Ann. Biomed. Eng.* **44,** 287–301 (2016).
388. Otsu, N. A threshold selection method from gray-level histograms. *IEEE Trans. Syst. Man. Cybern.* **9,** 62–66 (1979).
389. MathWorks, U. multithresh - Matlab R2017b Documentation. (2017).
390. Douglas, G. R. *et al.* Impact of fiber structure on the material stability and rupture mechanisms of coronary atherosclerotic plaques. *Ann. Biomed. Eng.* **45,** 1462–1474 (2017).
391. Holzapfel, G. a, Gasser, T. C. & Ogden, R. W. A new constitutive framework for arterial wall mechanics and a comparative study of material models. *J. Elast.* **61,** 1–48 (2000).
392. Holzapfel, G. A. & Ogden, R. W. Constitutive modelling of arteries. *Proc. R. Soc. A Math. Phys. Eng. Sci.* **466,** 1551–1597 (2010).
393. Gasser, T. C., Ogden, R. W. & Holzapfel, G. A. Hyperelastic modelling of arterial layers with distributed collagen fibre orientations. *J. R. Soc. Interface* **3,** 15–35 (2006).